

**INTRODUCTION TO GRAVITATIONAL WAVES  
AND DETECTION PRINCIPLES**

A dissertation submitted as partial fulfilment  
of the  
100 – Hour Certificate Course in  
Astronomy & Astrophysics

By

**SUDARSHAN .S. HARITHAS**

**M. P. Birla Institute of Fundamental Research  
Bangalore, India**

**October 2017**

## **DECLARATION**

I, Sudarshan.S.Harithas student of M. P. Birla Institute of Fundamental Research, Bangalore, hereby declare that the matter embodied in this dissertation has been compiled and prepared by me on the basis of available literature on the topic titled

**“INTRODUCTION TO GRAVITATIONAL WAVES AND DETECTION PRINCIPLES”**

as a partial fulfilment of the 100 – Hour Certificate Course in Astronomy and Astrophysics, 2017. This dissertation has not been submitted either partially or fully to any university or institute for the award of any degree, diploma or fellowship.

Date: 4-11-17

Place: BANGALORE

Sudarshan.S.Harithas

Senior Scientist

M.P .Birla Institute of Fundamental Research  
Bangalore

## TABLE OF CONTENTS

### **1) INTRODUCTION**

    1.1) HISTORY

### **2) GENERATION OF GRAVITATIONAL WAVES**

### **3) SOURCES OF GRAVITATIONAL WAVES**

    3.1) COMPACT BINARY COALESCENCE

    3.2) WHITE DWARF BINARIES

    3.3) BURSTS

    3.4) CONTINUOUS WAVES

    3.5) STOCHASTIC WAVES

    3.6) MAN MADE SOURCES

### **4) CHARACTERISTICS OF GRAVITATIONAL WAVES**

    4.1) POLARIZATION OF GRAVITATIONAL WAVES

    4.2) FREQUENCY OF GRAVITATIONAL WAVES

    4.3) AMPLITUDE OF GRAVITATIONAL WAVES

    4.4) LUMINOSITY OF GRAVITATIONAL WAVES

### **5) PHYSICS WITH GRAVITATIONAL WAVES**

    5.1) SPEED OF GRAVITATIONAL WAVES

    5.2) POLARIZATION OF GRAVITATIONAL WAVES

    5.3) GRAVITATIONAL RADIATION REACTION

    5.4) BLACK HOLE SPECTROSCOPY

    5.5) THE TWO BODY PROBLEM IN GENERAL RELATIVITY

        5.5.1) BINARIES AS STANDARD CANDLES : DISTANCE ESTIMATION

5.5.2) NUMERICAL APPROACH TO THE TWO BODY PROBLEM

5.5.3) POST NEWTONIAN APPROXIMATION IN THE TWO BODY PROBLEM

5.5.4) MEASURING PARAMETERS OF INSPIRING BINARIES

5.5.5) IMPROVEMENT FROM HIGHER FREQUENCIES

5.6) TESTS OF GENERAL RELATIVITY

5.6.1) TEST OF POST NEWTONIAN APPROXIMATION

5.6.2) QUANTUM GRAVITY

## 6) ASTROPHYSICS WITH GRAVITATIONAL WAVES

6.1) INTERACTING COMPACT BINARIES

6.1.1) RESOLVING MASS INCLINATION DEGENERACY

6.2) BLACK HOLE ASTROPHYSICS

6.2.1) GRAVITATIONAL WAVES FROM STELLAR MASS BLACK HOLES

6.2.2) STELLAR MASS BLACK HOLE BINARIES

6.2.3) INTERMEDIATE MASS BLACK HOLES

6.2.4) SUPER MASSIVE BLACK HOLES

6.3) NEUTRON STAR ASTROPHYSICS

6.3.1) GRAVITATIONAL COLLAPSE AND FORMATION OF NEUTRON STARS

6.3.2) NEUTRON STAR BINARY MERGES

6.3.3) NEUTRON STAR NORMAL MODE OF OSCILLATION

6.3.4) STELLAR INSTABILITIES

6.3.5) LOW MASS X-RAY BINARIES

6.3.6) GALACTIC POPULATION OF NEUTRON STARS

## 7) COSMOLOGY WITH GRAVITATIONAL WAVE OBSERVATIONS

7.1) DETECTING STOCHASTIC GRAVITATIONAL WAVE BACKGROUND

7.1.1) DESCRIBING A RANDOM GRAVITATIONAL FIELD

7.1.2) OBSERVATIONS WITH GRAVITATIONAL WAVES

7.1.3) OBSERVATIONS WITH PULSAR TIMINGS

7.1.4) OBSERVATIONS WITH COSMIC MICROWAVE BACKGROUND

**7.2) ORIGIN OF RANDOM BACKGROUND GRAVITATIONAL WAVE**

**7.2.1) GRAVITATIONAL WAVES FROM BIG BANG**

**7.2.2) ASTROPHYSICS SOURCES OF STOCHASTIC BACKGROUND**

**7.3) COSMOGRAPHY : GRAVITATIONAL WAVE MEASUREMENTS FROM  
COSMOLOGICAL PARAMETERS**

**8) GRAVITATIONAL WAVES VS ELECTROMAGNETIC WAVES**

**9) GRAVITATIONAL WAVE DETECTORS**

**9.1) OVERVIEW OF GRAVITATIONAL WAVE DETECTION**

**9.2) DETECTOR SENSITIVITY AND RESOLUTION CONSIDERATIONS**

**9.3) FIRST GENERATION LIGO INTERFEROMETERS**

**9.3.1) FABRY-PEROT CAVITY**

**9.3.2) POWER RECYCLED MICHELSON INTERFEROMETER AND INITIAL LIGO**

**9.3.3) ENHANCED LIGO**

**9.3.4) VIRGO INTERFEROMETER**

**9.3.5) GEO 600 INTERFEROMETER**

**9.3.6) TAMA INTERFEROMETER**

**9.4) SECOND GENERATION INTERFEROMETERS**

**10) ADVANCED LIGO**

**10.1) LAYOUT OF ADVANCED LIGO DETECTORS**

**10.2) INTERFEROMETER CONFIGURATION**

**10.2.1) INTERFEROMETER CONTROLS**

**10.2.2) STRAIN CALIBRATION**

**10.3) DESIGN OF INTERFEROMETER**

**10.3.1) ARM CAVITY DESIGN**

**10.3.2) RECYCLING CAVITY DESIGN**

**10.3.3) GRAVITATIONAL WAVE READOUT**

**10.3.4) HIGH POWER EFFECT**

**10.4) ANALYSIS OF INSTRUMENTAL NOISE**

- 10.4.1) SEISMIC AND THERMAL NOISE
  - 10.4.2) QUANTUM NOISE
  - 10.4.3) GAS NOISE
  - 10.4.4) CHARGING NOISE
  - 10.4.5) LASER AMPLITUDE AND FREQUENCY NOISE
  - 10.4.6) AUXILIARY DEGREES-OF-FREEDOM
  - 10.4.7) OSCILLATOR NOISE
  - 10.4.8) BEAM JITTER
  - 10.4.9) SCATTERED LIGHT NOISE
  - 10.4.10) SENSING ACTUATION AND ELECTRONICS NOISE
- 10.5) DETECTOR SUBSYSTEMS
- 10.5.1) LASER SOURCE
  - 10.5.2) INPUT OPTICS
  - 10.5.3) CORE OPTICS
  - 10.5.4) SUSPENSIONS
  - 10.5.5) SEISMIC ISOLATION
  - 10.5.6) THERMAL COMPENSATION
  - 10.5.7) SCATTERED LIGHT CONTROL
  - 10.5.8) GLOBAL SENSING AND CONTROL
  - 10.5.9) CALIBRATION
  - 10.5.10) PHYSICAL ENVIRONMENTAL MONITORING
  - 10.5.11) CONTROL AND DATA ACQUISITION
  - 10.5.12) OUTLOOK

## **11) CASE STUDY : GW150914**

- 11.1) OBSERVATION
- 11.2) VALIDATION OF DETECTORS

### **11.3) SEARCHES**

11.3.1) A GENERIC TRANSIENT SEARCH

11.3.2) BINARY COALESCENCE SEARCH

### **11.4) SOURCE DISCUSSION**

### **11.5) CONCLUSION**

## **BIBLIOGRAPHY**

## 1) INTRODUCTION

In Einstein's theory of general relativity, gravity is treated as a phenomenon resulting from the curvature of spacetime. This curvature is caused by the presence of mass. Generally, the more mass that is contained within a given volume of space, the greater the curvature of spacetime will be at the boundary of its volume. As objects with mass move around in spacetime, the curvature changes to reflect the changed locations of those objects. In certain circumstances, accelerating objects generate changes in this curvature, which propagate outwards at the speed of light in a wave-like manner. These propagating phenomena are known as gravitational waves.

As a gravitational wave passes an observer, that observer will find spacetime distorted by the effects of strain. Distances between objects increase and decrease rhythmically as the wave passes, at a frequency corresponding to that of the wave. This occurs despite such free objects never being subjected to an unbalanced force. The magnitude of this effect decreases proportional to the inverse distance from the source. Inspiring binary neutron stars are predicted to be a powerful source of gravitational waves as they coalesce, due to the very large acceleration of their masses as they orbit close to one another. However, due to the astronomical distances to these sources, the effects when measured on Earth are predicted to be very small, having strains of less than 1 part in  $10^{20}$ . Scientists have demonstrated the existence of these waves with ever more sensitive detectors. The most sensitive detector accomplished the task possessing a sensitivity measurement of about one part in  $5 \times 10^{22}$  (as of 2012) provided by the LIGO and VIRGO observatories. A space based observatory, the Laser Interferometer Space Antenna , is currently under development by ESA.

Gravitational waves can penetrate regions of space that electromagnetic waves cannot. They are able to allow the observation of the merger of black holes and possibly other exotic objects in the distant Universe. Such systems cannot be observed with more traditional means such as optical telescopes or radio telescopes, and so gravitational-wave astronomy gives new insights into the working of the Universe. In particular, gravitational waves could be of interest to cosmologists as they offer a possible way of observing the very early Universe. This is not possible with conventional astronomy, since before recombination the Universe was opaque to electromagnetic radiation. Precise measurements of gravitational waves will also allow scientists to test more thoroughly the general theory of relativity.

In principle, gravitational waves could exist at any frequency. However, very low frequency waves would be impossible to detect and there is no credible source for detectable waves of very high frequency. Stephen Hawking and Werner Israel list different frequency bands for gravitational waves that could plausibly be detected, ranging from  $10^{-7}$  Hz up to  $10^{11}$  Hz.

### 1.1) HISTORY

In 1905, Henri Poincaré first suggested that in analogy to an accelerating electrical charge producing electromagnetic waves, accelerated masses in a relativistic field theory of

gravity should produce gravitational waves. When Einstein published his theory of general relativity in 1915, he was skeptical of Poincaré's idea since the theory implied there were no "gravitational dipoles". Nonetheless, he still pursued the idea and based on various approximations came to the conclusion there must, in fact, be three types of gravitational wave (dubbed longitudinal-longitudinal, transverse-longitudinal, and transverse-transverse by Hermann Wey).

However, the nature of Einstein's approximations led many (including Einstein himself) to doubt the result. In 1922, Arthur Eddington showed that two of Einstein's types of waves were artifacts of the coordinate system he used, and could be made to propagate at any speed by choosing appropriate coordinates, leading Eddington to jest that they "propagate at the speed of thought". This also cast doubt on the physicality of the third (transverse-transverse) type (which Eddington showed always propagate at the speed of light regardless of coordinate system). In 1936, Einstein and Nathan Rosen submitted a paper to Physical Review in which they claimed gravitational waves could not exist in the full theory of general relativity because any such solution of the field equations would have a singularity. The journal sent their manuscript to be reviewed by Howard P. Robertson, who (anonymously) reported that the singularities in question were simply the harmless coordinate singularities of the employed cylindrical coordinates. Einstein, who was unfamiliar with the concept of peer review, angrily withdrew the manuscript, never to publish in Physical Review again. Nonetheless, his assistant Leopold Infeld, who had been in contact with Robertson, convinced Einstein that the criticism was correct, and the paper was rewritten with the opposite conclusion (and published elsewhere).

In 1956, Felix Pirani remedied the confusion caused by the use of various coordinate systems by rephrasing the gravitational waves in terms of the manifestly observable Riemann curvature tensor. At the time this work was mostly ignored because the community was focused on a different question: whether gravitational waves could transmit energy. This matter was settled by a thought experiment proposed by Richard Feynman during the first "GR" conference at Chapel Hill in 1957. In short, his argument (known as the "sticky bead argument") notes that if one takes a rod with beads then the effect of a passing gravitational wave would be to move the beads along the rod; friction would then produce heat, implying that the passing wave had done work. Shortly after, Hermann Bondi (a former gravitational wave skeptic) published a detailed version of the "sticky bead argument".

After the Chapel Hill conference, Joseph Weber started designing and building the first gravitational wave detectors now known as Weber bars. In 1969, Weber claimed to have detected the first gravitational waves, and by 1970 he was "detecting" signals regularly from the center of Milky Way; however, the frequency of detection soon raised doubts on the validity of his observations as the implied rate of energy loss of the Milky Way would drain our galaxy of energy on a timescale much shorter than its inferred age. These doubts were strengthened when, by the mid-1970s, repeat experiments from other groups building their own Weber bars across the globe failed to find any signals, and by the late 1970s general consensus was that Weber's results were spurious.

In the same period, the first indirect evidence for the existence of gravitational waves was discovered. In 1974, Russell Alan Hulse and Joseph Hooton Taylor, Jr. discovered the first binary pulsar (a discovery that earned them the 1993 Nobel Prize in Physics). In 1979, results were published detailing measurement of the gradual decay of the orbital period of the Hulse-Taylor pulsar, which fitted precisely with the loss of energy and angular momentum in gravitational radiation predicted by general relativity.<sup>[28]</sup>

This indirect detection of gravitational waves motivated further searches despite Weber's discredited result. Some groups continued to improve Weber's original concept, while others pursued the detection of gravitational waves using laser interferometers. The idea of using a laser interferometer to detect gravitational waves seems to have been floated by various people independently, including M. E. Gertsenshtein and V. I. Pustovoit in 1962, and Vladimir B. Braginskii in 1966. The first prototypes were developed in the 1970s by Robert L. Forward and Rainer Weiss. In the decades that followed, ever more sensitive instruments were constructed, culminating in the construction of GEO600, LIGO, and Virgo.

After years of producing null results, LIGO made the first direct detection of gravitational waves on 14 September 2015. It was inferred that the signal, dubbed GW150914, originated from the merger of two black holes with masses  $36^{+5}_{-4} \text{ M}_\odot$  and  $29^{+4}_{-4} \text{ M}_\odot$ , resulting in a  $62^{+4}_{-4} \text{ M}_\odot$  black hole.

A year earlier it appeared LIGO might have been beaten to the punch when the BICEP2 claimed that they had detected the imprint of gravitational waves in the cosmic microwave background. However, they were later forced to retract their result.

In 2017, the Nobel Prize in Physics was awarded to Rainer Weiss, Kip Thorne and Barry Barish for their role in the detection of gravitational waves.

## 1) GENERATION OF GRAVITATIONAL WAVES

when the gravitational field is strong there are a number of nonlinear effects that influence the generation and propagation of gravitational waves. For example, nonlinear effects are significant during the last phases of black hole formation. The analytic description of such a dynamically changing spacetime is impossible, and until numerical relativity provides us with accurate estimates of the dynamics of gravitational fields under such extreme conditions we have to be content with order of magnitude estimates. Furthermore, there are differences in the predictions of various relativistic theories of gravity in the case of high concentrations of rapidly varying energy distributions. However, all metric theories of gravity, as long as they admit the correct Newtonian limit, make similar predictions for the total amount of gravitational radiation emitted by "weak" gravitational wave sources, that is, sources where the energy content is small enough to produce only small deformations of the flat spacetime and where all motions are slow compared to the velocity of light.

Electromagnetic radiation emitted by slowly varying charge distributions can be decomposed into a series of multipoles, where the amplitude of the  $2^l$ -pole ( $l = 0, 1, 2, \dots$ ) contains a small factor  $a$ , with  $a$  equal to the ratio of the diameter of the source to the typical wavelength, namely,  $a^l$  number typically much smaller than 1. From this point of view the strongest electromagnetic radiation would be expected for monopolar radiation ( $l = 0$ ), but this is completely absent, because the electromagnetic monopole moment is proportional to the total charge, which does not change with time (it is a conserved quantity). Therefore, electromagnetic radiation consists only of  $l \geq 1$  multipoles, the strongest being the electric dipole radiation ( $l = 1$ ), followed by the weaker magnetic dipole and electric quadrupole radiation ( $l = 2$ ). One could proceed with a similar analysis for gravitational waves and by following the same arguments show that mass conservation (which is equivalent to charge conservation in electromagnetic theory) will exclude monopole radiation. Also, the rate of change of the mass dipole moment is proportional to the linear momentum of the system, which

is a conserved quantity, and therefore there cannot be any mass dipole radiation in Einstein's relativity theory. The next strongest form of electromagnetic radiation is the magnetic dipole. For the case of gravity, the change of the magnetic dipole is proportional to the angular momentum of the system, which is also a conserved quantity and thus there is no dipolar gravitational radiation of any sort. It follows that gravitational radiation is of quadrupolar or higher nature and is directly linked to the quadrupole moment of the mass distribution.

As early as 1918, Einstein derived the quadrupole formula for gravitational radiation. This formula states that the wave amplitude  $h_{ij}$  is proportional to the second time derivative of the quadrupole moment of the source:

$$h_{ij} = \frac{2G}{r c^4} \ddot{Q}_{ij}^{TT} \left( t - \frac{r}{c} \right)$$

Where ,

$$Q_{ij}^{TT}(x) = \int \rho \left( x^i x^j - \frac{1}{3} \delta^{ij} r^2 \right) d^3x$$

is the quadrupole moment in the TT gauge, evaluated at the retarded time  $t-r/c$  and  $\rho$  is the matter density in a volume element  $d^3x$  at the position  $x_i$ . This result is quite accurate for all sources, as long as the reduced wavelength  $\lambda = \lambda/2\pi$  is much longer than the source size  $R$ . It should be pointed out that the above result can be derived via a quite cumbersome calculation in which we solve the wave equation

$$\left( -\frac{\partial^2}{\partial t^2} + \nabla^2 \right) \tilde{h}^{\mu\nu} \equiv \partial_\lambda \partial^\lambda \tilde{h}^{\mu\nu} = 0$$

with a source term  $T_{\mu\nu}$  on the right-hand side. In the course of such a derivation, a number of assumptions must be used. In particular, the observer must be located at a distance  $r \gg \lambda$ , far greater than the reduced wavelength (in what is called the radiation zone) and  $T_{\mu\nu}$  must not change very quickly.

Using the formulae

$$t_{\mu\nu}^{GW} = \frac{1}{32\pi} \langle (\partial_\mu h_{ij}^{TT}) (\partial_\nu h_{ij}^{TT}) \rangle.$$

And

$$t_{00}^{GW} = \frac{t_{zz}^{GW}}{c^2} = -\frac{t_{0z}^{GW}}{c} = \frac{1}{32\pi G} \frac{c^2}{\omega^2} (h_+^2 + h_x^2),$$

for the energy carried by gravitational waves, one can derive the luminosity in gravitational waves as a function of the third-order time derivative of the quadrupole moment tensor. This is the quadrupole formula

$$L_{GW} = -\frac{dE}{dt} = \frac{1}{5} \frac{G}{c^5} \left( \frac{\partial^3 Q_{ij}}{\partial t^3} \right) \frac{\partial^3 Q_{ij}}{\partial t^3}.$$

Based on this formula, we derive some additional formulas, which provide order of magnitude estimates for the amplitude of the gravitational waves and the corresponding power output of a source. First, the quadrupole moment of a system is approximately equal to the mass M of the part of the system that moves, times the square of the size R of the system. This means that the third-order time derivative of the quadrupole moment is

$$\frac{\partial^3 Q_{ij}}{\partial t^3} \sim \frac{MR^2}{T^3} \sim \frac{Mv^2}{T} \sim \frac{E_{ns}}{T},$$

where v is the mean velocity of the moving parts,  $E_{ns}$  is the kinetic energy of the component of the source's internal motion which is non spherical, and T is the time scale for a mass to move from one side of the system to the other. The time scale (or period) is actually proportional to the inverse of the square root of the mean density of the system

$$T \sim \sqrt{R^3/GM}.$$

This relation provides a rough estimate of the characteristic frequency of the system  $f = 2\pi/T$ . Then, the luminosity of gravitational waves of a given source is approximately

$$L_{GW} \sim \frac{G}{c^5} \left( \frac{M}{R} \right)^5 \sim \frac{G}{c^5} \left( \frac{M}{R} \right)^2 v^6 \sim \frac{c^5}{G} \left( \frac{R_{Sch}}{R} \right)^2 \left( \frac{v}{c} \right)^6$$

where  $R_{Sch} = 2GM/c^2$  is the Schwarzschild radius of the source. It is obvious that the maximum value of the luminosity in gravitational waves can be achieved if the source's dimensions are of the order of its Schwarzschild radius and the typical velocities of the components of the system are of the order of the speed of light. This explains why we expect the best gravitational wave sources to be highly relativistic compact objects. The above formula sets also an upper limit on the power emitted by a source, which for  $R \sim R_{Sch}$  and  $v \sim c$  is

$$L_{GW} \sim c^5/G = 3.6 \times 10^{59} \text{ ergs/sec.}$$

This is an immense power, often called the *luminosity of the universe*.

Using the above order-of-magnitude estimates, we can get a rough estimate of the amplitude of gravitational waves at a distance r from the source:

$$h \sim \frac{G E_{ns}}{c^4 r} \sim \frac{G \varepsilon E_{kin}}{c^4 r}$$

where  $\varepsilon_{Ekin}$  (with  $0 \leq \varepsilon \leq 1$ ), is the fraction of kinetic energy of the source that is able to produce gravitational waves. The factor  $\varepsilon$  is a measure of the asymmetry of the source and implies that only a time varying quadrupole moment will emit gravitational waves. For example, even if a huge amount of kinetic energy is involved in a given explosion and/or implosion, if the event takes place in a spherically symmetric manner, there will be no gravitational radiation .

Another formula for the amplitude of gravitational waves relation can be derived from the flux formula

$$F = 3 \left( \frac{f}{1\text{kHz}} \right)^2 \left( \frac{h}{10^{-22}} \right)^2 \frac{\text{ergs}}{\text{cm}^2\text{sec}},$$

If, for example, we consider an event (perhaps a supernovae explosion) at the Virgo cluster during which the energy equivalent of  $10^{-4}M_{\odot}$  is released in gravitational waves at a frequency of 1 kHz, and with signal duration of the order of 1 msec, the amplitude of the gravitational waves on Earth will be

$$h \approx 10^{-22} \left( \frac{E_{GW}}{10^{-4}M_{\odot}} \right)^{1/2} \left( \frac{f}{1\text{kHz}} \right)^{-1} \left( \frac{\tau}{1\text{msec}} \right)^{-1/2} \left( \frac{r}{15\text{Mpc}} \right)^{-1}.$$

For a detector with arm length of 4 km we are looking for changes in the arm length of the order of

$$\Delta\ell = h \cdot \ell = 10^{-22} \cdot 4\text{km} = 4 \times 10^{-17}\text{!!!}$$

it is useful to know the damping time, that is, the time it takes for a source to transform a fraction 1/e of its energy into gravitational radiation. One can obtain a rough estimate from the following formula

$$\tau = \frac{E_{\text{kin}}}{L_{\text{GW}}} \sim \frac{1}{c} R \left( \frac{R}{R_{\text{Sch}}} \right)^3.$$

## 2) SOURCES OF GRAVITATIONAL WAVES

In electromagnetic observations, in every waveband there are sources so strong that they can be detected without knowing anything about the source. You don't need to understand nuclear fusion in order to see the Sun! In contrast, most of the expected sources of gravitational radiation are so weak that sophisticated statistical techniques are required to detect them. These techniques involve matching templates of expected waveforms against the observed data stream. Maximum sensitivity therefore requires a certain understanding of what the sources look like, hence of the characteristics of those sources. In addition, when detections occur, it will be important to put them into an astrophysical context so that the implications of the discoveries are evident.

Before discussing types of sources, we need to have some general perspective on how gravitational radiation is generated and how strong it is. We will begin by discussing radiation in a general context. By definition, a radiation field must be able to carry energy to infinity. If the amplitude of the field a distance  $r$  from the source in the direction  $(\theta, \varphi)$  is  $A(r, \theta, \varphi)$ , the flux through a spherical surface at  $r$  is  $F(r, \theta, \varphi) \propto A^2(r, \theta, \varphi)$ , for simplicity we assume that the radiation is spherically symmetric,  $A(r, \theta, \varphi) = A(r)$ , this means that the luminosity at a distance  $r$  is  $L(r) \propto A^2(r)4\pi r^2$ . Note, though, that when one expands the static field of a source in

moments, the slowest-decreasing moment (the monopole) decreases like  $A(r) \propto 1/r^2$ , implying that  $L(r) \propto 1/r^2$  and hence no energy is carried to infinity. This tells us two things, regardless of the nature of the radiation (e.g., electromagnetic or gravitational). First, radiation requires time variation of the source. Second, the amplitude must scale as  $1/r$  far from the source.

We can now explore what types of variation will produce radiation. We'll start with electromagnetic radiation, and expand in moments. For a charge density  $\rho_e(\mathbf{r})$ , the monopole moment is  $\int \rho_e(r) d^3r$ . This is simply the total charge  $Q$ , which cannot vary, hence there is no electromagnetic monopolar radiation. The next static moment is the dipole moment,  $\int \rho_e(r) r d^3r$ . There is no applicable conservation law, so electric dipole radiation is possible. One can also look at the variation of currents. The lowest order such variation (the “magnetic dipole”) is  $\int \rho_e(r) r \times v(r) d^3r$ . Once again this can vary, so magnetic dipole radiation is possible. The lower order moments will typically dominate the field unless their variation is reduced or eliminated by some special symmetry.

Now consider gravitational radiation. Let the mass-energy density be  $\rho(\mathbf{r})$ . The monopole moment is  $\int \rho_e d^3r$ , which is simply the total mass-energy. This is constant so there cannot be monopolar gravitational radiation. The static dipole moment is  $\int \rho_e(r) r d^3r$ . This, however, is just the centre of mass-energy of the system. In the centre of mass frame, therefore, this moment does not change, so there cannot be electric dipolar radiation in this frame (or any other, since the existence of radiation is frame-independent). The equivalent of the magnetic dipolar moment is  $\int \rho_e(r) r \times v(r) d^3r$ . This, however, is simply the total angular momentum of the system, so its conservation means that there is no magnetic dipolar gravitational radiation either. The next static moment is quadrupolar:  $I_{ij} = \int \rho(r) r_i r_j d^3r$ . This is not conserved, therefore there can be quadrupolar gravitational radiation.

This allows us to draw general conclusions about the type of motion that can generate gravitational radiation. A spherically symmetric variation is only monopolar, hence it does not produce radiation. No matter how violent an explosion or a collapse (even into a black hole!), no gravitational radiation is emitted if spherical symmetry is maintained. In addition, a rotation that preserves axisymmetry (without contraction or expansion) does not generate gravitational radiation because the quadrupolar and higher moments are unaltered. Therefore, for example, a neutron star can rotate arbitrarily rapidly without emitting gravitational radiation as long as it maintains axisymmetry.

This immediately allows us to focus on the most promising types of sources for gravitational wave emission. The general categories are: binaries, continuous wave sources (e.g., rotating stars with nonaxisymmetric lumps), bursts (e.g., asymmetric collapses), and stochastic sources (i.e., individually unresolved sources with random phases; the most interesting of these would be a background of gravitational waves from the early universe).

The sources of gravitational waves can be broadly classified into 4 categories

- Short lived and well defined for which coalescence of a compact binary system is a canonical example .
- Short lived and a priori poorly known for which a supernova is a canonical example .

- Continuous and well defined for which a spinning neutron star is a canonical example .
- Long lived and stochastic for which primordial gravitational waves from big bang is an example .

For currently available and upcoming terrestrial detectors the most promising category is the first . Detectable event rates for compact binary coalescence ( CBC ) can be estimated with great confidence and can imply highly for advanced LIGO detectors . For future spaced-based detectors, which can probe to lower frequencies, the pre-coalescence phase of galactic binaries NS-NS is accessible, at the same time that coalescence of binary super-massive black holes (SMBHs), e.g., from galaxy mergers should be detectable . Similarly, pulsar timing arrays can potentially detect a stochastic astrophysical background from the superposition of cosmologically distant SMBH binary systems at still lower frequencies ( $\sim$ nHz).

### 3.1) Compact binary coalescence :

Although binary star systems are common in our galaxy , only a few of these systems experience an evolution that arrives with two compact bodies in an orbit tight enough to lead to compact binary coalescence in Hubble time . That end results requires both stars to be massive enough to undergo collapse to a compact object without destroying its companion, without shedding so much mass that the orbit is no longer bound, and without undergoing a “birth kick” that disrupts the bound orbit.

Two distinct approaches (but with some common observational constraints) have been used to estimate the average rates at which NS-NS coalescences occur in the local region of the Universe.

The first method is based on priori calculations of binary star evolution , including the evolution of each star in presence of another star where a common envelope phase is unusual . This general approach can be used to estimate the rates for NS-BH and BH-BH coalescence too .

The second method is based on the extrapolation from the observed double neutron star systems , in our local galaxy albeit systems far from coalescence only a handful of binary neutron star systems are known .

The estimates for NS-NS coalescence yield “realistic” rates of once every  $10^4$  years in a galaxy the size of the Milky Way (“Milky Way Equivalent Galaxy” - MWEG), with “plausible” rates ranging from once every  $10^6$  years to once every  $10^3$  years. The corresponding rates for a NS-BH system are once per 300,000 years (“realistic”), with a plausible range from once per 20 million years to once per  $10^4$  years. For a BH-BH system (stellar masses), the corresponding rates are once per 2.5 million years (realistic) with a plausible range from once per 100 million years to once per 30,000 years. Table 1 summarizes these estimates more compactly in units of  $MWEG^{-1} \text{ Myr}^{-1}$ . An alternative rate unit is in terms of coalescences per  $\text{Mpc}^3$  per Myr. A rough conversion rate (for the local Universe) is  $0.01 \text{ MWEG}/\text{Mpc}^3$ , giving estimated realistic rates of 1, 0.03 and 0.005 coalescences  $\text{Mpc}^{-3} \cdot \text{Myr}^{-1}$  for NS-NS, NS-BH and BH-BH, respectively.

Corroborating evidences for these estimates come from the rate of observed short lived gamma ray bursts( GRBs) while the soft gamma ray bursts (>2s) are thought to arrive from the

death of massive stars from the coalescence of NS-BH and BH-BH systems although the large correction for the average beaming effects remain uncertain the short hard GRB rate per unit volume appears to be roughly consistent with the above range of estimates for a variety of galactic evolution models.

Source	$R_{\text{Low}}^{\text{Plausible}}$	$R^{\text{Realistic}}$	$R_{\text{High}}^{\text{Plausible}}$
NS-NS	1	100	1000
NS-BH	0.05	3	100
BH-BH	0.01	0.4	30

Table 1 : Summary of estimated coalescence rates ( $\text{MWEG}^{-1} \text{ Myr}^{-1}$ ) for NS-NS, NS-BH and BH-BH binary systems

The detection of CBC can offer an unprecedented view of the study of strong field gravity and offer challenging tests to the general theory of relativity , especially in the case of detection by multiple detectors allowing disentanglement of waves from polarizations . The coalescence of two compact massive objects such as BH-BH or NS-BH into a single final black hole can be divided into three reasonably distinct stages inspiral , merger and ring down

The inspiral stage leads itself to a natural perturbative approach . To illustrate with a simple, concrete example, consider two stars of equal mass  $M$  in an circular orbit of instantaneou s radius  $R(t)$  and angular velocity  $\omega(t)$  (assumed slowly changing), where the stars are treated as point masses far enough apart that tidal effects can be neglected. From simple Newtonian mechanics, we obtain Kepler's 3rd Law:

$$M\omega^2 R = GM^2 / (2R)^2 \Rightarrow \omega^2 = GM/4R^3$$

Total Energy (T.E )= Kinetic Energy (K.E )+Potential Energy (P.E)

$$E=-GM/4R$$

$$dE/dt = GM^2/4R^2 \times dR/dt$$

as the orbit shrinks

For convenience define the origin at the orbit's centre and the  $x-y$  plane to coincide with the orbital plane, with one star at  $x_1 = R$  at time  $t = 0$ :

$$x_1(t) = -x_2(t) = R\cos(\omega t); \quad y_1(t) = -y_2(t) = R\sin(\omega t); \quad z_1 = z_2 = 0.$$

from which one obtains

$$\ddot{r} = MR^2(2\omega)^3 \begin{pmatrix} \sin(2\omega t) & -\cos(2\omega t) & 0 \\ -\cos(2\omega t) & -\sin(2\omega t) & 0 \\ 0 & 0 & 0 \end{pmatrix}$$

and a total radiated luminosity can be obtained from the formula

$$\text{using equation } L = \frac{G}{5C^5} \langle I''_{ij} I''^{ij} \rangle$$

$\langle \rangle$  represents average over secured cycles ,  $I$  is a traceless Quadrupole tensor

$$\mathcal{L} = \frac{128}{5} \frac{GM^2}{c^5} R^4 \omega^6$$

Setting  $dE/dt = -L$ , one obtains a differential equation for  $R$ :

$$R^3 \frac{dR}{dt} = -\frac{8}{5} \frac{G^3 M^3}{c^5}$$

Integrating from a present time  $t$  to a future coalescence time  $t_{\text{coal}}$  when  $R \rightarrow 0$ , one finds the orbital radius

$$R(t) = \left[ \frac{32}{5} \frac{G^3 M^3}{c^5} (t_{\text{coal}} - t) \right]^{\frac{1}{4}}$$

from which the gravitational wave frequency  $f_{\text{GW}} = 2\omega/2\pi$

$$= \frac{1}{8\pi} [2 \cdot 5^3]^{\frac{1}{8}} \left[ \frac{c^3}{GM} \right]^{5/8} \frac{1}{(t_{\text{coal}} - t)^{\frac{3}{8}}}$$

As expected, the frequency diverges as  $t \rightarrow t_{\text{coal}}$ . Now consider the amplitude  $h_0$  of the circularly polarized wave observed a distance  $r$  away along the orbital axis of rotation.

From the equation

$$h^{ij}(t, x) \approx \frac{2G}{rC^4} \frac{d^2}{dt^2} [\Gamma^{ij} \left( t - \frac{r}{c} \right)]$$

One has

$$h_0(t) = \frac{1}{r} \left[ \frac{5G^5 M^5}{2c^{11}} \right]^{\frac{1}{4}} \frac{1}{(t_{\text{coal}} - t)^{\frac{1}{4}}}$$

The increase in frequency with  $\tau^{-\frac{3}{8}}$  and in amplitude with  $\tau^{-\frac{1}{4}}$  leads to a characteristic “chirp” in the gravitational waveform. Note that if the distance to the source is known, the common stellar mass of this system can be derived from either the frequency or amplitude evolution.

Thus the early phases of the inspiral stage should provide a well understood post-Newtonian system, from which stellar masses (and perhaps spins) can be determined. With these parameters determined (to some precision), one can then make detailed comparisons of observations in the merger stage with numerical predictions for those parameters. The ringdown mode frequencies and damping times are primarily governed by the total mass and spin of the final black hole,

allowing clean and analytic comparisons to the inspiral stage, largely independent of the merger uncertainties.

There has been a flurry of work in the last two decades to improve the numerical relativity calculations, to permit detailed comparisons between observation and theory during the difficult merger phase. A number of technical breakthroughs have led to dramatic progress in this area. In parallel, there is a coordinated effort to produce families of detailed waveform templates and evaluate algorithms for detecting them, not only for making comparisons after detection, but also to increase the chances of detection via matched-filter algorithms.

Coalescences involving neutron stars offer the potential for probing the neutron star equation of state via distortions of the detected waveform away from that expected for two point masses, because of tidal disruption of one or both stars . The effects are expected to be small, however, and their detection dependent on the detector sensitivity at the highest frequencies in the detector bands.

Very distant coalescences also offer interesting cosmological measurements via their role a “standard candles”, analogous to Type 1A supernovae . Since the masses of the system can be determined from the waveform shape (assuming polarization has been determined via coincidence detection in multiple detectors), the luminosity distance to the system can be determined (assuming the correctness of general relativity). If the redshift of the source’s host galaxy can be determined from electromagnetic measurements, *e.g.*, simultaneous detection of a short GRB or of an afterglow, then one obtains an independent measure of the Hubble constant.

Note, however, that the gravitational waves are subject to the same redshift as electromagnetic radiation, which leads to an ambiguity in determining the redshift directly from the gravitational waveform. For example, the reduction of the wave amplitude due to luminosity distance (correlated to redshift) can be compensated by changes to the assumed rest-frame mass of the system. Recently it has been appreciated, however, that for coalescences involving a neutron star, the tidal disruption can provide an independent clue to the stellar masses (in their local frame), allowing the use of the standard candle even in the absence of a known host galaxy . Similarly, the statistical distribution of neutron star masses provides another means to calibrate the standard candle . And if the host galaxy *is* known, then one has a valuable cross check on the relation between luminosity distance and redshift distance.

While stellar spin is thought to be unimportant in searches for NS-NS inspirals, it can be important for coalescences involving one or two black holes, for which high spin can create significant waveform distortions over a spinless assumption, where the maximum allowed angular momentum in general relativity is  $\frac{GM^2}{c}$  for a black hole of mass  $M$ . Both amplitude and phase can be modulated, making the parameter space over which one must search much larger than for the NS-NS case .

### 3.2) White dwarf binaries :

Binary systems at much more lower frequencies are much more abundant than coalescence binaries and would have a much longer lifetime . LISA would look for white dwarfs in our galaxy .White dwarfs are not as compact as black holes or neutron stars . Although their masses can be similar to that of neutron stars their sizes are much larger typically about  $3 \times 10^3$  Km in radius as a result the white dwarf binaries will never reach the last stable orbit , which would radiate roughly at 1.5KHz for their masses .

The maximum amplitude of radiation for a white dwarf will be several orders of magnitude smaller than that of a neutron star or a black hole binary at the same distance , however a binary system with a short period is long lived , so the effective amplitude improves as the square root of the observing time .Besides the near sources there are thousands of such sources in our galaxy that are radiating in the LISA 1mHz window ,for frequencies below 1mHz there are even more sources so many that LISA would not be able to resolve them individually but will see them blended together in stochastic background of radiation .

### 3.3) Bursts :

Gravitational wave bursts customarily refer to transients of poorly known or unknown phase evolution. Although the algorithms used to search for bursts are sensitive to high SNR, well predicted waveforms such as from NS-NS coalescence, they are necessarily less sensitive than matched-filter approaches, where known phase evolution can be exploited. More generic transient algorithms must be used for burst sources, such as supernovae, because of uncertain dynamics in these violent processes and because of uncertain but almost certainly varying initial stellar conditions.

As a reminder, a spherically symmetric explosion (or implosion) does not lead to gravitational waves in general relativity (no monopole term). To be detected via gravitational waves then, a supernova presumably needs to exhibit some asymmetry. The fact that many pulsars formed in supernovae have large measured speeds relative to their neighbours (high “birth kicks”) strongly suggests that some supernovae do exhibit substantial non-spherical motion, perhaps as a result of dynamical instabilities in rapidly rotating, massive progenitor stars. One recently appreciated mechanism for potentially strong gravitational wave emission during core-collapse supernovae is hydro dynamical oscillation of the protoneutron star core.

For gravitational wave detection much work has gone into detailed simulations of the supernova process, to predict possible resulting waveforms. As one might imagine, this violent process, in which strong magneto-hydrodynamics, nuclear physics and general relativity are all important, is a formidable challenge to simulate. Indeed, it has proven challenging to reproduce in these simulations the spectacular explosions that we associate with supernovae . Nonetheless, this recent work has given new insights into the strength and spectral content one might expect from supernovae. Unfortunately, predictions of strength remain subject to large uncertainties.

For scale, consider a supernova a distance  $r$  away in our galaxy that emits energy  $E$  in gravitational waves, with a characteristic duration  $T$  and characteristic frequency  $f$ .One expects a detectable strain amplitude at the Earth of about

$$h \sim 6 \times 10^{-21} \left( \frac{E}{10^{-7} M_{\odot} c^2} \right)^{\frac{1}{2}} \left( \frac{1 \text{ ms}}{T} \right) \left( \frac{1 \text{ kHz}}{f} \right) \left( \frac{10 \text{ kpc}}{r} \right)$$

For nominal (but not necessarily accurate) values of  $r$ ,  $E$ ,  $T$  and  $f$  in this expression, the initial LIGO and Virgo interferometers should have been able to detect a galactic supernova in gravitational waves. But no supernova was detected electromagnetically in our galaxy during initial LIGO and Virgo data taking, which is unsurprising, giving their expected low occurrence rate. With the expected order of magnitude improvement in sensitivity of the advanced detectors, a galactic supernova with 100 times smaller energy or a supernova with the same energy ten times further away would be accessible. Note, however, that until one reaches the Andromeda galaxy ( $\sim 780$  kpc), there is relatively little additional stellar mass beyond the edge of the Milky Way, with nearby dwarf galaxies contributing only a few percent additional mass. (Nonetheless, the most recent known nearby supernova – SN1987A – was in the Large Magellanic Cloud at  $\sim 50$  kpc.) .

One intriguing scenario in which a core collapse supernova could be seen in gravitational waves to much larger distances is via a bar mode instability , in which differential rotation in a collapsing star leads to a large, rapidly spinning quadrupole moment, generating waves detectable from well outside our own galaxy . Another type of instability ( $r$ -mode) may develop in the birth of a neutron star, but its lifetime is expected to be long enough, that it will be discussed below in the category of continuous wave sources.

Another potential transient source of poorly known gravitational waveform shape is the sudden release of energy from a highly magnetized neutron star (magnetar). Although “ordinary” neutron stars are characterized by extremely strong surface magnetic fields ( $\sim 10^{12}$  G), many magnetars appear to have fields  $\sim 100$ -1000 times still stronger, implying enormous pent-up magnetic energy. It is thought that soft gamma ray repeaters (SGRs) and anomalous X-ray pulsars (AXPs) are different observational manifestations of the same underlying system - a highly magnetized star which sporadically converts magnetic field energy into radiation . Whether this process involves rupture of the neutron star crust, vortex rearrangement in a core superconducting fluid, or some other process, is not yet well understood. Especially dramatic instances are superflares, such as the December 2004 flare from SGR 1806-20, in which  $\sim 10^{39}$  J ( $10^{46}$  erg) of electromagnetic energy was released . This radiation release from  $\sim 10$  kpc away disturbed the Earth’s ionosphere sufficiently to disrupt some radio communications . How much gravitational wave energy might be released in such events is unclear, although it has been proposed that the energy released into neutron star crustal vibrations could be comparable to that released electromagnetically , in which case gravitational radiation due to those vibrations could be substantial. For scale, the magnetic energy stored in a neutron star with surface field of  $10^{15}$  G is  $O(10^{40} \text{ J} = 10^{47} \text{ erg})$ , assuming an internal field no larger than the surface field. If the star had still stronger internal fields, the energy would be still larger. Given the uncertainties in the mechanism leading to these enormous radiation releases, it is hard to be confident of predicted waveforms. Hence generic GW transient algorithms are appropriate in searching for flares .

Another possible transient source is emission of bursts of gravitational radiation from “cosmic string cusps” . Cosmic strings might be defects remaining from the electroweak (or earlier) phase transition or possibly primordial superstrings redshifted to enormous distances.

In either model, kinks in these strings would travel at the speed of light with an isotropic distribution of directions, generating a model-dependent gravitational wave spectrum that is collimated along the direction of cusp travel. According to this idea, one would expect a cosmological background of GW bursts, that might be detected individually. This same model could lead to a steady-state, lower-level stochastic background from cusp radiation from more distant reaches of the universe.

A general consideration in burst searches is the energy release implicit for a given source distance and detectable strain amplitude. As the distance of the source increases, the energy required for its waves to be detectable on Earth increases as the square of the distance. Specifically,

$$E \sim (3 \times 10^{-3} M_{\odot} c^2) \left( \frac{h}{10^{-21}} \right)^2 \left( \frac{T}{1 \text{ ms}} \right) \left( \frac{f}{1 \text{ kHz}} \right) \left( \frac{r}{10 \text{ Mpc}} \right)^2$$

Hence for a source distance much beyond 10 Mpc and for initial LIGO/Virgo sensitivities to transients, one needs sources emitting significant fractions of a solar mass in gravitational radiation in frequency bands accessible to terrestrial detectors, such as is expected in the case of coalescing binary systems.

### 3.4) Continuous waves :

Continuous gravitational waves refer to those that are long-lasting and nearly monochromatic. In the frequency band of present and planned terrestrial detectors, the canonical sources are galactic, non axisymmetric neutron stars spinning fast enough that twice their rotation frequency is in the detectable band. (For future space-based gravitational wave detectors, the early stages of coalescing binaries provide another continuous-wave source, where the orbital decay leads to only a small secular departure from monochromaticity.)

Several different mechanisms have been proposed by which spinning neutron stars could generate detectable gravitational waves. Isolated neutron stars may have intrinsic non-axisymmetry from residual crustal deformation (*e.g.*, from cooling & cracking of the crust), or from non-axisymmetric distribution of magnetic field energy trapped beneath the crust .

An isolated star may also exhibit normal modes of oscillations, including *r*-modes in which quadrupole mass currents emit gravitational waves . These *r*-modes can be inherently unstable, arising from azimuthal interior currents that are retrograde in the star's rotating frame, but are prograde in an external reference frame. As a result, the quadrupolar gravitational wave emission due to these currents leads to an increase in the strength of the current. This positive-feedback loop leads to an intrinsic instability. The frequency of such emission is expected to be approximately 4/3 the rotation frequency . Serious concerns have been raised about the detection utility of this effect for young isolated neutron stars (other than truly newborn stars in our galaxy), where mode saturation appears to occur at low *r*-mode amplitudes because of various dissipative effects. This notion of a runaway rotational instability was first appreciated for high-frequency *f*-modes , (Chandrasekhar-Friedman-Schutz instability), but realistic viscosity effects seem likely to suppress the effect .

In addition, as discussed below, a binary neutron star may experience non-axisymmetry from non isotropic accretion (also possible for an isolated young neutron star that has experienced fall back accretion shortly after birth).

The detection of continuous gravitational waves from a spinning neutron star should yield precious information on neutron star structure and the equation of state of nuclear matter at extreme pressures when combined with electromagnetic measurements of the same star.

In principle, there should be  $O(10^{8-9})$  neutron stars in our galaxy , out of which only about 2000 have been detected, primarily as radio pulsars. The small fraction of detections is understandable, given several considerations. Radio pulsations appear empirically to require the combination of the magnetic field and rotation frequency to satisfy the approximate relation.

$$B \cdot f_{\text{rot}}^2 > 1.7 \times 10^{11} \text{ G}\cdot(\text{Hz})^2$$

As a result, isolated pulsars seem to have lifetimes of  $\sim 10^7$  years , after which they are effectively radio-invisible. On this timescale, they also cool to where X-ray emission is difficult to detect. There remains the possibility of X-ray emission from steady accretion of interstellar medium (ISM), but it appears that the kick velocities from birth highly suppress such accretion which depends on the inverse cube of the star's velocity through the ISM.

A separate population of pulsars and non-pulsating neutron stars can be found in binary systems. In these systems accretion from a non-compact companion star can lead to “recycling,” in which a spun-down neutron star regains angular momentum from the in falling matter. The rotation frequencies achievable through this spin-up are impressive – the fastest known rotator is J1748-2446ad at 716 Hz . One class of such systems is the set of low mass X-ray binaries (LMXBs) in which the neutron star ( $\sim 1.4 M_\odot$ ) has a much lighter companion ( $\sim 0.3 M_\odot$ ) that overfills its Roche lobe, spilling material onto an accretion disk surrounding the neutron star or possibly spilling material directly onto the star, near its magnetic polar caps. When the donor companion star eventually shrinks and decouples from the neutron star, the neutron star can retain a large fraction of its maximum angular momentum and rotational energy. Because the neutron star’s magnetic field decreases during accretion (through processes that are not well understood), the spin-down rate after decoupling can be very small. Equating rotational energy loss rate to magnetic dipole radiation losses, leads to the equation

$$\left( \frac{dE}{dt} \right) = - \frac{\mu_0 M_\perp^2 \omega^4}{6\pi c^3}$$

where  $M_\perp$  is the component of the star’s magnetic dipole moment perpendicular to the rotation axis model, the magnetic pole field strength at the surface is  $B_\perp = M \sin(\alpha)$ , with  $\alpha$  the angle between the axis and north magnetic pole. In a pure dipole moment  $B_0 = \mu_0 M / 2\pi R^3$ . Equating this energy loss to that of the (Newtonian) rotational energy  $\frac{1}{2} I_{zz} \omega^2$  leads to the prediction

$$\frac{d\omega}{dt} = - \frac{\mu_0 R^6}{6\pi c^3 I_{zz}} B_\perp^2 \omega^3.$$

Note that the spindown rate is proportional to the square of  $B_\perp = B_0 \sin(\alpha)$  and to the cube of the rotation frequency. The cubic dependence of  $d\omega/dt$  on  $\omega$  leads to a relation between the present day rotational frequency  $f$  and the star's spindown age  $\tau$ :

$$\tau = - \left[ \frac{f}{2\dot{f}} \right] \left[ 1 - \left( \frac{f}{f_0} \right)^2 \right]$$

where  $f_0$  was the frequency a time  $\tau$  in the past (assuming magnetic dipole radiation has dominated rotational energy loss). In the limit  $f \ll f_0$ , this reduces simply to

$$\tau = - \left[ \frac{f}{2\dot{f}} \right]$$

More generally, for a star spinning down with dependence:

$$\left( \frac{d\omega}{dt} \right) = K\omega^n$$

for some constant  $K$ , the value of  $\tau$  in the above equation becomes assuming  $n=1$

$$\tau = - \left[ \frac{f}{(n-1)\dot{f}} \right] \left[ 1 - \left( \frac{f}{f_0} \right)^{(n-1)} \right]$$

Assuming  $n$  (often called the “braking index”) and is three (as would be the case for a rotating magnetic dipole), leads to approximate inferred ages for many binary radio pulsars in excess of  $10^9$  and even well over  $10^{10}$  years. A calculation suggests that this surprising result can be explained by reverse-torque spindown during the Roche lobe decoupling phase. In fact, measured braking indices for even young pulsars tend to be less than three, suggesting that the model of a neutron star spinning down with constant magnetic field is inaccurate.

In summary, there are at least three distinct populations of neutron stars potentially detectable via continuous gravitational waves: relatively young, isolated stars with spin frequencies below  $\sim 50$  Hz, such as the Crab pulsar; actively accreting stars in binary systems; and recycled “millisecond” stars for which accretion has ceased and which generally have rotation frequencies above 100 Hz. In some cases the companion donor has disappeared, e.g., via ablation, leaving an isolated neutron star, but most known millisecond pulsars remain in binary systems.

Let's now consider the gravitational radiation one might expect from these stars. If a star at a distance  $r$  away has a quadrupole asymmetry, parametrized by its ellipticity

$$\epsilon \equiv \frac{I_{xx} - I_{yy}}{I_{zz}}$$

and if the star is spinning about the approximate symmetry axis of rotation ( $z$ ), (assumed optimal – pointing toward the Earth), then the expected intrinsic strain amplitude  $h_0$  is

$$h_0 = \frac{4\pi^2 G I_{zz} f_{\text{GW}}^2}{c^4 r} \epsilon = (1.1 \times 10^{-24}) \left( \frac{I_{zz}}{I_0} \right) \left( \frac{f_{\text{GW}}}{1 \text{ kHz}} \right)^2 \left( \frac{1 \text{ kpc}}{r} \right) \left( \frac{\epsilon}{10^{-6}} \right)$$

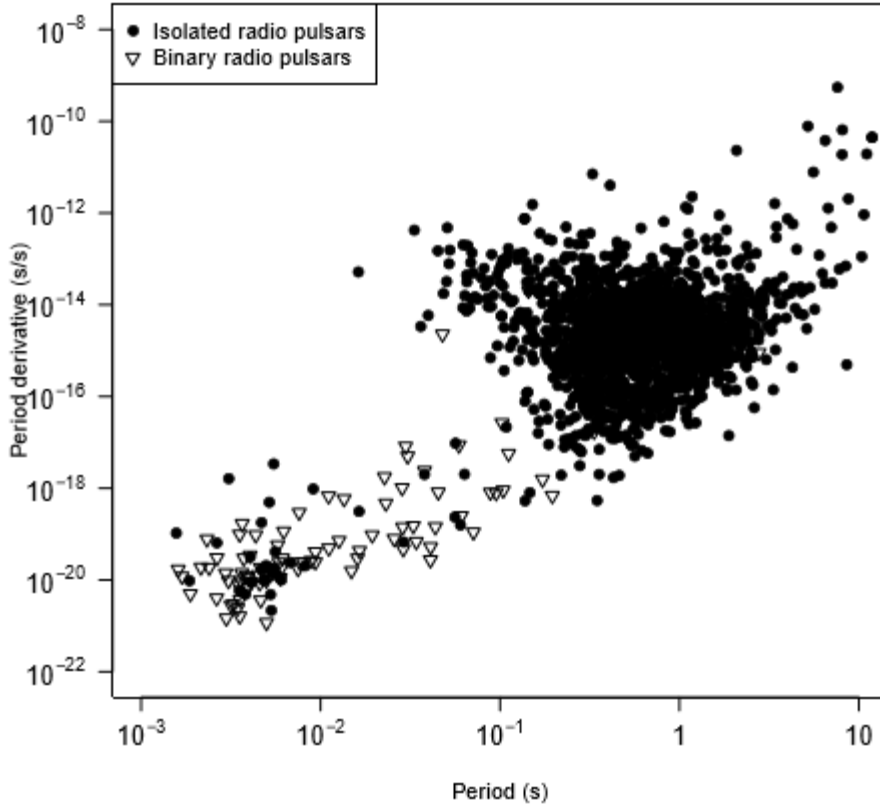


*Fig 1: Measured periods and period derivatives for known radio pulsars. Closed circles indicate isolated stars. Open triangles indicate binary stars.*

where  $I_0 = 1038 \text{ kg}\cdot\text{m}^2$  ( $1045 \text{ g}\cdot\text{cm}^2$ ) is a nominal quadrupole moment of a neutron star, and the gravitational radiation is emitted at frequency  $f_{\text{GW}} = 2f_{\text{rot}}$ . The total power emission in gravitational waves from the star (integrated over all angles) is

$$\frac{dE}{dt} = -\frac{32}{5} \frac{G}{C^5} I_{zz}^2 \epsilon^2 \omega^6 = -(1.7 \times 10^{33} \text{ J/s}) \left(\frac{I_{zz}}{I_0}\right)^2 \left(\frac{\epsilon}{10^{-6}}\right)^2 \left(\frac{f_{\text{GW}}}{1 \text{ kHz}}\right)^6.$$

For an observed neutron star of measured  $f$  one can define the “spindown limit” on maximum detectable strain by equating the power loss to the time derivative of the (Newtonian) rotational kinetic energy:  $\frac{1}{2}I\dot{\omega}^2$ , as above for magnetic dipole radiation. One finds:

$$\begin{aligned} h_{\text{spindown}} &= \frac{1}{r} \sqrt{-\frac{5}{4} \frac{G}{c^3} I_{zz} \frac{\dot{f}_{\text{GW}}}{f_{\text{GW}}}} \\ &= (2.5 \times 10^{-25}) \left(\frac{1 \text{ kpc}}{r}\right) \sqrt{\left(\frac{1 \text{ kHz}}{f_{\text{GW}}}\right) \left(\frac{-\dot{f}_{\text{GW}}}{10^{-10} \text{ Hz/s}}\right) \left(\frac{I_{zz}}{I_0}\right)} \end{aligned}$$

Hence for each observed pulsar with a measurable spindown and well determined distance  $r$ , one can determine whether energy conservation even permits detection of gravitational waves in an optimistic scenario. Unfortunately, nearly all known pulsars have strain spindown limits below what could be detected by the initial LIGO and Virgo detectors, as discussed below.

A similarly optimistic limit based only on the age of a known neutron star of unknown spin frequency can also be derived. If one assumes a star is spinning down entirely due to gravitational radiation, then the energy loss for this gravitar satisfies equation

$$\left(\frac{d\omega}{dt}\right) = K\omega^n$$

with a braking index of five. Assuming a high initial spin frequency, the star's age then satisfies:

$$\tau_{gravitar} = \frac{-f}{4f'}$$

If one knows the distance and the age of the star, e.g., from the expansion rate of its visible nebula, then under the assumption that the star has been losing rotational energy since birth primarily due to gravitational wave emission, then one can derive the following frequency-independent age-based limit on strain using the formula

$$h_{age} = (2.2 \times 10^{-24}) \left(\frac{1 \text{ kpc}}{r}\right) \sqrt{\left(\frac{1000 \text{ yr}}{\tau}\right) \left(\frac{I_{zz}}{I_0}\right)}$$

A notable example is the Compact Central Object (CCO) in the Cassiopeia A supernova remnant. Its birth aftermath may have been observed by Flamsteed in 1680, and the expansion of the visible shell is consistent with that date. Hence Cas A, which is visible in X-rays but shows no pulsations, is almost certainly a very young neutron star at a distance of about 3.4 kpc. From the above equation, one finds an age-based strain limit of  $1.2 \times 10^{-24}$ , which is accessible to initial LIGO and Virgo detectors in their most sensitive band.

A simple steady-state argument by Blandford led to an early estimate of the maximum detectable strain amplitude expected from a population of isolated gravitars of a few times  $10^{-24}$ , independent of typical ellipticity values, in the optimistic scenario that most neutron stars become gravitars. A later detailed numerical simulation revealed, however, that the steady-state assumption does not generally hold, leading to ellipticity-dependent expected maximum amplitudes that can be 2-3 orders of magnitude lower in the LIGO band for ellipticities as low as  $10^{-9}$  and a few times lower for ellipticity of about  $10^{-6}$ .

Yet another approximate strain limit can be defined for accreting neutron stars in binary systems, such as Scorpius X-1. The X-ray luminosity from the accretion is a measure of mass accumulation at the surface. As the mass rains down on the surface it can add angular momentum to the star, which in equilibrium may be radiated away in gravitational waves. Hence one can derive a torque-balance limit

$$h_{torque} = (5 \times 10^{-27}) \sqrt{\left(\frac{600 \text{ Hz}}{f_{GW}}\right) \left(\frac{F_x}{10^{-8} \text{ erg/cm}^2/\text{s}}\right)}$$

where  $F_x$  is the observed energy flux at the Earth of X-rays from accretion. Note that this limit is independent of the distance to the star.

The notion of gravitational wave torque equilibrium is potentially important, given that the maximum observed rotation frequency of neutron stars in LMXBs is substantially lower than

one might expect from calculations of neutron star breakup rotation speeds ( $\sim 1400$  Hz). It has been suggested that there is a “speed limit” governed by gravitational wave emission that governs the maximum rotation rate of an accreting star. In principle, the distribution of frequencies could have a quite sharp upper frequency cut off, since the angular momentum emission is proportional to the 5<sup>th</sup> power of the frequency. For example, for an equilibrium frequency corresponding to a particular accretion rate, doubling the accretion rate would increase the equilibrium frequency by only about 15%. A number of mechanisms have been proposed by which the accretion leads to gravitational wave emission. The simplest is localized accumulation of matter, e.g., at the magnetic poles (assumed offset from the rotation axis), leading to a non-axisymmetry. One must remember, however, that matter can and will diffuse into the crust under the star’s enormous gravitational field. This diffusion of charged matter can be slowed by the also-enormous magnetic fields in the crust, but detailed calculations indicate the slowing is not dramatic. Another proposed mechanism is excitation of r-modes in the fluid interior of the star, with both steady-state emission and cyclic spinup-spindown possible.

### 3.5) Stochastic Waves :

Stochastic gravitational waves arise from a superposition of incoherent sources. While a cosmological background from primordial gravitational waves created in the Big Bang are a natural possible source, other isotropic possibilities are from cosmic strings and from very distant mergers of neutron stars or of supermassive black holes (accessible to space-based detectors). Non-isotropic sources in the band of terrestrial detectors could include the superposition of pulsar radiation from, say, the Virgo Cluster. Over very long time scales, gravitational radiation from an accreting neutron star could also appear stochastic, as the phase of the narrowband signal wanders. A primordial isotropic gravitational wave background is predicted by most cosmological theories, although the predicted strengths of the background vary enormously. It is customary to parametrize the background strength vs. frequency  $f$  by its energy density per unit logarithm normalized to the present-day critical energy density  $\rho_{\text{crit}} = 3H_0^2c^2 / 8\pi G$  of the universe, where  $H_0$  is Hubble’s constant, taken here to be 70.5 km/s/Mpc.

$$\Omega_{\text{gw}}(f) = \frac{1}{\rho_{\text{crit}}} \frac{d\rho_{\text{gw}}(f)}{d \ln(f)}$$

The associated power spectral density can be written as

$$S_{\text{gw}} = \frac{3H_0^2}{10\pi^2} f^{-3} \Omega(f)$$

Note that, as for the Cosmic Microwave Background Radiation (CMBR), the primordial gravitational waves would be highly redshifted from the expansion of the universe, but likely to a much greater degree, since they would have decoupled from matter at vastly earlier times. A more convenient reformulation in amplitude spectral density can be written as

$$h(f) \equiv [S_{\text{GW}}(f)]^{\frac{1}{2}} = (5.6 \times 10^{-22}) h_{100} (\Omega(f))^{\frac{1}{2}} \left( \frac{100 \text{ Hz}}{f} \right)^{\frac{3}{2}} \text{ Hz}^{-\frac{1}{2}}$$

where  $h_{100} \equiv H_0/(100 \text{ km/s/Mpc})$ .

Figure 2 shows the range of values to expect for  $\Omega(f)$ . The bottom curve is a rough estimate expected from standard inflationary scenarios. This graph also shows direct limits on gravitational wave energy density from comparison of observed abundances of elements with predictions from Big Bang nucleosynthesis (BBN), in addition to limits derived from measurements of anisotropies in the CMBR. For reference, the normalized total energy density of the CMBR itself is about  $\Omega_{CMBRR} = 5 \times 10^{-5}$  and the energy density from primordial neutrinos is estimated to be bounded by  $\Omega < 0.014$ .

As discussed below, the  $\Omega(f)$  sensitivity of the initial LIGO and Virgo detectors to this isotropic background is order( $\text{several} \times 10^{-6}$ ), with an expected improvement of more than three orders of magnitude for advanced detectors. From figure 2, it is clear, though, that even advanced detectors fall far short of the sensitivity needed to probe standard inflation.

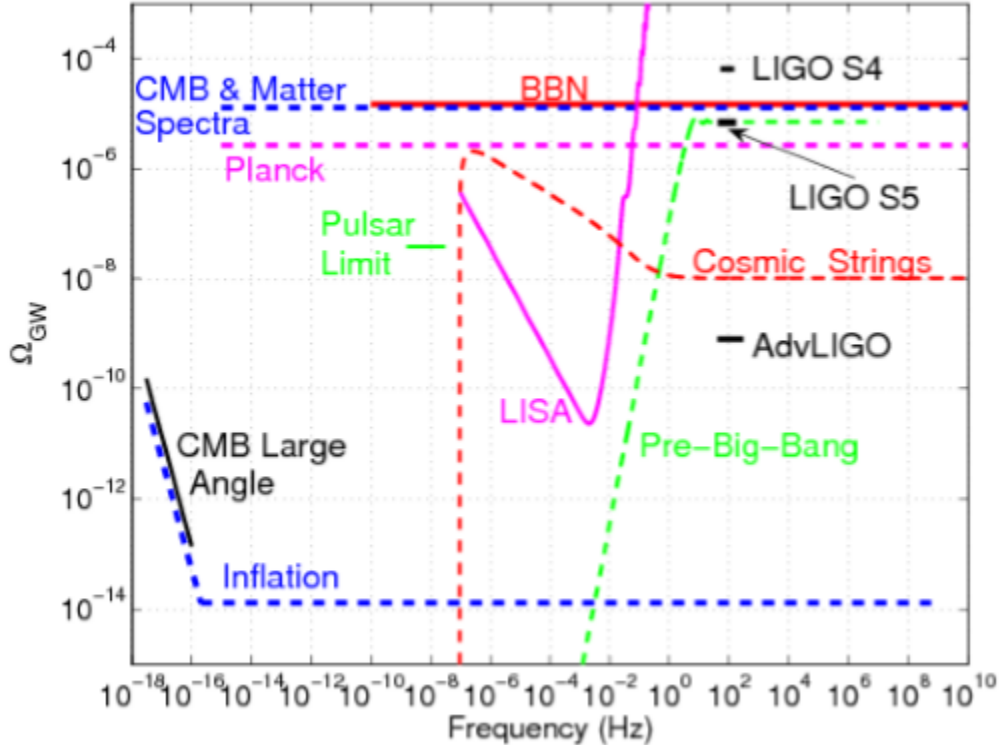


*Fig2: Comparison of different stochastic gravitational wave background measurements and models. Results for LIGO S4 and S5 searches are shown in the frequency band around 100 Hz, along with projected Advanced LIGO sensitivity. The indirect bounds due to BBN and CMBR matter power spectra apply to the integral of  $\Omega_{\text{GW}}(f)$  over the frequency bands denoted by the corresponding dashed curves. Projected sensitivities of the satellite-based Planck CMBR experiment and LISA GW detector are also shown. The pulsar bound is based on the fluctuations in the pulse arrival times of millisecond pulsars and applies at frequencies around  $10^{-8}$  Hz. Measurements of the CMBR at large angular scales constrain the possible redshift of CMBR photons due to a stochastic gravitational wave background, and therefore limit the amplitude of that background at largest wavelengths (smallest frequencies). Examples of*

*inflationary, cosmic strings, and pre-big-bang models are also shown (the amplitude and the spectral shape in these models can vary significantly as a function of model parameters).*

There are other Big Bang scenarios, however, that permit much higher primordial gravitational wave energy densities. In particular, the curve labeled “Pre-BigBang” in figure 4 shows an upper range expected in certain pre-Big Bang models . The advanced detectors can address the upper range of this region.

### 3.6) Man Made Sources :

In 1970, Vishveshwara discussed a gedanken experiment, similar in philosophy to Rutherford’s (real) experiment with the atom. In Vishveshwara’s experiment, he scattered gravitational radiation off a black hole to explore its properties. With the aid of such a gedanken experiment, he demonstrated for the first time that gravitational waves scattered off a black hole will have a characteristic waveform, when the incident wave has frequencies beyond a certain value, depending on the size of the black hole. It was soon realized that perturbed black holes have quasi-normal modes (QNMs) of vibration and in the process emit gravitational radiation, whose amplitude, frequency and damping time are characteristic of its mass and angular momentum .

We can easily estimate the amplitude of gravitational waves emitted when a black hole forms at a distance  $r$  from Earth as a result of the coalescence of compact objects in a binary. The effective amplitude is given by  $h \sim \frac{1}{\pi r} \sqrt{\frac{E}{f}}$ , which involves the energy  $E$  put into gravitational waves and the frequency  $f$  at which the waves come off. By dimensional arguments  $E$  is proportional to the total mass  $M$  of the resulting black hole. The efficiency at which the energy is converted into radiation depends on the symmetric mass ratio  $\nu$  of the merging objects. Flanagan and Hughes argue that  $E \sim 0.03(4\nu)^2 M$ . The frequency  $f$  is inversely proportional to  $M$ ; indeed, for Schwarzschild black holes  $f = (2\pi M)^{-1}$ . Thus, the formula for the effective amplitude takes the form

$$h_{\text{eff}} \sim \frac{4\alpha\nu M}{\pi r}$$

where  $\alpha$  is a number that depends on the (dimensionless) angular momentum  $a$  of the black hole and has a value between 0.7 (for  $a = 0$ , Schwarzschild black hole) and 0.4 (for  $a = 1$ , maximally spinning Kerr black hole). For stellar mass black holes at a distance of 200 Mpc the amplitude is:

$$h_{\text{eff}} \simeq 10^{-21} \left(\frac{\nu}{0.25}\right) \left(\frac{M}{20 M_\odot}\right) \left(\frac{r}{200 \text{ Mpc}}\right)^{-1}.$$

For SMBHs, even at cosmological distances, the amplitude of quasinormal mode signals is pretty large:

$$h_{\text{eff}} \simeq 3 \times 10^{-17} \left(\frac{\nu}{0.25}\right) \left(\frac{M}{2 \times 10^6 M_\odot}\right) \left(\frac{r}{6.5 \text{ Gpc}}\right)^{-1}.$$

In the first case we have a pair of  $10M_{\odot}$  black holes inspiraling and merging to form a single black hole. In this case the waves come off at a frequency of around 500 Hz. The initial ground-based network of detectors might be able to pick these waves up by matched filtering, especially when an inspiral event precedes the ringdown signal. A  $100M_{\odot}$  black hole plunging into a  $10^6 M_{\odot}$  black hole at a distance of 6.5 Gpc ( $z \approx 1$ ) gives out radiation at a frequency of about 15 mHz. Note that in the latter case the radiation is redshifted from 30 mHz to 15 mHz. Such an event produces an amplitude just large enough to be detected by LISA. At the same distance, a pair of  $10^6 M_{\odot}$  SMBHs spiral in and merge to produce a fantastic amplitude of  $3 \times 10^{-17}$ , way above the LISA background noise. In this case, the signals would be given off at about 7.5 mHz and will be loud and clear to LISA. It will not only be possible to detect these events, but also to accurately measure the masses and spins of the objects before and after merger and thereby test the black hole no-hair theorem and confirm whether the result of the merger is indeed a black hole or some other exotic object (e.g., a boson star or a naked singularity).

### 3) CHARACTERISTICS OF GRAVITATIONAL WAVES

#### 4.1) Polarization Of Gravitational Waves :

In general relativity the gravitational waves are represented by a second rank trace free tensor. In a general coordinate system and in arbitrary gauge, this tensor has 10 independent components. However in electromagnetic case the gravitational radiation has two independent states of polarization in Einstein theory + polarization and X polarization. In contrast to electromagnetic waves the angle between the two polarizations is  $\pi/4$  instead of  $\pi/2$ .

Effect of a ring of test particles :

For two particles initially separated in the  $x$ -direction, have a geodesic deviation vector which obeys the differential equations

$$\frac{\partial^2}{\partial t^2} \xi^x = \frac{1}{2} \epsilon \frac{\partial^2}{\partial t^2} h_{xx}^{(TT)} \quad (1)$$

And

$$\frac{\partial^2}{\partial t^2} \xi^y = \frac{1}{2} \epsilon \frac{\partial^2}{\partial t^2} h_{xy}^{(TT)} \quad (2)$$

Similarly, it is straightforward to show that two particles initially separated by in the  $y$ -direction, have a geodesic deviation vector which obeys the differential equations

$$\frac{\partial^2}{\partial t^2} \xi^x = \frac{1}{2} \epsilon \frac{\partial^2}{\partial t^2} h_{xy}^{(TT)} \quad (3)$$

And

$$\frac{\partial^2}{\partial t^2} \xi^y = -\frac{1}{2} \epsilon \frac{\partial^2}{\partial t^2} h_{xx}^{(TT)} \quad (4)$$

consider the geodesic deviation of two particles one at the origin and the other initially at coordinates  $x = \epsilon \cos \theta$ ,  $y = \epsilon \sin \theta$  and  $z = 0$ , i.e. in the  $x$ - $y$  plane – as a gravitational wave propagates in the  $z$ -direction. We can show that  $\xi^x$  and  $\xi^y$  obey the differential equations

$$\frac{\partial^2}{\partial t^2} \xi^x = \frac{1}{2} \epsilon \cos \theta \frac{\partial^2}{\partial t^2} h_{xx}^{(TT)} + \frac{1}{2} \epsilon \sin \theta \frac{\partial^2}{\partial t^2} h_{xy}^{(TT)} \quad (5)$$

And

$$\frac{\partial^2}{\partial t^2} \xi^y = \frac{1}{2} \epsilon \cos \theta \frac{\partial^2}{\partial t^2} h_{xy}^{(TT)} - \frac{1}{2} \epsilon \sin \theta \frac{\partial^2}{\partial t^2} h_{xx}^{(TT)} \quad (6)$$

Substituting from equation

$$h_{xy}^{TT} = A_{xy}^{TT} \cos[(\omega(t-z)] \quad (7)$$

We can identify the solution as

$$\xi^x = \epsilon \cos \theta + \frac{1}{2} \epsilon \cos \theta A_{xx}^{(TT)} \cos \omega t + \frac{1}{2} \epsilon \sin \theta A_{xy}^{(TT)} \cos \omega t \quad (8)$$

And

$$\xi^y = \epsilon \sin \theta + \frac{1}{2} \epsilon \cos \theta A_{xy}^{(TT)} \cos \omega t - \frac{1}{2} \epsilon \sin \theta A_{xx}^{(TT)} \cos \omega t \quad (9)$$

Suppose we now vary  $\theta$  between 0 and  $2\pi$ , so that we are considering an initially circular ring of test particles in the  $x$ - $y$  plane, initially equidistant from the origin. Figure 3 shows the effect of the passage of a plane gravitational wave, propagating along the  $z$ -axis, on this ring of test particles.

The upper panel shows the case where the metric perturbation has  $A_{xx}^{(TT)} = 0$  and  $A_{xy}^{(TT)} = 0$ . In this case the solutions for  $\xi^x$  and  $\xi^y$  reduce to

$$\xi^x = \epsilon \cos \theta \left( 1 + \frac{1}{2} A_{xx}^{(TT)} \cos \omega t \right) \quad (10)$$

And

$$\xi^y = \epsilon \sin \theta \left( 1 - \frac{1}{2} A_{xx}^{(TT)} \cos \omega t \right) \quad (11)$$

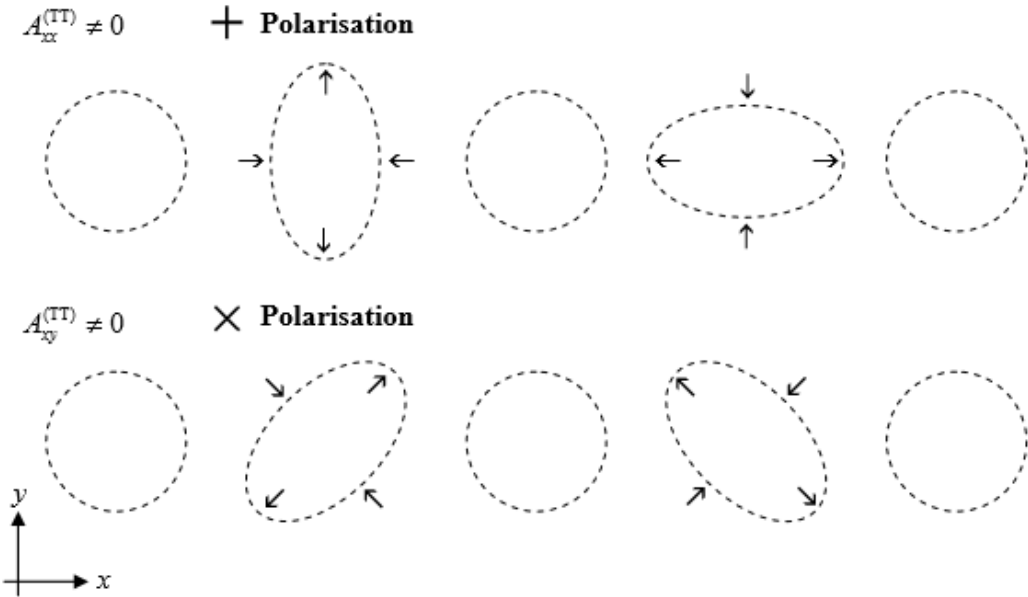


*Fig 3 : illustration of the effect of a gravitational wave on a ring of test particles. The upper panel shows a wave for which  $A_{xx}^{(TT)} = 0$  and  $A_{xy}^{(TT)} = 0$ , which we denote as the ‘+’ polarisation. The lower panel shows a wave for which  $A_{xy}^{(TT)} \neq 0$  and  $A_{xx}^{(TT)} = 0$ , which we denote as the ‘×’ polarisation.*

Each of the five rings across the upper panel of Figure 3 corresponds to a different phase (i.e. different value of  $\omega t$ ) in the oscillation of the wave: the first, third and fifth phases shown are all odd multiples of  $\pi/2$ , so that the  $\cos \omega t$  terms in equations (10) and (11) vanish. The second and fourth rings, on the other hand, correspond to a phase of  $\pi$  and  $2\pi$  respectively. At phase  $\pi$  we can see from equations (10) and (11) that the effect of the wave will be to move test particles on the  $x$ -axis inwards – i.e. the gravitational wave *reduces* their proper distance from the centre of the ring – while test particles on the  $y$ -axis are moved outwards – i.e. the gravitational wave *increases* their proper distance from the centre of the ring. At phase  $2\pi$ , on the other hand, the wave will produce an opposite effect,

increasing the proper distance from the ring centre of particles on the  $x$ -axis and reducing the proper distance of particles on the  $y$ -axis.

The lower panel of Figure 3 shows the contrasting case where the metric perturbation has  $A_{xy}^{(TT)} = 0$  and  $A_{xx}^{(TT)} = 0$ . Again, the ring of test particles is shown for five different phases in the oscillation of the gravitational wave:  $\pi/2$ ,  $\pi$ ,  $3\pi/2$ ,  $2\pi$  and  $5\pi/2$  respectively. In this case the solutions for  $\varepsilon^x$  and  $\varepsilon^y$  reduce to

$$\xi^x = \epsilon \cos \theta + \frac{1}{2} \epsilon \sin \theta A_{xy}^{(TT)} \cos \omega t \quad (12)$$

And

$$\xi^y = \epsilon \sin \theta + \frac{1}{2} \epsilon \cos \theta A_{xy}^{(TT)} \cos \omega t \quad (13)$$

To understand the relationship between these solutions and those for  $A_{xx}^{(TT)} \neq 0$ , we define new coordinate axes  $x^0$  and  $y^0$  by rotating the  $x$  and  $y$  axes through an angle of  $-\pi/4$ , so that

$$x' = \frac{1}{\sqrt{2}} (x - y) \quad (14)$$

And

$$y' = \frac{1}{\sqrt{2}} (x + y) \quad (15)$$

If we write the solutions for  $A_{xx}^{(TT)} \neq 0$  in terms of the new coordinates  $x^0$  and  $y^0$ , after some algebra we find that

$$\xi'^x = \epsilon \cos \left( \theta + \frac{\pi}{4} \right) + \frac{1}{2} \epsilon \sin \left( \theta + \frac{\pi}{4} \right) A_{xy}^{(TT)} \cos \omega t \quad (16)$$

And

$$\xi'^y = \epsilon \sin \left( \theta + \frac{\pi}{4} \right) + \frac{1}{2} \epsilon \cos \left( \theta + \frac{\pi}{4} \right) A_{xy}^{(TT)} \cos \omega t \quad (17)$$

Comparing the above two equations equation with equations 12 and 13 we see that our solutions with  $A_{xy}^{(TT)} \neq 0$  are identical to the solutions with  $A_{xx}^{(TT)} \neq 0$  apart from the rotation of  $\pi/4$  – as can be seen from the lower panel of Figure 3 .

We note some important features of the results of this section.

- The two solutions, for  $A_{xx}^{(TT)} \neq 0$  and  $A_{xy}^{(TT)} \neq 0$  represent two independent gravitational wave polarisation states, and these states are usually denoted by ‘+’ and ‘×’ respectively. In general any gravitational wave propagating along the  $z$ -axis can be expressed as a linear combination of the ‘+’ and ‘×’ polarisations, i.e. we can write the wave as

$$\mathbf{h} = a\mathbf{e}_+ + b\mathbf{e}_\times$$

where  $a$  and  $b$  are scalar constants and the *polarisation tensors*  $\mathbf{e}_+$  and  $\mathbf{e}_\times$  are

$$\mathbf{e}_+ = \begin{pmatrix} 0 & 0 & 0 & 0 \\ 0 & 1 & 0 & 0 \\ 0 & 0 & -1 & 0 \\ 0 & 0 & 0 & 0 \end{pmatrix}$$

and

$$\mathbf{e}_\times = \begin{pmatrix} 0 & 0 & 0 & 0 \\ 0 & 0 & 1 & 0 \\ 0 & 1 & 0 & 0 \\ 0 & 0 & 0 & 0 \end{pmatrix}$$

- We can see from the panels in Figure 3 that the distortion produced by a gravitational wave is quadrupolar. This is a direct consequence of the fact that gravitational waves are produced by changes in the curvature of spacetime, the signature of which is acceleration of the deviation between neighbouring geodesics. Geodesic deviation cannot distinguish between a zero gravitational field and a uniform gravitational field: only for a non-uniform, tidal gravitational field does the geodesic deviation accelerate. Such tidal variations are quadrupolar in nature.
- We can also see from Figure 3 that, at any instant, a gravitational wave is invariant under a rotation of  $180^\circ$  about its direction of propagation (in this case, the  $z$ -axis). By contrast, an electromagnetic wave is invariant under a rotation of  $360^\circ$ , and a *neutrino* wave is invariant under a rotation of  $720^\circ$ . This behaviour can be understood in terms

of the *spin states* of the corresponding gauge bosons: the particles associated with the quantum mechanical versions of these waves.

In general, the classical radiation field of a particle of spin,  $S$ , is invariant under a rotation of  $360^\circ/S$ . Moreover, a radiation field of spin  $S$  has precisely two independent polarisation states, which are inclined to each other at an angle of  $90^\circ/S$ . Thus, for an electromagnetic wave, corresponding to a photon of spin  $S = 1$ , the independent polarisation modes are inclined at  $90^\circ$  to each other.

We can, therefore, deduce from the inclination of the gravitational wave polarisation states, that the graviton (which is, as yet undiscovered, since we do not yet have a fully developed theory of quantum gravity!) must be a spin  $S = 2$  particle. The fact that electromagnetic waves correspond to a spin  $S = 1$  field and gravitational waves correspond to a spin  $S = 2$  field is also intimately connected to their mathematical description in terms of geometrical objects: spin  $S = 1$  fields are vector fields, which is why we require only a vector description for the electromagnetic field; spin  $S = 2$  fields, on the other hand, are tensor fields, which is why we required to introduce tensors to describe the properties of the gravitational field.

#### 4.2) Frequency Of Gravitational Waves

The signals for which the best waveform predictions are available have a well defined frequency , in some cases the frequency is dominated by existing motion such as the spin of a pulsar , but in most cases the frequency will be related to natural frequency of a self gravitating body defined

$$W_0 = (\pi G \mu)^{1/2} ; f_0 = W_0 / 2\pi$$

$$f_0 = (\pi G \mu)^{1/2} / 2\pi$$

where  $\mu$  is the mean density of mass- energy in the source . it is of the same order of the binary orbital frequency and fundamental pulsation frequency of a body , even though this is a Newtonian formula it provides good order of magnitude prediction of natural frequency , even for highly relativistic systems such as black holes and neutron stars .

The frequency of gravitational waves need not be equal to the natural frequency of the body even if it is a mechanism of oscillation with that frequency , in many cases such as binaries the frequency of gravitational waves comes out to be twice the oscillation frequency , but at this point we are not trying to be more accurate than a few factors we will ignore this distinction here .

The mean density and hence frequency are determined by the size  $R$  and mass  $M$  of some sources taking  $\mu = 3M / 4\pi R^3$

$$\text{We get } f_0 = (3M / R^3)^{1/2} \times 1/4\pi .$$

For a neutron star of mass  $1.4M_\odot$  and radius 10 km, the natural frequency is  $f_0 = 1.9$  kHz. For a black hole of mass  $10M_\odot$  and radius  $2M = 30$  km, it is  $f_0 = 1$  kHz. And for a large black hole of mass  $2.5 \times 10^6 M_\odot$ , such as the one at the centre of our galaxy, this goes down in

inverse proportion to the mass to  $f_0 = 4$  mHz. In general, the characteristic frequency of the radiation of a compact object of mass  $M$  and radius  $R$  is

$$f_0 = \frac{1}{4\pi} \left( \frac{3M}{R^3} \right)^{1/2} \simeq \left( \frac{10 M_\odot}{M} \right)$$

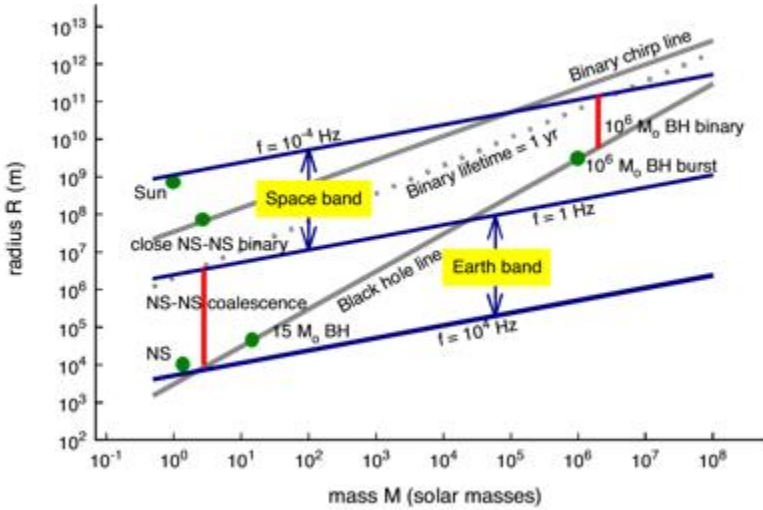


Fig: 4

The given graph shows mass vs radius diagram for likely sources of gravitational waves , 3 frequencies of  $f_0=1\text{Hz}$  ,  $f_0=10^{-4}\text{Hz}$ ,  $f_0=10^4\text{Hz}$ . These are interesting frequencies from the point of view of observing techniques . Gravitational waves between  $1 - 10^4\text{Hz}$  are in principle accessible for ground based detectors . Where as lower frequencies are observable from space . The line marking the black-hole boundary. This has the equation  $R = 2M$ . There are no objects below this line, because they would be smaller than the horizon size for their mass. This line cuts through the ground-based frequency band in such a way as to restrict ground-based instruments to looking at stellar-mass objects. No system with a mass above about  $10^4 M_\odot$  can produce quadrupole radiation in the ground-based frequency band.

A number of typical relativistic objects are placed in the diagram: a neutron star, a pair of neutron stars that spiral together as they orbit, some black holes. Two other interesting lines are drawn. The lower (dashed) line is the 1-year coalescence line, where the orbital shrinking timescale due to gravitational radiation back reaction is less than one year. The upper (solid) line is the 1-year chirp line: if a binary lies below this line, then its orbit will shrink enough to make its orbital frequency increase by a measurable amount in one year. (In a one-year observation one can, in principle, measure changes in frequency of  $1\text{yr}^{-1}$ , or  $3 \times 10^{-8}\text{Hz}$ .)

It is clear from the Figure 4 that any binary system that is observed from the ground will coalesce within an observing time of one year. Since pulsar binary statistics suggest that neutronstar-binary coalescences happen less often than once every  $10^5$  years in our galaxy, ground-based detectors must be able to register these events in a volume of space containing at least  $10^6$  galaxies in order to have a hope of seeing occasional coalescences. That corresponds to a volume of radius roughly 100 Mpc. For comparison, first-generation ground-

based interferometric detectors have a reach of around 20 Mpc for such binaries, while advanced interferometers should extend that to about 200 Mpc.

#### 4.3) Amplitude

The Einstein equations are too difficult to solve analytically in the generic case of a strongly gravitating source to compute the luminosity and amplitude of gravitational waves from an astronomical source. The most powerful available analytic approach is called the post-Newtonian approximation scheme. This approximation is suited to gravitationally bound systems, which constitute the majority of expected sources. In this solutions are expanded in the small parameter  $(v/c)^2$ , where  $v$  is the typical dynamical speed inside the system. Because of the virial theorem, the dimensionless Newtonian gravitational potential  $\phi/c^2$  is of the same order, so that the expansion scheme links orders in the expanded metric with those in the expanded source terms. The lowest-order post-Newtonian approximation for the emitted radiation is the quadrupole formula, and it depends only on the density ( $\rho$ ) and velocity fields of the Newtonian system. If we define the spatial tensor  $Q_{jk}$ , the second moment of the mass distribution, by the equation

$$Q_{jk} = \int \rho x_j x_k d^3x,$$

then the amplitude of the emitted gravitational wave is, at lowest order, the three-tensor

$$h_{jk} = \frac{2}{r} \frac{d^2 Q_{jk}}{dt^2}.$$

This is to be interpreted as a linearized gravitational wave in the distant almost-flat geometry far from the source, in a coordinate system (gauge) called the Lorentz gauge.

#### 4.4) Luminosity :

The general formula for the local stress-energy of a gravitational wave field propagating through flat spacetime, using the TT-gauge, is given by the Isaacson expression

$$T_{\alpha\beta} = \frac{1}{32\pi} \langle h_{jk,\alpha}^{TT} h_{,\beta}^{TTjk} \rangle,$$

where the angle brackets denote averages over regions of the size of a wavelength and times of the length of a period of the wave. The energy flux of a wave in the  $x^i$  direction is the  $T^{0i}$  component.

The gravitational wave luminosity in the quadrupole approximation is obtained by integrating the energy flux from the above equation over a distant sphere. When projection factors are taken into account , one obtains

$$L_{gw} = \frac{1}{5} \left( \sum_{j,k} \ddot{Q}_{jk} \ddot{Q}_{jk} - \frac{1}{3} \ddot{Q}^2 \right),$$

where  $Q$  is the trace of the matrix  $Q_{jk}$ . This equation can be used to estimate the back reaction effect on a system that emits gravitational radiation .

Notice that the expression for  $L_{gw}$  is dimensionless when  $c = G = 1$ . It can be converted to normal luminosity units by multiplying by the scale factor

$$L_0 = c^5/G = 3.6 \times 10^{52} \text{ W.}$$

This is an enormous luminosity. By comparison, the luminosity of the sun is only  $3.8 \times 10^{26}$  W, and that of a typical galaxy would be  $10^{37}$  W. All the galaxies in the visible universe emit, in visible light, on the order of  $10^{49}$  W. We will see that gravitational wave systems always emit at a fraction of  $L_0$ , but that the gravitational wave luminosity can come close to  $L_0$  and can greatly exceed typical electromagnetic luminosities. Close binary systems normally radiate much more energy in gravitational waves than in light. Black hole mergers can, during their peak few cycles, compete in luminosity with the steady luminosity of the entire universe!

The apparent luminosity of a radiation at great distances from the source in terms of the gravitational wave amplitude is given by the formula

$$\mathcal{F} \sim \frac{|\dot{h}|^2}{16\pi}.$$

The above relation can be used to make an order-of-magnitude estimate of the gravitational wave amplitude from a knowledge of the rate at which energy is emitted by a source in the form of gravitational waves. If a source at a distance  $r$  radiates away energy  $E$  in a time  $T$ , predominantly at a frequency  $f$ , then writing  $h = 2\pi f h$  and noting that  $F \sim E/(4\pi r^2 T)$ , the amplitude of gravitational waves is

$$h \sim \frac{1}{\pi f r} \sqrt{\frac{E}{T}}.$$

When the time development of a signal is known, one can filter the detector output through a copy of the expected signal . This leads to an enhancement in the SNR, as compared to its narrow-band value, by roughly the square root of the number of cycles the signal spends in the detector band. It is useful, therefore, to define an effective amplitude of a signal, which is a better measure of its detectability than its raw amplitude:

$$h_{\text{eff}} \equiv \sqrt{n} h.$$

Now, a signal lasting for a time  $T$  around a frequency  $f$  would produce  $n \approx fT$  cycles. Using this we can eliminate  $T$  and get the effective amplitude of the signal in terms of the energy, the emitted frequency and the distance to the source:

$$h_{\text{eff}} \sim \frac{1}{\pi r} \sqrt{\frac{E}{f}}.$$

Notice that this depends on the energy only through the total fluence , or time-integrated flux  $E/4\pi r^2$  of the wave. As in many other branches of astronomy, the detectability of a source is ultimately a function of its apparent luminosity and the observing time. However, one should not ignore the dependence on frequency in this formula. Two sources with the same fluence are not equally easy to detect if they are at different frequencies: higher frequency signals have smaller amplitudes.

#### 4) PHYSICS WITH GRAVITATIONAL WAVES

General relativity has passed all possible experimental and observational tests so far. The theory is elegant, self-consistent and mathematically complete (i.e., its equations are, in principle, solvable). However, theorists are uncomfortable with general relativity because it has so far eluded all efforts of quantization, making it a unique modern theory, whose quantum mechanical analogue is unknown. Although general relativity arises as a by-product in certain string theories, the physical relevance of such theories is unclear. Therefore, it has been proposed that general relativity is a low-energy limit of a more general theory, which in itself is amenable to both quantization and unification. There are also other theoretical motivations to look for modifications of general relativity or new theories of gravity. While there are some alternative candidates (including the Brans–Dicke theory), none has predictions that contradict general relativistic predictions in linear and mildly nonlinear gravitational fields. More precisely, the extra parameters of these other theories of gravity are constrained by the present experimental and astronomical observations, however, they are expected to significantly deviate from general relativistic predictions under conditions of strong gravitational fields. Gravitational wave observations provide a unique opportunity to test strongly nonlinear and highly relativistic gravity and hence provide an unprecedented testbed for confronting different theories of gravity. Every nonlinear gravitational effect in general relativity will have a counterpart in alternative theories and therefore a measurement of such an effect would provide an opportunity to compare the performance of general relativity with its competitors. Indeed, a single measurement of the full polarization of an incident gravitational wave can potentially rule out general relativity. This is a field that would benefit from an in-depth study. What we are lacking is a systematic study of higher-order post-Newtonian effects in alternative theories of gravity. For instance, we do not know how tails of gravitational waves or tails of tails would appear in any theory other than general relativity. In what follows we present strong field tests of general relativity . We will begin with observations of single black holes followed by black hole binaries (more generally, coalescing binaries of compact objects).

##### 5.1) Speed Of Gravitational Waves

Association of a gravitational wave event with an electromagnetic event, such as the observation of a gamma or X-ray burst coincidentally with a gravitational wave event, would help to deduce the speed of gravitational waves to a phenomenal accuracy. The best candidate sources for the simultaneous observations of both are the well-known extra-galactic gamma-ray bursts (GRBs). Depending on the model that produces the GRB, the delay between the emission of a GRB and gravitational waves might be either a fraction of a second (as in GRBs

generated by internal shocks in a fireball ) or 100's of seconds (as in GRBs generated when the fireball is incident on an external medium). It is unlikely that high-redshift gamma-ray observations will be visible in the gravitational wave band, since the amplitude of gravitational waves might be rather low. However, advanced detectors might see occasional low-redshift events, especially if the GRB is caused by black-hole-neutron-star mergers. Third generation detectors would be sensitive to such events up to  $z = 2$ . A single unambiguous association can verify the speed of gravitational waves relative to light to a fantastic precision.

For instance , even a day's delay between the arrival of gravitational and electromagnetic radiation from a source at a distance of 1 Giga lightyear is sufficient to estimate the speed of gravitational waves to one part in  $10^{11}$ . Coincident detection of gravitational and electromagnetic radiation would require good timing and precision to determine the direction of source so that the astronomical observations of associated gamma rays can be made . Consequently gravitational wave antennas around the globe will have to make a coincident detection of the event , if the speed of the gravitational waves is less than the speed of light it implies that a graviton has non zero mass .

## 5.2) Polarization Of Gravitational Waves

There are two independent polarizations for a gravitational wave  $h_x$  and  $h_+$  a general gravitation wave will be a linear combination of both . Rotating sources typically emit both the polarizations with a phase delay between them leading to elliptical polarization patterns , depending upon the nature of sources such polarizations can be detected with a single detector (in case of continuous waves) or a network of detectors ( in case of bursts).

While Einstein theory predicts only two possible orientation of gravitational waves there are other theories which predict additional states of polarization for instance the Fierz-Jordan-Brans-Dicke theory , there are four polarization degrees of freedom more than Einstein theory therefore an unambiguous determination of polarization of waves is of fundamental importance.

In case of a burst source to determine the two polarization states , source direction and amplitude requires 3 detectors , observing the other polarizations require the use of more than 3 detectors . The scalar polarization made by brans Dicke for example expands a traversing ring without changing its shape . This is the breathing mode or monopole polarization . If such a wave is incident from above on an interferometer it will not register at all , but if it comes along one of its arms , then, since it acts transversely, on one of its arms and it leaves a signal . If a wave is seen using enough detectors it is possible to determine the scalar potential . note that a measurement such as this can bring a quantitative change in physics and a single measurement can put the entire general theory of relativity in jeopardy .

Polarization measurements have an important application in astronomy . The polarization of waves contain information regarding the orientation of the source . For e.g. a binary system emits purely circular polarization along the angular momentum axis but a linear polarization along its equatorial plane . By measuring the polarizations from a binary one can determine the orientation and inclination of the spin axis , this piece of information is difficult to obtain from optical observations .

### 5.3) Gravitational Radiation Reaction :

In 1974, Hulse and Taylor discovered the first double neutron star binary PSR B1913+16, a system in which the emission of gravitational radiation has an observable effect . General relativity predicts that the loss of energy and angular momentum due to the emission of gravitational waves should cause the period of the system to decrease and, by carefully monitoring the orbital period of the binary, that it would be possible to measure the rate at which the period changes. The rate at which the period decays can be computed using the quadrupole formula for the luminosity of the emitted radiation combined with the energy-balance equation; namely that the energy carried away by the waves comes at the expense of the binding energy of the system. For a binary consisting of stars of masses  $m_1$  and  $m_2$ , in an orbit of eccentricity  $e$  and period  $P_b$ , the period decay is given by the equation :

$$\dot{P}_b = -\frac{192\pi}{5} \left( \frac{2\pi M}{P_b} \right)^{5/3} \left( 1 + \frac{73}{24}e^2 + \frac{37}{96}e^4 \right) (1 - e^2)^{-7/2}$$

M is given by the equation

$$M = (m_1 m_2)^{\frac{3}{5}} (m_1 + m_2)^{-\frac{1}{5}}$$

Where M is the chirpmass of the binary Since the masses of the binary and the eccentricity of the orbit can be measured by other means, one can use these parameters in the above equation to infer the rate at which the period is predicted to decrease according to general relativity. For the Hulse–Taylor binary the relevant values are:  $m_1 = 1.4414M_\odot$ ,  $m_2 = 1.3867M_\odot$ ,  $e = 0.6171338$ ,  $P_b = 2.790698 \times 10^4$  s. The predicted value  $P_b^{\text{GR}} = -(2.40242 \pm 0.00002) \times 10^{-12}$ , while the observed period decay is  $P_b^{\text{Obs}} = -(2.4056 \pm 0.0051) \times 10^{-12}$  and the two are in agreement to better than a tenth of a percent .

Observation of the decay of the orbital period in PSR B1913+16 is an unambiguous direct observation of the effect of gravitational radiation backreaction on the dynamics of the system. PSR B1913+16 was the first system in which the effect of gravitational radiation reaction force was measured. In 2004, a new binary pulsar PSR J0737-3039 was discovered . J0737 is in a tighter orbit than PSR B1913+16; with an orbital period of only 2.4 hrs, the orbit is shrinking by about 7 mm each day in good agreement with the general relativistic prediction.

### 5.4) Black Hole Spectroscopy :

An important question relating to the structure of a black hole is its stability. Studies that began in the 1970s showed that a black hole is stable under external perturbation. A formalism was developed to study how a black hole responds to generic external perturbations, which has come to be known as black hole perturbation theory . What we now know is that a distorted Kerr black hole relaxes to its axisymmetric state by partially emitting the energy in the distortion as gravitational radiation. The radiation consists of a superposition of QNMs ( quasi normal mode) , whose frequency and damping time depend uniquely on the mass  $M$  and spin angular momentum  $J$  of the parent black hole and not on the nature of the external perturbation. The amplitudes and damping times of different modes, however, are determined by the details of the perturbation and are not easy to calculate, except in some simple cases.

The uniqueness of the QNMs is related to the “no-hair” theorem of general relativity according to which a black hole is completely specified by its mass and spin. Thus, observing QNMs would not only confirm the source to be a black hole, but would be an unambiguous proof of the uniqueness theorem of general relativity.

The end state of a black hole binary will lead to the formation of a single black hole, which is initially highly distorted. Therefore, one can expect coalescing black holes to end their lives With the emission of QNM radiation often called as the ringdown radiation It was realized quite early that the energy emitted during the ringdown phase of a black-hole-binary coalescence could be pretty large. Although, the initial quantitative estimates have proven to be rather high, the qualitative nature of the prediction has proven to be correct. Indeed, numerical relativity simulations show that about 1–2% of a binary’s total mass would be emitted in QNMs . The effective one-body model , the only analytical treatment of the merger dynamics, gives the energy in the ringdown radiation to be about 0.7% of the total mass, consistent with numerical results. Thus, it is safe to expect that the ringdown will be as luminous an event as the inspiral and the merger phases. The fact that QNMs can be used to test the no-hair theorem puts a great emphasis on understanding their properties, especially the frequencies, damping times and relative amplitudes of the different modes that will be excited during the merger of a black hole binary and how accurately they can be measured.

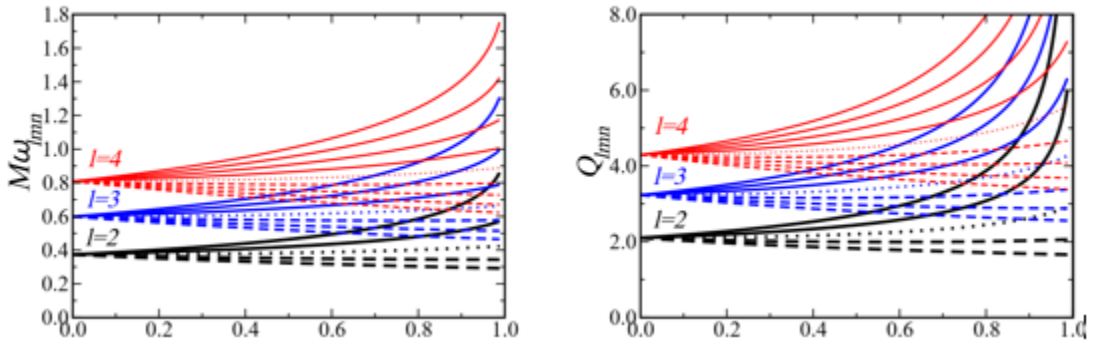


*Fig 5 : Normal mode frequencies (left) and corresponding quality factors (right) of fundamental modes with  $l = 2,3,4$ , as a function of the dimensionless black hole spin  $j$ , for different values of  $m = l,...,0,...,-l$  (for each  $l$ , different line styles from top to bottom correspond to decreasing values of  $m$ ).*

QNMs are characterized by a complex frequency  $\omega$  that is determined by three “quantum” numbers,  $(l, m, n)$  . Here  $(l, m)$  are indices that are similar to those for standard spherical harmonics. For each pair of  $(l, m)$  there are an infinitely large number of resonant modes characterized by another integer  $n$ . The time dependence of the oscillations is given by  $\exp(i\omega t)$ , where  $\omega$  is a complex frequency, its real part determining the mode frequency and the imaginary part (which is always positive) giving the damping time:  $\omega = \omega_{lmn} + i/\tau_{lmn}$ ,  $\omega_{lmn} = 2\pi f_{lmn}$  defining the angular frequency and  $\tau_{lmn}$  the damping time. The ringdown wave will

appear in a detector as the linear combination  $h(t)$  of the two polarizations  $h_+$  and  $h_\times$ , that is  $h(t) = F_+ h_+ + F_\times h_\times$ ,  $F_+$  and  $F_\times$  being the antenna pattern functions as defined in Equation

where  $\iota$  is the angle between the black hole's spin axis and the observer's line of sight and  $\phi_{lmn}$  is an unknown constant phase. The quality factor  $Q_{lmn}$  of a mode is defined as  $Q_{lmn} = \frac{w_{lmn} \tau_{lmn}}{2}$  and gives roughly the number of oscillations that are observable before the mode dies out. Figure 5 plots frequencies and quality factors for the first few QNMs as a function of the dimensionless spin parameter  $j = J/M^2$ . The mode of a Schwarzschild black hole corresponding to  $l=2$ ,  $m=n=0$ , is given by

$$\begin{aligned} h_+ &= \frac{A(f_{lmn}, Q_{lmn}, \epsilon_{rd})}{r} (1 + \cos^2 \iota) \exp\left(\frac{-\pi f_{lmn} t}{Q_{lmn}}\right) \cos(2\pi f_{lmn} t + \varphi_{lmn}) \\ h_\times &= \frac{A(f_{lmn}, Q_{lmn}, \epsilon_{rd})}{r} 2 \cos \iota \exp\left(\frac{-\pi f_{lmn} t}{Q_{lmn}}\right) \sin(2\pi f_{lmn} t + \varphi_{lmn}), \end{aligned}$$

$$f_{200} = \pm 1.207 \times 10^3 \frac{10 M_\odot}{M} \text{ Hz}, \quad \tau_{200} = 5.537 \times 10^{-4} \frac{M}{10 M_\odot} \text{ s}$$

For stellar-mass-black-hole coalescences expected to be observed in ground-based detectors the ringdown signal is a transient that lasts for a very short time. However, for space-based LISA the signal would last several minutes for a black hole of  $M = 10^7 M_\odot$ . In the latter case, the ringdown waves could carry the energy equivalent of  $10^5 M_\odot$  converted to gravitational waves – a phenomenal amount of energy compared even to the brightest quasars and gamma ray bursts. Thus, LISA should be able to see QNMs from black hole coalescences anywhere in the universe, provided the final (redshifted) mass of the black hole is larger than about  $10^6 M_\odot$ , as otherwise the signal lasts for far too short a time for the detector to accumulate the SNR.

Berti et al. have carried out an exhaustive study, in which they find that the LISA observations of SMBH binary mergers could be an excellent testbed for the no-hair theorem. Figure 6 (left panel) plots the fractional energy  $Q_{rd}$  that must be deposited in the ringdown mode so that the event is observable at a distance of 3 Gpc. Black holes at 3 Gpc with mass  $M$  in the range of  $10^6$ – $10^8 M_\odot$  would be observable (i.e., will have an SNR of 10 or more) even if a fraction  $Q_{rd} \simeq 10^{-7} M$  of energy is in the ringdown phase. Numerical relativity predicts that as much as 1% of the energy could be emitted as QNMs, when two black holes merge, implying that the ringdown phase could be observed with an SNR of 100 or greater all the way up to  $z \sim 10$ , provided their mass lies in the appropriate range<sup>1</sup>. Furthermore, they find that at this redshift it should be possible to resolve the fundamental  $l=2$ ,  $m=2$  mode. Since black holes forming from primordial gas clouds at  $z = 10$ – $15$  could well be the seeds of galaxy formation and large-scale structure, LISA could indeed witness their formation through out the cosmic history of the universe .

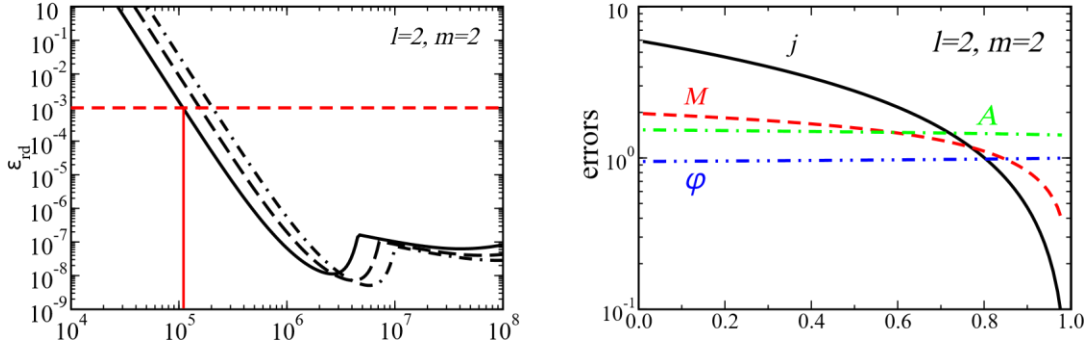


*Fig 6 : The smallest fraction of black hole mass in ringdown waveforms that is needed to observe the fundamental mode at a distance of 3 Gpc (left) for three values of the black hole spin,  $j = 0$  (solid line)  $j = 0.80$  (dashed line) and  $j = 0.98$  (dot-dashed line) and the error in the measurement of the various parameters as a function of the black hole spin for the same mode (right).*

(right panel) shows SNR-normalized errors (i.e., one-sigma deviations multiplied by the SNR) in the measurement of the various QNM parameters (the mass of the hole  $M$ , its spin  $j$ , the QNM amplitude  $A$  and phase  $\phi$ ) for the fundamental  $l=m=2$  mode. We see that, for expected ringdown efficiencies of  $Q_{rd} \simeq 10^{-2}M$  into the fundamental mode of an a-million-solar-mass black hole with spin  $j = 0.8$  at 3 Gpc ( $\rho \sim 2000$ ), the mass and spin of the black hole can be measured to an accuracy of a tenth of a percent. By observing a mode's frequency and damping time, one can deduce the (redshifted) mass and spin of the black hole. However, this is not enough to test the no-hair theorem. It would be necessary, although by no means sufficient, to observe at least one other mode (whose damping time and frequency can again be used to find the black hole's mass and spin) to see if the two are consistent with each other. Berti et al found that such a measurement should be possible if the event occurs within a redshift of  $z \sim 0.5$ .

## 5.5) The Two Body Problem In General Relativity

The largest effort in gravitational radiation theory in recent years has been to study the two-body problem using various approximations. The reason is that gravitationally bound binary systems are likely to be important gravitational wave sources, and until the evolution of such a system is thoroughly understood, it will not be possible to extract the maximum possible information from the observations. From Figure 7, we see that ground-based detectors will be sensitive to compact binaries with mass in the range of  $[1, 10^4]M_\odot$  while LISA will be sensitive to the mass range  $[10^4, 10^8]M_\odot$ . Most classes of binary sources will follow orbits that evolve strongly due to gravitational radiation reaction. In the case of ground-based detectors, they will all merge within a year of entering the observation band. In the case of LISA, we might observe sources (both stellar mass binaries as well as SMBH binaries), whose frequency hardly changes.

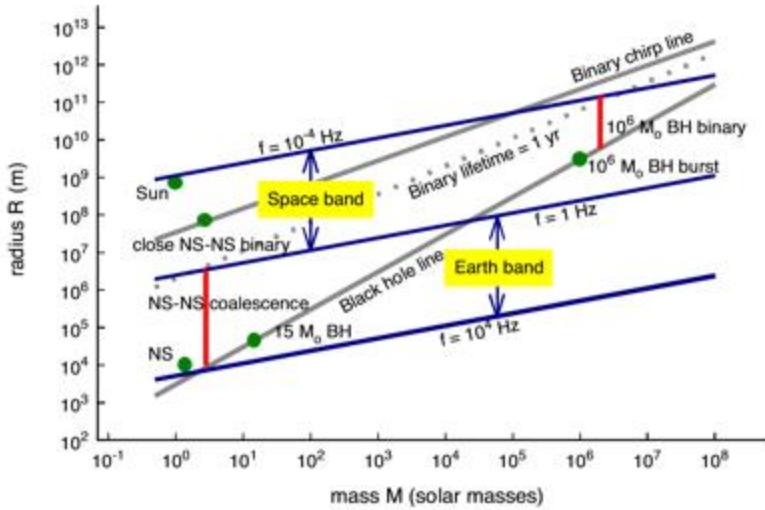


Fig 7

In contrast to Newtonian gravity, modelling a bound binary in general relativity is complicated by the existence of gravitational radiation and the nonlinearity of Einstein's equations. It must therefore be done approximately. The three most important approximation methods for solving gravitational wave problems are:

- **The post-Newtonian scheme:** This is a combination of a low-velocity expansion ( $v/c$  small) and a weak-field expansion ( $M/R$  small), in which the two small parameters are linked because a gravitationally-bound binary satisfies the virial relation  $v^2 \sim M/R$ , even in relativity. The zero-order solution is the Newtonian binary system. The post-Newtonian (PN) approximation has now been developed to a very high order in  $v/c$  because the velocities in late-stage binaries, just before coalescence, are very high.
- **Perturbation theory:** This is an expansion in which the small parameter is the massratio of the binary components. The zero-order solution is the field of the more massive component, and linear field corrections due to the second component determine the binary's orbital motion and the emitted radiation. This approximation is fully relativistic at all orders. It is being used to study the signals emitted by compact stars and stellar-mass black holes as they fall into SMBHs, an important source for LISA .
- **Numerical approaches:** With numerical relativity one can in principle simulate any desired relativistic system, no matter how strong the fields or high the velocities. It is being used to study the final stage of the evolution of binaries, including their coalescence, after the PN approximation breaks down. Although it deals with fully relativistic and nonlinear general relativity, the method needs to be regarded as an approximate one, since spacetime is not resolved to infinite precision. The accuracy of a numerical simulation is normally judged by performing convergence tests, that is by doing the simulation at a variety of resolutions and showing that there are no unexpected differences between them .

### 5.5.1) Binaries As Standard Candles : distance estimation

Astronomers refer to systems as standard candles if their intrinsic luminosity is known, so that when the apparent luminosity of a particular system is measured, then its distance can be deduced. Radiating binaries have this property, if one can measure the effects of radiation reaction on their orbits . Because of the one-dimensional nature of gravitational wave data, some scientists have begun calling these standard sirens . Over cosmological distances, the distance measured from the observation is the luminosity distance . This can be used to calculate the value of Hubble constant and acceleration of the universe in methods independent of cosmic ladder .

### 5.5.2) Numerical Approach To The Two Body Problem :

From the point of view of relativity, the simplest two-body problem is that of two black holes. There are no matter fields and no point particles, just pure gravity. Therefore, the physics is entirely governed by Einstein's equations, which are highly nonlinear and rather difficult to solve. A number of teams have worked for over three decades towards developing accurate numerical solutions for the coalescence of two black holes, using fully three-dimensional numerical simulations.

A breakthrough came in early 2005 with Pretorius announcing the results from the first stable simulation ever, followed by further breakthroughs by two other groups with successful simulations. The main results from numerical simulations of nonspinning black holes are rather simple. Indeed, just as the EOB had predicted, and probably contrary to what many people had expected, the final merger is just a continuation of the adiabatic inspiral, leading on smoothly to merger and ringdown. In Figure 8 we show the results from one of the numerical simulations (right panel) and that of the EOB (left panel), both for the same initial conditions. There is also good agreement in the prediction of the total energy emitted by the system, being 5.0% ( $\pm 0.4\%$ ) and 3.1% , by numerical simulations and EOB, respectively, as well as the spin of the final black hole (respectively, 0.69 and 0.8) that results from the merger.

The total energy emitted and the spin angular momentum of the black hole both depend on the spin angular momenta of the parent black holes and how they are aligned with respect to the orbital angular momentum. In the test-mass limit, it is well known that the last stable orbit of a test particle in prograde orbit will be closer to, and that of a retrograde orbit will be farther from, the black hole as compared to the Schwarzschild case. Thus, prograde orbits last longer and radiate more compared to retrograde orbits. The same is true even in the case of spinning black holes of comparable masses the emitted energy will be greater when the spins are aligned with the orbital angular momentum and least when they are anti-aligned. For instance, for two equal mass black holes, each with its spin angular momentum equal to 0.76, the total energy radiated in the aligned case is 6.7% (2.2%) and the spin of the final black hole is 0.89 (0.44) . Heuristically, in the aligned case the black holes experience a repulsive force, deferring the merger of the two bodies to a much later time than in the anti-aligned case, where they experience an attractive force, accelerating the merger.

Detailed comparisons show that we should be able to deploy the analytical templates from EOB (and other approximants ) that better fit the numerical data in our searches. With the availability of merger waveforms from numerical simulations and analytical templates, it will

now be possible to search for compact binary coalescences with a greater sensitivity. The visibility of the signal improves significantly for binaries with their component masses in the range  $[10, 100]M_{\odot}$ . Numerical relativity simulation in Gravitational wave searches help to increase the distance reach of interferometric detectors by a factor of 2 and correspondingly an order of magnitude increase in event rate .

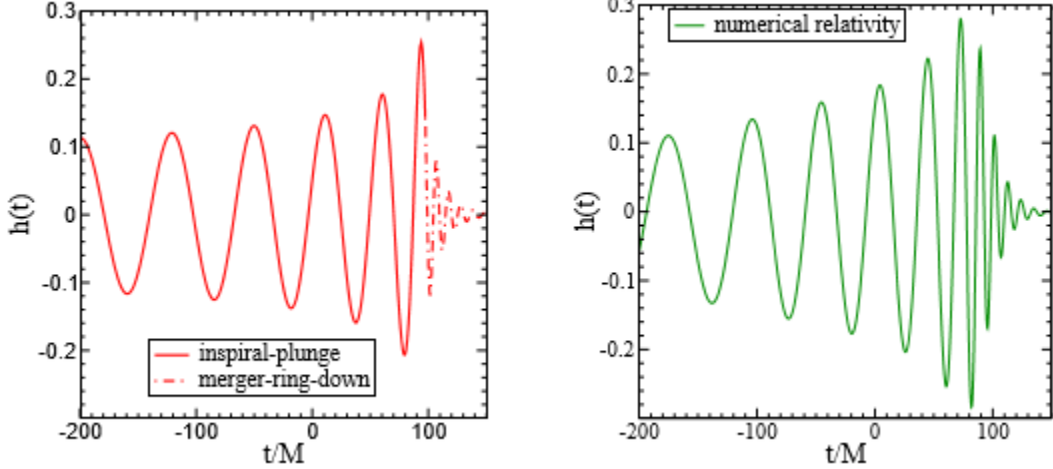


*Fig 8 : Comparison of waveforms from the analytical EOB approach (left) and numerical relativity simulations (right) for the same initial conditions. The two approaches predict very similar values for the total energy emitted in gravitational waves and the final spin of the black hole .*

Numerical relativity simulations have now greatly matured, allowing a variety of different studies. Some are studying the effect of the spin orientations of the component black holes on the linear momentum carried away by the final black hole, fancifully called “kicks” some have focused on the dependence of the emitted waveform phase and energy on the mass ratio and yet others have strived to evolve the system with high accuracy and for a greater number of cycles so as to push the techniques of numerical relativity to the limit . Of particular interest are the numerical values of black hole kicks that have been obtained for certain special configurations of the component spins. Velocities as large as  $4000 \text{ km s}^{-1}$  have been reported by several groups, but such velocities are only achieved when both black holes have large spins. Such velocities are in excess of escape velocities typical of normal galaxies and are, therefore, of great astronomical significance. These high velocities, however, are not seen for generic geometries of the initial spin orientations therefore, their astronomical significance is not yet clear.

Physics behind kicks : Beamed emission of radiation from a binary could result in imparting a net linear momentum to the final black hole. The radiation could be beamed either because the masses of the two black holes are not the same (resulting in asymmetric emission in the orbital plane) or because of the precession of the orbital plane arising from spin-orbit and spin-spin interactions, or both. In the case of black holes with unequal masses, the largest kick one can get is around  $170 \text{ km s}^{-1}$ , corresponding to a mass ratio of about 3:1. It was really with the

advent of numerical simulations that superkicks begin to be realized, but only when black holes had large spins.

The spin-orbit configurations that produce large kicks are rather unusual and at first sight unexpected. When the component black holes are both of the same mass and have equal but opposite spin angular momenta that lie in the orbital plane, frame dragging can lead to tilting and oscillation of the orbital plane, which, in the final phases of the evolution, could result in a rather large kick . SMBHs are suspected to have large spins and, therefore, the effect of spin on the evolution of a binary and the final spin and kick velocity could be of astrophysical interest too.

Curiously, a recent optical observation of a distant quasar, SDSS J0927 12.65+294344.0, could well be the first identification of a superkick, causing the SMBH to escape from the parent galaxy . From a fundamental physics point of view, kicks offer a new way of testing frame dragging in the vicinity of black holes, but much work is needed in this direction.

Predicting the spin of the final black hole, will help in further exploring interesting regions of the spin parameter space. In the relatively simple case of two black holes with equal and aligned spins of magnitude  $a$ , but unequal masses, with the symmetric mass ratio being  $\nu = m_1 m_2 / (m_1 + m_2)^2$ , have obtained an excellent fit for the final spin of the black hole by enforcing basic constraints from the test-mass limit:

$$a_{\text{fin}} = a + (2\sqrt{3} + t_0 a + s_4 a^2) \nu + (s_5 a + t_2) \nu^2 + t_3 \nu^3$$

where  $t_0 = -2.686 \pm 0.065$ ,  $t_2 = -3.454 \pm 0.132$ ,  $t_3 = 2.353 \pm 0.548$ ,  $S_4 = -0.129 \pm 0.012$ , and  $S_5 = -0.384 \pm 0.261$ . The top and middle panels of Figure 9 compare as functions of black hole spin and the symmetric mass ratio the goodness of their fit (blue short-dashed line, top panels) with the predictions of numerical simulations (circles and stars) from different groups (AEI , FAU–Jena , Jena and Goddard ). Their residuals (red dotted lines, bottom panels) are less than a percent over the entire parameter space observed. These figures also show the fits obtained for the equal-mass but variable-spin case (green long-dashed line, left panel) and for the non-spinning but unequal-mass case (green long-dashed line, middle panel) .

For the simple case of two equal mass black holes with aligned spins, the above analytical formula predicts that minimal and maximal final spin values of  $a_{\text{fin}} = 0.35 \pm 0.03$  and  $a_{\text{fin}} = 0.96 \pm 0.03$ , respectively . More interestingly, one can now ask what initial configurations of the mass ratios and spins would lead to the formation of a Schwarzschild black hole (i.e.,  $a_{\text{fin}}(a, \nu) = 0$ ) , which defines the boundary of the region on one side of which lie systems for which the spin of the final black hole flips relative to the initial total angular momentum .

Finally, the evolution of binaries composed of nonspinning bodies is characterized by a single parameter, namely the ratio of the masses of the two black holes. The study of systems with different mass ratios has allowed relativists to fit numerical waveforms with phenomenological waveforms . The advantage of the latter waveforms is that one is able to more readily carry out data analysis in any part of the parameter space without needing the numerical data over the entire signal manifold.

Numerical relativity is still in its infancy and the parameter space is quite large. In the coming years more accurate simulations should become available, allowing the computation of waveforms with more cycles and less systematic errors. However, the challenge remains to systematically explore the effect of different spin orientations, mass ratios and eccentricity. One area that has not been explored using perturbative methods or post-Newtonian theory is that of intermediate-mass-ratio inspirals. These are systems with moderate mass ratios of order 100:1, where neither black-hole perturbation theory nor post-Newtonian approximation might be adequate. Yet, the prospect for detecting such systems in ground and space-based detectors is rather high. Numerical relativity simulations might be the only way to set up effectual search templates for such systems.

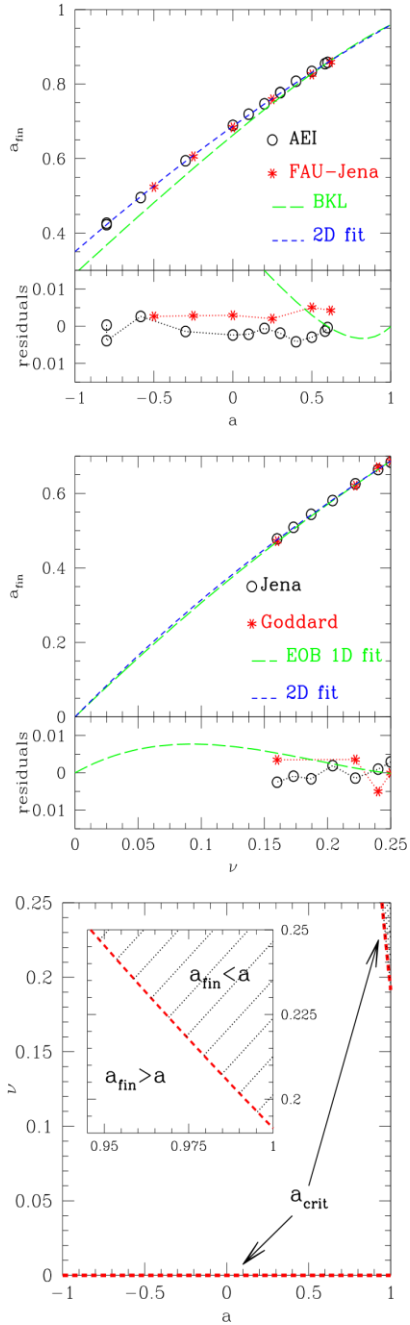


*Fig 9: The final spin of a black hole that results from the merger of two equal mass black holes of aligned spins (top panel) and nonspinning unequal mass black holes (middle panel). The bottom panel shows the region in the parameter space that results in an overall flip in the spin-orbit orientation of the system .*

### 5.5.3) Post Newtonian Approximation In The Two Body Problem :

For the interpretation of observations of neutron-star–binary coalescences, by upgraded detectors that are now taking data, it is necessary to understand their orbital evolution to a high order in the PN expansion. The first effects of radiation reaction are seen at 2.5 PN order (i.e., at order  $(v/c)^5$  beyond Newtonian gravity), but we probably have to have control in the equations of motion over the expansion at least to 3.5 PN order beyond the first radiation reaction (i.e., to order  $(v/c)^{12}$  beyond Newtonian dynamics).

Most work on this problem so far has treated a binary system as if it were composed of two point masses. This is, strictly speaking, inconsistent in general relativity, since the masses should form black holes of finite size. Blanchet, Damour ,Iyer, and collaborators have avoided this problem by a method that involves generalized functions. They first expand in the nonlinearity parameter, and, when they have reached sufficiently high order, they obtain the velocity expansion of each order. By ordering terms in the post-Newtonian manner they have developed step-by-step the approximations up to 3.5 PN order.

A different team, led by Will, works with a different method of regularizing the point-particle singularity and compares its results with those of Blanchet et al. at each order . There is no guarantee that either method can be continued successfully to any particular order, but so far they have worked well and are in agreement. Their results form the basis of the templates that are being designed to search for binary coalescences.

An interesting way of extending the validity of the expansion that is known to any order is to use Pad  approximants (rational polynomials) of the fundamental quantities in the theory, namely the orbital energy and the gravitational wave luminosity. This has worked rather well in improving the convergence of PN theory. Buonanno and Damour have proposed an EOB approach to two-body dynamics, which makes it possible to compute the orbit of the binary and hence the phasing of the gravitational waves emitted beyond the last stable orbit into the merger and ringdown phases in the evolution of the black hole binary. This analytical approach has been remarkably successful and gained a lot of ground after the success in numerical relativity .

Other methods have been applied to this problem. Futamase introduced a limit that combines the nonlinearity and velocity expansions in different ways in different regions of space, so that the orbiting bodies themselves have a regular (finite relativistic self-gravity) limit, while their orbital motion is treated in a Newtonian limit. This should not fail at any order , and has demonstrated its robustness by arriving at the same results as the other approaches, at least through 3 PN order. But it has a degree of arbitrariness in choosing initial data that could cause problems for gravitational wave search templates that integrate orbits for a long period of time.

Matched filtering , is a plausible method of testing the validity of different approaches to computing the inspiral and merger waveforms from binary systems. Though a single observation is not likely to settle the question as to which methods are correct, a catalogue of events will help to evaluate the accuracy of different approaches by studying the statistics of the SNRs they measure .

### **Post-Newtonian expansions of energy and luminosity :**

Post-Newtonian calculations yield the expansion of the gravitational binding energy  $E$  and the gravitational wave luminosity  $\mathcal{F}$  as a function of the post-Newtonian expansion parameter  $v$ . This is related to the frequency  $f_{\text{gw}}$  of the dominant component of gravitational waves emitted by the binary system by

$$v^3 = \pi M f_{\text{gw}}$$

where  $M$  is the total mass of the system. The expansions for a circular binary are

$$\begin{aligned} E &= -\frac{\nu M v^2}{2} \left\{ 1 + \left( -\frac{9+\nu}{12} \right) v^2 + \left( \frac{-81+57\nu-\nu^2}{24} \right) v^4 \right. \\ &\quad \left. + \left( -\frac{675}{64} + \left[ \frac{34445}{576} - \frac{205\pi^2}{96} \right] \nu - \frac{155}{96}\nu^2 - \frac{35}{5184}\nu^3 \right) v^6 + \mathcal{O}(v^8) \right\} \end{aligned}$$

And

$$\begin{aligned} \mathcal{F} &= \frac{32\nu^2 v^{10}}{5} \left\{ 1 - \left( \frac{1247}{336} + \frac{35}{12}\nu \right) v^2 + 4\pi v^3 + \left( -\frac{44711}{9072} + \frac{9271}{504}\nu + \frac{65}{18}\nu^2 \right) v^5 \right. \\ &\quad - \left( \frac{8191}{672} + \frac{583}{24} \right) \pi v^5 + \left[ \frac{6643739519}{69854400} + \frac{16}{3}\pi^2 - \frac{1712}{105}(\gamma + \ln(4v)) \right. \\ &\quad + \left. \left( -\frac{4709005}{272160} + \frac{41}{48}\pi^2 \right) \nu - \frac{94403}{3024}\nu^2 - \frac{775}{324}\nu^3 \right] v^6 \\ &\quad \left. + \left( -\frac{16285}{504} + \frac{214745}{1728}\nu + \frac{193385}{3024}\nu^2 \right) \pi v^7 + \mathcal{O}(v^8) \right\}, \end{aligned}$$

**Evolution equation for the orbital phase.** Starting from these expressions, one requires that gravitational radiation comes at the expense of the binding energy of the system

$$\mathcal{F} = -\frac{dE}{dt}$$

the energy balance equation. This can then be used to compute the (adiabatic) evolution of the various quantities as a function of time. For instance, the rate of change of the orbital velocity  $\omega(t) = v^3/M$  ( $M$  being the total mass) can be computed using:

$$\frac{d\omega(t)}{dt} = \frac{d\omega}{dv} \frac{dv}{dE} \frac{dE}{dt} = \frac{3v^2}{M} \frac{\mathcal{F}(v)}{E'(v)}, \quad \frac{dv}{dt} = \frac{dv}{dE} \frac{dE}{dt} = \frac{-\mathcal{F}(v)}{E'(v)}$$

where  $E'(v) = dE/dv$ . Supplemented with a differential equation for  $t$ ,

$$dt = \frac{dt}{dE} \frac{dE}{dv} = -\frac{E'(v)}{\mathcal{F}},$$

one can solve for the evolution of the system's orbital velocity. Similarly, the evolution of the orbital phase  $\phi(t)$  can be computed using

$$\frac{d\varphi(t)}{dt} = \frac{v^3}{M}, \quad \frac{dv}{dt} = \frac{-\mathcal{F}(v)}{E'(v)}.$$

**Phasing formulas:** The foregoing evolution equations for the orbital phase can be solved in several equivalent ways, each correct to the required post-Newtonian order, but numerically different from one another. For instance, one can retain the rational polynomial  $F(v)/E(v)$  in Equation

$$\frac{d\varphi(t)}{dt} = \frac{v^3}{M}, \quad \frac{dv}{dt} = \frac{-\mathcal{F}(v)}{E'(v)}.$$

and solve the two differential equations numerically, thereby obtaining the time evolution of  $\phi(t)$ . Alternatively, one might re-expand the rational function  $F(v)/E(v)$  as a polynomial in  $v$ , truncate it to order  $v^n$  (where  $n$  is the order to which the luminosity is given), thereby obtaining a parametric representation of the phasing formula in terms of polynomial expressions in  $v$ :

$$\varphi(v) = \varphi_{\text{ref}} + \sum_{k=0}^n \varphi_k v^k, \quad t(v) = t_{\text{ref}} + \sum_{k=0}^n t_k v^k$$

where  $\phi_{\text{ref}}$  and  $t_{\text{ref}}$  are a reference phase and time, respectively. The standard post-Newtonian phasing formula goes one step further and inverts the second of the relations above to express  $v$  as a polynomial in  $t$  (again truncated to appropriate order), which is then substituted in the first of the expressions above to obtain a phasing formula as an explicit function of time:

$$\begin{aligned} \varphi(t) &= \frac{-1}{\nu\tau^5} \left\{ 1 + \left( \frac{3715}{8064} + \frac{55}{96}\nu \right) \tau^2 - \frac{3\pi}{4}\tau^3 + \left( \frac{9275495}{14450688} + \frac{284875}{258048}\nu + \frac{1855}{2048}\nu^2 \right) \tau^4 \right. \\ &+ \left( -\frac{38645}{172032} + \frac{65}{2048}\nu \right) \pi\tau^5 \ln\tau + \left[ \frac{831032450749357}{57682522275840} - \frac{53}{40}\pi^2 - \frac{107}{56}(\gamma + \ln(2\tau)) \right. \\ &+ \left( -\frac{126510089885}{4161798144} + \frac{2255}{2048}\pi^2 \right) \nu + \frac{154565}{1835008}\nu^2 - \frac{1179625}{1769472}\nu^3 \Big] \tau^6 \\ &\left. + \left( \frac{188516689}{173408256} + \frac{488825}{516096}\nu - \frac{141769}{516096}\nu^2 \right) \pi\tau^7 \right\}, \end{aligned}$$

$$\begin{aligned} v^2 &= \frac{\tau^2}{4} \left\{ 1 + \left( \frac{743}{4032} + \frac{11}{48}\nu \right) \tau^2 - \frac{\pi}{5}\tau^3 + \left( \frac{19583}{254016} + \frac{24401}{193536}\nu + \frac{31}{288}\nu^2 \right) \tau^4 \right. \\ &+ \left( -\frac{11891}{53760} + \frac{109}{1920}\nu \right) \pi\tau^5 + \left[ -\frac{10052469856691}{6008596070400} + \frac{\pi^2}{6} + \frac{107}{420}(\gamma + \ln 2\tau) \right. \\ &+ \left( \frac{3147553127}{780337152} - \frac{451}{3072}\pi^2 \right) \nu - \frac{15211}{442368}\nu^2 + \frac{25565}{331776}\nu^3 \Big] \tau^6 \\ &\left. + \left( -\frac{113868647}{433520640} - \frac{31821}{143360}\nu + \frac{294941}{3870720}\nu^2 \right) \pi\tau^7 \right\}. \end{aligned}$$

In the above formulas  $v = \pi M f_{\text{gw}}$  and  $\tau = [v(t_C - t)/(5M)]^{-1/8}$ ,  $t_C$  being the time at which the two stars merge together and the gravitational wave frequency  $f_{\text{gw}}$  formally diverges.

**Waveform polarizations :** The post-Newtonian formalism also gives the two polarizations  $h_+$  and  $h_\times$  as multipole expansions in powers of the parameter  $v$ . To lowest order, the two polarizations of the radiation from a binary with a circular orbit, located at a distance  $D$ , with total mass  $M$  and symmetric mass ratio  $v = m_1 m_2 / M^2$ , are given by

$$h_+ = \frac{2\nu M}{D} v^2 (1 + \cos^2 \iota) \cos[2\varphi(t)], \quad h_\times = \frac{4\nu M}{D} v^2 \cos \iota \sin[2\varphi(t)]$$

where  $\iota$  is the inclination of the orbital plane with the line of sight and  $v$  is the velocity parameter introduced earlier.

An interferometer will record a certain combination of the two polarizations given by

$$h(t) = F_+ h_+ + F_\times h_\times$$

In the case of ground-based instruments, the signal duration is pretty small, at most 15 min for neutron star binaries and smaller for heavier systems. Consequently, one can assume the source direction to be unchanging during the course of observation and the above combination produces essentially the same functional form of the waveforms as in Equation

$$h_+ = \frac{2\nu M}{D} v^2 (1 + \cos^2 \iota) \cos[2\varphi(t)], \quad h_\times = \frac{4\nu M}{D} v^2 \cos \iota \sin[2\varphi(t)]$$

Indeed, it is quite straightforward to show that

$$h(t) = 4\nu M \frac{C}{D} v^2 \cos[2\varphi(t) + 2\varphi_0]$$

Where

$$C = \sqrt{A^2 + B^2}, \quad A = \frac{1}{2}(1 + \cos^2 \iota) F_+, \quad B = \cos \iota F_\times, \quad \tan 2\varphi_0 = \frac{B}{A}$$

The factor  $C$  is a function of the various angles and lies in the range  $[0,1]$  with an RMS value of  $2/5$ . These waveforms form the basis for evaluating the science that can be extracted from future observations of neutron star and black hole binaries. We will discuss the astrophysical and cosmological measurements that are made possible with such high precision waveforms in several sections that follow. It is clear from the expressions for the waveform polarizations that, at the lowest order, the radiation from a binary is predominantly emitted at twice the orbital frequency. However, even in the case of quasi-circular orbits the waves come off at other harmonics of the orbital frequency. As we shall see below, these harmonics are very important for estimating the parameters of a binary, although they do not seem to contribute much to the SNR of the system.

#### 5.5.4) Measuring the parameters of an inspiraling binary

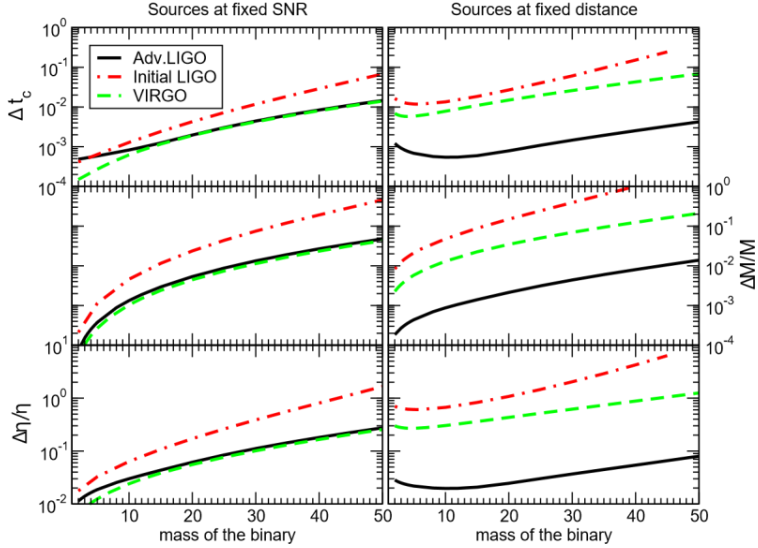


*Fig 10 : One-sigma errors in the time of coalescence, chirpmass and symmetric mass ratio for sources with a fixed SNR (left panels) and at a fixed distance (right panels). The errors in the time of coalescence are given in ms, while in the case of chirpmass and symmetric mass ratio they are fractional errors. These plots are for nonspinning black hole binaries; the errors reduce greatly when dynamical evolution of spins are included in the computation of the covariance matrix.*

The issue of parameter estimation in the context of black hole binaries has received a lot of attention . Most authors have used the covariance matrix for this purpose, although Markov Chain Monte Carlo (MCMC) techniques have also been used occasionally , especially in the context of LISA. Covariance matrix is often the preferred method, as one can explore a large parameter space without having to do expensive Monte Carlo simulations. However, when the parameter space is large, covariance matrix is not a reliable method for estimating parameter accuracies, especially at low SNRs but at high SNRs, as in the case of SMBH binaries in LISA, the problem might be that our waveforms are not accurate enough to facilitate a reliable extraction of the source parameters . Although MCMC methods can give more reliable estimates, they suffer from being computationally extremely expensive. However, they are important in ascertaining the validity of results based on the covariance matrix, at least in a small subset of the parameter space, and should probably be employed in assessing parameter accuracies of candidate gravitational wave events. In what follows we shall summarize the most recent work on parameter estimation in ground and space-based detectors for binaries with and without spin and the improvements brought about by including higher harmonics.

#### Ground-based detectors – nonspinning components:

In Figure 11 we have plotted the one-sigma uncertainty in the measurement of the time of coalescence, chirpmass and symmetric mass ratio for initial and advanced LIGO and VIRGO. The plots show errors for sources all producing a fixed SNR of 10 (left panels) or all at a fixed distance of 300 Mpc (right panels). The fractional error in chirpmass, even at a modest SNR of 10, can be as low as a few parts in ten thousand for stellar mass binaries, but the error stays

around 1%, even for heavier systems that have only a few cycles in a detector's sensitivity band. Error in the mass ratio is not as small, increasing to 100% at the higher end of the mass range explored. Thus, although the chirpmass can be measured to a good accuracy, poor estimation of the mass ratio means that the individual masses of the binary cannot be measured very well. Note also that the time of coalescence of the signal is determined pretty well, which means that we would be able to measure the location of the system in the sky quite well.

At a given SNR the accuracy is better in the case of low-mass binaries, since they spend a longer duration and a greater number of cycles in the detector band and the chirpmass can be determined better than the mass ratio, since to first order the frequency evolution of a binary is determined only by the chirpmass.

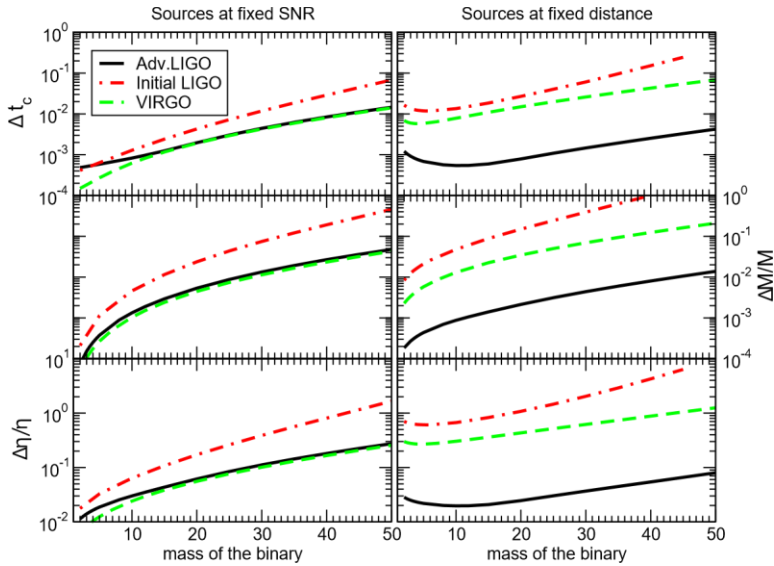


*Fig 11*

### Measuring the parameters of supermassive black hole binaries in LISA:

In the case of LISA, the merger of SMBHs produces events with extremely large SNRs, even at a redshift of  $z = 1$  (100s to several thousands depending on the chirpmass of the source). Therefore, one expects to measure the parameters of a merger event in LISA to a phenomenal accuracy. Figure 12 depicts the distribution of the errors for a binary consisting of two SMBHs of masses  $(10^6, 3 \times 10^5) M_\odot$  at a redshift of  $z = 1$ . The distribution was obtained for ten thousand samples of the system corresponding to random orientations of the binary at random sky locations with the starting frequency greater than  $3 \times 10^{-5}$  Hz and the ending frequency corresponding to the last stable orbit.

Each plot in Figure 12 shows the results of computations for binaries consisting of black holes with and without spins. Even in the absence of spin-induced modulations in the waveform, the parameter accuracies are pretty good. Note that spin-induced modulations in the waveform enable a far better estimation of parameters, chirpmass accuracy improving by more than an order of magnitude and reduced mass accuracy by two orders of magnitude. It is because of such accurate

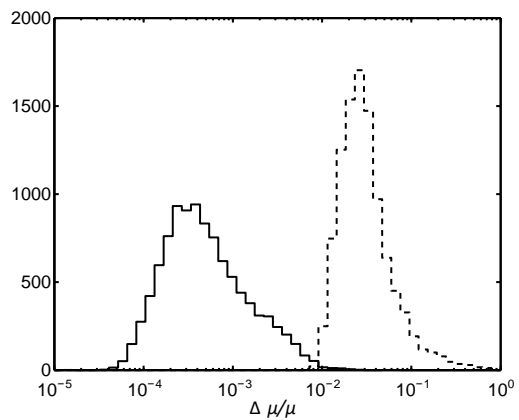
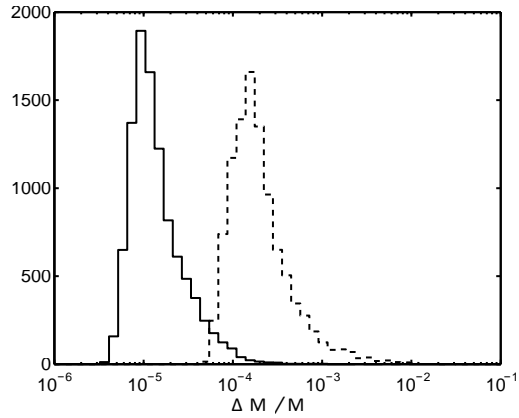


*Fig 12 : Distribution of measurement accuracy for a binary merger consisting of two black holes of masses  $m_1 = 10^6 M_\odot$  and  $m_2 = 3 \times 10^5 M_\odot$ , based on 10,000 samples of the system in which the sky location and orientation of the binary are chosen randomly. Dashed lines are for nonspinning systems and solid lines are for systems with spin.*

measurements that it will be possible to use SMBH mergers to test general relativity in the strong field regime of the theory . Although Figure 12 corresponds to a binary with specific masses, the trends shown are found to be true more generically for other systems too, the actual parameter accuracies and improvements are due.

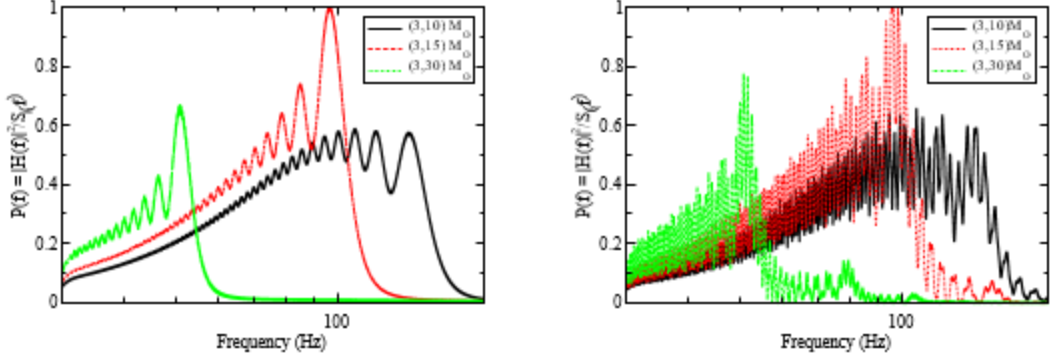


*Fig 13 : The SNR integrand of a restricted (left panel) and full waveform (right panel) as seen in initial LIGO. We have shown three systems, in which the smaller body's mass is the same, to illustrate the effect of the mass ratio. In all cases the system is at 100 Mpc and the binary's orbit is oriented at 45° with respect to the line of sight.*

### 5.5.5) Improvements from higher frequencies

The results discussed so far use the restricted post-Newtonian approximation in which the waveform polarizations contain only twice the orbital frequency, neglecting all higher-order corrections (including those to the second harmonic). The full waveform is a post-Newtonian expansion of the two polarizations as a power-series in  $v/c$  and consists of terms that have not only the dominant harmonic at twice the orbital frequency, but also other harmonics of the waveform. Schematically, the full waveform can be written as

$$h(t) = \frac{4M\eta}{D_L} \sum_{k=1}^7 \sum_{n=0}^5 A_{(k,n/2)} v^{n+2}(t) \cos [k\varphi(t) + \varphi_{(k,n/2)}]$$

where  $v = m_1 m_2 / M^2$  is the symmetric mass ratio, the first sum (index  $k$ ) is over the different harmonics of the waveform and the second sum (index  $n$ ) is over the different post-Newtonian orders. Note that post-Newtonian order weighs down the importance of higher-order amplitude corrections by an appropriate factor of the small parameter  $v$ . In the restricted post-Newtonian approximation one keeps only the lowest-order term. Since  $A_{1,0}$  happens to be zero, the dominant term corresponds to  $k = 2$  and  $n = 0$ , containing twice the orbital frequency.

The various signal harmonics, and the associated additional structure in the waveform, can potentially enhance our ability to measure the parameters of a binary to a greater accuracy. The reason we can expect to do so can be seen by looking at the spectra of gravitational waves with and without these harmonics. For a binary that is oriented face on with respect to a detector only the second harmonic is seen, while for any other orientation the radiation is emitted at all other harmonics, the influence of the harmonics becoming more pronounced as the inclination angle changes from 0 to  $\pi/2$ . Figure 14 compares, in the frequency band of

ground-based detectors, the spectrum of a source using the restricted post-Newtonian approximation (left panel) to the full waveform. In both cases the source is inclined to the line of sight at 45 degrees.

Following is a list of improvements brought about by higher harmonics. In the case of ground based detectors Van Den Broeck and Sengupta found that, when harmonics are included, the SNR hardly changes, but is always smaller, relative to a restricted waveform. However, the presence of frequencies higher than twice the orbital frequency means that it will be possible to observe heavier systems, increasing the mass reach of ground-based detectors by a factor of 2 to 3 in advanced LIGO and third generation detectors . The same effect was found in the case of LISA too, allowing LISA to observe SMBH masses up to a few $\times 10^8$  M<sub>○</sub> . More than the increased mass reach, the harmonics reduce the error in the estimation of the chirpmass, symmetric mass ratio and the time of arrival by more than an order of magnitude for stellar-mass black hole binaries. The same is true to a greater extent in the case of SMBH binaries, allowing as well a far greater accuracy in the measurement of the luminosity distance and sky resolution in LISA's observation of these sources . For instance, Figure 14 shows the gain in LISA's angular resolution for two massive black-hole-binary mergers as a consequence of using higher harmonics for a specific orientation of the binary. Improvements of order 10 to 100 can be seen over large regions of the sky. This improved performance of LISA makes it a good probe of dark energy .

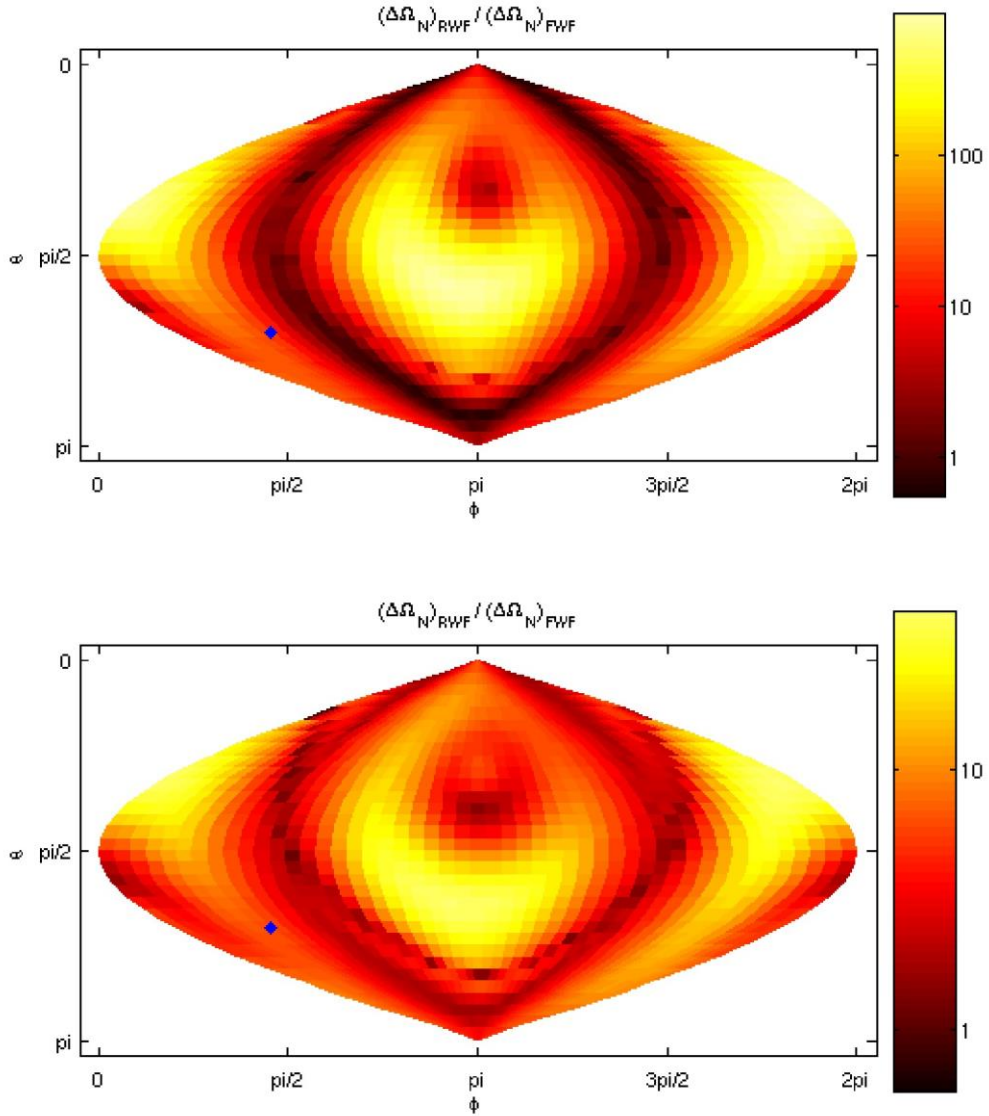


Fig 14: *Sky map of the gain in angular resolution for LISA observations of the final year of inspirals using full waveforms with harmonics versus restricted post-Newtonian waveforms with only the dominant harmonic, corresponding to the equal mass case ( $m_1 = m_2 = 107 M_\odot$ , top) and a system with mass ratio of 10 ( $m_1 = 10^7 M_\odot$ ,  $m_2 = 10^6 M_\odot$ , bottom). The sources are all at  $z = 1$ , have the same orientation ( $\cos\theta_L = 0.2$ ,  $\varphi_L = 3$ ) and zero spins  $\beta = \sigma = 0$ .*

With regard to the improvements brought about by higher harmonics. If the sensitivity of a detector has an abrupt lower frequency cutoff, or falls off rapidly below a certain frequency, then the harmonics bring about a more dramatic improvement than when the sensitivity falls off gently. Higher harmonics, nevertheless, always help in reducing the random errors associated with the measurement of parameters of a coalescing black-hole binary.

## 5.6) Tests Of General Relativity

Gravitational wave measurements of black holes automatically test general relativity in its strongfield regime. Observations of the mergers of comparable-mass black holes will be rich in details of their strong-field interactions. If measurements can determine the masses and spins of the initial black holes, as well as the eccentricity and orientation of their inspiral orbit, then one would hope to compare the actual observed waveform with the output of a numerical simulation of the same system. If measurements can also determine the final mass and spin (say from the ringdown radiation) then one can test the Hawking area theorem (the final area must exceed the sum of the areas of the initial holes) and the Penrose cosmic censorship conjecture (the final black hole should have  $J/M^2 < 1$ ).

Observations of stellar mass black holes inspiraling into SMBHs, the extreme mass ratio inspirals (EMRIs), have an even greater potential for testing general relativity. The stellar mass black hole spends thousands of precessing (both of periastron and the orbital plane) orbits along highly eccentric trajectories and slowly inspirals into the larger black hole. The emitted gravitational radiation literally carries the signature of the spacetime geometry around the central object. So fitting the orbit to theoretical templates could reveal small deviations of this geometry from that of Kerr. For example, if we know (from fitting the waveform) the mass and spin of the central black hole, then all its higher multipole moments are determined. If we can measure some of these and they deviate from Kerr, then that would indicate that either the central object is not a black hole or that general relativity needs to be corrected .

### 5.6.1) Testing of post Newtonian approximation

Current tests of general relativity rely on experiments in the solar system (using the sun's gravitational field) and observations of binary pulsars. In dimensionless units, the gravitational potential on the surface of the sun is about one part in a million and even in a binary pulsar the potential that each neutron star experiences due to its companion is no more than one part in ten thousand These are mildly relativistic fields, with the corresponding escape velocity being as large as a thousandth and a hundredth that of light, respectively.

Thus, gravitational fields in the solar system or in a binary pulsar are still weak by comparison to the largest possible values. Indeed, close to the event horizon of a black hole, gravitational fields can get as strong as they can ever get, with the dimensionless potential being of order unity and the escape velocity equal to that of the speed of light. Although general relativity has been found to be consistent with experiments in the solar system and observations of binary pulsars, phenomena close to the event horizons of black holes would be a great challenge to the theory. It would be very exciting to test Einstein's gravity under such circumstances.

The large SNR that is expected from SMBH binaries makes it possible to test Einstein's theory under extreme conditions of gravity . To see how one might test the post-Newtonian structure of Einstein's theory, let us consider the waveform from a binary in the frequency domain. Since an inspiral wave's frequency changes rather slowly (adiabatic evolution) it is possible to apply a stationary phase approximation to compute the Fourier transform  $H(f)$  of the waveform given in Equation below .

$$H(f) = \mathcal{A} f^{-7/6} \exp \left[ i\Psi(f) + i\frac{\pi}{4} \right]$$

with the Fourier amplitude  $A$  and phase  $\Psi(f)$  given by

$$\mathcal{A} = \frac{\mathcal{C}}{D \pi^{2/3}} \sqrt{\frac{5\nu}{24}} M^{5/6}, \quad \Psi(f) = 2\pi f t_C + \Phi_C + \frac{3}{128\nu} \sum_k \alpha_k (\pi M f)^{(k-5)/3}$$

Here  $\nu$  is the symmetric mass ratio ,  $C$  is a function of the various angles , and  $t_C$  and  $\Phi_C$  are the fiducial epoch of merger and the phase of the signal at that epoch, respectively. The coefficients in the PN expansion of the Fourier phase are given by

$$\begin{aligned} \alpha_0 &= 1, \quad \alpha_1 = 0, \quad \alpha_2 = \frac{3715}{756} + \frac{55}{9}\nu, \quad \alpha_3 = -16\pi, \\ \alpha_4 &= \frac{15293365}{508032} + \frac{27145}{504}\nu + \frac{3085}{72}\nu^2, \quad \alpha_5 = \pi \left( \frac{38645}{756} - \frac{65}{9}\nu \right) \left[ 1 + \ln \left( 6^{3/2} \pi M f \right) \right] \\ \alpha_6 &= \frac{11583231236531}{4694215680} - \frac{640}{3}\pi^2 - \frac{6848}{21}\gamma + \left( -\frac{15737765635}{3048192} + \frac{2255}{12}\pi^2 \right) \nu \\ &\quad + \frac{76055}{1728}\nu^2 - \frac{127825}{1296}\nu^3 - \frac{6848}{63} \ln(64\pi M f), \\ \alpha_7 &= \pi \left( \frac{77096675}{254016} + \frac{378515}{1512}\nu - \frac{74045}{756}\nu^2 \right). \end{aligned}$$

These are the PN coefficients in Einstein's theory; in an alternative theory of gravity they will be different. In Einstein's theory the coefficients depend only on the two mass parameters, the total mass  $M$  and symmetric mass ratio  $\nu$ . One of the tests we will discuss below concerns the consistency of the various coefficients. Note, in particular, that in Einstein's gravity the 0.5 PN term is absent, i.e., the coefficient of the term  $\nu$  is zero. Even with the very first observations of inspiral events, it should be possible to test if this is really so.

Figure 15 shows one such test that is possible with SMBH binaries . The observation of these systems in LISA makes it possible to measure the parameters associated with different physical effects. For example, the rate at which a signal chirps (i.e., the rate at which its frequency changes) depends on the binary's chirpmass. Given the chirpmass, the length of the signal depends on the system's symmetric mass ratio (the ratio of reduced mass to total mass).

Another example would be the scattering of gravitational waves off the curved spacetime geometry of the binary . producing the tail effect in the emitted signal, which is determined principally by the system's total mass . Similarly, spin-orbit interaction, spin-spin coupling, etc. depend on other combinations of the masses.

The binary will be seen with a high SNR, which means that we can measure the mass parameters associated with many of these physical effects. If each parameter is known precisely, we can draw a curve corresponding to it in the space of masses. However, our observations are inevitably subject to statistical (and possibly systematic) errors. Therefore, each parameter corresponds to a region in the parameter space . If Einstein's theory of gravitation is correct, the regions corresponding to the different parameters must all have at least one common region, a region that contains the true parameters of the binary. This is because Einstein's theory, or an alternative, has to be used to project the observed data onto the space of masses. If the region corresponding to one or more of these parameters does not overlap with the common region of the rest of the parameters, then Einstein's theory, or its alternative, is in trouble.

In Brans–Dicke theory the system is expected to emit dipole radiation and the PN series would begin an order  $v^{-2}$  earlier than in Einstein's theory. In the notation introduced above we would have an  $\alpha_{-2}$  term, which has the form

$$\alpha_{-2} = -\frac{5S^2}{84\omega_{BD}}.$$

Here  $S$  is the the difference in the scalar charges of the two bodies and  $\omega_{BD}$  is the Brans–Dicke parameter. Although this term is formally two orders lower than the lowest-order quadrupole term of Einstein's gravity (i.e., it is  $O(v^{-2})$  order smaller), numerically its effect will be far smaller than the quadrupole term because of the rather large bound on  $\omega_{BD} \gg 1$ . Nevertheless, its importance lies in the fact that there is now a new parameter on which the phase depends. Berti, Buonanno and Will conclude that LISA observations of massive black-hole binaries will enable scientists to set limits on  $\omega_{BD} \sim 10^4 - 10^5$ .

A massive graviton theory would also alter the phase. The dominant effect is at 1 PN order and would change the coefficient  $\alpha_2$  to

$$\alpha_2 \rightarrow \alpha_2 - \frac{128\nu}{3} \frac{\pi^2 DM}{\lambda_g^2(1+z)},$$

where  $v$  is the symmetric mass ratio. This term alters the time of arrival of waves of different frequencies, causing a dispersion, and a corresponding modulation, in the wave's phase, depending on the Compton wavelength  $\lambda_g$  and the distance  $D$  to the binary .

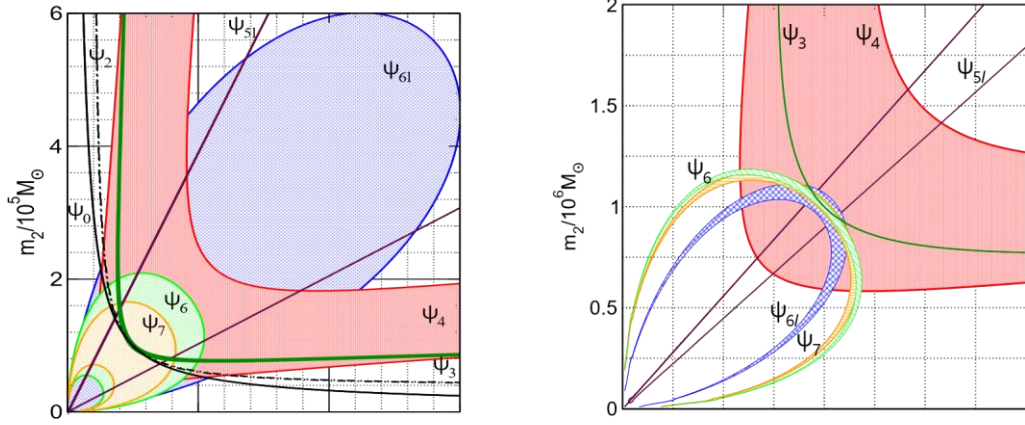


*Fig 15 : By fitting the Fourier transform of an observed signal to a post-Newtonian expansion, one can measure the various post-Newtonian coefficients  $\psi_k(m_1, m_2)$ ,  $k = 0, 2, 3, 4, 6, 7$  and coefficients of log-terms  $\psi_{5l}(m_1, m_2)$  and  $\psi_{6l}(m_1, m_2)$ . In Einstein's theory, all the coefficients depend only on the two masses of the component black holes. By treating them as independent parameters one affords a test of the post-Newtonian theory. Given a measured value of a coefficient, one can draw a curve in the  $m_1 - m_2$  plane. If Einstein's theory is correct, then the different curves must all intersect at one point within the allowed errors. These plots show what might be possible with LISA's observation of the merger of a binary consisting of a pair of  $10^6 M_\odot$  black holes. In the right-hand plot all known post-Newtonian parameters are treated as independent, while in the left-hand plot only three parameters  $\psi_0$ ,  $\psi_2$  and one of the remaining post-Newtonian parameter are treated as independent and the procedure is repeated for each of the remaining parameters. The large SNR in LISA for SMBH binaries makes it possible to test various post-Newtonian effects, such as the tails of gravitational waves, tails of tails, the presence of log-terms, etc., associated with these parameters.*

The range of mass ratios is also wide. LISA's central black holes might have masses between  $10^3$  and  $10^7 M_\odot$ . inspiraling neutron stars and white dwarfs might have masses between 0.5 and  $2M_\odot$ . inspiraling stellar-population black holes might be in the range of  $7-50M_\odot$ , while intermediate mass black holes formed by the first generation of stars (Population III stars) might have masses around  $300M_\odot$  or even  $1000M_\odot$ . So the mass ratios might be anything in the range  $10^{-7}$  to 1.

The techniques that must be used to compute these signals depend on the mass ratio. Ratios near one are treated by post-Newtonian methods until the objects are so close that only numerical relativity can follow their subsequent evolution. For ratios below  $10^{-4}$  (a dividing line that is rather very uncertain and that depends on the bandwidth being used to observe the system, i.e., on how long the approximation must be valid for), systems are treated by fully

relativistic perturbation theory, expanding in the mass ratio. Intermediate mass ratios have not been studied in much detail yet; they can probably be treated by post-Newtonian methods up to a certain point, but it is not yet clear whether their final stages can be computed accurately by either numerical relativity or perturbation theory.

### 5.6.2) Quantum gravity

It seems inevitable that general relativity's description of nature will one day yield to a quantum based description, involving uncertainties in geometry and probabilities in the outcome of gravitational observations. This is one of the most active areas of research in fundamental physics today, and there are many speculations about how quantum effects might show up in gravitational wave observations.

The simplest idea might be to try to find evidence for “gravitons” directly in gravitational waves, by analogy with the way that astronomers count individual photons from astronomical sources. But this seems doomed to failure. The waves that we can observe have very low frequency, so the energy of each graviton is extremely small. And the total energy flux of the waves is enormous. So the number of gravitons in a detectable gravitational wave is far more than the number of photons in the light from a distant quasar.

Quantum gravity might involve new gravity-like fields, whose effects might be seen indirectly in the inspiral signals of black holes or neutron stars, as we have noted above. String theory might lead to the production of cosmic strings, which might be observed through their gravitational wave emission . If our universe is just a 4-dimensional subspace of a large-scale 10 or 11-dimensional space, then dynamics in the larger space might produce gravitational effects in our space, and in particular gravitational waves .

It might be possible to observe the quantum indeterminacy of geometry directly using gravitational wave detectors, if Hogan's principle of holographic indeterminacy is valid . Hogan speculates that quantum geometry might be manifested by an uncertainty in the position of a beam splitter, and that this could be the explanation for an unexpectedly large amount of noise at low frequencies in the GEO600 detector. In this connection it is interesting to construct, from fundamental constants alone, a quantity with the dimensions of amplitude spectral noise density.  $(S_h)^{1/2}$ . This has units of  $s^{1/2}$ , so one can define the “Planck noise power”  $S_{Pl} = t_{Pl} = \left(\frac{G\hbar}{C^5}\right)^{\frac{1}{2}}$ . Then the amplitude noise is  $S^{1/2} Pl = \left(\frac{G\hbar}{C^5}\right)^{\frac{1}{4}} = 2.3 \times 10^{-22} \text{ Hz}^{-1/2}$ . This is comparable to or larger than the instrumental noise in current interferometric gravitational wave detectors, as shown in Figure 16 . This in itself does not mean that Planckian noise will show up in gravitational wave detectors, but Hogan argues that the particular design of GEO600 might indeed make it subject to this noise more strongly than other large interferometers.

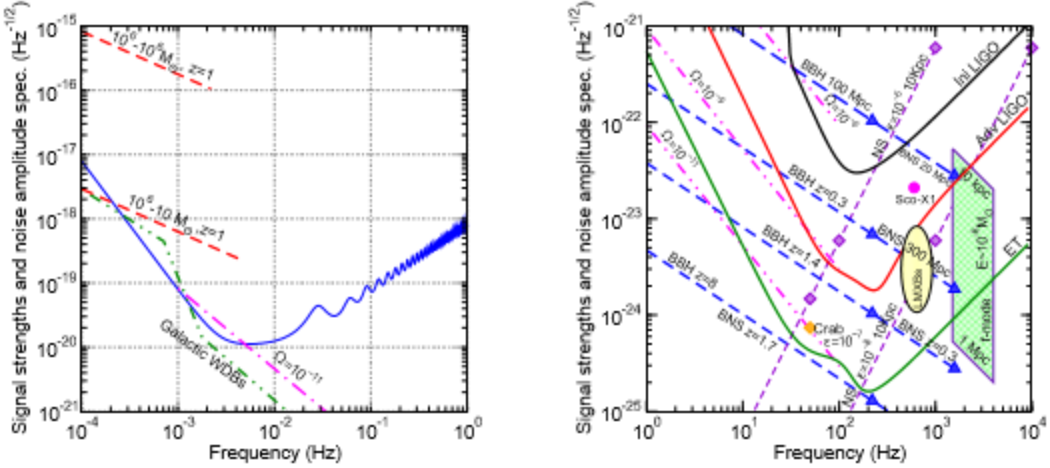


*Fig 16 : The right panel plots the noise amplitude spectrum,  $\sqrt{f S_h(f)}$ , in three generations of ground-based interferometers. For the sake of clarity, we have only plotted initial and advanced LIGO and a possible third generation detector sensitivities. VIRGO has similar sensitivity to LIGO at the initial and advanced stages, and may surpass it at lower frequencies. Also shown are the expected amplitude spectrum of various narrow and broad-band astrophysical sources. The left panel is the same as the right except for the LISA detector. The SMBH sources are assumed to lie at a redshift of  $z = 1$ , but LISA can detect these sources with a good SNR practically anywhere in the universe. The curve labelled “Galactic WDBs” is the confusion background from the unresolvable Galactic population of white dwarf binaries.*

## 5) ASTROPHYSICS WITH GRAVITATIONAL WAVES

Gravitational radiation plays an observable role in the dynamics of many known astronomical systems. In some, such as cataclysmic variables and neutron-star-binary systems , the role of gravitational radiation has been understood for years. In others, such as young neutron stars and low-mass X-ray binaries , the potential importance of gravitational radiation has been understood only recently. As further observations, particularly at X-ray wavelengths, become available, the usefulness of gravitational radiation as a tool for modelling astronomical systems is increasing .

A great emphasis has been laid on calculation of sources is on prediction : trying to anticipate what might be seen . This has helped in motivating the construction of detectors and guided the details of their design and very importantly the design of data analysis methods. Historically, many predictions of emission strengths and the capability of detectors to extract information from signals have relied on estimates using the quadrupole formula. This was justifiable because, given the uncertainties in our astrophysical understanding of potential sources, more accurate calculations would be unjustified in most cases.

But these rough estimates are now replaced by more and more detailed source models where ever possible. This applies particularly in two cases. One is binary orbits, where the pointmass approximation is good over a large range of observable frequencies, so that fully relativistic calculations (using the post-Newtonian methods described above) are not only possible, but are necessary for the construction of sensitive search templates in the data analysis. The second exception is the numerical simulations of the merger of black holes and neutron stars, where the dynamics is so complex that none of our analytic approximations offers us reliable guidance. In fact, these two methods are currently joined to produce uniform models of signal evolution over as long an observation time as the signal allows. From these models we not only improve detection algorithms, but we also learn much more about the kinds of information that detections will extract from the signals.

Since the gravitational waves has been observed emphasis is laid on the interpretation of the data ,and extraction of observable parameters such as waveforms, polarizations, source location, etc.

### 6.1) Interacting Compact Binaries

The first example of the use of gravitational radiation in modelling an observed astronomical system was the explanation by Faulkner of how the activity of cataclysmic binary systems is regulated. Such systems, which include many novae, involve accretion by a white dwarf from a companion star. Unlike accretion onto neutron stars, where the accreted hydrogen is normally processed quickly into heavier elements, on a white dwarf the unprocessed material can build up until there is a nuclear chain reaction, which results in an outburst of visible radiation from the system.

Now, in a circular binary system that conserves total mass and angular momentum, a transfer of mass from a more massive to a less massive star will make the orbit shrink, while a transfer in the opposite direction makes the orbit grow. If accretion onto a white dwarf begins with the dwarf as the less massive star, then the stars will draw together, and the accretion will get stronger. This runaway process stops when the stars are of equal mass, and then accretion begins to drive them apart again. Astronomers observed that in this phase accretion in certain very close binaries continued at a more or less steady rate, instead of shutting off as the stars separated more and more. Faulkner pointed out that gravitational radiation from the orbital motion would carry away angular momentum and drive the stars together . The two effects together result in steady accretion at a rate that can be predicted from the quadrupole formula and simple Newtonian orbital dynamics, and which is in good accord with observations in a number of systems.

Binaries consisting of two white dwarfs in very tight orbits will be direct LISA sources we won't have to infer their radiation indirectly, but will actually be able to detect it. Some of them will also be close enough to tidally interact with one another, leading in some cases to

mass transfer. Others will be relatively clean systems in which the dominant effect will be gravitational radiation reaction.

### 6.1.1) Resolving The Mass Inclination Degeneracy

Gravitational-wave-polarization measurements can be very helpful in resolving the degeneracy that occurs in the measurement of the mass and inclination of a binary system. As is well known, astronomical observations of binaries cannot yield the total mass but only the combination  $m \sin\phi$ , where  $\phi$  is the inclination of the binary's orbit to the line of sight. However, measurement of polarization can determine the angle  $\phi$  since the polarization state depends on the binary's inclination with the line of sight.

For instance, consider a circular binary system with total mass  $M$  at a distance  $D$ . Suppose its orbital angular momentum vector makes an angle  $\phi$  with the line of sight (the standard definition of the inclination of a binary orbit). The two observed polarizations are given in the quadrupole approximation by equation :

$$h_+ = \frac{2\nu M}{D} v^2 (1 + \cos^2 \iota) \cos[2\varphi(t)], \quad h_\times = \frac{4\nu M}{D} v^2 \cos \iota \sin[2\varphi(t)],$$

We can eliminate the distance  $R$  between the stars that is implicit in the velocity  $v = R\omega$  (where  $\omega$  is the instantaneous angular velocity of the orbit, the derivative of the orbital phase function  $\phi(t)$ ) by using the Newtonian orbital dynamics equation  $\omega^2 = M/R^3$ . Then we find

$$h_+ = \frac{2\nu M}{D} [\pi M f(t)]^{2/3} (1 + \cos^2 \iota) \cos[2\varphi(t)], \quad h_\times = \frac{4\nu M}{D} [\pi M f(t)]^{2/3} \cos \iota \sin[2\varphi(t)],$$

where  $M$  is the total mass of the binary and, as before,  $v$  is the symmetric mass ratio  $m_1 m_2 / M^2$ . The frequency  $f = \omega/\pi$  is the gravitational wave frequency, twice the orbital frequency.

It is clear that the ratio of the two polarization amplitudes determines the angle  $\phi$ . In this connection it is interesting to relate the polarization to the orientation. When the binary is viewed from a point in its orbital plane, so that  $\phi = \pi/2$ , then  $h_\times = 0$ ; the radiation has pure + polarization. From the observer's point of view, the motion of the binary stars projected onto the sky is purely linear; the two stars simply go back and forth across the line of sight. This linear projected motion results in linearly polarized waves. At the other extreme, consider viewing the system down its orbital rotation axis, where  $\iota = 0$ . The stars execute a circular motion in the sky, and the polarization components  $h_+$  and  $h_\times$  have equal amplitude and are out of phase by  $\pi/2$ . This is circularly polarized gravitational radiation. So, when the radiation

is produced in the quadrupole approximation, the polarization has a very direct relationship to the motions of the masses when projected on the observer's sky plane. If the radiation is produced by higher multipoles it becomes more complex to make these relations, but it can be done .

While a single detector is linearly polarized, it can still measure the two polarizations if the signal has a long enough duration for the detector to turn (due to the motion of the Earth) and change the polarization component it measures. Alternatively, a network of three detectors can determine the polarization and location of the source even over short observation times.

Such a measurement would lead to a potentially very interesting interplay between gravitational and electromagnetic observations, with applications in the observations of isolated neutrons stars, binary systems, etc.

## 6.2) Black Hole Astrophysics :

Black holes are the most relativistic systems possible. Observing gravitational waves from them, individually or in binaries, helps to test some of the predictions of general relativity in the strongly nonlinear regime, such as the tails of gravitational waves, spin-orbit coupling induced precession, nonlinear amplitude terms, hereditary effects, etc. . They are also good test beds to constrain other theories of gravity. Gravitational waves – emitted either during the inspiral and merger of rotating SMBHs or when a stellar-mass compact object falls into a SMBH – can be used to map the structure of spacetime and test uniqueness theorems on rotating black holes . LISA will be able to see the formation of massive black holes at cosmological distances by detecting the waves emitted in the process . We give below a brief discussion of the physics that will follow from the observation of gravitational waves from black holes.

### 6.2.1) Gravitational Waves From Stellar Mass Black Holes

Astronomers now recognize that there is an abundance of black holes in the universe. Observations across the electromagnetic spectrum have located black holes in X-ray binary systems in our galaxy in the centres of star clusters, and in the centres of galaxies.

These three classes of black holes have very different masses. Stellar black holes typically have masses of around  $10M_{\odot}$ , and are thought to have been formed by the gravitational collapse of the centre of a large, evolved red giant star, perhaps in a supernova explosion. Black holes in clusters have been found in the range of  $10^4 M_{\odot}$ , and are called intermediate-mass black holes. Black holes in galactic centres have masses between  $10^6$  and  $10^{10} M_{\odot}$ , and are called SMBHs. The higher masses are found in the centres of active galaxies and quasars.

The history and method of formation of intermediate-mass and supermassive black holes are not yet well understood.

All three kinds of black hole can radiate gravitational waves. According to Figure 17 , stellar black-hole radiation will be in the ground-based frequency range, while galactic holes are detectable only from space. Intermediate-mass black holes may lie at the upper end of the LISA band or between LISA and ground-based detectors. The radiation from an excited black hole itself is strongly damped, lasting only a few cycles at its natural frequency ( $R=2M$ ).

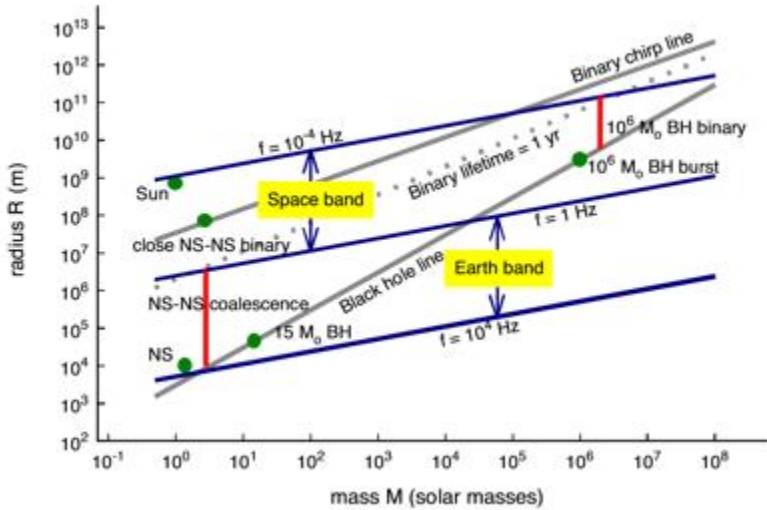


Fig 17

$$f_{BH} \sim 1000 \left( \frac{M}{10 M_\odot} \right)^{-1}$$

### 6.2.2) Stellar Mass Black Hole Binaries :

Radiation from stellar-mass black holes is expected mainly from coalescing binary systems, when one or both of the components is a black hole. Although black holes are formed more rarely than neutron stars, the spatial abundance of binary systems consisting of neutron stars with black holes, or of two black holes, is amplified relative to neutron-star binaries because binary systems are much more easily broken up when a neutron star forms than when a black hole forms. When a neutron star forms, most of the progenitor star's mass ( $6M_\odot$  or more) must be expelled from the system rapidly. This typically unbinds the binary: the companion star has the same speed as before but is held to the neutron star by only a fraction of the original gravitational attraction. Observed neutron-star binaries are thought to have

survived because the neutron star was coincidentally given a kick against its orbital velocity when it formed. When a black hole forms, most of the original mass may simply go down into the hole, and the binary will have a higher survival probability. However, this argument may not lead to observable black hole binaries – there is a possibility that systems that would form black holes close enough to coalesce in a Hubble time do not become binaries, but rather the two progenitor stars are so close that they merge before forming black holes.

On the other hand, double black-hole binaries may in fact be formed abundantly by capture processes in globular clusters, which appear to be efficient factories for black-hole binaries . Being more massive than the average star in a globular cluster, black holes sink towards the centre, where three-body interactions can lead to the formation of binaries. The key point is that these binaries are not strongly bound to the cluster, so they can easily be expelled by later encounters. From that point on they evolve in isolation, and typically have a lifetime shorter than  $10^{10}$  years .

The larger mass of stellar black-hole systems makes them visible from a greater distance than neutron-star binaries. If the abundance of binaries with black holes is comparable to that of neutron-star binaries, black hole events will be detected much more frequently than those involving neutron stars. They may even be seen by first-generation detectors in the S5 science run of the LSC , although that is still not very probable, even with optimistic estimates of the black-hole binary population. It seems very possible, however, that the first observations of binaries by interferometers was eventually of black holes.

More speculatively, black hole binaries may even be part of the dark matter of the universe. Observations of Massive Compact Halo Objects (MACHOs) – microlensing of distant stars by compact objects in the halo of our galaxy – have indicated that up to half of the galactic halo could be made up of dark compact objects of  $0.5M_{\odot}$  . This is difficult to understand in terms of stellar evolution, as we understand it today: neutron stars and black holes should be more massive than this, and white dwarfs of this mass should be bright enough to have been identified as the lensing objects. One speculative possibility is that the objects were formed primordially, when conditions may have allowed black holes of this mass to form. If so, there should also be a population of binaries among them, and occasional coalescences should, therefore, be expected. In fact, the abundance would be so high that the coalescence rate might be as large as one every 20 years in each galaxy, which is higher than the supernova rate. Since binaries are maximally non-axisymmetric, these systems could be easily detected by first-generation interferometers out to the distance of the Virgo Cluster .

The estimates used here of detectability of black hole systems depend mainly on the radiation emitted as the orbit decays, during which the point-particle post-Newtonian approximation should be adequate. But the inspiral phase will, of course, be followed by a burst of gravitational radiation from the merger of the black holes that will depend in detail on the masses and spins of the objects. Numerical simulations of such events will be used to interpret this signal and to provide templates for the detection of black holes too massive for

their inspiral signals to be seen. There is an abundance of information in these signals: population studies of the masses and spins of black holes, studies of typical kick velocities for realistic mergers, tests of general relativity.

### 6.2.3) Intermediate Mass Black Holes :

Intermediate-mass black holes, with masses between  $100M_{\odot}$  and  $10^4 M_{\odot}$ , are expected on general evolutionary grounds, but have proved hard to identify because of their weaker effect on surrounding stellar motions. Very recently strong evidence has been found for such a black hole in the star cluster Omega Centauri. If such black holes are reasonably abundant, then they may be LISA sources when they capture a stellar-mass black hole or a neutron star from the surrounding cluster. For these merger events the mass ratio is not as extreme as for EMRIs, and so these are accordingly called IMRIs: Intermediate Mass-Ratio Inspirals.

The problem of modelling the signals from these systems has not yet been fully studied. If these signals can be detected, they will tell us how important black holes were in the early stellar population, and whether these black holes have anything to do with the central black holes in the same galaxies.

### 6.2.4) Super Massive Black Holes

Gravitational radiation is expected from SMBHs in two ways. In one scenario, two massive black holes spiral together in a much more powerful version of the coalescence we have just discussed. The frequency is much lower, in inverse proportion to their masses, and the amplitude is higher. Equation

$$\mathcal{A} = \frac{\mathcal{C}}{D \pi^{2/3}} \sqrt{\frac{5\nu}{24}} M^{5/6}, \quad \Psi(f) = 2\pi f t_C + \Phi_C + \frac{3}{128\nu} \sum_k \alpha_k (\pi M f)^{(k-5)/3}.$$

implies that the effective signal amplitude (which is what appears in the expression for the SNR) is almost linear in the masses of the black holes, so that a signal from two  $10^6 M_{\odot}$  black holes will have an amplitude  $10^5$  times bigger than the signal from two  $10M_{\odot}$  holes at the same distance. Even allowing for differences in technology, this indicates why space-based detectors will be able to study such events with a very high SNR, no matter where in the universe they occur. Observations of coalescing massive black-hole binaries will therefore provide unique insight into the behaviour of strong gravitational fields in general relativity.

The event rate for such coalescences is not easy to predict, but is likely to be large. It seems that the central core of most galaxies may contain a black hole of at least  $10^6 M_\odot$ . This is known to be true for our galaxy and for a very large proportion of other galaxies that are near enough to be studied in sufficient detail. SMBHs (up to a few times  $10^9 M_\odot$ ) are believed to power quasars and active galaxies, and there is a good correlation between the mass of the central black hole and the velocity dispersion of stars in the core of the host galaxy.

If black holes are formed with their galaxies, in a single spherical gravitational collapse event, and if nothing happens to them after that, then coalescences will never be seen. But this is unlikely for two reasons. First, it is believed that galaxies may have formed through the merger of smaller units, sub-galaxies of masses upwards of  $10^6 M_\odot$ . If these units had their own black holes, then the mergers would have resulted in the coalescences of many of the black holes on a timescale shorter than the present age of the universe. This would give an event rate of several mergers per year in the universe, most of which would be observable by LISA, if the more massive black hole is not larger than about  $10^7 M_\odot$ . If the  $10^6 M_\odot$  black holes were formed from smaller black holes in a hierarchical merger scenario, then the event rate could be hundreds or thousands per year. The second reason is that we see large galaxies merging frequently. Interacting galaxies are common, and if galaxies come together in such a way that their central black holes both remain in the central core, then dynamical friction with other stars will bring them close enough together to allow gravitational radiation to bring about a merger on a timescale of less than  $10^{10}$  yrs. There is considerable evidence for black hole binaries in a number of external galaxies. There is even a recent report of an SMBH having been ejected from a galaxy, possibly by the kick following a merger and of an SMBH binary that will coalesce in about 10,000 yrs!

Besides mergers of holes with comparable masses, the capture of a small compact object by a massive black hole can also result in observable radiation. The tidal disruption of main-sequence or giant stars that stray too close to the black hole is thought to provide the gas that powers the quasar phenomenon. These disruptions are not expected to produce observable radiation. But the clusters will also contain a good number of neutron stars and stellar-mass black holes. They are too compact to be disrupted by the black hole, even if they fall directly into it.

Such captures, therefore, emit a gravitational wave signal that will be well approximated as that from a point mass near the black hole. This will again be a chirp of radiation, but in this case the orbit may be highly eccentric. The details of the waveform encode information about the geometry of spacetime near the black hole. In particular, it may be possible to measure the mass and spin of the black hole and thereby to test the uniqueness theorem for black holes. The event rate is not very dependent on the details of galaxy formation, and is probably high enough for many detections per year from a space-based detector, provided that theoretical calculations give data analysts accurate predictions of the motion of these point particles over many hundreds of thousands of orbits. These Extreme Mass-Ratio Inspiral sources (EMRIs) are a primary goal of the LISA detector. By observing them, LISA will provide information about the stellar population near central black holes. When

combined with modelling and spectroscopic observations, this will facilitate a deep view of the centres of galaxies and their evolution .

### 6.3) Neutron Star AstroPhysics

#### 6.3.1) Gravitational collapse and formation of neutron stars :

The event that forms most neutron stars is the gravitational collapse that results in a supernova. It is difficult to predict the waveform or amplitude expected from this event. Although detecting this radiation has been a goal of detector development for decades, little more is known about what to expect than 30 years ago. The burst might be at any frequency between 100 Hz and 1 kHz, and it might be a regular chirp (from a rotating deformed core) or a more chaotic signal (from convective motions in the core). Considerable energy is released by a collapse, and on simple energetic grounds this source could produce strong radiation if the emitted energy is more than about  $0.01M_{\odot}$ , then second-generation detectors would have no trouble seeing events that occur in the Virgo Cluster. This energetic consideration drove the early development of bar detectors.

But numerical simulations tell a different story, and it seems very likely that radiation amplitudes will be much smaller. Such signals might be detectable by second-generation detectors from a supernova in our galaxy, but not from much greater distances. When they are finally detected, the gravitational waves will be extremely interesting, providing our only information about the dynamics inside the collapse, and helping to determine the equation of state of hot nuclear matter.

If gravitational collapse forms a neutron star spinning very rapidly, then it may be followed by a relatively long period (perhaps a year) of emission of nearly monochromatic gravitational radiation, as the r-mode instability forces the star to spin down to speeds of about 100–200 Hz . If as few as 10% of all the neutron stars formed since star formation began (at a redshift of perhaps four) went through such a spindown, then they may have produced a detectable random background of gravitational radiation at frequencies down to 20 Hz .

#### 6.3.2) Neutron-Star Binary Merges

When two neutron stars merge, they will almost certainly have too much mass to remain as a star, and will eventually collapse to a black hole, unless they can somehow expel a significant amount of mass. The collision heats up the nuclear matter to a point where, at least initially, thermal pressure becomes significant. Numerical simulations can use theoretical equations of state to predict the merger radiation, and observations will then test the nuclear physics assumptions that go into the equation of state. Simulations show that the choice of

equation of state makes a big difference to the emitted waveform, as do the masses of the stars there is no mass scaling as there is for black holes .

When a neutron star encounters a black hole in a stellar compact binary merger, the star may not be heated very much by the tidal forces, and the dynamics may be governed by the cold nuclear matter equation of state, about which there is great uncertainty. Again, comparing observed with predicted waveforms may provide some insight into this equation of state. Simulations suggest that these systems may give rise to many of the observed short, hard gamma-ray bursts Simultaneous gravitational wave and gamma ray detections would settle the issue and open the way to more detailed modelling of these systems.

### 6.3.3) Neutron Star Normal Mode Of Oscillation

Gravitational wave observations at high frequencies of neutron-star vibrations may also constrain the cold-matter equation of state. In Figure 18 there is a dot for the typical neutron star. The corresponding frequency is the fundamental vibrational frequency of such an object. In fact, neutron stars have a rich spectrum of non-radial normal modes, which fall into several families: f, g, p, w, and r-modes have all been studied. If their gravitational wave emissions can be detected, then the details of their spectra would be a sensitive probe of their structure and of the equation of state of neutron stars, in much the same way that helioseismology probes the interior of the sun. Even knowing accurately the frequency and decay time of just the fundamental  $\ell = 2$  f-mode would be enough to eliminate most current equations of state .

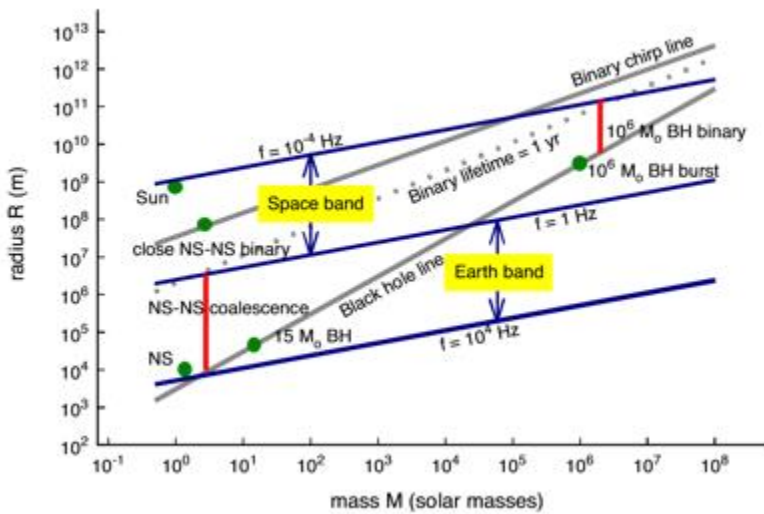


Fig 18

This is a challenge to ground-based interferometers, which have so far focussed their efforts on frequencies below 1 kHz. But Advanced LIGO and the upgraded GEO-HF detector has the capability to perform narrow-banding and enhance their sensitivity considerably at frequencies up to perhaps 2 kHz, which could put the f-modes of neutron stars into range.

The f-modes of neutron stars, which could be excited by glitches or by the nuclear explosions on accreting neutron stars that are thought to produce X-ray flares and soft gamma-ray repeater events. The rise-time of X-ray emission can be as short as a few milliseconds, which might be impulsive enough to excite acoustic vibrations. If the rise time of the explosion matches the period of the mode well enough, then a substantial fraction of the energy released could go into mechanical vibration, and almost all of this fraction would be carried away by gravitational waves, since other mode-damping mechanisms inside neutron stars are much less efficient.

Radio-pulsar glitches seem to release energies of order  $10^{35}$  J, and X-ray and gamma ray events can be much more energetic. Using Equation

$$h_{\text{eff}} \sim \frac{1}{\pi r} \sqrt{\frac{E}{f}}.$$

we can estimate that the release of that much energy into gravitational waves at 2 kHz at a distance of 1 kpc would create a wave of effective amplitude around  $3 \times 10^{-22}$ . (The effective amplitude assumes we can do matched filtering, which in this case is not very difficult.) This kind of amplitude should be within the reach of Advanced LIGO and perhaps GEO-HF, provided they implement narrow banding. This will not be easy, either scientifically or operationally, but the payoff in terms of our understanding of neutron star physics could be very substantial.

Observations of these modes would immediately constrain the cold-matter nuclear equation of state in significant ways . In fact, modes of neutron stars may have already been observed in X-rays . But these are likely to be crustal modes, whose restoring force is the shear strength of the crust. While the physics of the crust is interesting in itself, such observations provide only weak constraints on the interior physics of the neutron star.

#### 6.3.4) Stellar Instabilities :

**The CFS instability :** In 1971 Chandrasekhar applied the quadrupole formula to calculate the corrections to the eigenfrequencies of the normal mode vibrations of rotating stars, and he found to his surprise that some modes were made unstable, i.e., coupling to gravitational radiation could destabilize a rotating star. Subsequent work by Friedman and Schutz showed

that there was a key signature for the mode of a Newtonian star that would be unstable in general relativity. This was the pattern speed of the mode, i.e., the angular velocity at which the crests of the pattern rotated about the rotation axis of the star. If this speed was in the same sense as the rotation of the star, but slower than the star, then the mode would be unstable in a perfect-fluid star . This instability is known as CFS instability .

The basic theory was developed for perfect-fluid stars. However, Lindblom and Detweiler showed that the effect of viscosity ran counter to that of radiation reaction, so that the instability was strongest in modes with the longest wavelengths, i.e., in the quadrupolar modes. Full numerical calculations on Newtonian stellar models with realistic viscosity models showed that the standard fundamental and acoustic modes of rotating neutron stars were not vulnerable to this instability. Subsequent work on fully relativistic models has hinted that the instability may be stronger than the Newtonian models indicate, but it is still at the margins of astrophysical interest.

**The r-mode instability :** The situation changed in 1997 when Andersson pointed out that there is another class of modes of Newtonian stars that should be unstable in the same way, but which had not been studied in this context before, the Rossby or r-modes. These are momentum dominated modes, where the gravitational radiation comes from the current-quadrupole terms, rather than from the mass quadrupole. Investigations by a number of authors have shown that this instability could be very strong in hot, rapidly-rotating stars. This is particularly relevant to young neutron stars, which may well be formed with rapid spin and which will certainly be hot. For their first year, stars spinning faster than about 100k Hz could spin down to about 100 Hz by losing angular momentum to gravitational radiation. The instability might also operate in old accreting neutron stars, such as those in LMXB X-ray binaries. However, the instability is, like other CFS instabilities, sensitive to viscosity, and there is great uncertainty about the amount of viscosity inside neutron stars .

### 6.3.5) Low mass x-ray binaries

Observations by the Rossi satellite (RXTE) have given evidence that the class of X-ray sources called Low-Mass X-ray Binaries (LMXB's) contains neutron stars with a remarkably narrow range of spins, between perhaps 250 Hz and 320 Hz . These are systems in which it is believed that neutron stars are spun up from the low angular velocities they have after their lifetime as normal pulsars to the high spins that millisecond pulsars have. One would expect, therefore, that the spins of neutron stars in such systems would be spread over a wide range. The fact that they are not requires an explanation.

The most viable explanation offered so far is the suggestion of Bildsten that gravitational radiation limits the rotation rate. The proposed mechanism is that anisotropic accretion onto the star creates a temperature gradient in the crust of the neutron star, which in turn creates a gradient in the mass of the nucleus that is in local equilibrium, and this in turn creates a

density gradient that leads, via the rotation of the star, to the emission of gravitational radiation. This radiation carries away angular momentum, balancing that which is accreted, so that the star remains at an approximately constant speed .

According to the model, the gravitational wave luminosity of the star is proportional to the measured flux of X-rays, since the X-ray flux is itself proportional to the accreted angular momentum that has to be carried away by the gravitational waves. If this model is correct, then the X-ray source Sco X-1 might be marginally detectable by advanced interferometers, and other similar systems could also be candidates .

### 6.3.6) Galactic population of neutron stars

Neutron stars are known to astronomy through the pulsar phenomenon. As radio surveys improve, the number of known pulsars is increasing rapidly . But the galactic population of neutron stars is orders of magnitude larger, perhaps as many as  $10^8$ . Most are much older than typical pulsars, which seem to stop emitting after a few million years. X-ray surveys reveal a number of unidentified point sources, which might be hot neutron stars, but older neutron stars are probably not even hot enough to show up in such surveys.

Gravitational wave observations have the potential to discover more neutron stars, but in the foreseeable future the numbers will not be large. Spinning neutron stars can be found in searches for continuous-wave signals, but there is no a priori reason to expect significant deformations that would lead to large gravitational wave amplitudes. One mechanism, proposed by Cutler , is that a large buried toroidal magnetic field could, by pulling in the waist of a spinning star, turn it into a prolate spheroid. This is classically unstable and would tip over and spin about a short axis, emitting gravitational waves. Millisecond pulsars could, in principle, be spinning down through the emission of gravitational waves in this way. Only deep observations by Advanced LIGO could begin to probe this possibility.

In fact, strong emission of gravitational waves is in some sense counterproductive, since it causes a neutron star to spin down and move out of the observing band quickly. This places important limits on the likely distribution of observable continuous-wave amplitudes from neutron stars . This is important input into the blind searches for such signals being conducted by the LSC.

Radio observations of pulsars have, of course, revealed a fascinating population of binary systems containing neutron stars, including the original Hulse–Taylor pulsar and the double pulsar PSR J0737-3039 . But radio surveys only cover a small fraction of our galaxy, so there may be many more interesting and exotic systems waiting to be discovered, including neutron stars orbiting black holes. In fact, not all neutron stars are pulsars, so there are likely to be nearby binary systems containing neutron stars that are not known as pulsars at all.

LISA has enough sensitivity to detect all such binaries in the galaxy whose gravitational wave emission is above 1 mHz, i.e., with orbital periods shorter than half an hour. Below that frequency, systems may just blend into the confusion noise of the white-dwarf background, unless they are particularly close. The Hulse–Taylor system is a bit below the LISA band, and even its higher harmonics are likely to be masked by the dense confusion noise of white-dwarf galaxies at low frequencies. Double pulsars should be detectable by LISA with low SNR (around five in five years) above the confusion background at a frequency of 0.2 mHz . In all, LISA might detect several tens or even hundreds of double neutron-star systems, and potentially even a handful of double black hole binaries.

Neutron stars are the fossils of massive stars, and so a population census of binaries can help normalize our galaxy’s star-formation rate in the past. Finally, it is possible to search for gravitational waves from individual spinning neutron stars in binary systems. Although more rare than isolated neutron stars, these systems might have a different history and a different distribution of amplitudes.

## 6) COSMOLOGY WITH GRAVITATIONAL WAVE OBSERVATIONS

Gravitational wave observations may inform us about cosmology in at least two ways: by studies of individual sources at cosmological distances that give information about cosmography (the structure and kinematics of the universe) and about early structure formation, and by direct observation of a stochastic background of gravitational waves of cosmological origin. In turn, a stochastic background could either be astrophysical in origin (generated by any of a myriad of astrophysical systems that have arisen since cosmological structure formation began ), or it could come from the Big Bang itself (generated by quantum processes associated with inflation or with spontaneous symmetry breaking in the extremely early universe ). The observation of a cosmic gravitational wave background (CGWB) is probably the most fundamentally important observation that gravitational wave detectors can make. But the astrophysical gravitational wave background (AGWB) also contains important information and may mask the CGWB over much of the accessible spectrum.

The detection of discrete sources at cosmological distances will require high sensitivity. Advanced ground-based detectors is able to see a few individual sources (mainly stellar-mass black hole binaries) at redshifts approaching 1, with which they may be able to make a good determination of the Hubble constant. But LISA’s observations of the coalescences of massive black hole binaries at all redshifts should make LISA a significant tool for cosmography These high-z observations may also contain interesting information about early structure formation, such as the relationship between SMBH formation and galaxy formation.

Other detection methods are also being used to probe the spectrum of the background radiation at longer wavelengths. Pulsar timing observations are already being used to set limits on the background at periods of a few years, and they will reach much greater sensitivity

when coherent antenna arrays (like the Square Kilometer Array) are available. And observations of the temperature fluctuations of the cosmic microwave background have the potential to reveal the gravitational wave content of the universe at the redshift of decoupling, which means at wavelength scales comparable to the size of the universe .

## 7.1) Detecting Stochastic Gravitational Wave Background :

### 7.1.1) Describing random gravitational field

By definition, a stochastic background of gravitational waves is a superposition of waves arriving at random times and from random directions, overlapping so much that individual waves are not identifiable. We assume that there are so many sources (either astrophysical sources or the quantum fluctuations that create the CGWB) that individual ones are not distinguishable. Such a gravitational wave field will appear in detectors as a time-series noise, which by the central limit theorem should have a Gaussian-normal distribution function if there are enough overlapping sources. This kind of background will compete with instrumental noise. It will be detectable by a single detector, if it is stronger than instrumental noise, but a weaker background could still be detected by using a pair of detectors and looking for a correlated component of their “noise” output, on the assumption that their instrumental noise is not correlated .

As a random phenomenon, the gravitational wave fields at two different locations are uncorrelated, because gravitational waves arrive from all directions and at all frequencies. It might, therefore, be thought that two detectors’ responses would be correlated only if they were located at the same position. But if one considers one component of the wave field with a single frequency, then it is clear that there will be strong correlations between points if they are separated along the wave’s propagation direction by much less than a wavelength. These frequency dependent correlations allow one to detect a background by cross-correlating the output of two separated detectors, albeit with less sensitivity than if they were co-located. This co-relation can also be used as a detection method .

Random gravitational waves are conventionally described in terms of their energy density spectrum  $\rho_{\text{gw}}(f)$ , rather than their mean amplitude. It is convenient to normalize this energy density to the critical density  $\rho_c$  required to close the universe, which is given in terms of the Hubble constant  $H_0$  as

$$\rho_c = \frac{3H_0^2}{8\pi G}$$

We then define

$$\Omega_{\text{gw}} := \frac{d\rho_{\text{gw}}/\rho_c}{d \ln f}.$$

This can be interpreted as the fraction of the closure energy density that is in random gravitational waves between the frequency  $f$  and  $\times f$ . If the source of radiation is scale-free (which means that there is no preferred length or time scale in the process), then it will produce a power-law spectrum, i.e., one in which  $\Omega_{\text{gw}}(f)$  depends on a power of  $f$ . Inflation, as we describe below, predicts a flat energy spectrum, one in which  $\Omega_{\text{gw}}$  is essentially independent of frequency .

The energy in the cosmological background is, of course, related to the spectral density of the noise that the background would produce in a gravitational wave detector. Since we describe the gravitational wave noise in terms of amplitude rather than energy, there are scaling factors involving the frequency between the two. An isotropic gravitational wave background incident on an interferometric detector will induce a strain spectral noise density equal to

$$S_{\text{gw}}(f) = \frac{3H_0^2}{10\pi^2} f^{-3} \Omega_{\text{gw}}(f).$$

Note that the explicit dependence on frequency is  $f^{-3}$ : two factors come from the relation of energy and squared-strain, and one factor from the fact that  $\Omega_{\text{gw}}$  is an energy distribution per unit logarithmic frequency. Note also that there are no explicit factors of  $c$  or  $G$  needed in this formula if one wants to work in non-geometrized units .

If we scale  $H_0$  by  $h_{100} = H_0/(100 \text{ km s}^{-1} \text{ Mpc}^{-1})$ , and we note that  $100 \text{ km s}^{-1} \text{ Mpc}^{-1} = 3.24 \times 10^{-18} \text{ s}^{-1}$ , then this equation implies that the strain noise is

$$S_{\text{gw}}^{1/2} = 5.6 \times 10^{-22} \text{ Hz}^{-1/2} \Omega_{\text{gw}}^{1/2} \left( \frac{f}{100 \text{ Hz}} \right)^{-3/2} h_{100}.$$

### 7.1.2) Observation with gravitational wave detectors

To be observed by a single gravitational wave detector, the gravitational wave noise must be larger than the instrumental noise. This is a bolometric method of detection of the background, and it requires great confidence in the understanding of the detector, in order to

believe that the observed noise is external. This is how the cosmic microwave background was originally discovered in a radio telescope by Penzias and Wilson.

If there are two detectors, then one may be able to get better sensitivity by cross-correlating their output . This works best when the two detectors are close enough together to respond to the same random wave field. Even when they are separated, however, they are correlated well at lower frequencies.

From equation

$$S_{\text{gw}}^{1/2} = 5.6 \times 10^{-22} \text{ Hz}^{-1/2} \Omega_{\text{gw}}^{1/2} \left( \frac{f}{100 \text{ Hz}} \right)^{-3/2} h_{100}.$$

it is straightforward to deduce that two co-located detectors, each with spectral noise density  $S_h$  and fully uncorrelated instrumental noise, observing over a bandwidth  $f$  at frequency  $f$  for a time  $T$ , can detect a stochastic background with energy density

$$\Omega_{\text{gw}}^{1/2} h_{100} = \left( \frac{S_h^{1/2}}{3.1 \times 10^{-18} \text{ Hz}^{-1/2}} \right) \left( \frac{f}{10 \text{ Hz}} \right)^{5/4} \left( \frac{T}{3 \text{ yrs}} \right)^{-1/4}.$$

The two LIGO detectors (separated by about 10 ms in light-travel time) are reasonably well placed for performing such correlations, particularly when upgrades push their lower frequency limit to 20 Hz or less. Two co-located first-generation LIGO instruments operating at 100 Hz could, in a one-year correlation, reach a sensitivity of  $\Omega_{\text{gw}} \sim 1.7 \times 10^{-8}$ . But the separation of the actual detectors takes its toll at this frequency, so that they can actually only reach  $\Omega_{\text{gw}} \sim 10^{-6}$ . Advanced LIGO improved this by two or three orders of magnitude, going well below the nucleosynthesis bound. The third-generation instrument ET, with instrumental noise as shown in Figure 19, can go even deeper. Two co-located ETs, observing at 10 Hz for three years, could reach  $\Omega_{\text{gw}} \sim 10^{-12}$ . At this frequency the detectors could be as far apart as 5000 km without a substantial loss in correlation sensitivity. The numbers given here are reflected in the curves in Figure 19 .

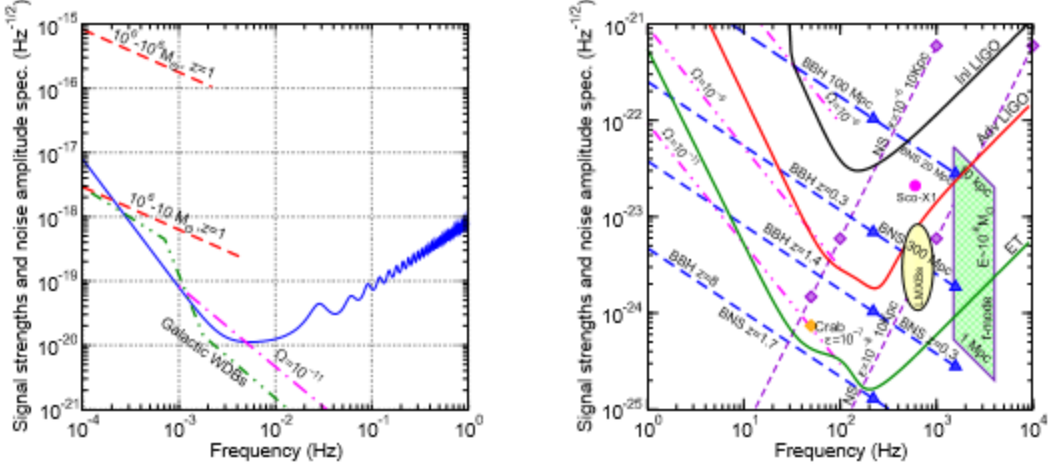


*Fig 19 : The right panel plots the noise amplitude spectrum , $\sqrt{f}S_h(f)$ , in three generations of ground-based interferometers. For the sake of clarity, we have only plotted initial and advanced LIGO and a possible third generation detector sensitivities. VIRGO has similar sensitivity to LIGO at the initial and advanced stages, and may surpass it at lower frequencies. Also shown are the expected amplitude spectrum of various narrow and broad-band astrophysical sources. The left panel is the same as the right except for the LISA detector. The SMBH sources are assumed to lie at a redshift of  $z = 1$ , but LISA can detect these sources with a good SNR practically anywhere in the universe. The curve labelled “Galactic WDBs” is the confusion background from the unresolvable Galactic population of white dwarf binaries.*

Correlation searches are also possible between resonant detectors or between one resonant and one interferometric detector . This has been implemented with bar detectors and between LIGO and the ALLEGRO bar detector .

LISA does not gain by a simple correlation between any two of its independent interferometers, since they share a common arm, which contributes common noise that competes with that of the background. A gravitational wave background of  $\Omega_{\text{gw}} \sim 10^{-10}$  would compete with LISA’s expected instrumental noise. However, using all three interferometers together can improve things for LISA at low frequencies, assuming that the LISA instrumental noise is well behaved . This might enable LISA to go below  $10^{-11}$ .

### 7.1.3) Observations with pulsar timing :

Other less-direct methods are also being used to search for primordial gravitational waves. pulsar timing can, in principle, detect gravitational-wave-induced fluctuations in the arrival times of pulses. Millisecond pulsars are such stable clocks when averaged over years of observations that they are being used to search for gravitational waves with periods longer

than one year. A single pulsar can set limits on a stochastic background by removing the slow spindown and looking for random timing residuals. Although one would never have enough confidence in the stability of a single pulsar to claim a detection, this sets upper limits in the important frequency range below that accessible to man-made instruments. The best such limits are on pulsar PSR B1855+09, with an upper limit (at 90% confidence) of  $\Omega_{\text{gw}} < 4.8 \times 10^{-9}$  at  $f = 4.4 \text{ nHz}$ .

Arrays of pulsars offer the possibility of cross-correlating their fluctuations, which makes it possible to distinguish between intrinsic variability and gravitational-wave-induced variability. Pulsars are physically separated by much more than a wavelength of the gravitational waves even with periods of 10 yrs, so that the correlated fluctuations come from the wave amplitudes at Earth. It will soon be possible to monitor many pulsars simultaneously with multi-beam instruments. This method could push the limits on  $h_c \equiv (fS_{\text{gw}})^{1/2}$  down to  $10^{-16}$  at 10 nHz, which translates into a limit on  $\Omega_{\text{gw}}$  of around  $10^{-12}$ .

#### 7.1.4) Observations using cosmic microwave background

Observations of the cosmic microwave background (CMB) may in fact make the first detections of stochastic (or any other!) gravitational waves. The temperature fluctuations first detected by the Cosmic Background Explorer (COBE) and measured with great precision by the Wilkinson Microwave Anisotropy Probe (WMAP) are produced by both density perturbations and long-wavelength gravitational waves in the early universe. Inflation suggests that the gravitational wave component may be almost as large as the density component, but it can only be separated from the density perturbations by looking at the polarization of the cosmic microwave background. WMAP made the first measurements of polarization, but it did not have the sensitivity to see the weak imprint of gravitational waves, which appears in the B-component of the polarization, the part that is divergence-free on the whole sky. The QUaD detector, a cryogenic detector that operated for three seasons in Antarctica. This had improved the limits of B component.

The gravitational waves detectable in the CMB have wavelengths a good fraction of the horizon size at the time of decoupling, and today they have been redshifted to much longer wavelengths. They are, therefore, much lower frequency than the radiation that would be observed directly by LISA or ground-based detectors, or even by pulsar timing.

### 7.2) Origin of random background gravitational waves

#### 7.2.1) Gravitational waves from big bang

Gravitational waves have travelled almost unimpeded through the universe since they were generated. The cosmic microwave background is a picture of the universe at a time  $3 \times 10^5$  yrs after the Big Bang, and studies of nucleosynthesis (how the primordial hydrogen, helium, deuterium, and lithium were created) reveal conditions in the universe a few minutes after the Big Bang. Gravitational waves, on the other hand, were produced at times earlier than  $10^{-24}$  s after the Big Bang. Observing this background would undoubtedly be one of the most important measurements that gravitational wave astronomy could make. It would provide a test of inflation, and it would have the potential to give information about the fundamental interactions of physics at energies far higher than we can reach with accelerators.

The most well-defined predictions about the energy in the cosmological gravitational wave background come from inflationary models. Inflation is an attractive scenario for the early universe because, among other things, it provides a natural mechanism for producing the initial density perturbations that evolved into galaxies and galaxy clusters as the universe expands. These perturbations start out as quantum fluctuations in the (hypothetical) scalar inflation field that is responsible for the inflationary expansion of the universe. The fluctuations are parametrically amplified by the expansion and lead to fluctuations in the density of normal matter after inflation ends.

Several strands of evidence – among them the statistical distribution of density perturbations seen in the cosmic microwave background (most recently by WMAP), the present distribution of galaxies, and numerical simulations of structure formation in the early universe – are fully consistent with the now-standard model of a universe dominated by dark energy and whose matter density is dominated by some kind of cold (i.e., massive) dark matter particles with density perturbations consistent with those that inflation could have produced.

The scalar inflation fluctuations are accompanied by tensor quantum fluctuations in the gravitational field that similarly get amplified by inflation and form a random background. Different models of inflation make different predictions about the relative strength of the scalar and tensor components.

Although inflation is in excellent agreement with observation, other mechanisms in the early universe may have led to the additional production of gravitational waves. Defects that arise from symmetry breaking as the presumed early unified interactions separate from one another can lead to cosmic strings, which can produce both a continuous observable gravitational wave background and characteristic isolated bursts of gravitational waves. String theory and brane theory may also provide mechanisms for generating observable radiation.

The various models usually predict significantly different spectra for background radiation. Standard inflationary models predict that the spectrum of  $\Omega_{\text{gw}}$  should be nearly flat, independent of frequency, but variants exist that allow a spectrum that rises with frequency

(positive spectral index) or falls. Symmetry-breaking and brane model cosmologies can make very different predictions, even leading to narrow spectral features. It is, therefore, important to measure the spectrum at as many frequencies as possible. Limits on power at one frequency (such as at the very low frequency end in the cosmic microwave background) do not necessarily predict the power at other frequencies (such as at ground-based frequencies, a factor  $10^{20}$  times higher).

It is even possible that there will be a feature in the spectrum in the observing band of ground based or space-based detectors. In standard cosmologies, the radiation observable by LISA (1 mHz) had a wavelength comparable to the (then) horizon size at around the time when the temperature of the universe was equal to the electroweak symmetry-breaking energy. If electroweak symmetry breaking led to a first-order phase transition, where density fluctuations occurred on the length scale of the typical symmetry domain size, then it is likely that these density fluctuations produced gravitational waves with wavelengths of the size of the horizon, which would be in the LISA band today. Detection of this radiation would have deep implications for fundamental physics.

The other expected phase transition is the GUTs (Grand Unified Theory) transition, whose energy might have been  $10^{13}$  times higher. Any gravitational radiation from this transition today would then be at a frequency  $10^{13}$  times that from the electroweak transition, i.e., at centimetre wavelengths. This is one motivation for building microwave-based table-top detectors aimed at high frequencies. For this radiation to be observable by standard interferometers, the GUTs transition would have to have an energy  $10^7$  times smaller than expected, i.e., around  $10^9$  GeV.

In addressing the possibility of new physics, observation of gravitational waves in the cosmic microwave background would play a unique role. These waves originated long after nucleosynthesis, at energies where physics is presumably well understood. They would, therefore, normalize the amount of power in the initial tensor perturbations. Then observations at higher frequencies can use this normalization to measure the excess energy due to any exotic effects due to string theory, phase transitions, or other unknown physics.

Pulsar timing arrays will also be used to search for a CGWB at frequencies of a few nano Hertz. As for the microwave background, the physics of the universe when gravitational waves at these frequencies originated is well understood, so they could be used to normalize the spectrum. If the power at pulsar frequencies and that in the microwave background are not consistent, then this could indicate something about the conditions in the universe before inflation began.

The predicted spectrum from inflation, strings, and symmetry breakings is highly non-thermal. Any thermal radiation produced in the Big Bang would have been redshifted away to such that it can not be observed by the subsequent inflationary expansion. If inflation did

not in fact occur, then this radiation today would have a temperature only a little below that of the cosmological microwave background. So far no instrument has been proposed that would be sensitive to this radiation, but its detection would presumably be inconsistent with inflation.

### 7.2.2) Astrophysics sources of stochastic background

After galaxy formation, it is possible that many systems arose that have been radiating gravitational waves in the bands observable by pulsar timing, LISA, and ground-based detectors. There are likely to be strong extra-galactic backgrounds in the LISA band from compact binary systems, which would limit searches for a CGWB by LISA, even if the sensitivity were better. At lower frequencies, even down to pulsar timing frequencies, black hole binaries may make the strongest background, while at frequencies above the LISA band (i.e., above 0.1 Hz) the universe should be relatively free of serious backgrounds .

In the LISA band our galaxy is a strong source of backgrounds . This presents a serious confusion noise in searching for other sources at frequencies below 1 mHz. It should be possible to distinguish this from a CGWB by its intrinsic anisotropy .

## 7.3) Cosmography : Gravitational wave Measurements From Cosmological Parameters

Since inspiral signals are standard candles , observations of massive black hole coalescences at cosmological distances by space-based detectors can facilitate an accurate determination of the distance to the source. Our earlier expressions for the chirp waveform can be generalized to the cosmological case (a source at redshift  $z$ ) by multiplying all masses by  $1+z$  and by replacing the physical distance  $D$  by the cosmological luminosity distance  $D_L$  . If the wave amplitude, frequency, and chirp rate of the binary can be measured, then its luminosity distance can be inferred. It is not, however, possible to infer the redshift  $z$  from the observed signal: the scale-invariance of black hole solutions means that a signal with a redshift of two and a chirp mass  $M$  looks identical to a signal with no redshift and a chirp mass of  $M/3$ . To use these distance measures for cosmography, one has to obtain redshifts of the host galaxies.

Before considering how this might be done, we should ask about the accuracy with which the distance can be measured. The relative error in the distance is dominated by the relative error in the measurement of the intrinsic amplitude of the gravitational wave, because the masses will normally be much more accurately measured (by fitting the evolving phase of the signal) than the amplitude. Several factors contribute to the amplitude uncertainty:

- **Signal to noise ratio :** The intrinsic measurement uncertainty in the amplitude of the detector's response is simply the inverse of the SNR. Since LISA can have an SNR of

several thousand when it observes an SMBH coalescence at high redshift, LISA has great potential for cosmography.

- **Position error :** From the detector response one must infer the intrinsic amplitude of the wave, which means projecting it on the antenna pattern of the detectors. This requires a knowledge of the source position, and this will be potentially a bigger source of uncertainty because the sensitivity of LISA depends on the location of the source in its antenna pattern. Recent work has shown that LISA may be able to achieve position accuracies between one and ten arcminutes. At, say, three arcminutes error, the amplitude uncertainty will be of order 0.1%. This error can be reduced to the SNR-limited error if the source can be identified. Although the coalescence of two SMBHs itself may not have an immediate effect on the visible light from a galaxy, the host galaxy might be identifiable either because it shows great irregularity (mergers of black holes follow from mergers of galaxies) or because some years after the merger an X-ray source turns on (accretion will be disrupted by the tidal forces of the orbiting black holes, but will start again after they merge). Other effects that might lead to an identification include evidence that stars have been expelled from the core of a galaxy, fossil radio jets going in more than two directions from a common centre, and evidence for accretion having stopped in the recent past.
- **Microlensing :** If the source is at a redshift larger than one, as we can expect for LISA, then random microlensing can produce a magnification or demagnification on the order of a few percent. The measured intrinsic amplitude then does not match the amplitude that the signal would have in an ideal smooth cosmology.

The relatively small error boxes within which the LISA coalescences can be localized are promising for identifications, especially if the X-ray indicators mentioned above pick out the host in the error box. These factors and their impact on cosmography measurements have been examined in detail by Holz and Hughes , who coined the term “standard siren” for the chirp sources whose distance can be determined by gravitational wave measurement . Nearby coalescences and IMRIs should provide an accurate determination of the Hubble Constant . Perhaps the most interesting measurement will be to characterize the evolution of the dark energy, which is usually characterized by inserting a parameter  $\omega$  in the equation of state of dark energy,  $p = \omega \rho$ . If  $\omega = -1$ , then the dark energy is equivalent to a cosmological constant and the energy density will be the same at all epochs. If  $\omega > -1$ , the dark energy is an evolving field whose energy density diminishes in time. According to , gravitational wave measurements have the potential to measure  $w$  to an accuracy better than 10% (for advanced ground-based detectors) and around 4% (for LISA). The accuracy with which parameters can be measured improves greatly when one includes in the computation of the covariance matrix the harmonics of the binary inspiral signal that is normally neglected . have shown that the source location in the sky can be greatly improved when the signal harmonics (up to fifth harmonic) are included, which further helps in measuring the parameter  $\omega$  even better .

## 7) GRAVITATIONAL WAVES VS ELECTROMAGNETIC WAVES

Similarities :

- Gravitational waves and electromagnetic waves propagate at the speed of light ( $c=3\times 10^8$  m/s) .
- The amplitude decreases as  $1/r$ .
- In both the cases frequency red shift is observed .

Differences :

- Gravitational waves travel through matter with a little interaction and they carry uncontaminated information about their sources .
- Electromagnetic waves interact with matter , simple experiments can be performed to detect its presence .
- Electromagnetic waves are varying electric and magnetic fields, perpendicular to each other and the direction of propagation. So basically, if the wave is moving along the x axis, then the electric field varies along the y axis and the magnetic field along the z axis.

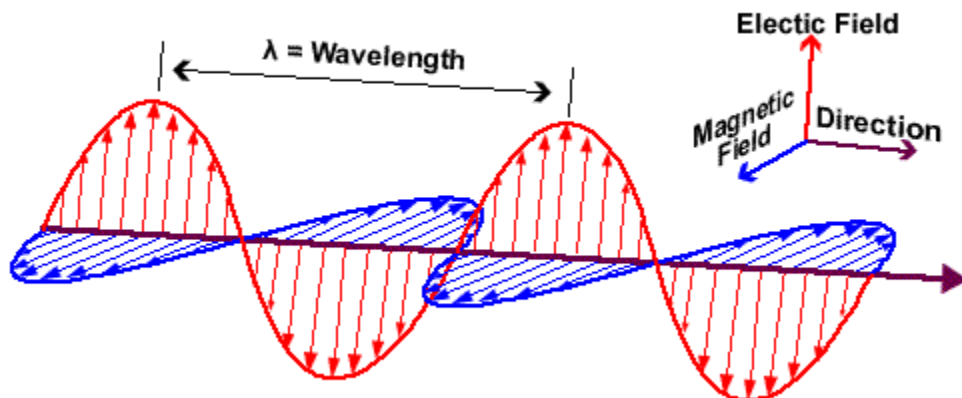


Fig 20

- Gravitational waves, on the other hand, are ripples in the curvature of spacetime that travel outwards from their source. Picture the fabric of spacetime as a blanket. Now, spacetime has a curvature due to objects with a large amount of mass, which can be imagined just like a heavy object placed on a blanket.

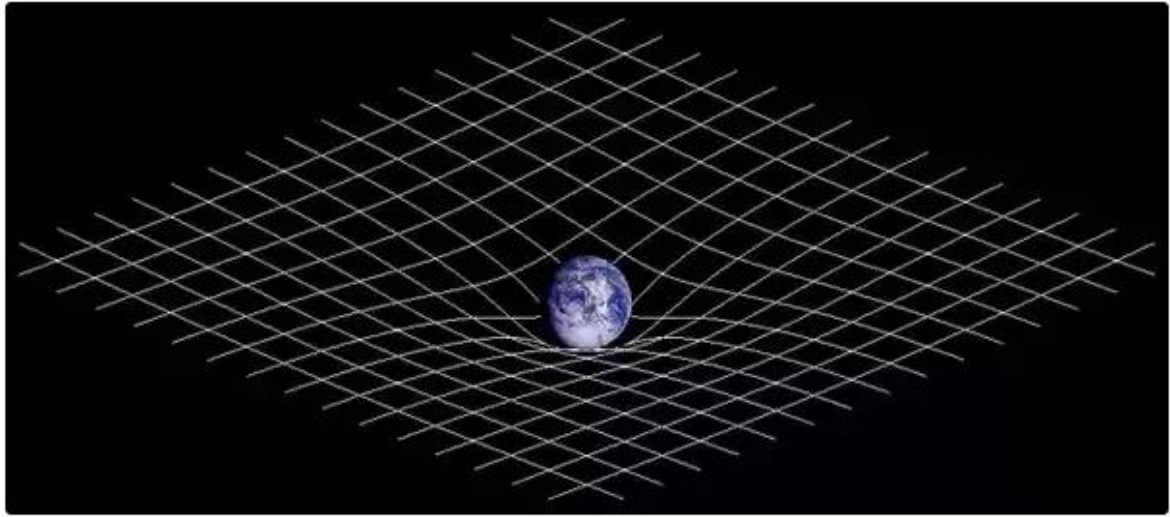


Fig 21

- So we can say that the curvature of spacetime is due to the presence of mass. Generally, the more mass that is contained in a given volume of space, the greater the curvature of spacetime. As objects with mass move around, the curvature also moves to reflect the change in location of the object. Accelerating objects can generate waves in certain circumstances. Gravitational waves are not radiated by objects in motion that is spherically symmetric or cylindrically symmetric. A simple example is a spinning dumbbell where the ends spin end-over-end. Two objects in such an orbit would radiate energy as gravitational waves.

## 8) GRAVITATIONAL WAVE DETECTORS

### 9.1) An overview of gravitational wave detection

Until the mid 20th century there remained some question as to whether or not gravitational waves were truly predicted by general relativity . It was not obvious that what appeared to be a wave phenomenon could not be explained away as an artifact of coordinate/gauge transformations . The reality of gravitational wave prediction was confirmed, however, by the realization that energy could be extracted from the waves, i.e., it was possible, in principle, to build a detector that could register their passage .

The earliest manmade gravitational wave detectors were based on a simple gedanken experiment: if two masses on a spring are momentarily stretched apart and then compressed by a gravitational wave, potential energy is imparted to the spring, independent of how coordinates are defined. If the characteristic frequency of the wave is near the resonance frequency of the

mechanical system, the response to the wave is magnified, not unlike an LRC antenna circuit's response to a passing electromagnetic wave. One early approach was to search for excitations of the Earth's crustal vibrational normal modes ( $\sim$ sub-mHz and higher harmonics), a technique useful for setting upper limits, but large earthquakes made it unattractive for detection.

In practice, since it is the elastic energy that matters, the first gravitational wave detectors were simple metal cylinders, where the energy converted to longitudinal oscillations of the bar was measured via piezoelectric transducers near the "waist" of the bar, as shown in . One looked for a sudden change in the amplitude of nominally thermal motion of the bar. Joe Weber of the University of Maryland pioneered this detector design and implementation; he also reported anomalies attributed to gravitational waves, such as coincident transients in geographically separated pairs of bars, but subsequent experiments with comparable or more sensitive instruments failed to confirm the reported detections .

In the following years the technology of bar detectors improved steadily, with the introduction of cryogenic detectors to reduce thermal noise, cryogenic squid transducers for more efficient detection of bar excitations, and increasingly sophisticated analysis techniques. In the late 1990s, before 1st-generation gravitational wave interferometers came online, there were five major bar detectors operating cooperatively in the International Gravitational Event Collaboration (IGEC) Allegro at Louisiana State University; Auriga at Padua University, Explorer at CERN, Nautilus at Frascati Laboratory, and Niobe at the University of Western Australia. These bars achieved impressive strain amplitude spectral noise densities near  $10-21/\sqrt{\text{Hz}}$ , but only in narrow bands of  $\sim 1-30$  Hz near their resonant frequencies (ranging from  $\sim 700$  Hz to  $\sim 900$  Hz). Hence waveform reconstruction for all but very narrowband gravitational wave sources was not feasible with these detectors. As of 2012, only the Auriga and Nautilus detectors are still collecting data, since the major interferometer detectors LIGO and Virgo have achieved broadband sensitivities better than the narrowband sensitivities of the bars. It should be noted, however, that as of 2012, the LIGO and Virgo detectors are undergoing major upgrades , leaving GEO 600 as the only major gravitational wave interferometer collecting data routinely for the next several years. Should a supernova occur in our galaxy during that time, only GEO 600 and the remaining bar detectors would have a chance of detecting it in gravitational waves.

Gravitational-wave interferometers take a different approach to detection from that of resonant bars. Setting aside enhancements to be discussed below, a simple right-angle Michelson laser interferometer, as shown in the cartoon in figure 22 is a natural gravitational-wave detector. For example, a linearly polarized wave impinging normally on the interferometer with its polarization axis aligned with the arms will alternately stretch one arm while contracting the other. One common question is how this alternation is detected, given that the laser light is stretched and compressed too. The answer is that the detection is based on the phase difference between the light returning from each arm, and that phase difference increases with time, following the passage of the gravitational wave. The red-shifted light simply takes longer to complete its round-trip in the arm than the blue-shifted light. Hence even an idealized, simple gravitational-wave interferometer has a finite and frequency-dependent response time.

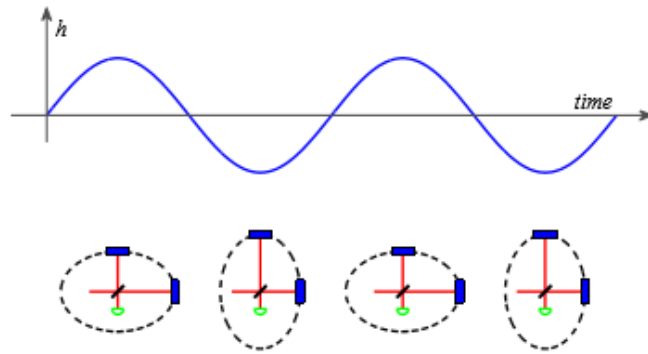


*Fig 22 : Cartoon illustration of the effect of a gravitational wave on the arms of a Michelson interferometer, where the readout photodiode is denoted by the green semi-circle .*

The basic idea for a gravitational wave interferometer was first written down by Gertsenshtein and Pustovoit in 1962 . Weber's group developed this idea further into the first gravitational wave interferometer prototype built by Weber graduate Robert Forward at Hughes Aircraft Research Lab . It was early work carried out in parallel by Rai Weiss , however, that laid the groundwork for present-day gravitational wave interferometers. As discussed further below, it became appreciated quickly that laser interferometers had the potential to surpass bar detectors in sensitivity, and there was rapid development of ideas and technology. Subsequent improvements included (among many others) using Fabry-Perot cavities for the interferometer arms to increase the time of exposure of the laser light to the gravitational wave , introduction of a “recycling” mirror between the laser and beam-splitter, to increase effective laser power , and introduction of another mirror between the beam splitter and photodetector to allow tuning of the interferometer’s frequency response .

## 9.2) Detector Sensitivity And Resolution Considerations :

A bar detector can be considered as a energy detection device and an interferometer as a strain amplitude detector . Consider a bar of length  $L$  , mass  $M$  , at an operating temperature  $T$  , having a resonant frequency  $f$  , Mechanical quality factor  $Q$  . From equipartition theorem the average energy of vibration of the mode is  $K_B T$  , where  $K_B$  is Boltzmann constant . For simplicity treat the bar fundamental longitudinal mode of vibration as a simple harmonic oscillator of spring constant  $k$  with displacement of one end of the bar from its nominal distance of  $L/2$  from the centre as the spring’s displacement from equilibrium with the half of the bar providing mass  $M/2$ . Then we expect an RMS strain motion of

$$\frac{1}{2} Kx^2 = \frac{1}{2} (M/2)(2\pi f_0)^2 = \frac{1}{2} K_B T$$

$$h_{\text{RMS}} \sim \frac{x_{\text{rms}}}{L/2} \sim \frac{2}{L} \sqrt{\frac{k_{rmB}T}{2\pi^2 f_0^2 M}}.$$

Taking the LSU Allegro bar as an example, for which  $L = 3.0$  m,  $f_0 = 907$  Hz,  $M = 2296$  kg, and  $T = 4.2$  K, one obtains  $h_{\text{RMS}} \sim 3 \times \sim 10^{-17}$ . Naively then, one might think that only gravitational waves with characteristic amplitude much greater than  $10^{-17}$  would be detectable with such a bar. Fortunately, the fact that resonant bars are deliberately designed with high mechanical quality factors  $Q$  allows much better sensitivity than this naive calculation suggests. The impulse imparted by a passing wave is dissipated over a time scale of  $\sim Q/f_0$ . Hence by measuring over many cycles (but less than  $Q$ ) of the resonance, one can reduce the effective noise by a factor comparable to  $\sqrt{Q}$ . It is interesting to examine relations involving the energy  $E_{\text{dep}}$  deposited in the bar by the passing gravitational wave. The characteristic strain amplitude  $h_c$  of a burst wave of duration of characteristic time  $\tau_{\text{burst}}$ .

$$h_c \approx \frac{\sqrt{15}}{2} \frac{L}{\tau_{\text{burst}} v_s^2} \sqrt{\frac{E_{\text{dep}}}{M}},$$

The above calculations ignore non-fundamental but important additional sources of noise, such as in the readout electronics or from the terrestrial environment, including magnetic fields. Measuring the deposited gravitational wave energy is non-trivial. The original piezo-electric transducers at the waists of the original bar detectors evolved into transducers at the ends of the detectors, where vibration amplitude is maximum. Using a transducer with an intrinsic resonant frequency very near that of the bar leads to a coupled oscillator with two normal modes and a beat frequency that defines the time scale for the energy of the resonant bar to leak into the transducer. This amplification trick permits more efficient detection readout.

There is a nominal quantum limit, however, to the performance of a bar detector (as there is for an interferometer, as discussed below). The readout of the energy in the fundamental harmonic is limited by the quantum noise of the system at that frequency. The nominal quantum limit on strain sensitivity on an ideal bar is

$$h_{\text{rms}} \approx \frac{1}{h} \sqrt{\frac{\hbar}{2\pi f_0 M}}$$

This nominal quantum limit need not be truly fundamental. By exploiting quantum “squeezing” (sacrificing phase information for amplitude information), one can, in principle, do somewhat better. But squeezing is notoriously delicate, in practice, offering little hope of improvement by orders of magnitude.

It is amusing to compare the energy loss of a gravitational wave impinging on a bar detector with that of high-energy neutrinos, which are famous for their penetration. For example, 1-GeV muon neutrinos traveling along the axis of a 3-meter long aluminium bar have a probability of interacting of about  $3 \times 10^{-12}$ . In comparison, a monochromatic (1 kHz), planar linearly polarized gravitational wave of amplitude  $h_+ = 10^{-19}$  has an energy flux  $F$  through the bar of  $1.6 \text{ kW/m}^2$ , while the energy deposition rate for a resonant bar with quality factor  $Q = 10^6$  is approximately  $1.2 \times 10^{-22} \text{ W}$  on resonance, giving a fractional energy loss of  $O(10^{-25})$ , making the “elusive neutrino” seem relatively easy to stop. Saulson computes effective “cross sections” of resonant bars and finds, for example,  $\sigma_{\text{bar}}/L^2_{\text{bar}} \sim 10^{-22}$ . Such a tiny value can be thought of as a measure of the weakness of the gravitational interaction, or alternatively, as a measure of the impedance mismatch between matter and extremely stiff space-time.

Let's turn now to the expected sensitivity of interferometers. For concreteness, consider a gravitational wave burst with a duration of 1 ms and characteristic frequency in the detector's sensitive band. In order to obtain a “5- $\sigma$  detection,” the intensity of the light at the photodetector must change by at least what is required to be seen over shot noise (photon count statistical fluctuations). For a 10-W ( $\lambda = 1064$  nm) laser impinging on the photodetector (after recombination at the beam splitter), one has a relative statistical fluctuation of  $1/[(5.3 \times 10^{19} \text{ s}^{-1})(10^{-3} \text{ s})]^{1/2} \sim 4 \times 10^{-9}$ . Assuming a simple Michelson interferometer of the same size as LIGO (4-km arms) with the beam splitter positioned to give a nominal light intensity at half its maximum (constructive interference of the returning beams), one has a gain factor of

$$\frac{1}{I} \frac{dI}{dh} = 8\pi \frac{L}{\lambda} \approx 10^{11}$$

Hence to obtain 5- $\sigma$  detection, one needs a strain amplitude of  $O(2 \times 10^{-19})$ , which even in this relatively simple configuration, already gives impressive broadband sensitivity. As discussed in more detail below, the LIGO and Virgo interferometers have achieved significant improvement over this sensitivity by using Fabry-Perot cavities in the arms and a recycling mirror to increase effective light power. Other improvements, such as elaborate laser intensity and frequency stabilization, along with a heterodyne RF readout scheme that allows the interferometer to operate with near-destructive interference at the photodiode, mitigate non-fundamental noise sources that would otherwise invalidate the above simple model.

As with bars, there is a nominal quantum limit. Naively, one could improve sensitivity arbitrarily by increasing laser power, to reduce shot noise ( $\propto 1/(N_{\text{phot}})^{1/2}$ ), but at some intensity, radiation pressure fluctuations ( $\propto (N_{\text{phot}})^{1/2}$ ) become limiting. Note that the effects of radiation pressure are reduced by increasing the masses of the mirrors. For example, Advanced LIGO mirrors will be 40 kg, much heavier than the 11-kg mirrors used for Initial LIGO, in order to cope with the increased laser power ( $\sim 180$  W vs  $\sim 10$  W). One could imagine increasing mirror mass with laser power indefinitely, but sustaining the high optical quality and high mechanical quality factor becomes more challenging. In addition, it becomes more difficult to prevent internal vibrational modes from contaminating the detection band .

Once again, as with bars, the standard quantum limit can be evaded via squeezing , but with the opposite intent. In interferometer squeezing, one sacrifices intensity sensitivity to achieve lower phase noise, using an optical parametric amplifier at the output beam of the interferometer. A useful way to think about the quantum fluctuations is that when the interferometer is operated near a point of destructive interference, vacuum fluctuations in the quantum field “leak” back into the interferometer. In some sense, squeezing the interferometer is actually squeezing the vacuum state with which it interacts. Squeezing has been demonstrated not only in table top experiments , but also on two large-scale gravitational wave interferometers (GEO 600 and LIGO ). In the future squeezing may be used to go beyond design sensitivities for Advanced LIGO and Virgo, or in the event that technical obstacles arise at full laser power for those interferometers, squeezing offers an alternative to reach design sensitivity at lower laser powers.

Both bars and interferometers are better thought of as antennae than as telescopes, because their sizes are small compared to the wavelengths they are meant to detect. For example, a bar detector of length 3 m with a resonant frequency of 900 Hz has  $L/\lambda \sim 10^{-5}$ , while even the LIGO detectors when searching at 4 kHz have  $L/\lambda$  of only about 0.05. These small ratios imply broad antenna lobes. Figure 23 shows the antenna lobes for +,  $\times$  linear polarizations and circular polarizations vs. incident direction for a Michelson interferometer in the long-wavelength limit. As a result, a single interferometer observing a transient event has very poor directionality.

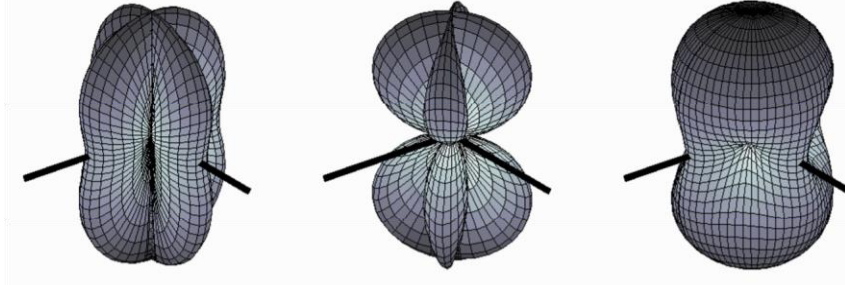


*Fig 23: Antenna response pattern for a Michelson interferometer in the long-wavelength approximation. The interferometer beam splitter is located at the centre of each pattern, and the thick black lines indicate the orientation of the interferometer arms. The distance from a point of the plot surface to the centre of the pattern is a measure of the gravitational wave sensitivity in this direction. The pattern on the left is for + polarization, the middle pattern is for  $\times$  polarization, and the right-most one is for unpolarized waves*

One can do substantially better by triangulating detections via multiple detectors. For a given SNR, consistency of timing between each detector in a pair leads to an allowed annulus on the sky with angular thickness  $\propto 1/\text{SNR}$ . Combining each allowed pair in a network of three or more detectors favours intersections of these annular rings. In principle, requiring amplitude consistency of a putative sky location and the known relative orientations of the detectors resolves resulting ambiguities from multiple intersections, but polarization effects complicate that resolution, since detected amplitudes depend on the typically unknown orientation of the gravitational wave source.

A notable exception to the  $L/\lambda \ll 1$  rule of thumb is detection of a long-lived continuous-wave source, where the Earth's orbit around the solar system barycenter, gives a single detector over the course of a year an effective aperture radius comparable to the distance from the Earth to the Sun. For a nearly monochromatic, continuous-wave source at 1 kHz, e.g., from a millisecond pulsar, Rayleigh's criterion gives an angular resolution of approximately:

$$\theta \approx \frac{3 \times 10^5}{3 \times 10^{11}} = 10^{-6} \text{ radians}$$

$\theta$  is approximately 0.2 arcsec



*Fig 24 : Aerial photographs of the LIGO observatories at Hanford, Washington (left) and Livingston, Louisiana (right) . The lasers and optics are contained in the white and blue buildings. From the large corner building, evacuated beam tubes extend at right angles for 4 km in each direction (the full length of only one of the arms is seen in each photo); the tubes are covered by the arched, concrete enclosures seen here*

### 9.3) FIRST GENERATION INTERFEROMETERS

The “first generation” of ground-based gravitational wave interferometers is not well defined, since many of the prototype interferometers used to demonstrate new technology developments were also used in prototype gravitational wave searches, some of which led to journal publications. Saulson provides a nice summary of these experiments and searches. Prototype interferometers were built and operated around the world in Australia, Europe, Japan and the United States. These prototypes led eventually to the building of six major interferometers: TAMA (300-m arms) near Tokyo , GEO 600 (600-m arms) near Hannover , Virgo (3000-m arms) near Pisa , and LIGO (two with 4000-m arms and one with 2000-m arms) in the states of Washington and Louisiana . Figure 24 shows aerial views of the two LIGO sites in Hanford, Washington and Livingston, Louisiana. The major interferometers share many design characteristics, but also display significant differences.

#### 9.3.1) FABRY-PEROT CAVITIES

Consider a cavity formed by two flat, parallel mirrors, as shown in figure 25 with a polarized plane electromagnetic wave of wavelength  $\lambda$  incident from the left, where the intra-cavity surfaces have amplitude reflectivity

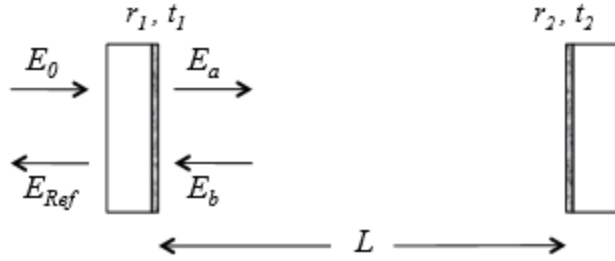


Fig 25 : Schematic diagram of a flat-flat Fabry-Perot cavity with reflective coatings on the intra-cavity mirror surfaces. The  $E_i$  labels and arrows refer to (signed) electric field amplitudes of waves traveling in the directions of the arrow.  $E_0$  denotes the incident field on the cavity, and  $E_{\text{Ref}}$  denotes the net reflected field.  $r_i$  and  $t_i$  denote the amplitude reflection and transmission coefficients of the coated surfaces.

coefficients  $r_1$  and  $r_2$  and where the extra-cavity surfaces are taken, for simplicity, to have perfect antireflective coatings. For input laser power of electric field amplitude  $E_0$  and in the steady state, after start-up transients have settled down, one has the following relations among the electric field amplitudes of the light entering, leaving and residing in the cavity at the two mirror surfaces:

$$\begin{aligned} E_a &= t_1 E_0 - r_1 E_b \\ E_b &= -r_2 e^{i\phi} E_a \\ E_{\text{Ref}} &= r_1 E_0 + t_1 E_b \end{aligned}$$

where  $E_a$  refers to the rightward-moving wave at the 1st mirror,  $E_b$  refers to the leftward moving wave at the 1st mirror,  $E_{\text{Ref}}$  refers to the wave reflected from the 1st mirror, and  $\phi = 4\pi L/\lambda$  is the length dependent phase shift due to propagation from the 1st mirror to the 2nd mirror and back. The sign convention chosen here is to take  $r_1$  and  $r_2$  both positive. Solving these steady-state relations leads to

$$\begin{aligned} E_a &= \frac{t_1}{1 - r_1 r_2 e^{i\phi}} E_0, \\ E_b &= -\frac{t_1 r_2 e^{i\phi}}{1 - r_1 r_2 e^{i\phi}} E_0 \\ E_{\text{Ref}} &= \frac{r_1 - r_2 e^{i\phi}}{1 - r_1 r_2 e^{i\phi}} E_0. \end{aligned}$$

The cavity resonates when  $\phi = 2\pi N$  for an integer  $N$ . If, as is typically the case for Fabry-Perot arm cavities used in gravitational wave interferometers, the reflectivity of mirror 2 is much closer to unity than that of mirror 1, then on resonance:

$$\begin{aligned} E_a &\approx \frac{t_1}{1-r_1} E_0, \\ E_b &\approx -\frac{t_1}{1-r_1} E_0 \\ E_{\text{Ref}} &\approx -E_0. \end{aligned}$$

In practice, there are small losses in the cavity, in the coatings and transmission through mirror 2 that lead to small corrections to these relations. Note that in the above lossless approximation, energy conservation requires  $|E_{\text{Ref}}| = |E_0|$ .

Imagine that a single Fabry-Perot is on resonance, but that a gravitational wave passes, leading to a momentary increase of the cavity's length by an amount  $\Delta L$ . Then the change in  $E_{\text{Ref}}$  is governed by the derivative :

$$\left[ \frac{dE_{\text{Ref}}}{dL} \right]_{\phi=2\pi N} = -i \frac{(1-r_1^2) r_2}{(1-r_1 r_2)^2} \frac{2\pi}{\lambda} E_0$$

Again, taking the case  $r_2 \rightarrow 1$  and  $\delta r_1 \equiv 1-r_1 \ll 1$ ,

$$\left[ \frac{dE_{\text{Ref}}}{dL} \right]_{\phi=2\pi N} \approx -i \frac{2}{\delta r_1} \frac{2\pi}{\lambda} E_0$$

which implies a large amplification in phase sensitivity for small  $\delta r_1$ . One figure of merit is the cavity finesse  $F \approx \pi(r_1/(1-r_1))^{1/2}$ . In principle, a single cavity can therefore act as a gravitational wave detector, but one gains in sensitivity by simultaneously monitoring another, identical arm oriented at a right angle, not merely because of the potential to double the signal strength from optimum quadrupole orientation, but much more important, mundane noise sources that affect the input field amplitude  $E_0$  and phase cancel in the difference-signal.

The above analysis idealized the laser light as a plane wave and used planar mirrors. But high-quality lasers produce Gaussian beams with curved wavefronts. Fabry-Perot cavities are normally designed with at least one curved mirror (usually concave as seen from the cavity), such that a Gaussian beam resonates with a spherical wavefront at the mirror(s) with radii of wavefront curvature at those locations to match those of the mirror(s). For a cavity of length  $L$  with two concave mirrors of radii  $R_1$  and  $R_2$ , it is useful to define mirror g factors  $g_i \equiv 1-L/R_i$ , from which one can derive the beam's characteristic intensity radii at the mirrors ( $w_1$  and  $w_2$ ) and the beam's "waist" (minimum radius):

$$w_1^2 = \frac{L\lambda}{\pi} \sqrt{\frac{g_2}{g_1(1-g_1g_2)}}, \quad w_2^2 = \frac{L\lambda}{\pi} \sqrt{\frac{g_1}{g_2(1-g_1g_2)}}$$

And ,

$$w_0^2 = \frac{L\lambda}{\pi} \sqrt{\frac{g_1g_2(1-g_1g_2)}{(g_1+g_2-2g_1g_2)^2}},$$

Although the radii of curvature of the initial LIGO mirrors vary slightly, round numbers for the four different 4-km arm cavities are  $R_1 \approx 14,000$  m (input mirror near the beam splitter) and  $R_2 \approx 7,300$  m (end mirror), leading to beam radii at the input mirrors or about 3.6 cm and 4.5 cm, respectively , with an inferred beam waist of 3.5 cm about 1 km from the input mirror. Ensuring that the mirror aperture is much larger than the maximum beam radius is an important design constraint.

It should be noted that an infinite number of Gaussian-modulated waveforms can resonate in a cavity (e.g., with Hermite-Gaussian or Laguerre-Gaussian envelopes), but their resonant lengths differ slightly because of differing Gouy phases . As a result, a servo-locked cavity resonating in the fundamental mode (normally desired) will not generally simultaneously resonate in higher order modes that could introduce confusion into the servo error signal. Matching the waist size and location of the input laser beam to the cavity is delicate, with mismatches leading to degraded resonant power and reduced phase sensitivity in  $E_{\text{Ref}}$ .

Another important consideration is the finite time response of a Fabry-Perot cavity to length changes, ignored in the above steady-state analysis. There is a characteristic time scale  $\tau \approx L/\pi c$  for the information of a disturbance to “leak” into the reflected light  $E_{\text{REF}}$  ( $\sim 1$  ms for LIGO 4-km interferometers). For a fixed arm length  $L$ , the time constant  $\tau$  increases with the cavity finesse. Hence, while increasing finesse increases phase sensitivity at DC, it leads to more rapid onset of amplitude loss with higher frequencies, as measured by the cavity pole  $f_{\text{Pole}} = 1/(4\pi\tau)$  ( $\sim 85$  Hz for LIGO 4-km interferometers).

To maintain Fabry-perot cavity in resonance when the mirrors are suspended like a free pendula , One needs a negative-feedback servo control system with an error signal proportional to the deviation of the cavity from resonance and with an actuation mechanism to bring the cavity back to resonance by forcing the error signal to zero (to a level consistent with a necessarily finite gain). For gravitational-wave interferometers, the servo control system is based on Pound-Drever-Hall (PDH) locking . In this scheme, the laser light is phase-modulated at a radio frequency  $f_{\text{mod}}$  and a photodetector viewing the reflected light is demodulated at that frequency. To see why this method is effective, consider the Bessel function expansion of a phase-modulated field:

$$\begin{aligned} E_0 e^{i[\omega t + \Gamma \cos(\Omega_{\text{mod}} t)]} &= E_0 [J_0(\Gamma) e^{i\omega t} + iJ_1(\Gamma) e^{i(\omega+\Omega_{\text{mod}})t} + iJ_1(\Gamma) e^{i(\omega-\Omega_{\text{mod}})t} \\ &\quad - J_2(\Gamma) e^{i(\omega+2\Omega_{\text{mod}})t} - J_2(\Gamma) e^{i(\omega-2\Omega_{\text{mod}})t} + \dots] \end{aligned}$$

The field can be treated as a carrier with sidebands at integer harmonics of the modulation frequency, where for a moderate modulation depth (< 1 radian), the strengths of the higher-

order harmonics fall off rapidly. Note, however, that the time-averaged intensity of a purely phase modulated beam is monochromatic:

$$|E_0 e^{i\omega + \Gamma \cos(\Omega_{\text{mod}} t)}|^2 = E_0^2$$

that is, no sidebands are apparent (imagine measuring power over many cycles of  $\omega$ , but over only a fraction of a cycle of  $\Omega_{\text{mod}}$ , where typically  $\Omega_{\text{mod}}/\omega < 10^{-6}$ ). The key to the PDH scheme is that the carrier and sidebands have different resonant characteristics in a Fabry-Perot cavity. For example, the carrier might resonate, while the fundamental sidebands reflect promptly with negligible leakage into the cavity. In that case (for  $\Omega_{\text{mod}} 2\pi f_{\text{FSR}}$ , where  $f_{\text{FSR}} = c/2L$  is the free spectral range of the cavity) the beat between the reflected carrier and sideband will cancel for carrier resonance, but will have a non-zero residual beat when the carrier is off resonance. For small deviations from resonance, the strength at the beat frequency is proportional to the deviation in cavity length from its resonance value. Hence an error signal for locking the cavity frequency to the laser frequency can be derived. One can just as well, treat the error signal as a measure of the laser frequency's deviation from what resonates in the cavity, and feed back to the laser frequency to lock the servo, e.g., by actuating on a piezoelectric controller on one mirror of the Fabry-Perot lasing cavity .

### 9.3.2) POWER RECYCLED MICHELSON INTERFEROMETRY AND INITIAL LIGO

The initial LIGO detector was a set of three power-recycled Michelson interferometers with the parameters given in table 2 . Power recycled interferometry is explained in this section, along with noise considerations. The LIGO laser source was a diode-pumped, Nd:YAG master oscillator and power amplifier system, and emitted 10 W in a single mode at 1064 nm. The beam passed through an ultra-high vacuum system ( $10^{-8}$ - $10^{-9}$  Torr) to reduce phase fluctuations from light scattering off residual gas and to ensure acoustical isolation. The 4-km stainless steel tubes of 1.2-m diameter were baked at 160° C for 20 days to remove hydrogen.

The mirrors defining the interferometer were fused-silica substrates with multilayer dielectric coatings having extremely low scatter, low absorption and high optical quality. These mirrors were suspended as pendula with a natural oscillation frequency of ~0.76 Hz, designed to respond as essentially free “test masses” to gravitational waves while being isolated from ground motion by the  $\sim 1/\omega^2$  filtering of the pendulum. The suspension came from a single loop of steel wire around each mirror’s waist. Mirrors were controlled by electromagnetic actuators – magnets bonded to the optics and influenced by currents in nearby coils mounted on the support structure. For further isolation from ground motion, the pendulum support structures were mounted on four stages of mass-spring isolation stacks

	<b>H1</b>	<b>L1</b>	<b>H2</b>
Laser type and wavelength		Nd:YAG, $\lambda = 1064$ nm	
Arm cavity finesse		220	
Arm length	3995 m	3995 m	2009 m
Arm cavity storage time, $\tau_s$	0.95 ms	0.95 ms	0.475 ms
Input power at recycling mirror	4.5 W	4.5 W	2.0 W
Power Recycling gain	60	45	70
Arm cavity stored power	20 kW	15 kW	10 kW
Test mass size & mass	$\phi 25$ cm $\times$ 10 cm, 10.7 kg		
Beam radius ( $1/e^2$ power) ITM/ETM	3.6 cm / 4.5 cm	3.9 cm / 4.5 cm	3.3 cm / 3.5 cm
Test mass pendulum frequency		0.76 Hz	

*Table 2 : Parameters of the LIGO interferometers. H1 and H2 refer to the interferometers at Hanford, Washington, and L1 is the interferometer at Livingston Parish, Louisiana*

In addition to locking the arms on resonance, in order to obtain exquisite sensitivity to distance changes between the arm mirrors, one must also “lock” the relative position of the beam splitter with respect to the arm input mirrors so as to establish a well defined interference condition at the output photodetector. Although one might naively choose the interference to be halfway between fully destructive and fully constructive, in order to maximize the derivative of intensity with respect to relative phase of the light returning from the arms, it pays instead to choose an interference operating point that is at or near fully destructive (a null condition) .

The initial LIGO interferometers chose a null operating point for all but the final science data runs, where a small offset was introduced, as discussed below. The primary advantage of destructive interference is reduction of effective noise. In principle, the disturbance from a gravitational wave produces a non-zero light intensity where there was previously only dark current. One might worry that the increase in intensity would lead to a phase ambiguity, but the PDH signals used to control the interferometer arms provided a neat solution. By introducing a deliberate asymmetry (355 mm for LIGO) in the distance between the beam splitter and the arm input mirrors, one obtains non-cancelling PDH sidebands at the photodetector that stand ready to beat with any non-cancelling carrier light induced by a passing gravitational wave, where the phase of the beat signal reveals the phase of the gravitational wave.

In the optical configuration described so far there are three longitudinal degrees of freedom that must be controlled: the distances between the pairs of mirrors forming the Fabry-Perot arms and the difference in distance between the beam splitter and the two input mirrors. Now we add one more primary mirror to control, namely the recycling mirror located between the laser and the beam splitter. By ensuring that the average optical path length between the recycling mirror and the arm input mirrors is a half integer of laser wavelengths, one achieves resonance of the light in what is called the recycling cavity. Hence the light returning toward the laser that would have otherwise been discarded by the Faraday isolation optics (to prevent interference with the laser itself), is recycled back into the main interferometer. This recycling effectively increases the laser power in the entire interferometer and thereby decreases shot noise due to limited photon statistics. The addition of this mirror increases the number of primary longitudinal servo-controlled degrees of freedom to four.

As one might expect, simultaneously controlling these four degrees of freedom is a technical challenge for free-swinging pendulum mirrors subject to environmental disturbances. The challenge is increased by several factors: the small time window in each swing during which the PDH error signal is effective (having high gain), the power transients associated with individual arm locks, and the overall change in sign of the differential arm signal as both arms resonate, requiring the servo feedback to reverse sign in tens of milliseconds. A technique based on allowing the servo to “coast” through that delicate transition period provides a robust solution, albeit one that still relies upon stochastic swinging of mirrors to bring the degrees of freedom under simultaneous control.

In addition to controlling the longitudinal degrees of freedom, one must also address alignment of the mirrors, and to a lesser degree, transverse displacement. Wobbling of the mirrors modulates interferometer gain, leading to non-linear noise. Hence each angular degree of freedom is also servo controlled. There are two distinct stages of angular control. The first, which works well for initial control authority, is based on shining an auxiliary laser on each mirror at a non-normal angle and observing the transverse displacement of the reflected beam. This “optical lever” method is straightforward and does not require the longitudinal degrees of freedom to be locked, but it comes with the risk of introducing extra noise due to the auxiliary laser and due to any ground motion of the external photodiode. The second angular control method is known as “wave front sensing” and uses the PDH sidebands to sense the misalignment of optical cavity degrees of freedom. This second method can only be used when the longitudinal degrees of freedom are locked, at which point it “takes over” from the optical lever (at least at lower frequencies) after fully recycled lock is achieved. Because the method is based on spatial asymmetries in carrier-sideband phase differences caused by cavity misalignment, one can obtain a DC alignment signal without relying on the external reference points that introduce additional positional noise.

There are also degrees of freedom to control for the input laser light before it impinges on the power recycling mirror. The laser itself, of course, has servo-controlled mirrors defining the lasing cavities. In addition, a triangular “mode cleaner” cavity between it and the recycling cavity provides a means to transmit only a Gaussian wavefront to the main interferometer. The intrinsic frequency stability of the laser is increased by locking the laser to the interferometer arms. It should be noted that tidal effects from the Moon and Sun lead to compression and stretching of LIGO’s arms at the level of hundreds of microns, well outside the dynamic range of the low-noise direct actuation on the mirrors (based on sending currents through voice coils surrounding cylindrical magnets bonded to the faces of the mirrors near their edges). To cope with this predictable and very slowly changing disturbance, a feed-forward actuation is applied via piezoelectric transducers to the positions of the vacuum chambers supporting the mirrors and to the frequency of the laser via a temperature controlled reference cavity with respect to which the laser frequency is offset ( $\sim 10$  pm), via an acousto-optic modulator.

The interferometric noise sources are discussed in detail in the later sections. Summarizing the sources of noise Figure 26 shows an example of a LIGO noise budget graph for the Hanford 4-km (H1) interferometer. At low frequencies ( $<\sim 45$  Hz), the noise is dominated by seismic ground motion, despite the strong isolation provided by the multiple stages of passive oscillators. At high frequencies ( $>\sim 100$  Hz), sensing shot noise dominates. At intermediate frequencies important known contributions come from noise coupled to two auxiliary servoed degrees of freedom, which can be thought of as the positions of the beam splitter and recycling

mirrors; from thermal noise in the suspension wires; from noise coupled to mirror alignment fluctuations (due to residual beam non-centering); and from current noise in the actuation electronics, which must support demanding dynamic range requirements . Less important noise contributions come from thermal noise in the mirrors; from dark-current noise in the photodiodes; from laser frequency noise; from laser amplitude noise; and from phase noise in the RF oscillator used for PDH locking and for the heterodyne readout. Some of the noise curves shown in the budget are based on models, while others can be determined from measured transfer functions.

At the minimum of the noise curve one expects (by design) the most important noise source to be from the thermal noise of the suspension wires, where there is  $k_B T$  of vibrational energy over the entire band. One strives for high mechanical Q's for the wires so that the bulk of the energy is contained in a narrow band around the wire resonant frequencies ("violin modes" –  $\sim 350$  Hz and harmonics). A priori predictions of suspension thermal noise are challenging, depending on detailed modelling of the dissipative losses in the wire and in the contact points with the mirrors and supports.

There are also electromagnetic environmental effects from ambient power mains magnetic fields, despite the careful anti-alignments of magnets used in actuation, as suggested from the 60-Hz harmonics seen in figure 26 .

In addition to these mostly well understood noise sources, there were suspected additional technical sources of noise to account for the difference between measured and expected sensitivity seen in figure 10. In particular, it is likely that the gap in agreement between  $\sim 40$ -120 Hz was mainly due to non-linear upconversion of low-frequency noise. Upconversion can arise, for example, from mirror wobble, modulated beam apertures, and modulated beam backscattering . Scattering from surfaces attached rigidly to the ground is strongly suppressed by elaborate serrated-edge baffling along the length of beam pipe and in other strategic locations, but even tiny scattering contributions can be deleterious when the surface is moving relative to the mirrors .

More important, however, it is now believed that a substantial contribution to initial LIGO detector upconversion was Barkhausen noise from interactions between magnetic material used in the mirror actuation system and the voice actuation coils. The stochastic flipping of magnet domains creates a fluctuating force contribution. Another likely contributor at times was electrostatic charging of mirrors, which can lead to fluctuating forces on the mirrors as charges move to reduce local charge density .

Other sources of noise come from imperfection in the optical configurations, including small asymmetries between the effective reflectivities and losses in the interferometer arms and higher-order Gaussian modes (carrier and sideband). A particularly troublesome noise source was instability of the recycling cavity with respect to sidebands. The recycling cavity was nearly flat-flat, leading to intrinsic instability ("walk off") of the beam. Since the sidebands resonated in the cavity, but not in the arms, their strengths were especially susceptible to misalignment and wobble of the input mirrors, recycling mirror and beam splitter.

It should be noted that passive isolation did not suffice to enable 24-hour operations at LIGO Livingston Observatory in Louisiana. The observatory is surrounded by a pine forest used by loggers. The sawing and removal of trees generated excess seismic noise in the few-Hz band,

which the passive mass-and-spring stacks did little to mitigate and, in some cases, amplified. To cope with this nearly constant weekday environmental disturbance, an active feed-forward system based on hydraulic actuation exerted on vacuum chambers, driven by signals from seismometers, geophones and accelerometers was installed and commissioned, using technology originally developed as part of Advanced LIGO research and development.

Another technical issue arose from higher-than-expected thermal absorption in the input mirrors of each arm, causing thermal lensing and degrading the matching of beam shapes into the arm Fabry-Perot cavities . To cope with this degradation, a thermal compensation system was developed, based on shining a CO<sub>2</sub> laser on the input mirrors so as to compensate the thermal lensing (to lowest order) . Commissioning of the LIGO interferometers required several years, as the sensitivities of the instruments approached their designs. The official design requirement was to reach a band-limited RMS strain in a 100-Hz band as low as 10<sup>-21</sup>. In addition, a more optimistic aspirational target curve was produced. Figure 27 shows typical sensitivities of the three interferometers in the S5 data run (November 2005 - September 2007), along with the target curve. As seen, the final S5 sensitivities of the two 4-km interferometers did indeed reach the target curve over a broad band and easily achieved the design band-limited strain in the best (non-contiguous because of 60-Hz harmonics) 100-Hz band. These measured sensitivities depend in part on a model of the interferometer response to gravitational waves , but primarily upon stimulus-response calibration. Three distinct methods have been used for calibrating LIGO interferometers

- 1) calibration of voice coil actuators via fringe counting in a simpler, unlocked Michelson interferometer configuration .
- 2) frequency modulation of the laser in a 1-arm configuration in which frequency modulation is mapped to length modulation of the cavities .
- 3) calibration from photon radiation pressure using an auxiliary laser in the full interferometer.

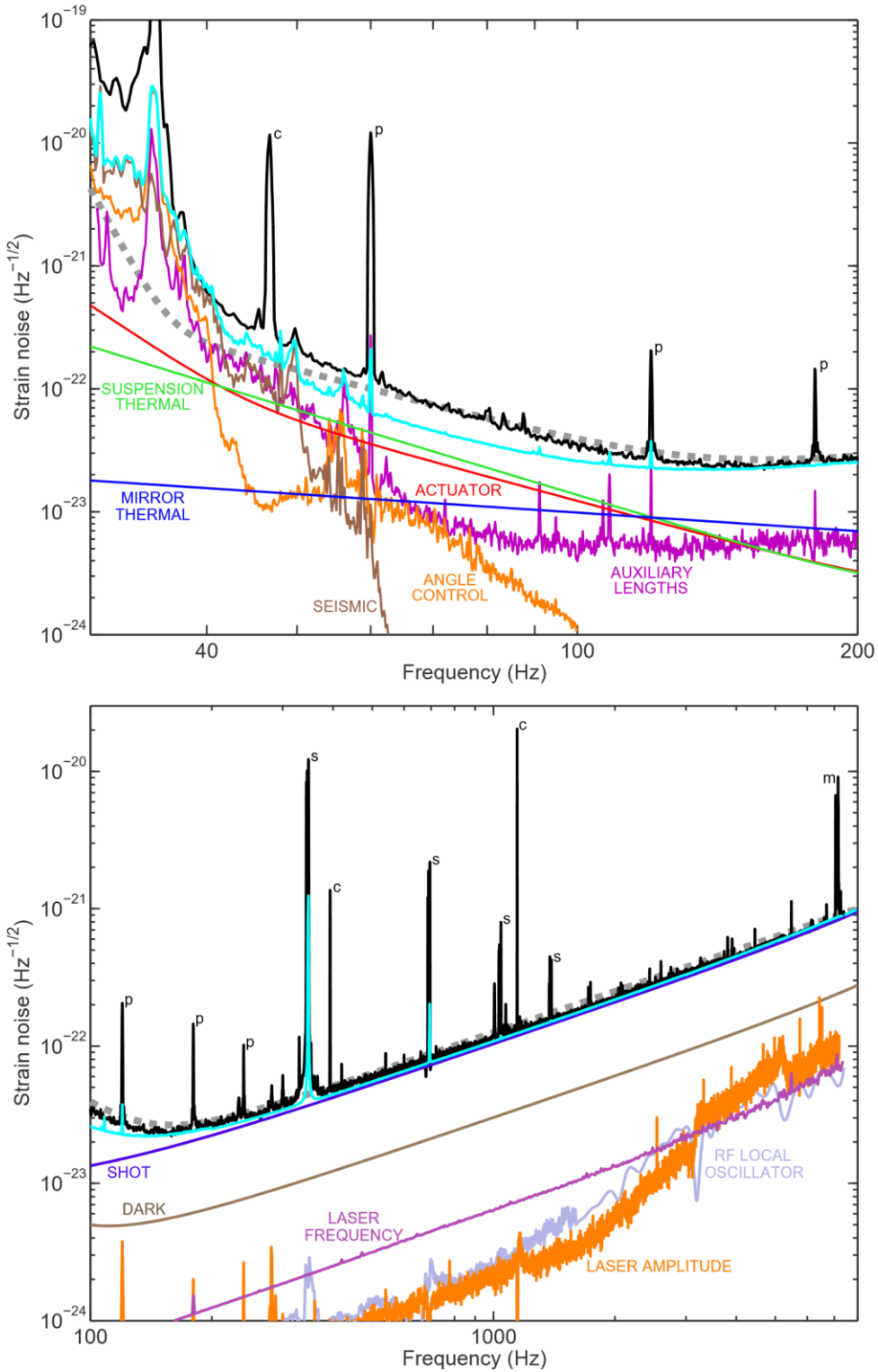
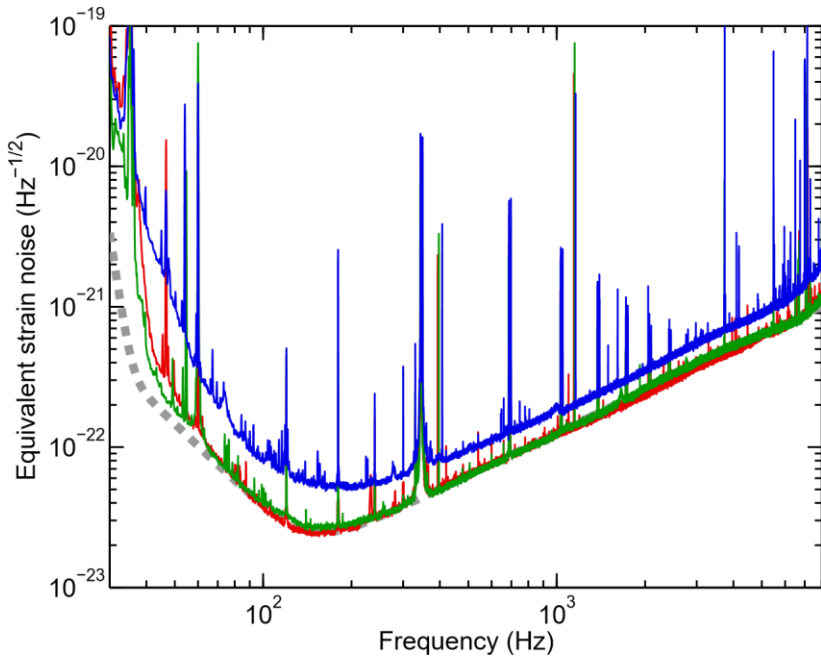


Fig 26 : Primary known contributors to the H1 detector noise spectrum . The upper panel shows the displacement noise components, while the lower panel shows sensing noises (note the different frequency scales). In both panels, the black curve is the measured strain noise , the dashed grey curve is the design goal, and the cyan curve is the root-square-sum of all known contributors (both sensing and displacement noises). . The known noise sources explain the observed noise very well at frequencies above 150 Hz, and to within a factor of 2 in the 40–100 Hz band. Spectral peaks are identified as follows: *c*, calibration line; *p*, power line harmonic; *s*, suspension wire vibrational mode; *m*, mirror (test mass) vibrational mode.



*Fig 27 : Strain sensitivities (amplitude spectral densities) of the LIGO interferometers during the S5 data run . and Virgo interferometer . Shown are typical high sensitivity spectra for each of the three interferometers (red: H1; blue: H2; green: L1), along with the design goal for the 4-km detectors (dashed grey).*

### 9.3.3) ENHANCED LIGO

Following the S5 run, the LIGO interferometers underwent an “enhancement” to improve strain sensitivity by a factor of two in the shot-noise regime. This upgrade was based on increasing laser power from 6 W to more than 20 W, but a simple increase in power would have led to unacceptably high noise from higher-order-modes light impinging on the photodetector. To avoid this problem, an “output mode cleaner” (4-mirror bow-tie configuration) was installed between the beam splitter and the photodetector, to ensure that higher-order modes (carrier and sidebands) were filtered out, leaving only a clean Gaussian measure of interferometer light . This cleaning method also filters out the PDH sideband light, preventing those sidebands from being used in the fully null experiment described above.

Instead, a small, deliberate offset ( $\sim 10$  pm) was introduced into the differential arm servo so that a gravitational wave disturbance would lead to a change in intensity of photodetector light (“DC Readout” ) . Although this technique would seem to lead to the worry of intensity fluctuations in the laser mimicking a gravitational wave, aggressive gain in the laser intensity stabilization servo allowed operation in this mode . The Enhanced LIGO upgrades were applied to the Hanford and Livingston 4-km interferometers (H1 and L1) from fall 2007 to summer 2009, with commencement of the sixth science run (S6) in July 2009 and completion in October 2010. By the end of the S6 run, the sensitivities of the interferometers had increased approximately by a factor of two in instantaneous sensitivity above  $\sim 300$  Hz, as expected, given the higher laser power. It had been hoped that noise at lower frequencies would also be reduced after replacement of the primary actuation magnets, using material with smaller

Barkhausen noise (NdFeB replaced with SmCo), but upconversion noise remained, and it was later hypothesized (but not conclusively established) that

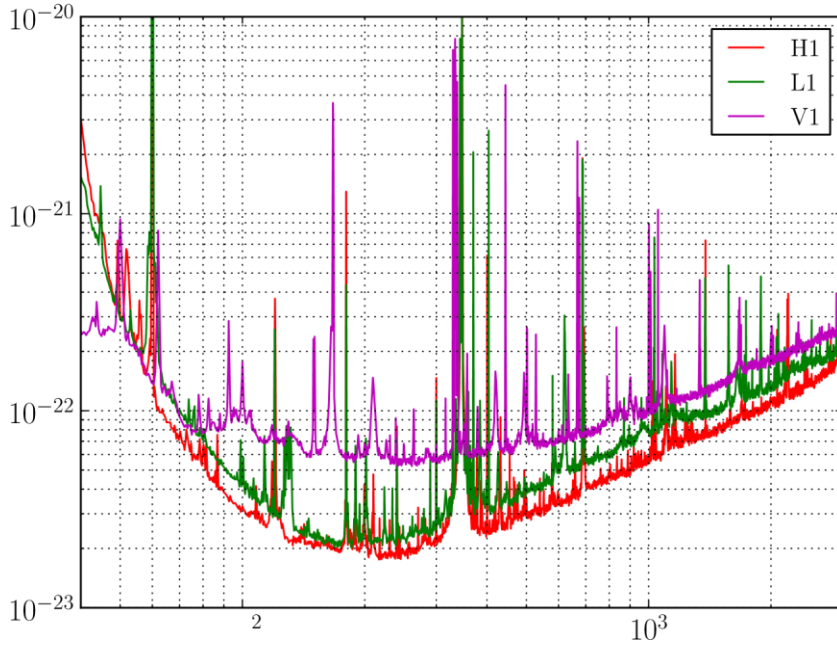


*Fig 28 : Typical detector strain amplitude spectral densities for the LIGO S6 and Virgo VSR2/3 runs. From lowest to highest at  $10^2$  Hz, the curves are for the LIGO interferometers (H1 and L1) and Virgo interferometer*

#### 9.3.4) VIRGO DETECTORS

The Virgo interferometer has a quite similar design to that of LIGO and comparable performance. The primary differences are in the arm lengths (3 km vs. 4 km), laser power (17 W vs 10 W) and in the seismic isolation. While not as sensitive as LIGO in the most sensitive band near 150 Hz, Virgo is substantially more sensitive at frequencies below 40 Hz because of aggressive seismic isolation. Virgo's mirrors are suspended as 5-stage pendula supported by a 3-legged inverted pendulum, a system known as the superattenuator. This extreme seismic isolation permitted Virgo to probe gravitational waves down to  $\sim$ 10-20 Hz, in contrast to LIGO's  $\sim$ 40-50 Hz. This lower reach offers the potential to detect low-frequency spinning neutron stars like Vela that are inaccessible to LIGO. Figure 29 shows the sensitivity achieved by the Virgo interferometer during the VSR2/3 runs.

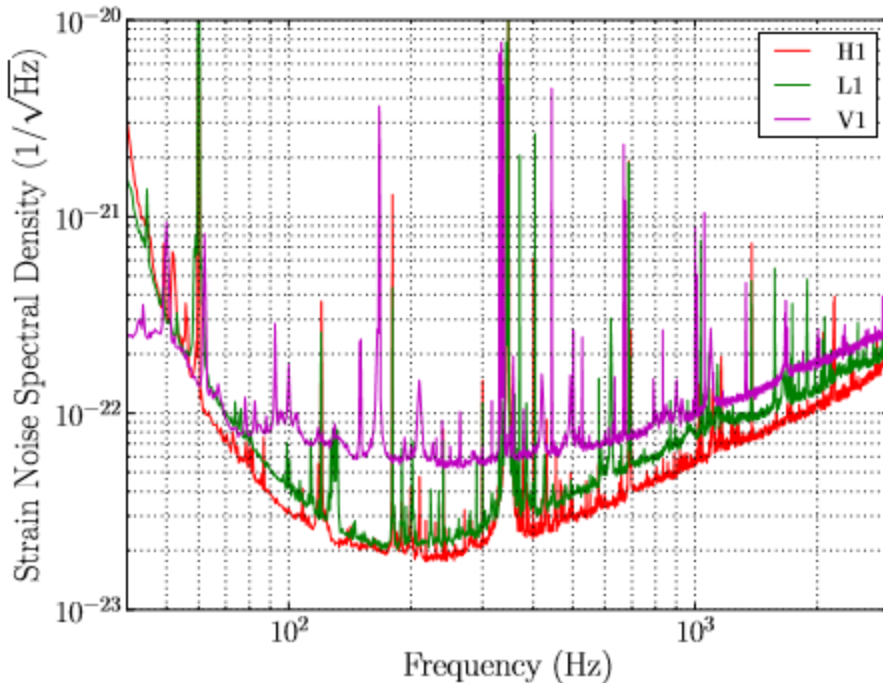


*Fig 29 : Typical detector strain amplitude spectral densities for the LIGO S6 and Virgo VSR2/3 runs. From lowest to highest at 102 Hz, the curves are for the LIGO interferometers (H1 and L1) and Virgo interferometer .*

### 9.3.5) GEO 600 INTERFEROMETER

The GEO 600 interferometer has served not only as an observatory keeping watch on the nearby galaxy when the LIGO and Virgo interferometers have been down (and serving as a potential confirmation instrument in the event of a very loud event candidate), it has also served as a testbed for Advanced LIGO technology. With 600-meter, folded (non-Fabry-Perot) arms and a 12-W input laser and built on a relatively small budget, GEO 600 cannot match the sensitivity of the LIGO or Virgo interferometers, but it has pioneered several innovations to be used in Advanced LIGO: multiple-pendulum suspensions, signal recycling, rod-laser amplification, and squeezing. As of 2012, GEO 600 is operating at high duty factor in “AstroWatch” mode, primarily in case of a nearby galactic supernova, as the LIGO and Virgo detectors underwent major upgrades .

### 9.3.6) TAMA INTERFEROMETER

The 300-meter TAMA interferometer in Japan was similar to the LIGO detectors (power recycled Michelson interferometer), but with much shorter arms and comparable laser power, its sensitivity was limited. Nonetheless, it operated at comparable sensitivity to LIGO in LIGO’s early runs, and joint data analysis was carried out on S2 data . The Japanese collaboration that built TAMA built the 2nd-generation KAGRA detector .

## 9.4) SECOND GENERATION INTERFEROMETERS

The first generation LIGO and Virgo detectors went through major upgrades and became Advanced LIGO AND Advanced Virgo . These upgrades improved their broadband strain sensitivities by an order of magnitude, thereby increasing their effective ranges by the same amount. Since the volume of accessible space grows as the cube of the range, one can expect the advanced detectors to probe roughly 1000 times more volume and therefore have expected transient event rates O(1000) times higher than for the 1st-generation detectors.

The key improvements in Advanced LIGO are:

- 1) Increased laser power ( $\sim 10 \text{ W} \rightarrow \sim 180 \text{ W}$ ) with rod-laser amplification developed by GEO collaborators , to improve shot noise at high frequencies .
- 2) Quadruple-pendulum suspensions (also pioneered by GEO) to lower the seismic wall to just above  $\sim 10 \text{ Hz}$  .
- 3) High-mechanical-Q silica-fiber suspension to reduce suspension thermal noise .
- 4) More massive, higher-mechanical-Q test-mass mirrors to reduce thermal noise from the mirrors and mitigate the increased radiation pressure noise from the higher laser power .
- 5) Active, feed-forward in-vacuum active isolation of optical tables, using accelerometer, seismometer and geophone sensing (supplemental to hydraulic pre-isolation discussed above which was used already for the Livingston interferometer)
- 6) The addition of a signal recycling mirror between the beam splitter and photodetector . The addition of a signal-recycling mirror with its adjustable relative position with respect to the beam splitter will give Advanced LIGO some flexibility in its frequency-dependent sensitivity. Figure 30 shows example design curves for different laser powers and optical configurations.

The baseline design for Advanced Virgo detectors is higher laser power and improved thermal noise in suspensions and test masses. Note that the aggressive passive isolation used already in Virgo means that no major changes are expected in order to match the current, already-impressive low-frequency seismic wall of 10-20 Hz. Ultimate Advanced Virgo sensitivity is expected to be comparable to that of Advanced LIGO .

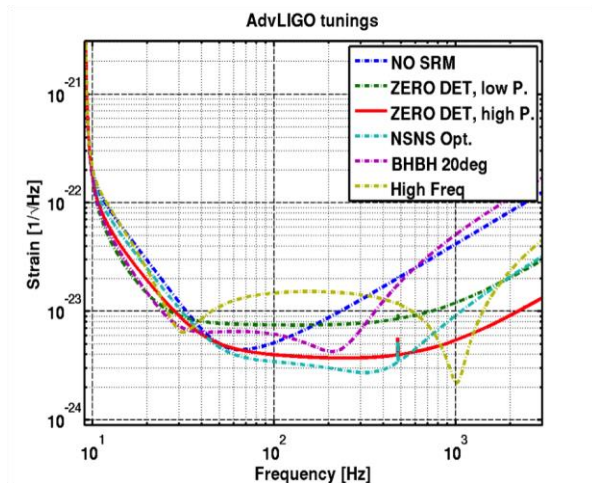


*Fig 30 : Projected Advanced LIGO strain amplitude spectral noise densities for several different possible configurations . The curve labelled “ZERO DET, high P’ corresponds to the nominal Advanced LIGO high-power broadband operation. Sensitivity curves are also shown for a lower power and for sample interferometer tunings that favor certain frequency bands.*

## 9) ADVANCED LIGO

The possibility of using interferometers as gravitational wave detectors was first considered in the early 1960s . In the 1970s and 1980s, long-baseline broadband laser interferometric detectors were proposed with the potential for an astrophysically interesting sensitivity . Over several decades, this vision evolved into a world-wide network of ground based interferometers. These instruments target gravitational waves produced by compact binary coalescences, supernovae, non-axisymmetric pulsars, cosmological background as well as any unknown astrophysical sources in the audio frequency band, from 10Hz to 10kHz .

The first generation of LIGO detectors consisted of two 4-km-long and one 2-km-long interferometers in the United States L1 in Livingston, Louisiana, H1 and H2 in Hanford, Washington. They were operational until 2010 and reached their designed strain sensitivity over the detection band, with a peak sensitivity of  $2 \times 10^{-2} / \sqrt{\text{Hz}}$  at 200Hz. Astrophysically relevant results were produced by the initial LIGO detectors , however, no gravitational wave signals were detected.

The second generation Advanced LIGO detectors were installed in the existing facilities from 2010 to 2014. This new generation of instruments was designed to be 10 times more sensitive than initial LIGO, and promised to increase the volume of the observable universe by a factor of 1000. Commissioning of the newly-installed detectors took place from mid 2014 to mid 2015. In September 2015, Advanced LIGO began the era of gravitational wave astronomy with its first observation run (O1), collecting data until January 2016. This run has culminated in the first direct detection of gravitational waves from the black hole coalescence, GW150914. This system consisted of two black holes of about 35 solar mass each which merged about 500Mpc away .

While the detectors were not yet operating at design sensitivity during the first observation run, their astrophysical reach was already significantly greater than that of any previous detector in the frequency range 10Hz– 10kHz. Around 100Hz, the strain sensitivity was  $8 \times 10^{-24} / \sqrt{\text{Hz}}$  . For a system consisting of two  $30M_{\odot}$  black holes the sky location and source orientation-averaged range was 1.3Gpc, whereas for a binary neutron star system the range was 70–80Mpc. This range is  $\approx 4.1$  and  $\approx 3.5$  times higher than that of the initial LIGO detectors, resulting in a factor of  $\approx 70$  and  $\approx 40$  improvement, respectively, of the volume that is probed and LIGO’s detection potential .

### 10.1) LAYOUT OF ADVANCED LIGO DETECTOR

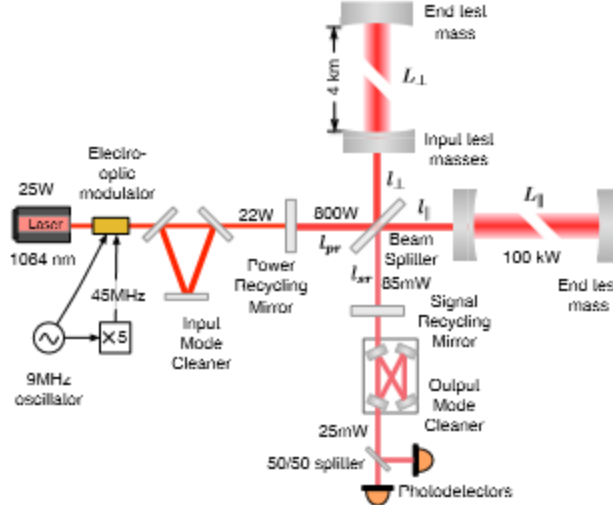


Fig 31 layout of aadvanced LIGO detector

Layout of an Advanced LIGO detector figure 31. The annotations show the optical power in use during O1. These power levels are a factor of  $\approx 8$  smaller compared to the designed power levels. The Nd:YAG laser , with wavelength  $\lambda=1064\text{nm}$ , is capable of producing up to 180W, but only 22W were used. A suspended, triangular Fabry-Perot cavity serves as an input mode cleaner to clean up the spatial profile of the laser beam, suppress input beam jitter, clean polarization, and to help stabilize the laser frequency. The Michelson interferometer is enhanced by two 4km-long resonant arm cavities, which increase the optical power in the arms by a factor of  $G_{\text{arm}} \approx 270$ . Since the Michelson interferometer is operated near a dark fringe, all but a small fraction of the light is directed back towards the laser. The power recycling mirror resonates this light again to increase the power incident on the beamsplitter by a factor of  $\approx 40$ , improving the shot noise sensing limit and filtering laser noises. On the antisymmetric side, the signal recycling mirror is used to broaden the response of the detector beyond the linewidth of the

arm cavities. An output mode cleaner is present at the antisymmetric port, to reject unwanted spatial and frequency components of the light, before the signal is detected by the main photodetectors.

## 10.2) INTERFEROMETER CONFIGURATION

In general relativity, a gravitational wave far away from the source can be approximated as a linear disturbance of the Minkowski metric,  $g_{\mu\nu} = \eta_{\mu\nu} + h_{\mu\nu}$  with the spacetime deformation expressed as a dimensionless strain,  $h_{\mu\nu}$ . In a Michelson interferometer we define the differential displacement as  $L = L_{\parallel} - L_{\perp}$ , where  $L_{\parallel}$  and  $L_{\perp}$  are the lengths of the inline arm and the perpendicular arm, respectively, as shown in Figure 31. With equal macroscopic arm lengths,  $L_0 = L_{\parallel} = L_{\perp}$ , the gravitational wave strain and the differential arm length are related through the simple equation  $L(f) = L_{\parallel} - L_{\perp} = h(f)L_0$ , where  $h$  is the average differential strain induced into both arms at frequency  $f$ .

The test masses are four suspended mirrors that form Fabry-Perot arm cavities. These mirrors can be considered as inertial masses above the pendulum resonance frequency ( $\sim 1\text{Hz}$ ). Any noise present in the differential arm channel is indistinguishable from a gravitational wave signal. Residual seismic noise, thermal noise associated with the vertical suspension resonance, and the gravity-gradient background limits the useful frequency range to above 10Hz. Motion of the four test masses form the two most relevant degrees of freedom differential and common arm lengths. While gravitational waves couple to the differential arm length, the common arm length is highly sensitive to changes in the laser frequency according to the equation

$$L_+(f) = \frac{L_{||} + L_{\perp}}{2} = L_0 \frac{V(f)}{\nu},$$

where  $\nu = 2.82 \times 10^{14}\text{ Hz}$  is the laser carrier frequency,  $V(f)$  is the laser frequency noise. Signal  $L_+$  is used for frequency stabilization of the main laser .

The central part of the interferometer is usually called the dual-recycled Michelson interferometer. Its function is to optimize the detector's response to gravitational waves. The power recycling cavity, formed by the power recycling mirror and the two input test masses, increases optical power incident on the arm cavities and passively filters laser noises . The signal recycling cavity, formed by the signal recycling mirror and the two input test masses, is used to broaden the response of the detector beyond the linewidth of the arm cavities. The Michelson interferometer, formed by the beam splitter and the two input test masses, is controlled to keep the antisymmetric port near the dark fringe. The dual recycled Michelson interferometer can thus be described by three degrees of freedom: power recycling cavity length  $l_{p,+}$ , signal recycling cavity length  $l_{s,+}$  and Michelson length  $l_-$ , defined as

$$\begin{aligned} l_{p,+} &= l_{pr} + \frac{l_{||} + l_{\perp}}{2} \\ l_{s,+} &= l_{sr} + \frac{l_{||} + l_{\perp}}{2} \\ l_- &= l_{||} - l_{\perp}, \end{aligned}$$

where distances  $l_{pr}, l_{sr}, l_{||}$  and  $l_{\perp}$  are defined in Figure 31.

The most important optical parameters of the Advanced LIGO interferometers are summarized in Table 3. The beam size here is defined as the distance from the beam center to the point when intensity is reduced by a factor  $1/e^2$ . The cavity pole  $f_p$  determines the width of the cavity resonance and is given by

$$f_p = \frac{Yc}{8\pi L_0}$$

where  $c$  is the speed of light and  $Y \ll 1$  is the total optical loss in the cavity, including transmission of the input and output cavity couplers as well as scattering and absorption losses. The response of the Advanced LIGO interferometers is diminished at high frequencies due to common and differential coupled cavity poles ( $f_+$  and  $f_-$ ) according to the transfer functions

$$K_+ = \frac{f_+}{if + f_+} \quad K_- = \frac{f_-}{if + f_-}$$

Several critical improvements distinguish Advanced LIGO from the initial detectors . The much improved seismic isolation system reduces the impact of ground vibrations. All photodetectors, used in the observing mode, are installed in vacuum to avoid the coupling of ambient acoustic noise to the gravitational wave channel. The larger and heavier test masses lead to a reduction of quantum radiation pressure induced motion and thermal noise . Multi-stage pendulums with a monolithic lower suspension stage filter ground motion and improve suspension thermal noise. Furthermore, instead of using coil-magnet actuation pairs to exert control forces on the test masses, electrostatic interaction is employed. This actuation scheme helps to avoid coupling of magnetic noise to the gravitational wave channel .

Lower arm cavity loss, coupled with an increase in the available power from the Nd:YAG laser, allows up to 800kW of laser power to circulate in the arm cavities— 20 times higher than in initial LIGO – significantly reducing the high frequency quantum noise. The use of optically stable folded recycling cavities allows for better confinement of the spatial eigenmodes of the optical cavities . The signal recycling cavity , which was not present in initial LIGO, was introduced at the antisymmetric port to broaden the frequency response of the detector and improve its sensitivity at frequencies below 80Hz and above 200Hz.

Because O1 was the first observing run, and work remains to be done on the detectors to bring them to their design sensitivity, not all of the interferometer parameters were at their design values during O1. Most notably, the laser power resonating in the arm cavities was 100kW instead of the planned 800kW. More power in the arm cavities improves the shot noise level . Circulating optical power will be increased in future observational runs. Additionally, the signal recycling mirror transmissivity was 36%, in contrast to the design value of 20%. This higher transmissivity of the signal recycling mirror improves the quantum noise in the frequency range from 60Hz to 600Hz at the price of reducing the sensitivity at other frequencies. Finally, the best measured Advanced LIGO sensitivity in the frequency range 20–100Hz , is limited by a wide range of understood technical noise sources as well as currently unknown noise sources.

Figure 32 shows the Advanced LIGO detector’s sensitivity during the first observing run. The performance of both the L1 and H1 detectors is compared to the initial LIGO sensitivity and the design sensitivity: the improvement with respect to S6 was 3–4 times at 100Hz and higher frequencies. Below 100Hz, the upgraded seismic isolation system yielded even larger improvements, with more than an order-of-magnitude-better strain sensitivity for frequencies below 60Hz. The sensitivity of Advanced LIGO can also be quantified as maximum distance at which a given astrophysical source would be detectable, known as “horizon distance”. Figure 33 shows the horizon distance as a function of the chirp mass for coalescence of neutron star ( $\mathcal{M} \lesssim 2M_{\odot}$ ) and black hole ( $\mathcal{M} \gtrsim 2M_{\odot}$ ) . binaries. For chirp masses  $\lesssim 100M_{\odot}$  horizon distance increases with chirp mass since gravitational wave signal is stronger from heavier binary systems. However, the signal also shifts towards lower frequencies (and out of LIGO frequency band) for massive binary systems, and horizon distance decreases for chirp masses  $\gtrsim 100M_{\odot}$ .

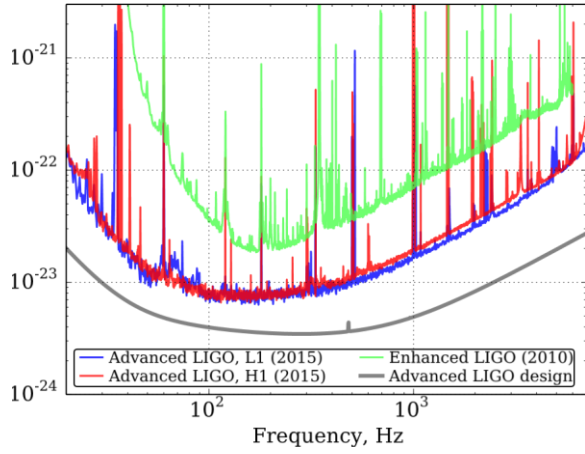


*Fig 32 : The strain sensitivity for the LIGO Livingston detector (L1) and the LIGO Hanford detector (H1) during O1. Also shown is the noise level for the Advanced LIGO design (gray curve) and the sensitivity during the final data collection run (S6) of the initial detectors.*

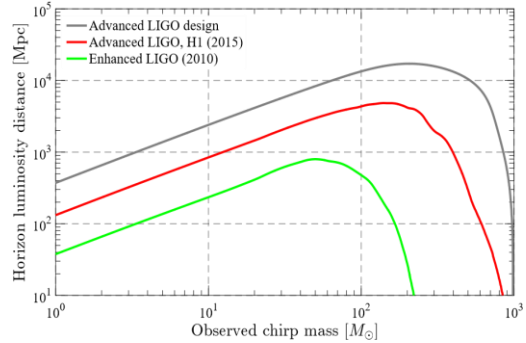


*Fig 33 : The sensitivity to coalescing compact binaries for the Advanced LIGO design, first observation run (O1) and the final run with the initial detectors (S6). The traces show the horizon distance, which is the distance along the most sensitive direction of the interferometer for a binary inspiral system that is seen head-on and for a signal-to-noise ratio of 8. The horizontal axis is the chirp mass which is defined as  $M = (1 + z)\mu^{3/5} M^{2/5}$ , where  $M = M_1 + M_2$  is the total mass,  $\mu = M_1 M_2 / M$  is the reduced mass, and  $z$  is the cosmological redshift. Units are in solar masses,  $M$ . The horizon distance is computed for the case of equal masses  $M_1 = M_2$  and using the inspiral–merger model from*

Table 3 : list of optical paramters

Parameter	Value	Unit
Laser wavelength	1064	nm
Arm cavity length, $L_0$	3994.5	m
Power recycling cavity length, $l_{p,+}$	57.66	m
Signal recycling cavity length, $l_{s,+}$	56.01	m
Michelson asymmetry, $l_-$	8	cm
Input mode cleaner length (round trip)	32.95	m
Output mode cleaner length (round trip)	1.13	m
Input mode cleaner finesse	500	
Output mode cleaner finesse	390	
Round trip loss in arm cavity, $Y_{\text{arm}}$	85-100	ppm
Arm cavity build-up, $G_{\text{arm}}$	270	
Power recycling gain, $G_{\text{prc}}$	38	
Signal recycling attenuation, $1/G_{\text{src}}$	0.11	
Common coupled cavity build-up, $G_+$	5000	
Differential coupled cavity build-up, $G_-$	31.4	
Common coupled cavity pole, $f_+$	0.6	Hz
Differential coupled cavity pole, $f_-$	335-390	Hz
RF modulation index	0.13-0.26	rad
Test mass diameter	34	cm
Test mass thickness	20	cm
Beam size at end test mass	6.2	cm
Beam size at input test mass	5.3	cm

### 10.2.1) INTERFEROMETER CONTROLS

In operation the laser light needs to resonate inside the optical cavities. This requires that the residual longitudinal motion of the optical cavities be kept within a small fraction of the laser wavelength. The suspended mirrors naturally move by  $\sim 1\mu\text{m}$  at the micro seismic frequencies around 100mHz—much larger than the width of a resonance. To suppress this motion, a sophisticated length sensing and control system is employed, using both the well-known Pound-Drever-Hall technique and a version of homodyne detection known as “DC readout”. Table 4 shows linewidths and requirements for residual root-mean-square (RMS) motion of the main interferometric degrees of freedom.

An electro-optic modulator generates radio frequency (RF) phase modulation sidebands at 9MHz and 45MHz,

Degree of freedom	Linewidth	Residual
Common arm length	6 pm	1 fm
Differential arm length	300 pm	10 fm
Power recycling cavity length	1 nm	1 pm
Michelson length	8 nm	3 pm
Signal recycling cavity length	30 nm	10 pm

*Table 4 : The linewidths of Pound-Drever-Hall signals and the requirements for residual RMS motion for the main interferometric degrees of freedom.*

symmetrically spaced about the laser carrier frequency. The Pound-Drever-Hall technique is used to sense all longitudinal degrees of freedom except for the differential arm channel. Feedback control signals actuate on the suspended mirrors, using either coil-magnet or electrostatic actuation. The common arm cavity length is also used as a reference to stabilize the laser frequency, with sub-mHz residual fluctuations (in detection band).

The gravitational wave signal is extracted at the antisymmetric port of the interferometer, where fluctuations in the differential arm cavity length are sensed. The arm cavities are held slightly off-resonance by an amount referred to as the differential arm offset  $\Delta L$ . This offset of roughly 10pm generates the local oscillator field, which is necessary for the DC readout. An output mode cleaner located between the antisymmetric output and the homodyne readout detectors, is used to filter out the RF sidebands as well as any higher-order optical modes, as these components do not carry information about the differential arm cavity length.

A similar feedback control scheme is employed to keep the optical axes aligned relative to each other and the laser beam centred on the mirrors . This system is required to maximize the optical power in the resonant cavities and keep it stable during data collection. A set of optical wavefront sensors is used to sense internal misalignments . At the same time, DC quadrant photodetectors sense beam positions relative to a global reference frame. The test mass angular motions are stabilized to 3nrad rms, keeping power fluctuations in the arm cavities smaller than 1% on the time scale of a few hours.

### 10.2.2) STRAIN CALIBRATION

For the astrophysical analyses, the homodyne readout of the differential arm cavity length needs to be calibrated into dimensionless units of strain . This is complicated by the fact that the feedback servo for this degree-of-freedom has a bandwidth of about 100Hz, extending well into the band of interest. Denoting the control signal sent to the end test masses with  $s$ , and the error signal, as measured by the photodiodes in units of W, with  $e$ , the strain signal  $h$  is

$$h = As + C^{-1}e,$$

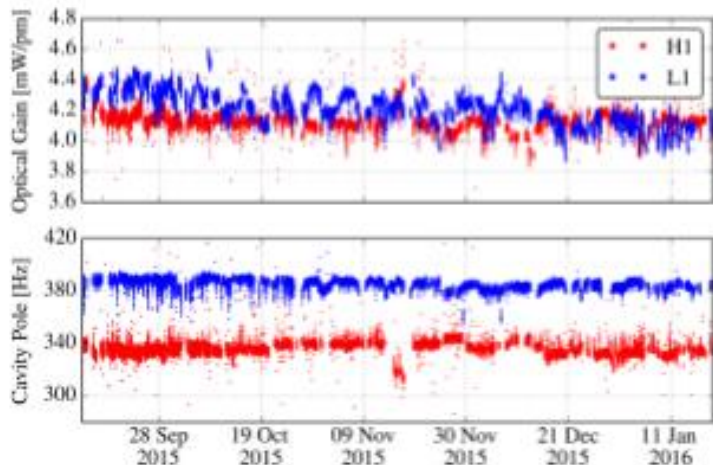
where  $A$  is the calibration of the actuator strength into strain and is computed using dynamical models. Transfer function  $C$  is the optical response from strain to the error signal and is given by

$$C(f) = \frac{4\pi G_{\text{arm}} L_0}{\lambda} \left( \frac{G_{\text{prc}} P_{\text{in}} P_{\text{LO}}}{G_{\text{src}}} \right)^{1/2} K_{-}(f)$$

where  $P_{\text{in}}$  is the interferometer input power and  $P_{\text{LO}}$  is power of the local oscillator coming out from the interferometer. Signal recycling cavity gain  $G_{\text{src}}=9.2$  is in the denominator since differential arm signal is anti resonant in this cavity. Ideally, the actuator transfer function  $A$  is stable over time. In practice, a time-varying charge accumulates on the test masses, changing the actuation strength and introducing noise into the gravitational wave channel . The optical transfer function  $C$  is also nonstationary, being modulated mainly by angular motion of the test masses.

The optical response  $C$  is tracked using a system known as the “photon calibrator”, which consists of an auxiliary Nd: YLF laser (operating at a wavelength of 1047 nm), an acousto-optic modulator, and a set of integrating spheres . This calibration system actuates on the end test masses, applying set of sinusoidal excitations via radiation pressure, to track variations of the optical gain and of the differential coupled cavity pole frequency. Three weeks of such data are shown in Figure 34, showing that the optical response of the detectors is stable over time .

*Fig 34: Time-varying response of the Advanced LIGO detectors. The top panel shows the optical gain variations over a time span of one month, whereas the bottom panel shows the variations of the differential coupled cavity pole frequency over the same time span. The blue traces are for the LIGO Livingston Observatory (L1) and the red traces for the LIGO Hanford Observatory (H1).*



The absolute accuracy of the photon calibrator is limited by the uncertainties in its photodetector calibration, as well as any optical losses between the test mass and the photodetector. Overall, the uncertainty in the calibration of the interferometer over the entire operational frequency range from 10Hz–5kHz is estimated to be smaller than 10% and 10 degrees .

### 10.3) DESIGN OF INTERFROMETER :

#### 10.3.1) Arm cavity design

With signal recycling, the quantum noise-limited strain sensitivity is in principle independent of the arm cavity finesse, and depends only on the power stored in the arms; thus the choice of finesse is guided by other practical considerations. Higher arm cavity finesse carries the benefits of lower laser power in the power recycling cavity and reduced coupling from the vertex Michelson degree-of-freedom. Lower finesse reduces the sensitivity to optical loss and noise in the signal recycling cavity. The arm cavity finesse of 450 represents a trade-off between these effects .

In order to reduce test mass thermal noise, the beam size on the test masses is made as large as practical so that it averages over more of the mirror surface. The dominant noise mechanism here is mechanical loss in the dielectric mirror coatings, for which the displacement thermal noise scales inversely with beam size. This thermal noise reduction is balanced against increased aperture loss and decreased mode stability with larger beams. The slightly asymmetric design of the arm cavity takes advantage of the fact that the ITMs contribute less to thermal noise because their coatings are half as thick as on the ETMs. Therefore the beam can be somewhat smaller on the ITMs—with negligible increase in thermal noise—in order to limit aperture losses in the beam splitter and recycling cavities; the ETM beam size is maximized to reduce this thermal noise contribution. The resonator  $g$  parameter product for the arm cavity is  $g_1 g_2 = 0.83$ , which is approaching the stability limit of  $g_1 g_2 \rightarrow 1$ . Lower thermal noise thus comes at the expense of greater sensitivity to angular misalignment .

The specified mirror beam sizes can be achieved with either of two designs: a nearly-planar cavity or a nearly-concentric one. The nearly-concentric design is preferred for its higher stability with high stored power operation when torques due to optical radiation pressure become significant. In this case, the torsional mode with the higher optical stiffness is statically stable, whereas it would be statically unstable for a near-planar design .

#### 10.3.2) Recycling cavity design

Both the power recycling and signal recycling cavities are designed to be stable for the fundamental Gaussian modes they support. That is, the fundamental cavity mode accrues a non-negligible Gouy phase in a one-way propagation through the cavity. The benefit of this design (new in Advanced LIGO) is that both recycling cavities have well defined spatial eigenmodes and transversal mode-spacings much greater than the linewidth of the cavities .

The modes become less sensitive to mirror imperfections, resulting in more efficient signal detection. The stable design results in the folded layout shown in figure 31 for these cavities. Each of the six recycling cavity mirrors is a curved optic; they produce a one-way Gouy phase of 25 and 19 degrees in the power and signal recycling cavities, respectively, and transform the beam radius from 5.3 cm at the ITMs to 2.2 mm at the PRM, and 2.1 mm at the SRM.

### 10.3.3) Gravitational wave readout

Readout of the gravitational wave signal is accomplished using an output mode cleaner in conjunction with homodyne, or DC detection. In this scheme, a local oscillator field is generated by offsetting the arm cavities slightly from their resonance (typically a few picometers), thereby pulling the Michelson slightly off the dark fringe . The output mode cleaner filters out non-TEM00 mode carrier power, and any power in RF modulation sidebands, so that only the carrier TEM00 mode is detected. This greatly reduces the power that must be detected at the output. Homodyne readout is a significant departure from the heterodyne readout used in Initial LIGO. Compared to heterodyne detection, it is less susceptible to a number of technical noise couplings, but its primary benefits lie in lower quantum noise and compatibility with the future use of squeezed light .

### 10.3.4) High power effects

Several effects may hinder interferometer operation at high power and need to be considered in the design: optical distortion produced by thermal effects from absorbed power; optical torques that can significantly impact alignment stability; and parametric instabilities arising from coupling between test mass acoustic modes and higher-order optical modes of the arm cavities.

As mentioned above, the torque induced by radiation pressure becomes comparable to the mechanical restoring torque of the test mass suspension, and must be accounted for in the angular controls system. It is known that the unstable alignment modes have very low frequency, and can be readily stabilized with a suitable control filter .

The dominant source of thermal distortion is thermal lensing in the ITM substrates due to power absorbed in the ITM reflective coatings. Next in importance, at high power, coating absorption in the ITMs and ETMs causes a non-negligible change their radii of curvature through thermo-elastic distortion. The thermal compensation system is designed to compensate both of these effects. The compensation plates (CP) allow some of the distortion correction to be applied to these elements, which are more noise-tolerant than the ITMs. The use of ultra-low absorption fused silica for the ITMs, the BS, and the CPs ensures that power absorbed in the bulk is negligible compared to that absorbed in the test mass high reflectivity coatings.

Parametric acousto-optic couplings have the potential to lead to unstable build-up of such coupled, higher-order modes . Unchecked, this could impose a limit on the power stored in the arms. Uncertainties in the parameters relevant to the process prevent an exact calculation of the situation. Instead, statistical analyses can indicate the probability of instability at a given power level. The general conclusion of these analyses is that there may be 5-10 modes per test mass that could become unstable at full power. One or more of several mitigation methods may thus

need to be applied. The simplest is to use the thermal compensation actuators to slightly change the radius of curvature of one or more test masses; this would shift the eigen-frequency of the higher-order optical mode to avoid overlap with the corresponding acoustic mode. A second technique would be to actively damp any unstable acoustic modes. Each test mass is equipped with an electro-static actuator that can be used to apply a damping feedback force at the acoustic mode frequencies. A third technique, still in the research phase, is to apply passive tuned dampers to the test masses.

#### 10.4) Analysis of instrumental noise

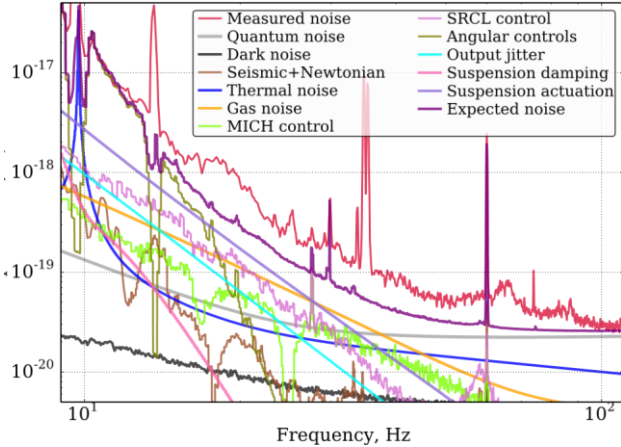
The calibrated gravitational wave signal is compared to the known noises in order to understand what limits the sensitivity of the instrument as a function of frequency. Figure 35 summarizes the noise contributions from various sources to the gravitational wave channel for the Livingston and Hanford detectors. The coupling of each noise source to the gravitational wave channel at a frequency  $f$  is estimated using the following equation:

$$L(f) = L_0 h(f) = T(f) \times N(f),$$

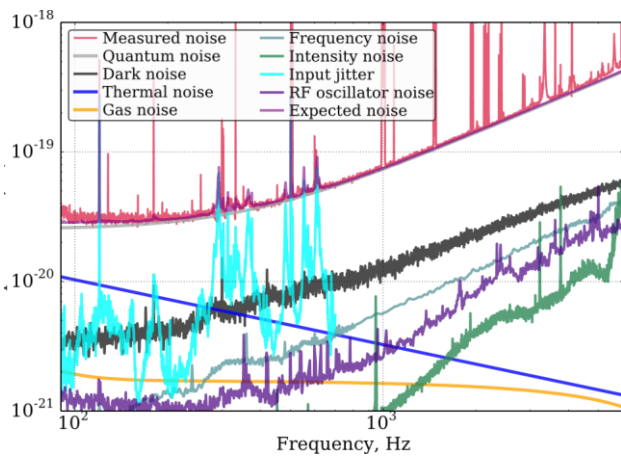
where  $N(f)$  is the noise spectrum measured by an auxiliary (witness) sensor or computed using analytical model, and  $T(f)$  is the measured or simulated transfer function from this sensor to the gravitational wave channel.

Noise sources can be divided into classes according to their origins and coupling mechanisms. One clear way to differentiate noises is to split them into displacement and sensing noises: displacement noises cause real motion of the test masses or their surfaces, while sensing noises limit the ability of the instrument to measure test mass motion. However, this distinction is not perfect, since some noise sources (e.g., laser amplitude noise) can be assigned to both categories. Another way to classify noise sources is to divide them into fundamental, technical and environmental noises. Fundamental noises can be computed from first principles, and they determine the ultimate design sensitivity of the instrument. This class of noises, which includes thermal and quantum noise, cannot be reduced without a major instrument upgrade, such as the installation of a new laser or the fabrication of better optical coatings. Technical noises, on the other hand, arise from electronics, control loops, charging noise and other effects that can be reduced once identified and carefully studied. Environmental noises include seismic motion, acoustic and magnetic noises. The design of Advanced LIGO calls for the contributions of technical and environmental noises to the gravitational wave channel to be small compared to fundamental noises. In practice, the sensitivity can be reduced due to unexpected noise couplings. Many technical and environmental noises have been identified and are discussed in the following sections. At the same time, the dominant noise contributor in the frequency range 20–100Hz has not yet been identified.

The narrowband features in the sensitivity plots shown in Figure 35 are caused by power lines (60Hz and harmonics), suspension mechanical resonances, and excitations that are deliberately added to the instrument for calibration



a) *LIGO livingston observatory*



b) *LIGO Hanford observatory*

*Fig. 35 : Noise budget plots for the gravitational wave channels of the two LIGO detectors. The strain sensitivities are similar between the two sites. Plot (a) shows the low-frequency curves for L1, whereas Plot (b) shows the high-frequency curves for H1 detector. Quantum noise is the sum of the quantum radiation pressure noise and shot noise. Dark noise refers to electronic noise in the signal chain with no light incident on the readout photodetectors. Thermal noise is the sum of suspension and coating thermal noises. Gas noise is the sum of squeezed film damping and beam tube gas phase noises. The coupling of the residual motion of the Michelson (MICH) and signal recycling cavity (SRCL) degrees of freedom to gravitational wave channel is reduced by a feedforward cancellation technique. At low frequencies, there is currently a significant gap between the measured strain noise and the root-square sum of investigated noises. At high frequencies, the sensitivity is limited by shot noise and input beam jitter.*

and alignment purposes. These very narrow lines are easily excluded from the data analysis, while the broadband noise inevitably limits the instrument sensitivity. The latter is therefore a more important topic of investigation.

#### 10.4.1) Seismic and thermal noise :

Below 10Hz, there is significant displacement noise from residual seismic motion. On average, at both the Livingston and Hanford sites, the ground moves by  $\sim 10^{-9}$  m/ $\sqrt{\text{Hz}}$  at 10Hz—ten orders of magnitude larger than the Advanced LIGO target sensitivity at this frequency. To address this difference, seismic noise is filtered using a combination of passive and active stages. The test masses are suspended from quadruple pendulums . These passive filters have resonances as low as 0.4Hz and provide isolation as  $1/f^8$  in the detection bandwidth. The pendulums are mounted on multistage active platforms . These systems use very-lownoise inertial sensors to provide the required isolation in the detection band and at lower frequencies (below 10Hz). This isolation is crucial for bringing the interferometer into the linear regime and allowing the longitudinal control system to maintain it on resonance. The active platforms combine feedback and feedforward control to provide one order of magnitude of isolation at the microseism frequencies (around 0.1 Hz) and three orders of magnitude between 1Hz and 10Hz. Most of the suspension resonances are located in this band, where ground excitation from anthropogenic noise and wind is significant.

Fluctuations of local gravity fields around the test masses—caused by ground motion and vibrations of the buildings, chambers, and concrete floor—also couple to the gravitational wave channel as force noise (gravity gradient noise). The coupling to the differential arm length displacement is given by

$$L(f) = 2 \frac{N_{\text{grav}}(f)}{(2\pi f)^2}$$

$$N_{\text{grav}}(f) = \beta G \rho N_{\text{sei}}(f),$$

where  $N_{\text{grav}}$  is the fluctuation of the local gravity field projected on the arm cavity axis, the factor of 2 accounts for the incoherent sum of noises from the four test masses,  $G$  is the gravitational constant,  $\rho \approx 1800$  kg  $\text{m}^{-3}$  is the ground density near the mirror,  $\beta \approx 10$  is a geometric factor, and  $N_{\text{sei}}$  is the seismic motion near the test mass. Since the ground near the test masses moves by  $\approx 10-9$  m /  $\sqrt{\text{Hz}}$  at 10Hz, local gravity fluctuations at this frequency are  $N_{\text{grav}} \approx 10-15$  m  $\text{s}^{-2}/\sqrt{\text{Hz}}$  and the total noise coupled into the gravitational wave channel at 10Hz is  $L \approx 5 \times 10-19$  m/ $\sqrt{\text{Hz}}$ . Gravity gradient noise is one of the limiting noise sources of the Advanced LIGO design in the frequency range 10–20Hz. However, the typical sensitivity measured during O1 is still far from this limitation.

Thermal noises arise from finite losses present in mechanical systems and couple to the gravitational wave channel as displacement noises. Several sources of thermal noise can be identified. Suspension thermal noise causes motion of the test masses due to thermal vibrations of the suspension fibers. Coating Brownian noise is caused by thermal fluctuations of the optical coatings, multilayers of silica and titania-doped tantalum . Thickness of the coatings was optimized to reduce their thermal noise and provide the required high reflectivity of the mirrors. Thermal noise also arises in the substrates of the test masses , but this effect is less significant. Thermal noise levels are analytically computed using the fluctuation-dissipation theorem and independent measurements of the losses of materials. The model predicts that thermal noise limits the Advanced LIGO design sensitivity in the frequency band 10–500Hz, but is below current sensitivity by a factor of  $\geq 3$ .

#### 10.4.2) Quantum noise

Quantum noise is driven by fluctuations of the optical vacuum field entering the interferometer through the antisymmetric port . This fundamental noise couples to the interferometer sensitivity in two complementary ways . For one, vacuum fluctuations disturb the optical fields resonating in the arm cavities, creating displacement noise by exerting a fluctuating radiation pressure force that physically moves the test masses . The vacuum field is amplified by the optical cavities, and the noise seen in the differential arm channel is given by:

$$L(f) = \frac{2}{cM\pi^2 f^2} (h\nu G_- P_{\text{arm}})^{1/2} K_-(f)$$

$$L(f) = \frac{1.38 \times 10^{-17}}{f^2} \left( \frac{P_{\text{arm}}}{100 \text{ kW}} \right)^{1/2} K_-(f) \frac{\text{m}}{\sqrt{\text{Hz}}},$$

Local oscillator power PLO cancels out in the final equation, and shot noise level is independent of the differential arm offset for small offsets  $\Delta L < 100\text{pm}$  .

The Advanced LIGO optical configuration is tuned to maximize power circulating in the arm cavities. Common coupled cavity build-up (ratio between the power resonating in the arms and power entering the interferometer) is related to the losses in the arm cavities by

$$G_{\text{comm}} \lesssim \frac{1}{2Y_{\text{arm}}},$$

where  $Y_{\text{arm}}$  is round trip optical loss in one arm. During O1 the power circulating in the arm cavities was  $G_{\text{comm}} \approx 5000$  greater than the power entering the interferometer, corresponding to a round trip optical loss of  $Y_{\text{arm}} \approx 100\text{ppm}$  in each arm cavity. The target optical gain for Advanced LIGO was 7500, which corresponds to round trip losses in the arm cavities of about 75ppm. This number can possibly be achieved once the test masses are replaced after the second science run. The discrepancy in the round trip losses between the predicted and measured values is currently under study. Shot noise limits the design sensitivity above 40Hz, and the current sensitivity above 100Hz .

#### 10.4.3) Gas noise

where  $Y_{\text{arm}}$  is round trip optical loss in one arm. During O1 the power circulating in the arm cavities was  $G_{\text{comm}} \approx 5000$  greater than the power entering the interferometer, corresponding to a round trip optical loss of  $Y_{\text{arm}} \approx 100\text{ppm}$  in each arm cavity. The target optical gain for Advanced LIGO was 7500, which corresponds to round trip losses in the arm cavities of about 75ppm. This number can possibly be achieved once the test masses are replaced after the second science run. The discrepancy in the round trip losses between the predicted and measured values is currently under study. Shot noise limits the design sensitivity above 40Hz, and the current sensitivity above 100Hz .

**squeezed film damping :** Residual gas in the vacuum system exerts a damping force on the test masses and introduces displacement noise. This noise is amplified by a factor of  $\sim 10$  below

100Hz due to the small gap of 5mm between the end test and reaction masses (the top view of a test mass and its surroundings is shown in Figure 36). The total noise

can be estimated by applying the fluctuation-dissipation theorem or by running a Monte Carlo simulation .

The coupling coefficient depends on the gas pressure and the molecular mass, and it is found to be (below 100Hz)

$$F(f) = 1.5 \times 10^{-14} \left( \frac{p}{10^{-6}} \right)^{1/2} \left( \frac{m}{m_{H_2}} \right)^{1/4} \frac{N}{\sqrt{\text{Hz}}},$$

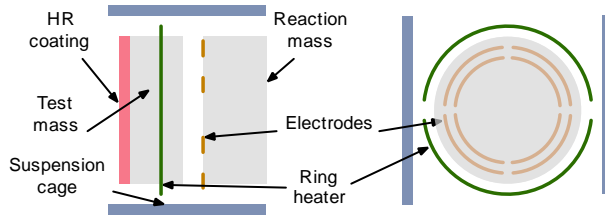


*Fig 36 : Top and front views of a test mass showing the arrangement of the electrodes, high reflective (HR) coating, ring heater and surrounding metal cage. Electrodes are used for actuation on the test mass. The ring heater is used to correct the curvature of the mirror.*

where  $p$  is the residual gas pressure in Pa, and  $m$  is the mass of a gas molecule. The calculated squeezed film damping noise shown in Figure 37 is the sum of contributions from nitrogen ( $p_{N2} \approx 6 \times 10^{-7}$  Pa), hydrogen ( $p_{H2} \approx 2 \times 10^{-6}$  Pa) and water ( $p_{H2O} \approx 10^{-7}$  Pa).

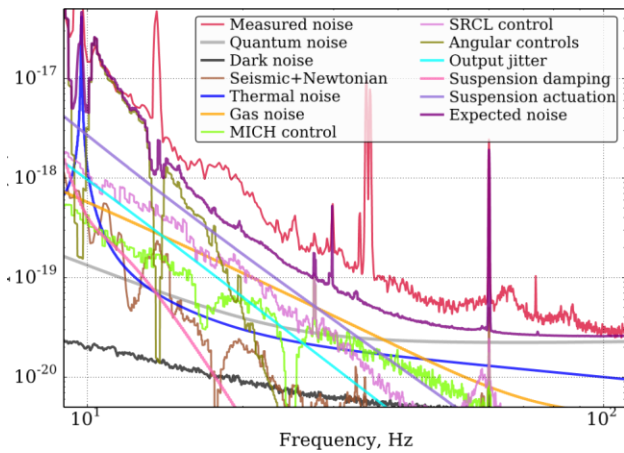


*Fig 37 : Noise budget plots for the gravitational wave channels of the two LIGO detectors. The strain sensitivities are similar between the two sites. Plot shows the low-frequency curves for L1.*

**phase noise:** Phase noise induced by the stochastic transit of molecules through the laser beam in the arm cavities, can be modelled by calculating the impulsive disturbance to the phase of the laser field as a gas molecule moves through the beam . Such a model was used to estimate the high frequency part of gas noise curve shown in Figure 38. This estimation accounts for the pressure distribution in the arm cavities along with the profile of the laser beam, with the most significant noise contribution coming from the geometrical centre of the tube,

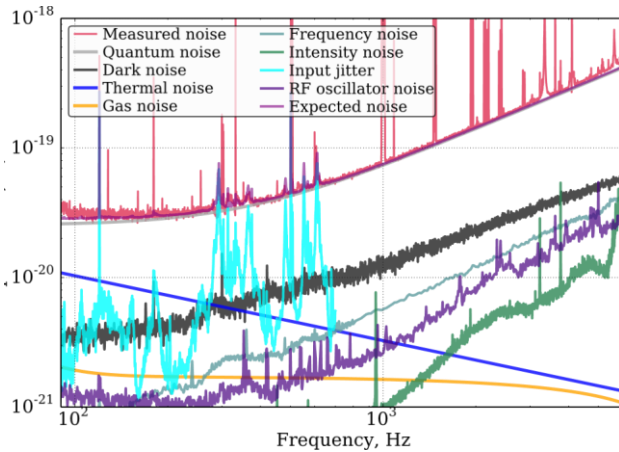


Fig 38 :Plot shows the high-frequency curves for H1 detector.

where the beam waist is located. The expected noise from residual gas is given by

$$L(f) = 4 \times 10^{-21} N_{\text{gas}} \frac{m}{\sqrt{\text{Hz}}}$$

$$N_{\text{gas}} = \left( \frac{a_{\text{gas}}}{a_{H_2}} \right) \left( \frac{m_{\text{gas}}}{m_{H_2}} \right)^{1/4} \left( \frac{p}{10^{-8}} \right)^{1/2},$$

where  $a_{\text{gas}}$  is the polarization of the gas molecules. The estimation of the gas phase noise was verified by changing the pressure in one of the arms by a factor of 3 at the end station and factor of 1.7 at the half-way point. A variation of differential arm noise was measured using relative intensity fluctuations at the output port, as shown in Figure 37 . the sensitivity above 100Hz is limited by shot noise, classical noise can be revealed by incoherent subtraction of shot noise from the measured signal. Using this technique, classical noise was observed to change during this test as predicted by the model.

#### 10.4.4) Charging noise

During the Advanced LIGO commissioning, it was discovered that the electrostatic actuation on the test masses was not symmetric among the four electrodes located on the reaction mass . This mismatch in actuation strength is caused by electrostatic charge , which is distributed on the test masses in a non-uniform manner and is time dependent.

Ideally, there should be no charge on the test masses, except for the one accumulated due to electrostatic actuation. However, some electric charge may be left by imperfect removal of the First Contact polymer used for cleaning and protection of the optics . Moreover, surfaces of the test masses also lose electrons due to UV photons, generated by nearby ion pumps used in the vacuum system. Dust particles in the vacuum system provide yet another source of

charging. It was discovered that the charge distribution changes on the week time scale. An order-of-magnitude estimate of the charge density on the front and back surfaces of the end test masses is  $\sigma \sim 10^{-11} \text{ C/cm}^2$ . This number was achieved by exciting the electrodes and the potential of the ring heaters while measuring the longitudinal and angular motion of the test mass.

There are two coupling mechanisms of charging noise to the gravitational wave channel. The first mechanism arises due to interaction of the time – variant charge with the metal cage around the test mass. The second coupling mechanism comes from voltage fluctuations of the various pieces of grounded metal in the vicinity of the test mass. Voltage noise creates fluctuations of the electric field  $E$  and applies a force  $F_{ch}$  on the test mass according to the following equation

$$F_{ch} = \int E \sigma dS,$$

where the integral is computed over both the front and back surfaces of the test mass. In this paper, we consider only the second coupling mechanism, since it is estimated to be the dominant one.

The broadband voltage noise on the ground plane is measured to be roughly  $1\text{uV} / \sqrt{\text{Hz}}$ . This number was measured between the grounded suspension cage and the floating ring heaters. Since the characteristic distance between the test masses and the metal cage is 10cm, the fluctuations in the electric field near the test mass are  $\sim 10^{-5} \text{ V/m}/\sqrt{\text{Hz}}$ . The total noise coupling above 10Hz is estimated using the equation

$$L(f) = \frac{F_{ch}}{M(2\pi f)^2} \approx \frac{10^{-16}}{f^2} \frac{\sigma}{10^{-11} \text{ C/cm}^2} \frac{m}{\sqrt{\text{Hz}}}.$$

The coupling of voltage fluctuations on the ground plane to the gravitational wave signal was reduced by a factor of 10–100 by discharging the test masses. Charge from the front surface can be efficiently removed using ion guns : positive and negative ions are introduced into the chamber, when the pressure inside is  $\sim 10^3 \text{ Pa}$ , and annihilate surface charges on the front surface of the test mass. During the discharge procedure, it was found that the ions cannot efficiently reach the back surface due to the small gap between the test mass and the reaction mass, as shown in Figure 39. The back surface of the end test masses was discharged by opening the chambers, separating the test and reaction mass, and directing an ion gun at close range towards the surfaces in the gap .

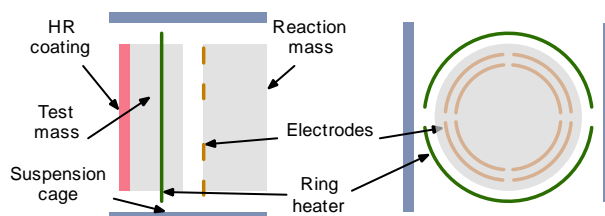


*Fig 39 : . Top and front views of a test mass showing the arrangement of the electrodes, high reflective (HR) coating, ring heater and surrounding metal cage. Electrodes are used for actuation on the test mass. The ring heater is used to correct the curvature of the mirror.*

#### 10.4.5) Laser amplitude and frequency noise

Advanced LIGO employs a Nd:YAG nonplanar ring oscillator as the main laser. Intensity and frequency fluctuations of such a laser can be roughly approximated as  $10^{-4}/f/\sqrt{\text{Hz}}$  and  $10^4/f\text{ Hz}/\sqrt{\text{Hz}}$ , respectively, in the frequency range 10Hz–5kHz. In the same band, the Advanced LIGO requirements are  $\sim 10^{-8}/\sqrt{\text{Hz}}$  for intensity noise and  $\sim 10^{-6}\text{ Hz}/\sqrt{\text{Hz}}$  for frequency noise. In order to meet those requirements, a hierarchical control system is implemented. First of all, laser noises are actively suppressed using intensity and frequency stabilization servos. Additionally, laser noise on the beam entering the main interferometer is passively filtered by  $K_+$  due to the common-mode coupled cavity pole.

For laser amplitude noise, there are several coupling mechanisms. First of all, the presence of the nonzero differential arm offset  $\Delta L$  needed for the homodyne readout means that the carrier light at the antisymmetric port is directly modulated by amplitude noise entering the interferometer. In addition, mismatches in the circulating arm powers and in the mirror masses also lead to intensity noise coupling through radiation pressure force at low frequencies (below 50Hz).

Above 100Hz, the most significant broadband coupling of laser amplitude noise comes from unequal effective lenses in the input test masses, due to substrate inhomogeneity. The presence of imbalanced lenses creates a direct conversion of the fundamental laser mode into higher-order spatial modes. As these modes do not resonate in the arm cavities, they are not filtered by the common-mode coupled cavity, and they therefore contribute to the coupling of laser intensity noise with a flat transfer function. A thermal compensation system (TCS), which employs auxiliary CO<sub>2</sub> laser beams and ring-shaped heating elements, has been installed to compensate for such imbalances. Figure 40 shows that the coupling of intensity noise can be significantly reduced by equalizing the substrate lenses using the TCS system: if no correction is applied, the differential lens power is 40μD and the coupling coefficient at 300Hz is more than 40dB larger than the lowest value attainable with a proper TCS correction.

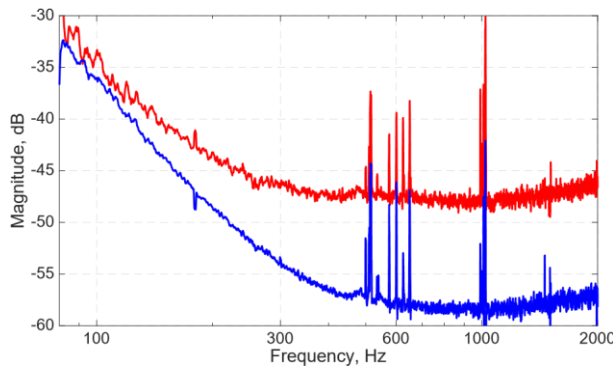


*Fig 40: Measured transfer function of intensity fluctuations from interferometer input to the antisymmetric port. The blue trace corresponds to the case when substrate lenses of input test masses are matched. The red trace shows the coupling when substrate lenses are different by 7.5μD. For the difference of 40μD the coupling above 60Hz increases up to -25dB.*

Laser frequency noise is largely cancelled at the antisymmetric port by virtue of the Michelson interferometer common-mode rejection ( $\sim 1000$  at 100Hz). However, residual frequency noise couples into the gravitational wave channel through the intentional asymmetry that is introduced into the Michelson interferometer to produce the necessary interference conditions for the RF control sidebands, and through imbalances in arm cavity reflectivities and pole frequencies. The achieved laser frequency noise performance is limited primarily by sensing noises (shot noise, photodiode noise, and electronics noise) in the feedback control that stabilizes the laser frequency to the interferometer's common (mean) arm length. In Advanced LIGO, noise in the frequency stabilization error signals limits the residual frequency noise of the beam entering the main interferometer to  $\approx 10^{-6}$  Hz/ $\sqrt{\text{Hz}}$  between 10 and 100Hz, and increasing as  $f$  above 100Hz.

#### 10.4.6) Auxiliary degrees-of-freedom

The use of a dual-recycled Michelson interferometer optimizes the detector response to gravitational waves. Additionally, active control of the mirror angular degrees of freedom is important to stabilize the interferometer optical response. However, any noise in the associated auxiliary degrees of freedom will couple to the gravitational wave channel at some level. Figure 41 shows the typical noise in the auxiliary longitudinal degrees of freedom calibrated into displacement, as well as the typical angular noise in one of the arm cavity pitch degrees of freedom.

Any residual fluctuation of the Michelson length  $N_{\text{mich}}$  couples to the transmitted power of the output mode cleaner, where the gravitational wave channel is transduced. The coupling mechanism is similar to that of a differential arm length fluctuation, but without the amplification factor provided by the arm cavity build-up  $G_{\text{arm}} = 270$ :

$$L(f) = \frac{1}{G_{\text{arm}}} N_{\text{mich}}(f).$$

This coupling coefficient depends only weakly on the differential arm offset and alignment, unless the power build-up in the arm cavities is significantly changed.

Residual fluctuations of the signal recycling cavity length also couple to the gravitational wave channel, due to the differential arm offset  $\Delta L$ , through a radiation pressure force exerted on the test masses by the resonating optical fields. In the frequency range from 10 to 70Hz, the differential arm noise  $L(f)$  due to signal recycling cavity longitudinal noise  $N_{\text{srel}}$  can be modelled as

$$L(f) = \frac{0.16}{f^2} \frac{\Delta L}{10 \text{ pm}} N_{\text{srel}}(f),$$

where the numerical factor is determined mainly by the signal recycling mirror reflectivity and the masses of the cavity mirrors. Besides this linear coupling, a non-linear component

appears due to low-frequency modulation of the differential arm offset  $\Delta L$  (by  $\approx 10 - 20\%$ ), which arises from unsuppressed angular motion of the interferometer mirrors. Such motion generates higher-order mode content in the beam exiting the interferometer through the antisymmetric port, leading to modulation of the power transmitted by the output mode cleaner and forcing the differential arm length servo to compensate by changing the offset  $\Delta L$ . At higher frequencies (above 70Hz), the coupling of the signal recycling cavity longitudinal noise depends on the mode matching between the signal recycling cavity and the arm cavities. This can be tuned using the thermal compensation system discussed above.

The coupling of the power recycling cavity length to the differential arm channel is caused by imbalances in the two arm cavities and cross couplings with other longitudinal degrees of freedom. Residual power recycling cavity length noise is less significant (by a factor of  $\geq 10$ ) compared to other degrees of freedom of the dual-recycled Michelson interferometer.

Finally, any residual angular motion of the test masses  $N_{\text{ang}}$  couples to the gravitational wave channel geometrically due to beam mis-centring  $d$  on the mirrors, according to the equation

$$L(f) = d \times N_{\text{ang}}(f).$$

The beam mis- centring itself is also modulated by the mirror angular motion  $d = d' + d_{\text{ac}}$ , where  $d'$  and  $d_{\text{ac}} \propto N_{\text{ang}}$  are stationary and non-stationary components of the beam position. For this reason, the coupling of the angular motion can be linear and non-linear. The angular feedback servos are optimized to suppress low-frequency motion of the cavity axis and  $d_{\text{ac}}$  while avoiding injection of sensor noise at high frequencies.

The linear coupling of the auxiliary degrees of freedom to the gravitational wave channel is mitigated using a real-time feed-forward cancellation technique. Witness signals are properly reshaped using time-domain filters, and the cancellation signals are applied directly to the test masses. This feed-forward scheme significantly reduces the contribution of noise in auxiliary degrees of freedom to the gravitational wave channel in the frequency range 10–150Hz. The typical subtraction factors for Michelson length noise, signal recycling cavity length noise, and angular noise are 30, 7 and 20, respectively.

#### 10.4.7 Oscillator noise

The RF oscillator used to generate the Pound-DreverHall control sidebands has phase and amplitude noise, and these couple to the gravitational wave channel via both sensing intensity noise and displacement noise in the dual-recycled Michelson degrees of freedom.

Noise in the oscillator amplitude causes the RF modulation index to vary with time, thus changing the amount of power contained in the RF sidebands. Since the total power in the carrier and the RF sidebands is actively controlled, fluctuations in the RF sideband field amplitudes produce fluctuations in the carrier field amplitude (i.e., audio sidebands). These audio sidebands propagate through the interferometer and couple into the gravitational wave channel via the same mechanisms as laser intensity noise . Additionally, as intensity noise of

RF sidebands is not filtered by the common coupled cavity pole and the output mode cleaner has a finite attenuation at the RF sideband frequencies ( $\approx 6 \times 10^{-5}$  W/W for the 45MHz sidebands), a small amount of sideband power fluctuations appears directly on the GW readout photodiodes. The oscillator amplitude noise coupling for the 9MHz and 45MHz sidebands was measured to be

$$L(f) = 5 \times 10^{-22} \left( \frac{N_{\text{amp}}^9}{10^{-6}} \right) \frac{1}{K_-(f)} \frac{\text{m}}{\sqrt{\text{Hz}}}$$

$$L(f) = 5 \times 10^{-21} \left( \frac{N_{\text{amp}}^{45}}{10^{-6}} \right) \frac{1}{K_-(f)} \frac{\text{m}}{\sqrt{\text{Hz}}},$$

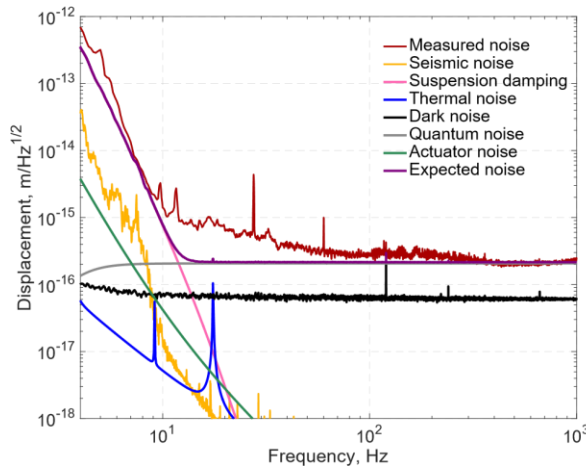
where  $N_{\text{amp}}^9$  and  $N_{\text{amp}}^{45}$  is the relative amplitude noise of 9MHz and 45MHz sidebands in units of  $1/\sqrt{\text{Hz}}$ .

Oscillator phase noise is converted to RF sideband amplitude noise through any optical path length imbalance in the interferometer's Michelson degree of freedom. The main sources of imbalance are the intentional asymmetry in the Michelson interferometer and a transmissivity difference of the input test masses (which produces a differential phase delay when the sidebands are reflected from each arm). The oscillator phase noise coupling for the 9MHz and 45MHz sidebands was measured to be

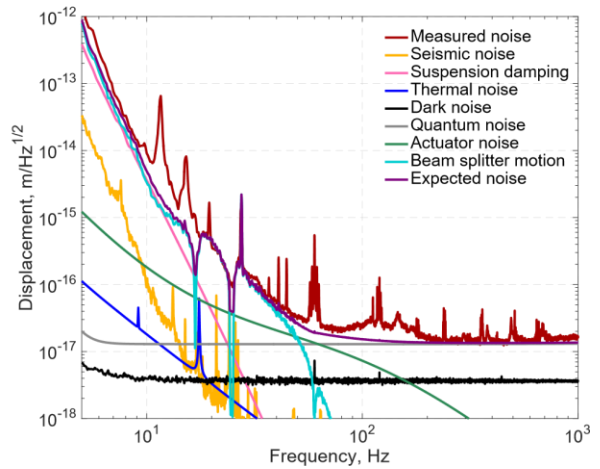
$$L(f) = 10^{-21} \left( \frac{N_{\text{ph}}^9 f}{10^{-2}} \right) \frac{1}{K_-(f)} \frac{\text{m}}{\sqrt{\text{Hz}}}$$

$$L(f) = 10^{-22} \left( \frac{N_{\text{ph}}^{45} f}{10^{-2}} \right) \frac{1}{K_-(f)} \frac{\text{m}}{\sqrt{\text{Hz}}},$$

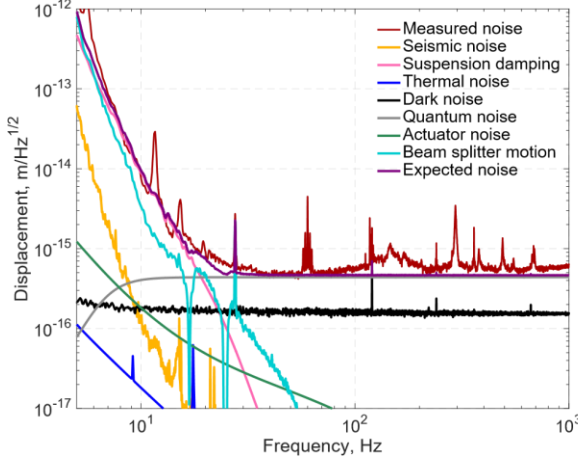
where  $N_{\text{ph}}^9$  and  $N_{\text{ph}}^{45}$  is the relative phase noise of 9MHz and 45MHz sidebands in units of  $1/\sqrt{\text{Hz}}$ .



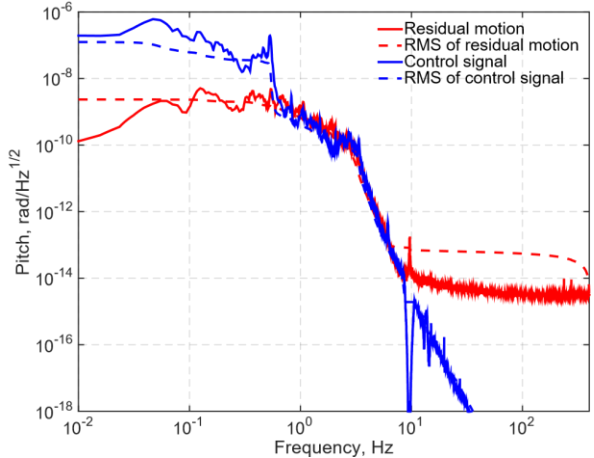
a) Michelson length



b) Power recycling cavity length



c) Signal recycling cavity length



d) Test mass angular motion(pitch)

*Fig 41 : Noise budgets for auxiliary degrees of freedom. Plot (a) shows the noise curves for the Michelson length, Plot (b) for the power recycling cavity length, Plot (c) for the signal recycling cavity length, and Plot (d) for the angular motion of one of the test masses in pitch. The signals are measured with the full interferometer operating in the linear regime. The most significant noise sources in the dual-recycled Michelson degrees of freedom are seismic noise, shot noise and electronics noise in the interferometric readout chains and in local sensors on the individual suspensions. Quantum noise in the signal recycling cavity length is significantly affected by the differential arm offset below 10Hz. In addition to coupling to the gravitational wave channel, auxiliary degrees of freedom also couple to each other. For example, beam splitter motion above 10Hz is caused by the Michelson control loop and dominates the power and signal recycling cavity length fluctuations in the frequency range 10-50Hz.*

#### 10.4.8) Beam jitter

Pointing fluctuations, quantified by the factor  $\Delta w/w$ , where  $w$  is the beam size and  $\Delta w$  is the transverse motion of the beam, are also a source of noise. On the input side, significant beam jitter is caused by angular and longitudinal motion of the steering mirrors, located in air. The input mode cleaner, located in vacuum, attenuates the input beam jitter by a factor of  $\approx 150$ . Figure 42 shows the relative pointing fluctuations before and after the input mode cleaner.

Residual input beam jitter is converted into intensity fluctuations by the interferometer resonant cavities: the power and signal recycling cavities, the arm cavities, and finally the output mode cleaner cavity. In the frequency range 100Hz–1kHz, the coupling coefficient from relative pointing noise at the interferometer input to the relative intensity noise at the antisymmetric port is  $\sim 0.01$ .

The contribution of the beam jitter is close to the measured strain noise at a few peaks between 200 and 600Hz. These structures in the noise are due to resonances of mirror mounts

in the in-air input beam path. This contribution has been reduced by improving the stiffness of the optical elements, thus reducing the motion.

On the output side, beam jitter is caused by angular motion of the output steering mirrors. These are single pendulum stage suspended optics, located in vacuum. While interferometer alignment is actively controlled to reduce beam jitter, any residual angular motion modulates the power transmitted by the output mode cleaner and thereby couples to the gravitational wave channel.

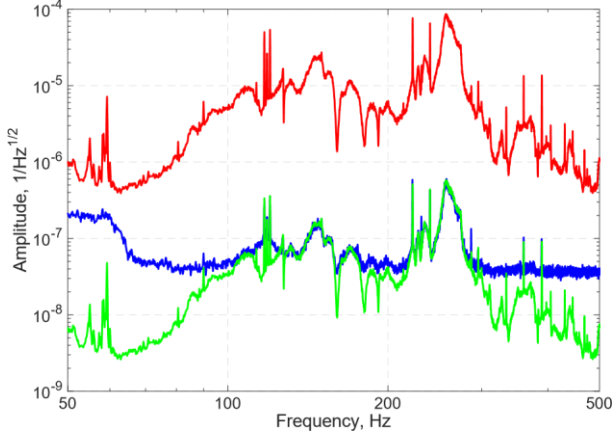


*Fig 42 : Relative pointing noise before and after the input mode cleaner in L1 interferometer. Acoustic peaks in the L1 and H1 interferometers are at slightly different frequencies. The red trace shows the spectrum measured before the input mode cleaner, where laser beam enters the vacuum system. The blue trace shows the measured jitter after the input mode cleaner. This measurement is limited by the sensing noise of the quadrant photodetector at a level of  $4 \times 10^{-8} \text{ } \text{Hz}^{-1/2}$ . The green trace is the estimated relative pointing noise used in the calculation of the jitter coupling to the gravitational wave channel. This curve is computed by dividing the red spectrum by the filtering coefficient of the input mode cleaner.*

#### 10.4.9) Scattered light noise

Motion of the suspended optics is significantly reduced compared to the ground. However, the vacuum chambers and arm tubes are not isolated from the ground seismic or the ambient acoustic noises. This motion can couple to the gravitational wave channel through scattered light.

A small portion of the laser light scatters out of the main beam when it hits the optical components. Part of this light is scattered back from the moving chamber walls, baffles, mirrors, or photodiodes, and couples into the main beam. Backscattered light modulates the main beam in phase and amplitude, and introduces noise into the gravitational wave channel. The phase modulation is directly detected at the antisymmetric port, and amplitude modulation moves the test masses by means of radiation pressure. Significant scattering processes occur inside the arm cavities, at the input and output ports, and in the recycling cavities.

**Beam tubes :** Light scattered out from the main beam by the test masses couples motion of the 4-km beam tube to the gravitational wave channel. The bi-directional Reflectivity Distribution (BRDF) function of the test masses depends on the imperfections in the mirror surface. If the wavelength of a coating ripple is  $\lambda_r$ , then the angle between the scattered light and the main beam is  $\theta = \lambda/\lambda_r$ . The amount of power scattered out from the main beam depends on the amplitude of the ripple. The fractional power scattered out in the cone with half angle  $\theta \ll 1$  and width  $d\theta$  is given by:

$$\frac{dP_s}{P_{\text{arm}}} \approx \left(\frac{4\pi}{\lambda}\right)^2 S \frac{d\theta}{\lambda} = \text{BRDF}_m \times d\Omega$$

where  $S(\theta/\lambda) = S(\lambda^{-1} r)$  is the power spectral density of the coating aberrations , and  $d\Omega = 2\pi\theta d\theta$  is solid angle of scattering. For  $\theta \sim 1$ , the BRDF can be approximated as  $\text{BRDF}_m = 3 \times 10^{-6} \cos(\theta) \text{sr}^{-1}$ .

Light scattered out from the main beam hits a baffle in the arm tube and scatters back into the main beam. The measured BRDF of the baffle at large angles is  $\text{BRDF}_b = 0.02 \text{sr}^{-1}$ . In order to get back into the main beam, light from the baffle scatters into the solid angle  $\lambda^2/r^2 \times \text{BRDF}_m$  where  $r$  is the distance from the baffle to the test mass. The total optical power  $P_r$  that recombines with the main beam is determined by the following equation :

$$\frac{dP_r}{P_{\text{arm}}} = \frac{\lambda^2}{r^2} \text{BRDF}_m^2 \text{BRDF}_b d\Omega.$$

The coating profiles were measured and can be approximated as a smooth polynomial function in the wide range of  $\lambda_r$  for narrow angle scattering. However, the high-reflectivity coatings applied on the end test masses show a distinct azimuthal ripple in the coating surface height. The spatial wavelength of the ripple is 7.85mm and its maximum amplitude is 1nm pk-pk. This ripple is located at radii beyond about 3cm from the mirror centre and significantly contributes to the scattered light noise . The total scattered light noise contribution to the differential arm channel from the tube motion  $N_{\text{tube}}$  is

$$L(f) = \sqrt{2 \int \frac{dP_r}{P_{\text{arm}}} N_{\text{tube}}(f)} \approx 10^{-11} N_{\text{tube}}(f),$$

where the integral is computed over all scattering angles (the factor of 2 accounts for the incoherent sum of all four test masses and for the fact that 1/2 of the baffle motion, in power, is in the phase quadrature of the main field). Above Equation accounts only for the phase quadrature and ignores radiation pressure noise. This is a valid assumption for the current optical power  $P_{\text{arm}} \approx 100 \text{kW}$ .

The estimated scattered light noise, coming from the arm cavities, is a factor of 30-100 below the current sensitivity of the interferometer. This result was confirmed by applying periodic mechanical excitation to the beam tube at different frequencies and measuring the response in the gravitational wave channel.

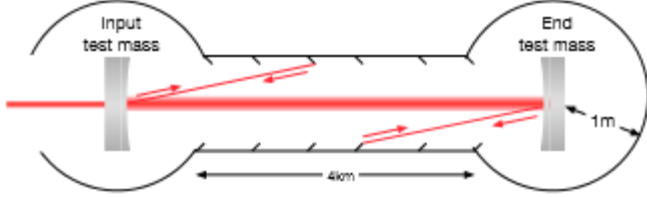


*Fig 43 : Scattering inside the arm cavity. The test mass coating irregularities and dust determines how much light can be scattered in and out from the main beam. After the scattered light hits the beam tube baffles, which are not isolated from ground motion or acoustic noise, it partially scatters back into the main beam. This process couples motion of beam tubes to the gravitational wave channel.*

**Vacuum tubes :** Similar scattering processes occur in the chambers and short tubes in the corner station, where the dual-recycled Michelson interferometer is located. One method to assess the contribution of scattering noise to the detector background is to inject known acoustic signals and measure the response in the gravitational wave channel . In general, coupling of scattered light noise is not linear but rather modulated by the low frequency motion of the scattering surfaces. For this reason, instead of measuring the transfer function from the excitation to the sensor, we monitor excess power in the signal spectrum. Then we make a projection of scattered light noise to the gravitational wave channel according to the following equation

$$L(f) = N_{\text{amb}}(f) \frac{L_{\text{exc}}(f)}{N_{\text{exc}}(f)},$$

where  $L_{\text{exc}}$  and  $N_{\text{exc}}$  are the spectra of the gravitational wave channel and of the back scattering element motion, respectively, when an excitation to the element is applied, and  $N_{\text{amb}}$  is the motion of the scattering element without any excitation. Figure 44 shows that the projected ambient acoustic noise coupling to the gravitational wave channel is below the measured sensitivity.

**Fringe wrapping :** Scattered light may also manifest itself through upconversion of the scattering element motion. One example of such a non-linear scattering process is fringe wrapping. In Advanced LIGO fringe wrapping occurs at the antisymmetric port of the interferometer. Optical imperfections in the output mode cleaner cause a fraction of the light ( $\sim 1\text{ppm}$ ) to travel back into the interferometer. Most of this light is rejected by the output Faraday isolator, but a small fraction of scattered light gets through. Then this light is reflected from the instrument and travels back to the output mode cleaner, with an additional varying phase shift due to the relative motion of the output mode cleaner and the interferometer. The relative intensity fluctuation (RIN) at the output mode cleaner transmission due to backscattering is given by

$$\text{RIN}(t) = 2r \cos(4\pi N_{\text{ome}}(t)/\lambda),$$

where  $r = 10^{-5} - 10^{-4}$  is effective field reflectivity of the interferometer output port and  $N_{omc}(t)$  is the distance fluctuation between the interferometer and the output mode cleaner. Since this distance is not controlled, the amplitude of  $N_{omc}(t)$  can be as large as several wavelengths, and the cosine in the above equation wraps this rapidly varying phase between 0 and  $2\pi$ , leading to up-conversion of the low frequency motion of the length. The resulting “scattering shelves” are seen in the differential arm length spectrum with a cutoff frequency of  $2/\lambda \times dN_{omc}/dt$ . In Advanced LIGO, when the micro-seismic motion is higher than normal, this process increases the gravitational wave channel noise below 20Hz. Figure 44 shows scattering shelves in the gravitational wave channel during the low frequency modulation of the distance  $N_{omc}$ .

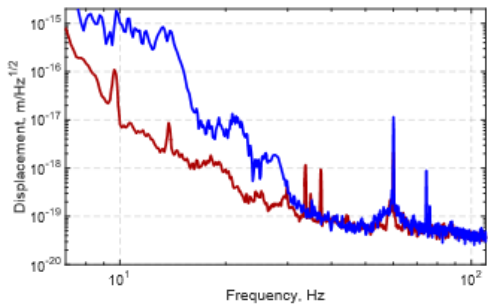


*Fig 44 : Scattering shelves in the differential arm channel. The red trace shows the spectrum when RMS of the ground velocity is below  $\approx 2\text{um/sec}$  (usual conditions). The blue trace shows the spectrum when the distance between the output mode cleaner and the interferometer was modulated at low frequencies by  $\approx 6\text{um/sec}$ .*

#### 10.4.10) Sensing and actuation electronics noise

This section summarizes noise contributions from electronic circuits in photodetectors, actuators, analog-to-digital (ADC) and digital-to-analog (DAC) converters and whitening boards, all of which are essential for sensing optical signals and actuating on suspensions. From a design perspective, all electronics noise should be smaller than fundamental noises.

For the differential arm length signal, a pair of reverse biased InGaAs photodiodes, equipped with in-vacuum preamplifiers, measures the light transmitted by the output mode cleaner. Subsequently, these signals are acquired by a digital system through analog-to-digital converters, further dividing sensing noise into two types: dark noise and ADC noise. Dark noise includes any dark current produced by the photodiodes, Johnson-Nyquist noise of the readout transimpedance, and noise in all other downstream analog electronics. A current noise level of  $\sim 10\text{pA}/\sqrt{\text{Hz}}$ , at 100Hz, is present in each photo detection circuit, equivalent to the shot

noise of a DC current of 0.3mA. This can be compared against the actual operating current of 10mA. Taking the coherent sum of two photodetectors into account, we estimate the dark noise to be a factor of 8.2 lower than the shot noise at 100Hz, ADC input noise is suppressed by inserting additional analog gain and filtering, referred to as “whitening filters”. An offline measurement of the ADC noise shows that it is below the current best noise level by a factor of more than 10 over the entire measurement frequency band.

The other important noise in this category is noise in the actuation used to apply feedback control forces on the mirrors. Any excess noise at the level of the required actuation couples directly to mirror displacement. The most critical actuation noise is due to the digital-to-analog convertors that bridge the digital real-time control process and the analog suspension drive electronics. It is a significant challenge to achieve both the high-range actuation, needed to bring the interferometer into the linear regime from an uncontrolled state (lock acquisition) , and low-noise actuation for operation in the observation state. This issue has been tackled by installing a gain-switchable force controller, which has several operational states. After the interferometer is brought into the linear regime, the controller state is changed from the high-dynamic-range to the low-noise state. Also, noise from the digital-to-analog converter is mechanically filtered via the suspension force-to-displacement transfer function above  $\sim 0.5\text{Hz}$ . The current estimate puts the actuation noise is as low as  $3 \times 10^{-18} \text{ m}/\sqrt{\text{Hz}}$  at 10 Hz .

Lastly, active damping of the suspension systems is known to introduce noise. Below 5Hz, the high-Q suspension resonances are damped by sensing the motion of the suspension relative to its support using shadow sensors . According to dynamical suspension models, noise from the local damping control is estimated to be  $2 \times 10^{-18} \text{ m}/\sqrt{\text{Hz}}$  at 10Hz, and rapidly decreases at higher frequencies.

## 10.5) DETECTOR SUBSYSTEMS :

### 10.5.1) Laser source

The interferometer employs a multi-stage Nd:YAG laser that can supply up to 180 W at the laser system output. The pre-stabilized laser (PSL) system consists of this laser light source, and control systems that stabilize the laser in frequency, beam direction, and intensity. The laser was developed and supplied by the Max Planck Albert Einstein Institute in collaboration with Laser Zentrum Hannover e.V. A schematic drawing of the PSL is shown in Figure 45.

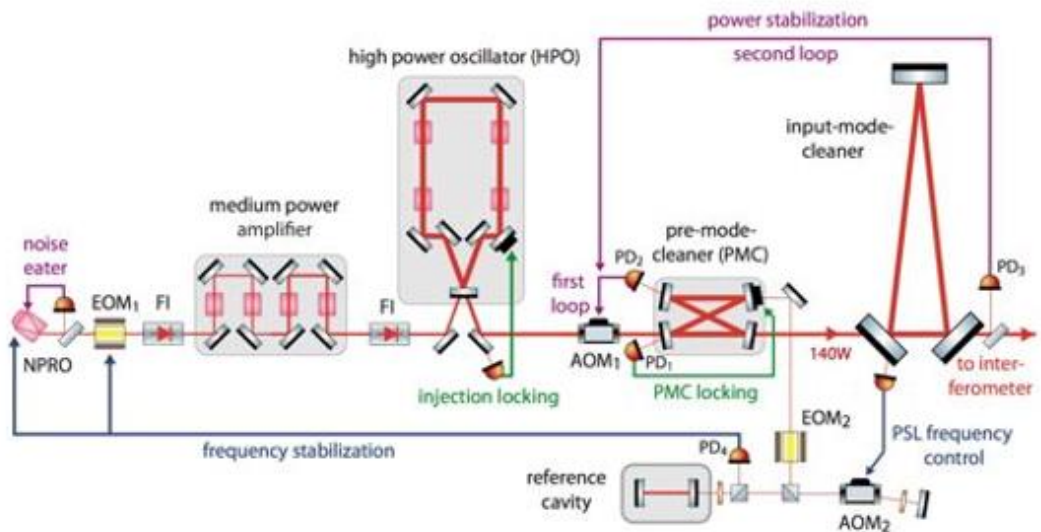


*Fig 45: Schematic of the pre-stabilized laser system. AOM: acousto-optic modulator; EOM: electro-optic modulator; FI: Faraday isolator; PD: photodetector.*

The laser comprises three stages. The first stage is a commercial non-planar ring oscillator (NPRO) manufactured by InnoLight GmbH. The second stage (medium power amplifier) is a single-pass amplifier that boosts the NPRO power to 35 W, and the third stage is an injection-locked ring oscillator with a maximum output power of about 220 W. All stages are pumped by laser diodes; the pump diodes for the second and third stages are fibre coupled and located far from the laser table for easier management of power and cooling. The system may be configured for 35 W output by using the NPRO and medium power stages, bypassing the high power oscillator; this configuration will be in the early operations of Advanced LIGO.

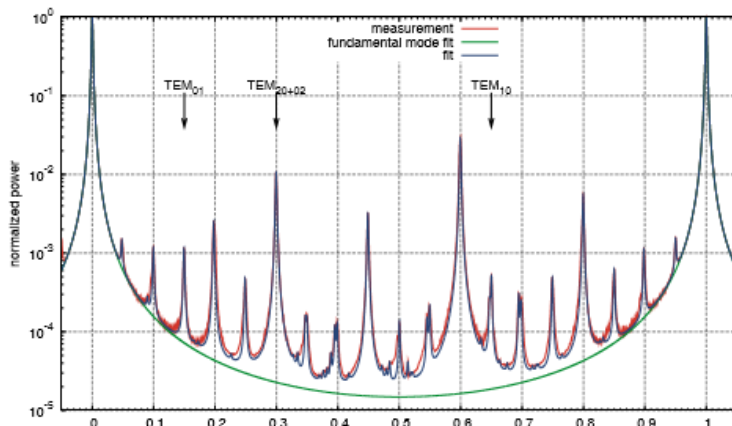
The source laser is passed through the pre-mode cleaner (PMC). The PMC is a bowtie cavity (2m round trip length) designed to strip higher-order modes from the beam, to reduce beam jitter (amplitude reduction factor for TEM01/TEM10 modes of 63), and to provide low-pass filtering for RF intensity fluctuations (cavity pole at 560 kHz).

Intensity stabilization requirements are quite stringent across the GW band. At full laser power, radiation pressure effects in the arm cavities lead to a residual intensity noise specification of  $2 \times 10^{-9} \text{ Hz}^{-1/2}$  at 10 Hz, at the input to the PRM. This stability is achieved through cascaded sensors and feedback loops. The first sensor measures the power in the PMC mode, and the second sensor samples light transmitted through the Input Mode Cleaner. To ensure that an accurate low-noise measurement is made, the second sensor profits from the beam stability post-mode-cleaner, is in vacuum, and consists of multiple diodes used at low power. An acousto-optic modulator (AOM1) is the actuator for the control loop.

The initial frequency stabilization of the laser is performed in the PSL by locking its frequency to an isolated, high-finesse reference cavity (bandwidth of 77 kHz) using the standard reflection locking technique. Three actuators are used to provide wide bandwidth and large dynamic range: a PZT attached to the NPRO crystal; an electro optic modulator (EOM1)—used as a broadband, phase corrector—between the NPRO and medium power amplifier; and the NPRO crystal temperature for slow, wide-range control. The servo bandwidth is 400 kHz. The beam used for this frequency pre-stabilization is taken after the PMC, and is double-passed through an AOM before being sent to the reference cavity. This AOM is driven by a voltage-controlled oscillator to provide laser frequency actuation (1 MHz range, 100 kHz bandwidth) for subsequent stages of stabilization.

Figure 46 shows a mode scan of the L1 high-power laser beam when operating at full output power. The total power in higher-order (non- $\text{TEM}_{00}$ ) modes is 5.3% of the total. This is measured before the PMC, which will filter out this high-order mode content.

*Figure 46 Mode scan of the high power laser used on the L1 interferometer. Close to 95% of the power is in the  $\text{TEM}_{00}$  mode.*



### 10.5.2) Input optics

The input optics subsystem (IO) accepts the light from the pre-stabilized laser, stabilizes and conditions it, and performs matching and pointing into the main interferometer core optics. A schematic view is shown in Figure 47 . The optical efficiency of the IO, from the PSL output to the PRM, is designed to be at least 75%. The system can be broken down into the following functional units.

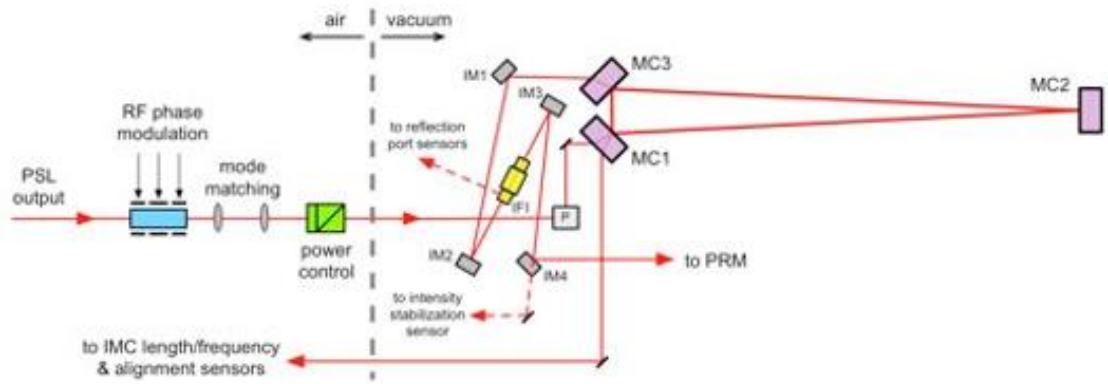


*Fig 47 : Schematic of the input optics components. IFI: input Faraday isolator. P: periscope. IM<sub>n</sub>: input mirror 1-4.*

**Rf modulation:** Radio-frequency (RF) phase modulation is impressed on the beam and used for global sensing of the interferometer and for sensing of the IMC. Three modulation frequencies are applied, all with small modulation depth: 9 MHz and 45 MHz for the main interferometer sensing; 24 MHz for IMC sensing. The modulator must exhibit good phase modulation efficiency, low residual amplitude modulation, and negligible thermal lensing up to a beam power of 165 W. The EOM uses a 40mm long, 4×4 mm cross-section, wedged RTP (rubidium titanyl phosphate) crystal as the electro-optic material. Three pairs of electrodes are used to apply the three modulation frequencies to the crystal.

**input mode cleaner :** The IMC supplies a key function of the IO system: to stabilize the PSL beam in position and mode content, and to provide a high-quality laser frequency reference. The beam pointing stability at the input to the PRM, expressed relative to the beam radius and beam divergence angle, must be  $<1\times10^{-8}$  Hz $^{-1/2}$  at 100 Hz. The frequency stability at the IMC output must be  $<1\times10^{-3}$  Hz/Hz $^{1/2}$  at 100 Hz.

The IMC is a three-mirror ring cavity used in transmission. Each mirror is suspended in a triple pendulum suspension with metal wire loops to provide vibration isolation and acceptable thermal noise. The IMC finesse is 500, the round trip length is 32.9 m, and the linewidth is 18 kHz. The 24 MHz phase modulation sidebands are used both for reflection locking and wavefront-sensor alignment control of the IMC. Additionally, the IMC is used as a frequency actuator for the final level of frequency stabilization to the long arm cavities.

**Faraday Isolator:** An in-vacuum Faraday Isolator is mounted between the IMC output and the PRM; the isolator extracts the beam reflected from the interferometer and prevents this beam from creating parasitic interference in the input chain. The isolator must deliver a minimum of 30dB of isolation up to 125 W of laser power. To compensate thermally induced birefringence, the isolator uses two terbium gallium garnet (TGG) crystals for Faraday rotation, with a quartz rotator in between. Compensation of thermal lensing is achieved by incorporating

a negative  $dn/dT$  material (deuterated potassium dihydrogen phosphate, or ‘DKDP’) in the assembly .

**Mode Matching:** The IMC output beam must be matched to the interferometer mode, with a targeted efficiency of 95% or better. This mode matching is accomplished with two curved mirrors, in combination with two flat mirrors used for beam routing. All four of these reflective optics are mounted in single stage suspensions for vibration isolation; the suspensions also have actuators to provide remote steering capability .

### 10.5.3) Core optics

The ‘Core Optics’ are central to the interferometer performance. For each interferometer they include (see table 5):

- Two input and two end test masses which form the Fabry-Perot arms .
- A 50/50 beamsplitter at the vertex of the Michelson interferometer.
- Two compensation plates that serve as actuation reaction masses for the input test masses, and to which thermal compensation can be applied .
- Two actuation reaction masses for the end test masses .
- Four reflective curved mirrors in the signal and power recycling cavities .
- Signal and power recycling mirrors .

Optic	Dimensions:			Beam size	
	diam.×thickness	Mass	Transmission	ROC	(1/e <sup>2</sup> radius)
ITM	34×20 cm	40 kg	1.4% (0.5-2%)	1934 m	5.3 cm
ETM	34×20 cm	40 kg	5 ppm (1-4%)	2245 m	6.2 cm
CP	34×10 cm	20 kg	AR< 50 ppm	flat	5.3 cm
ERM	34×13 cm	26 kg	AR< 1000 ppm	flat	6.2 cm
BS	37×6 cm	14 kg	50%	flat	5.3 cm
PR3	26.5×10 cm	12 kg	< 15 ppm	36.0 m	5.4 cm
SR3	26.5×10 cm	12 kg	< 15 ppm	36.0 m	5.4 cm
PR2	15×7.5 cm	2.9 kg	225 ppm (>90%)	-4.56 m	6.2 mm
SR2	15×7.5 cm	2.9 kg	< 15 ppm	-6.43 m	8.2 mm
PRM	15×7.5 cm	2.9 kg	3.0%	-11.0 m	2.2 mm
SRM	15×7.5 cm	2.9 kg	20%	-5.69 m	2.1 mm

*Table 5 : Parameters of the core optics. ETM/ITM: end/input test mass; CP: compensation plate; ERM: end reaction mass; BS: beam splitter; PR3/2: power recycling mirror 3/2; SR3/2: signal recycling mirror 3/2; PRM/SRM: power/signal recycling mirror. ROC: radius of curvature; AR: anti-reflection. Transmission values are at 1064 nm .*

All the core optics are made with fused silica substrates. Their fabrication involves three components: material type; substrate polishing; and coatings. The test masses naturally have the most stringent requirements for all three aspects.

The fused silica material used for the input test masses, the compensation plates, and the beamsplitter is Heraeus Suprasil 3001. This is an ultra-low absorption grade, with absorption at 1064 nm of < 0.2 ppm/cm. The material also has a low level of inhomogeneity and low mechanical loss. The material for the other core optics is less critical, and less expensive grades of fused silica are used (ETMs use Heraeus Suprasil 312).

The surface quality required of the polishing is determined largely by the targeted round-trip optical loss in the arm cavities. For a given input laser power, this loss determines the achievable stored power in the arms, and thus the quantum noise level of the interferometer. For Advanced LIGO the arm round-trip loss goal is set at 75 ppm. This would allow a total arm cavity stored power (both arms) of up to:  $1/75 \text{ ppm} = 1.3 \times 10^4$  times the input power. Table 6 lists the test mass substrate polishing requirements, as well as typical achieved levels. The substrates for the large core optics are produced by a combination of super-polishing for small scale smoothness, followed by ion-beam milling to achieve the large scale uniformity.

	<b>Surface error, central 160 mm diam., power &amp; astigmatism removed, rms</b>		<b>Radius of curvature spread</b>
	$> 1 \text{ mm}^{-1}$	$1 - 750 \text{ mm}^{-1}$	
Specification	< 0.3 nm	< 0.16 nm	-5, +10 m
Actual	0.08—0.23 nm	0.07—0.14 nm	-1.5, +1 m

*Table 6 : Polishing specifications and results for the test masses .*

All the optical coatings are ion-beam sputtered, multi-layer dielectrics. The test masses are coated by Laboratoire Matériaux Avancés (LMA, Lyon, France); all other large core optics are coated by CSIRO (Sydney, Australia). The critical properties of the coating materials are low optical absorption, low scatter, and low mechanical loss (particularly for the test masses). For all optics other than the test masses, the coatings are traditional alternating layers of silicon-dioxide and tantalum pentoxide, each of  $\frac{1}{4}$ wavelength optical thickness. For the test masses, the TaO<sub>5</sub> is doped with 25% titanium dioxide, a recipe that reduces the mechanical loss by about 40%. In addition, the layer thicknesses are altered: the SiO<sub>2</sub> layers are a little thicker and the Ti-TaO<sub>5</sub> layers are a little thinner than a  $\frac{1}{4}$ -wavelength. This design not only achieves the transmission specifications at 532 nm, but it also gives a further, modest reduction in thermal noise because less Ti-TaO<sub>5</sub> is used; see Table 7 for the coating material parameters that are used to calculate the thermal noise .

Parameter	Low-index: silica	High-index: tantalum
Mechanical loss	$4 \times 10^{-5}$ [29]	$2.3 \times 10^{-4}$ [30]
Index of refraction	1.45	2.0654
$dn/dT$	$8 \times 10^{-6} / K$	$1.4 \times 10^{-5} / K$ [30]
Thermal expansion coefficient	$5.1 \times 10^{-7} / K$	$3.6 \times 10^{-6} / K$ [30]
Young's modulus	72 GPa [29]	140 GPa [30]
Layer optical thickness, ITM / ETM	$0.308 \lambda / 0.27 \lambda$	$0.192 \lambda / 0.23 \lambda$

Table 7 : Test mass coating material parameters used to calculate coating thermal noise (i.e., this represents our model of the coating).

All core optics are characterized with high precision metrology, before and after coating. As an example, Figure 48 shows power spectra of the measured phase maps of the test masses used in one arm of the L1 interferometer. The coating contributes additional non-uniformity greater than the substrate at larger spatial scales. Comparing the phase map residuals over the central 160 mm diameter, after subtracting tilt and power, gives

- ETM substrate: 0.18 nm-rms coated: 0.69 nm-rms .
- ITM substrate: 0.15 nm-rms coated: 0.31 nm-rms .

Optical simulations of an arm cavity formed with these two test mass mirrors predict a total round trip loss of about 44 ppm (20 ppm due to distortions captured in the phase map, 20 ppm due to smaller scale roughness that causes wider angle scatter, 4 ppm from ETM transmission). This is well within the goal of 75 ppm, though particulate contamination of installed optics can contribute a few tens of ppm additional loss.

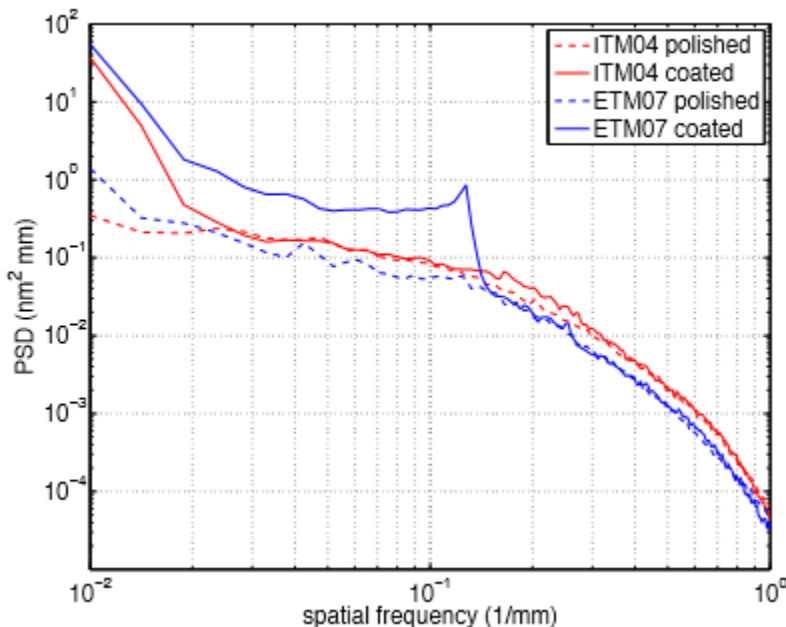


Fig 48 : Power spectra of the surface maps, coated and un-coated, for the ITM and ETM used in one arm of the L1 interferometer.

Though coating absorption is a negligible component of the total loss, it is critical for higher power operation . Absorption in the test mass high-reflectivity coatings is specified at less than 0.5 ppm, and actual coatings show measured absorption of 0.2—0.4 ppm. Other coatings are specified to have absorption less than 1 ppm.

The test mass coatings delivered to date meet many of their challenging requirements such as absorption and scattering, but some of the properties are not ideal:

- For the ETMs, a systematic error in the layer thicknesses left the 1064 nm transmission in spec, but caused the 532 nm transmission to be larger than desired by an order of magnitude. This has made the arm length stabilization system much more challenging .
- Features of the coating planetary system produce a ~1 nm peak-to-peak thickness ripple, with an 8 mm period, in the outer regions of the mirror. This surface ripple scatters light out of the arm cavity; the optical loss is not significant (6 ppm), but the scattered light impinges on the beam tube baffles and can cause excess phase noise .
- Spherical aberration of the ETM coatings is 2-3 times higher than the specification of 0.5 nm. This will alter slightly the shape of the cavity fundamental mode compared to an ideal Gaussian TEM00 mode. However, the aberration is very similar from ETM to ETM, so the arm cavity modes are well matched and this defect does produce significant loss.
- The anti-reflection coatings on the ITMs have 2-3 times higher reflectivity than the specification of 50 ppm. Though not significant in terms of loss, the higher AR produces higher power ghost beams that may need better baffling to control scattered light noise.

#### 10.5.4) Suspensions

All of the primary in-vacuum interferometer optical components are suspended by pendulum systems of varying designs. These suspension systems provide passive isolation from motion of the seismically isolated optics tables in all degrees of freedom and acceptable thermal noise. The suspensions also provide low noise actuation capability, used to align and position the optics based on interferometer sensing and control signals.

##### **Requirements:**

The suspension designs employed for each optical element depend upon the performance requirements and physical constraints, as listed in Table 8 Most of the suspensions employ multiple pendulum and vertical isolation stages.

Optical Component	vertical isolation stages	pendulum stages	Final stage fiber type	Longitudinal noise requirement @ 10 Hz (m/ $\sqrt{\text{Hz}}$ )
Test Masses (ITM, ETM)	3	4	Fused silica	$1 \times 10^{-19}$
Beamsplitter (BS)	2	3	Steel wire	$6 \times 10^{-18}$
Recycling cavity optics	2	3	Steel wire	$1 \times 10^{-17}$
Input Mode Cleaner (IMC) optics	2	3	Steel wire	$3 \times 10^{-15}$
Output Mode Cleaner (OMC) Assy	2	2	Steel wire	$1 \times 10^{-13}$
ETM Transmission Monitor	2	2	Steel wire	$2 \times 10^{-12}$
Auxiliary suspensions	1	1	Steel wire	$2 \times 10^{-11}$

Table 8 : Suspension types. Auxiliary suspensions are for optical pick-off beams, beam steering and mode matching.

### Design description :

The most challenging design is the quadruple pendulum suspension for the test masses . Each of these suspensions is comprised of two adjacent chains, each chain having four masses suspended from one another. The main chain includes the test mass optic as the lowest mass. The adjacent, reaction chain provides an isolated set of masses for force reaction. The bottom mass in the reaction chain is the Compensation Plate (CP) optic in the case of an ITM suspension, and the End Reaction Mass (ERM) in the case of an ETM suspension. A structure surrounds and cages the suspended masses and mounts to the seismically isolated optics table.

Vibration isolation for the test mass is accomplished with a 4-stage pendulum and 3 stages of cantilevered blade springs, providing isolation in all 6 degrees-of-freedom above approximately 1 Hz. The suspension is designed to couple 22 of the 24 quasi-rigid body modes (all but the 2 highest frequency) of each isolation chain so that they are observable and controllable at the top mass (4 wires between masses to couple pitch and roll modes; non-vertical wires to couple pendulum modes). The blade springs are made of maraging steel to minimize noise resulting from discrete dislocation movements associated with creep under load

For each chain, all the quadruple suspension rigid body modes below 9 Hz can be actively damped from the top stage. Sensing for this local damping is accomplished with integral optical shadow sensors , or with independent optical lever sensors. The shadow sensors are collocated with the suspension actuators and have a noise level of  $3 \times 10^{-10} \text{ m}/\sqrt{\text{Hz}}$  at 1 Hz.

Force actuation on the upper three masses is accomplished with coil/magnet actuators . Six degree-of-freedom actuation is provided at the top mass of each chain, by reacting against the suspension structure. These actuators are used for the local damping of 22 modes (each chain). The next two masses can be actuated in the pitch, yaw and piston directions, by applying forces between adjacent suspended masses. These stages are used for global interferometer control. Low noise current drive electronics, combined with the passive filtering of the suspension, limit the effect of actuation noise at the test mass.

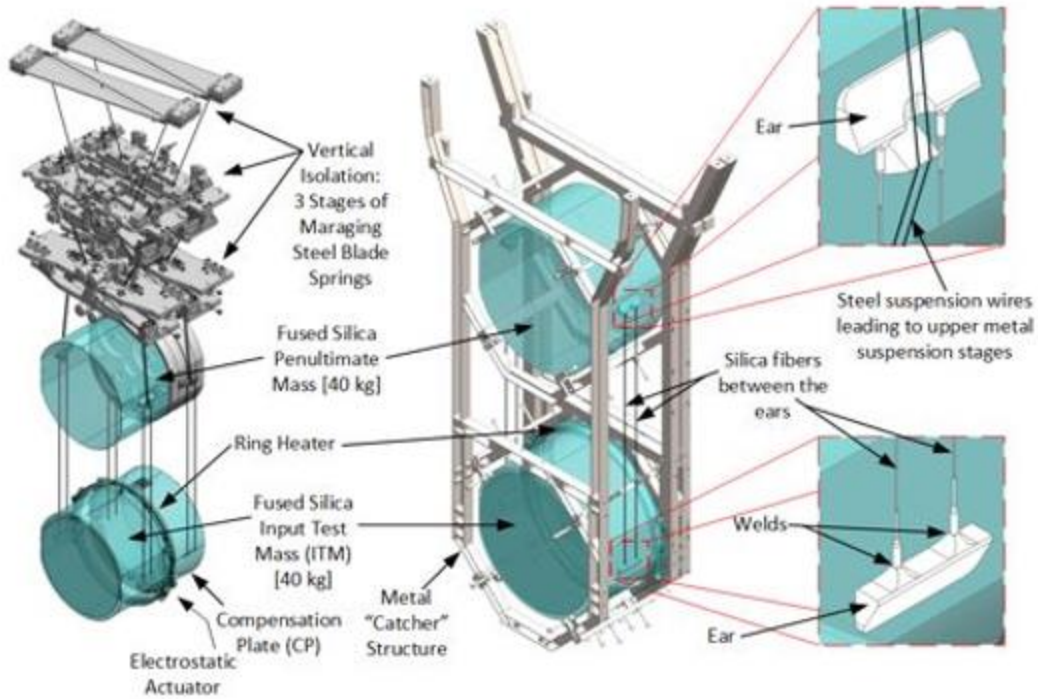


*Fig 49 : Quadruple pendulum suspension for the Input Test Mass (ITM) optic*

Direct low-noise, high-bandwidth actuation on the test mass optic is accomplished with electro-static actuation . The CP and ERM each have an annular pattern of gold electrodes, deposited on the face adjacent to the test mass, just outside the central optical aperture. The pattern is separated into 4 quadrants, which enables actuation in pitch, yaw and piston. The force coefficient is highly dependent on the separation between the test mass and its reaction mass. The ETM-ERM separation is 5 mm, which provides a maximum force of about 200 micro-Newtons using a high-voltage driver. Less actuation is needed on the ITMs, so the CP-ITM gap is increased to 20 mm to mitigate the effect of squeezed film damping .

The test mass and the penultimate mass are a monolithic fused silica assembly, designed to minimize thermal noise . Machined fused silica elements (“ears”) are hydroxide-catalysis (silicate) bonded to flats polished onto the sides of the TM and penultimate mass. Custom drawn fused silica fibres are annealed and welded to the fused silica ears with a CO<sub>2</sub> laser system . The shape of the fibres is designed to minimize thermal noise (400 µm dia. by 596 mm long with 800 µm dia. by 20 mm long ends), while achieving a low suspension vertical “bounce” mode (9 Hz, below band) and high first violin mode frequency (510 Hz, above the instrument’s most sensitive frequency range). The fibre stress (800 MPa) is well below the immediate, static, breaking strength (5 GPa) .

The other suspension types employ the same basic key principles as the test mass quadruple suspensions, except for using steel wire in the final stage.

### **Performance :**

The transfer functions (actuation to response) in all degrees of freedom in general match very well the model for the test mass suspension; Figure 50 . shows one such comparison. Furthermore, the transfer functions are well matched from suspension to suspension, so that very small, if any, parameter value changes are required for the control filters of the multi-input, multi-output control system.

The thermal noise performance of the suspension cannot be verified until the interferometer is fully commissioned and operating at design sensitivity. The displacement thermal noise spectrum for the monolithic stage is made up of quadrature sum of contributions from the horizontal pendulum mode, the vertical mode (with a vertical-horizontal cross-coupling assumed of 0.1%), the first violin mode and the loss associated with the silicate bonded ears. The as-installed quality factor (Q) of the first violin modes of the fibres has been measured to be  $1.1\text{--}1.6 \times 10^9$ , which is about a factor of 2 higher than anticipated from prototype testing , and is consistent with the anticipated level of thermal noise.

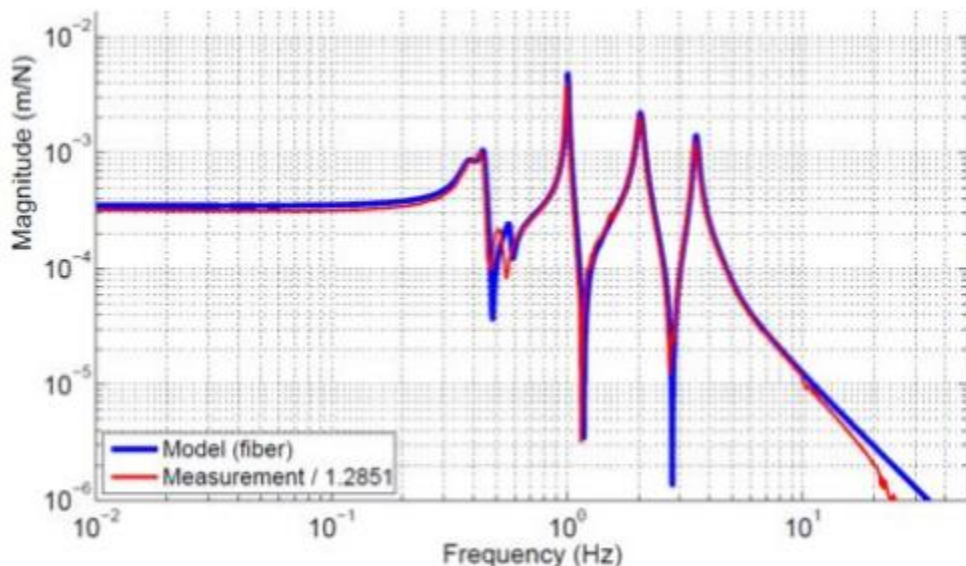


*Fig 50 : Transfer function (magnitude) from longitudinal force to longitudinal position of the top mass of an ITM suspension.*

#### 10.5.5 ) Seismic isolation

The general arrangement of the seismic isolation system and its relationship to the vacuum system and the suspension systems is illustrated in Figure 51 , where a cut-away view of one of the test mass vacuum chambers is also shown.

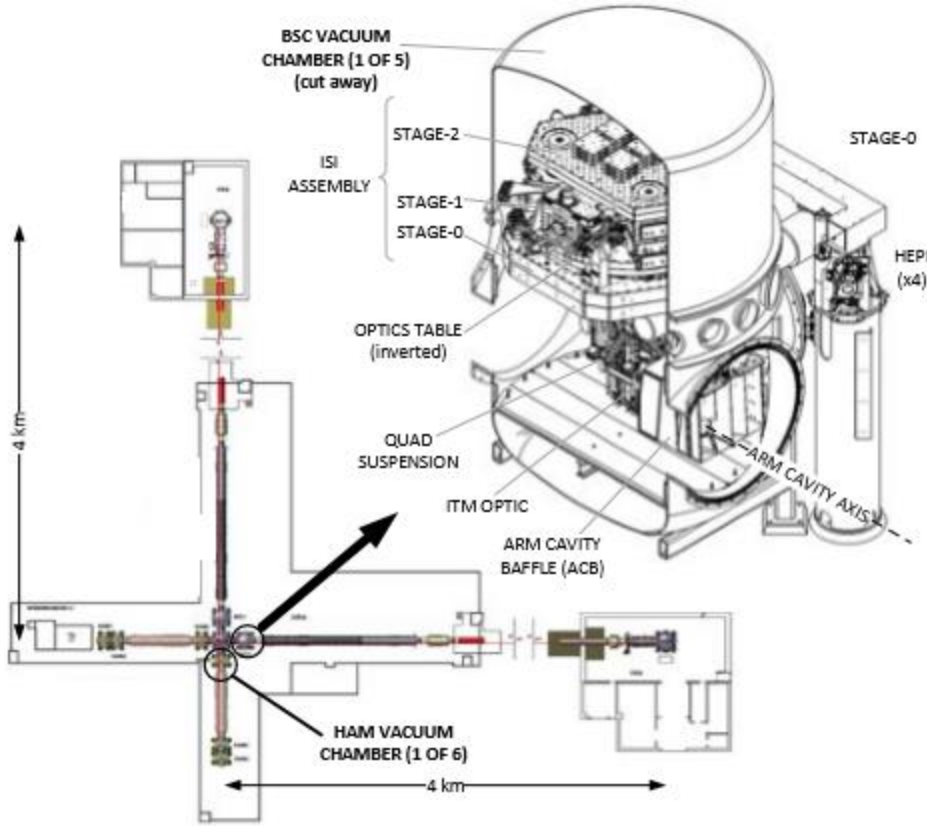


*Fig 51 : An Input Test Mass (ITM) vacuum chamber*

### Requirements :

The motion of the detector components, especially the interferometer optics, must be limited to very small amplitudes. The conceptual approach for seismic isolation is to provide multiple stages of isolation, as depicted in Figure 51. The stages topologically closest to the ground are referred to as the seismic isolation system; they provide coarse alignment, and employ both active and passive isolation to deal with the highest amplitude of motion. An optics table provides the interface between the seismic isolation system and the subsequent suspension system. The optics tables in the smaller (HAM) vacuum chambers are 1.9 m by 1.7 m; the downward-facing optics tables in the larger (BSC) vacuum chambers are 1.9 m diameter. The limits to optics table motion Table 9 are derived from the allowed motion for the interferometer optics using the passive isolation performance of the suspension systems.

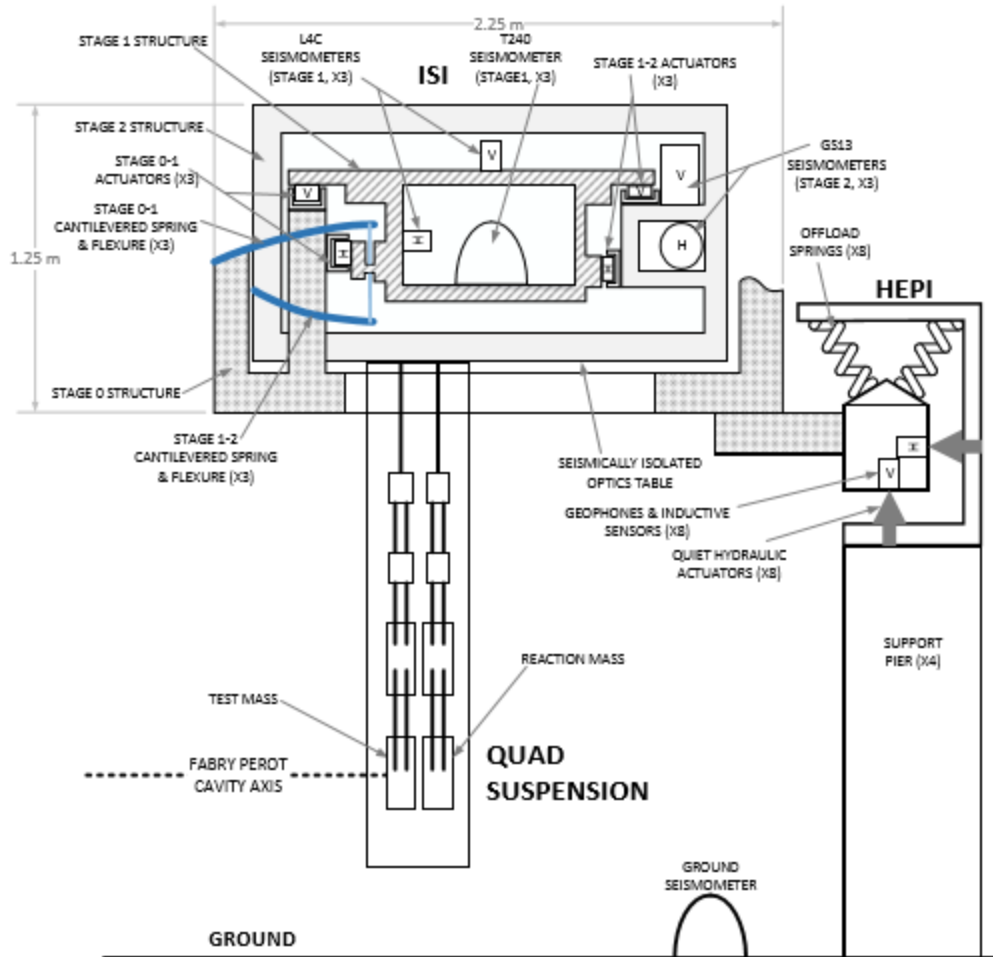


Fig 52 : Seismic isolation for the test mass optic.

systems.

Requirement	value
Payload Mass	800 kg
Positioning/alignment range	$\pm 1$ mm $\pm 0.25$ mrad
Tidal & microseismic actuation range	$\pm 100$ $\mu$ m
Isolation (3 translations)	$2 \times 10^{-7}$ m/ $\sqrt{\text{Hz}}$ @ 0.2 Hz $1 \times 10^{-11}$ m/ $\sqrt{\text{Hz}}$ @ 1 Hz $2 \times 10^{-13}$ m/ $\sqrt{\text{Hz}}$ @ 10 Hz $3 \times 10^{-14}$ m/ $\sqrt{\text{Hz}}$ @ > 30 Hz
Isolation (3 rotations)	$< 10^{-8}$ rad rms, for $1 < f < 30$ Hz

Table 9 : Seismic isolation performance requirements for the BSC chamber, 3 stage systems.

## **Design description.:**

The first measure taken to reduce ground motion was to site the observatories in seismically quiet locations . The observatory facilities were then designed to limit vibration source amplitudes (e.g., the chiller plant for the HVAC system is remote from the experimental hall). Additional isolation from the already seismically quiet ground motion is provided by the seismic isolation and suspension subsystems.

All in-vacuum interferometer elements are mounted on seismically isolated optics tables (with the exception of some stray light control elements). The typical seismic isolation system consists of two or three stages of isolation Figure 52. The first stage is accomplished with the Hydraulic External Pre-Isolator (HEPI) system, external to the vacuum system. The next one or two stages are referred to as the Internal Seismic Isolation (ISI) system and are contained within the vacuum system. The test mass, beamsplitter and transmission monitor suspensions are supported by inverted optics tables which have two in-vacuum stages, housed in the BSC chambers. All other interferometer elements are supported by upright optics tables connected to one-stage ISI systems, housed in smaller (HAM) vacuum chambers.

The in-vacuum payload is supported by a structure that penetrates the vacuum chamber at four locations, through welded bellows. Each of these four points is supported by a HEPI assembly; each HEPI system supports a total isolated mass of 6400 kg. HEPI employs custom designed, laminar flow, quiet hydraulic actuators (8 per vacuum chamber) in a low frequency (0.1—10 Hz), 6 degree-of-freedom active isolation and alignment system. The actuators employ servo-valves in a hydraulic Wheatstone bridge configuration to control deflection of a diaphragm by differential pressure. For sensors, HEPI uses a blend of geophones and inductive position sensors. In addition, a ground seismometer provides a signal for feed-forward correction. The HEPI system was deployed for the initial LIGO L1 interferometer and remains essentially the same for Advanced LIGO.

The ISI consists of three stages (each a stiff mechanical structure) that are suspended and sprung in sequence: stage 0 is the support structure connected to the HEPI frame; stage 1 is suspended and sprung from stage 0; stage 2 is suspended and sprung from stage 1. The elastic, structural modes of stages 1 and 2 are designed to be > 150 Hz in order to keep them high above the upper unity gain frequency (~40 Hz) of the control system. The stage 2 structure includes the optics table upon which payload elements, such as the suspensions, are attached. Each suspended stage is supported at 3 points by a rod with flexural pivot ends, which are in turn supported by cantilevered blade springs. The springs provide vertical isolation and the flexure rods provide horizontal isolation. They are both made of high strength maraging steel in order to reduce noise resulting from discrete dislocation movement events associated with creep under load. The springs and flexures allow control in all 6 rigid body degrees-of-freedom of each stage, through the use of electromagnetic force actuation between the stages. Passive isolation from base (stage 0) motion is achieved at frequencies above the rigid body frequencies of these stages.

Stage 1 of the ISI is instrumented with 6 capacitive position sensors (MicroSense), 3 three-axis seismometers (Nanometric Trillium T240) and 6 geophones (Sercel L4C). Stage 2 is instrumented with 6 capacitive position sensors (MicroSense) and 6 geophones (Geotech

GS13). The single-axis sensors are equally divided into horizontal and vertical directions. All of the inertial sensors are sealed in vacuum-tight canisters. The 12 electromagnetic actuators (6 between stages 0-1 and 6 between stages 1-2) are equally split between vertical and horizontal orientations, and are a custom, ultra-high vacuum compatible design.

The capacitive position sensor signals provide positioning capability, and are lowpass filtered in the isolation band. For stage 1 control, the T240 and L4C seismometer signals are blended together to provide very low noise and broadband inertial sensing; they are high-pass filtered to remove sensor noise and other spurious low frequency signals, such as tilt for the horizontal sensors. The T240 signals are also used for feedforward to the stage 2 controller. Before filtering, the sensors are transformed into a Cartesian basis by matrix multiplication in the multi-input, multi-output digital control system.

### **Performance :**

An example of the isolation performance achieved to date for the three-stage seismic isolation system is shown in Figure 53 .

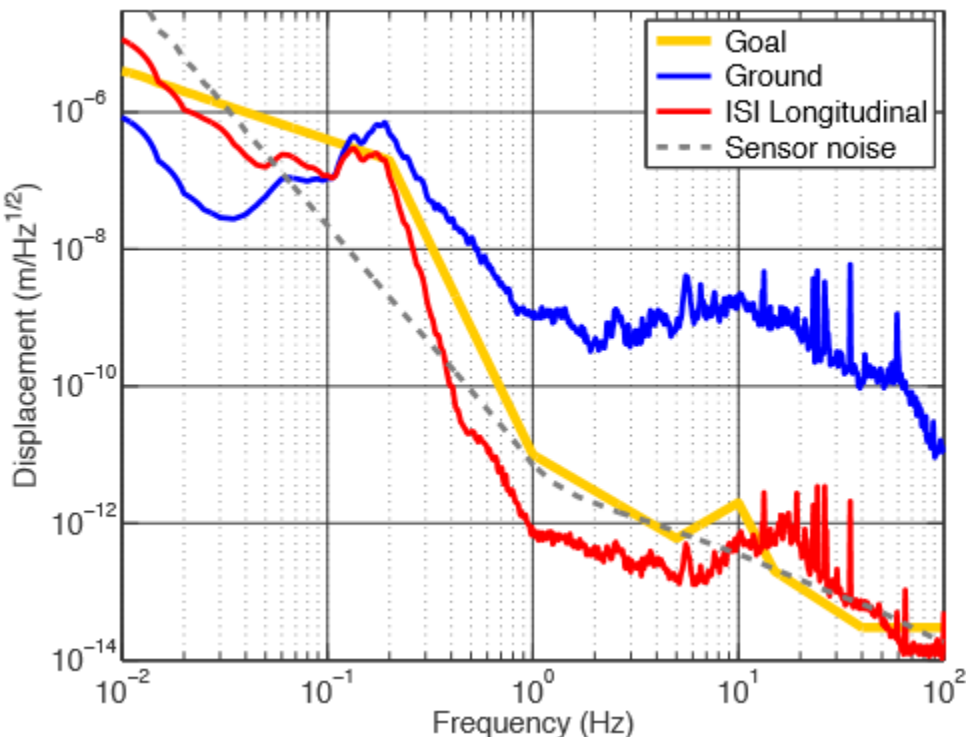


*Fig 53 : Example of the BSC ISI optics table isolation performance (from LHO). The blue curve shows the horizontal ground motion adjacent to the vacuum chamber. The gold curve shows the goal performance. The red curve is an in-loop measurement of the optics table longitudinal motion, using the stage 2 inertial sensors. At the mid-frequencies, these inertial sensor signals are pulled below their intrinsic noise floor by the feedback loop. Below ~30 mHz, the horizontal inertial sensors are likely contaminated by tilt coupling.*

### 10.5.6) Thermal compensation

Absorption of the Gaussian-profiled laser beam in the core optics causes a non-uniform temperature increase leading to wavefront aberration through the thermo-optic and thermo-elastic effects (elasto-optic effects are negligible). While thermal aberrations will occur in all the optics to some extent, only the test mass optics are anticipated to require active compensation.

The projected thermal effects, without compensation, are indicated in Table 10 . The only place of significant power absorption is at the test mass high-reflectivity surfaces, and the largest optical distortion is the resulting thermal lensing in the test mass substrate. The ITM thermal lensing affects primarily the RF sideband mode in the recycling cavities; the carrier mode is enforced by the arm cavities and is much less perturbed by the ITM lensing. The test mass surface distortion due to thermo-elastic expansion is about 10x smaller than the substrate lensing distortion, but at high power it becomes significant. Uncompensated, the surface distortion would increase the ITM and ETM radii of curvature by a few tens of meters, which would reduce the beam size on each test mass by about 10%. This would increase coating thermal noise, and reduce the coupling efficiency between the arm cavity and recycling cavity modes.

<b>Element</b>	<b>Absorbed power</b>	<b>Surface distortion</b>	<b>Lensing optical path distortion</b>
Test mass HR surface	375 mW	15 nm	190 nm
ITM & CP substrates	< 32 mW	< 0.4 nm	< 20 nm
BS 50/50 surface	2.6 mW	0.1 nm	1.3 nm
BS substrate	< 8 mW	< 0.1 nm	< 4 nm

*Table 10: Absorbed power and corresponding thermal distortion at full power: 750 kW in each arm cavity, 5.2 kW in the PRC. Assumes absorption of 0.5 ppm at each HR surface. The distortion values are peak-to-valley over the beam diameter ( $1/e^2$ ). The undistorted sagitta of a test mass is 725/850 nm (ITM/ETM) .*

### Requirements :

The TCS is required to:

- adjust the arm cavity spot size by adding up to 30 micro-diopters of power to all test mass HR surfaces
- compensate thermal aberrations in the recycling cavities sufficiently to maintain adequate RF sideband power buildup.
- maintain recycling cavity and arm cavity mode overlap to within 95%.
- maintain the contrast defect ratio by limiting the additional DC power at the output mode cleaner (OMC) to within 1 mW

The TCS capability to alter the test mass radius-of-curvature can also be used to adjust the transverse optical mode spacing and potentially control optical-acoustic parametric instabilities at high optical power.

### **Design description :**

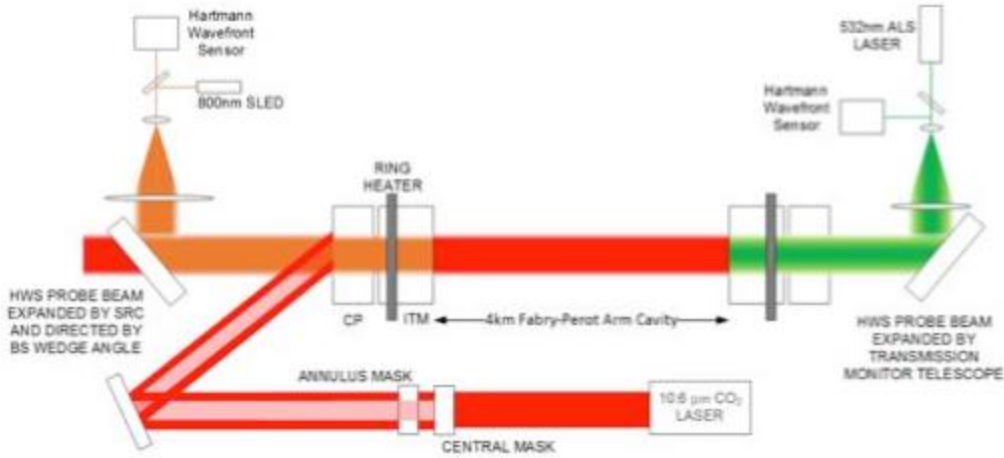
The TCS consists of three major elements (see Figure 54): a radiative ring heater (RH), a CO<sub>2</sub> laser projector (CO<sub>2</sub>P) and a Hartmann wavefront sensor (HWS). The RH is used to correct surface deformation of the ITM and ETM, and to partially correct the ITM substrate thermal lens. The CO<sub>2</sub>P is used to compensate residual ITM substrate distortions not corrected by the RH. The HWS is used to measure the test mass thermal aberrations.

The basic intent of the combination of the RH and CO<sub>2</sub>P is to add heat to form the conjugate aberration to the thermal lens formed by the main beam heating. Whereas the RH power stability is good enough to permit direct actuation on the test mass, the CO<sub>2</sub>P actuates on the compensation plate to limit the effects of CO<sub>2</sub> laser noise.

The RH assembly is comprised of nichrome heater wire wound around two semicircular glass rod formers, which are housed within a reflective shield; the inner radius of the assembly is 5 mm larger than the test mass radius. The nichrome wire spacing along the glass former is variable in order to partially compensate for boundary condition effects and achieve better uniformity. The RH is mounted around and radiates onto the test mass barrel. It is positioned near the test mass anti-reflection face so that the thermal flexure of the optic produces a concavity of the high-reflectivity face, correcting the convex deformation caused by the main beam heating. The thermal flexure is very closely approximated by a spherical curvature at the high-reflectivity face. In addition, the thermal lensing produced by the RH partially compensates the lensing produced by the main beam. The effectiveness of the corrections can be expressed by considering a TEM00 mode probe beam that passes through or reflects from the optics; the correction factor is defined as the power scattered out of the TEM00 mode by the distorted optic, relative to the scattered power for the compensated optic. The RH provides a correction factor of about 10 for both types of test mass distortion (surface and substrate).

The CO<sub>2</sub>P is configured to make static pattern corrections via both central and annular projected heating patterns. These two patterns are created using masks that are inserted into the beam using flipper mirrors. The annular pattern augments and refines the RH correction, providing another factor of 10 or more correction of the substrate lensing. The central pattern can be used to maintain central heating upon lock loss, for faster return to operation; it can also be used to correct non-thermal power terms due to substrate inhomogeneity. The power is adjusted with a polarizer and rotatable  $\frac{1}{2}$ waveplate; power fluctuations are stabilized using an AOM. The CO<sub>2</sub>P is designed to deliver at least 15W to the compensation plate.

*Fig 54 : Schematic layout of the Thermal Compensation System for the X-arm. A similar configuration is implemented on the Y-arm, with the SLED probe beam instead transmitting through the BS. Each of the masks can be independently flipped in or out of the beam path.*



The HWS is used to measure the thermal distortions, both before and after compensation. The HWS can measure thermal wavefront distortions with a sensitivity of  $< 1.4$  nm and a spatial resolution of  $\leq 1$  cm, both over a 200 mm diameter at the ITM. In the vertex, the HWS uses super-luminescent LEDs (SLED) for probe beams. Independent probe beam paths for the X and Y-arms of the Michelson are achieved through choice of SLED wavelength, given the spectral properties of the beam splitter coating: 800 nm is used for the X-arm and 833 nm for the Y-arm (5 mW for both). Cross-talk between the X and Y paths is less than 1 part in 100. Both probe beams make use of the beam expansion telescope integral to the signal recycling cavity (SR2 & SR3) to achieve a large profile at the BS, CP and ITM. The HWS for the ETM uses the ALS green laser beam as a probe.

#### 10.5.7) Scattered light control

A significant fraction of the input laser light ends up outside the interferometer mode through scattering or reflections from the various optics. This light will hit and scatter from surfaces that are typically not as well mechanically isolated as the suspended optics, picking up large phase fluctuations relative to the main interferometer light. Thus even very small levels of scattered light can be a noise source if it re-joins the interferometer mode. Scattered light phase noise is proportional to the electric field amplitude, and for small surface motion proportional to the amplitude of motion. For large motion amplitude, fringe wrapping occurs, resulting in up conversion .

The severity of a potential light scattering surface depends upon the location within the interferometer. Light scattered into a single arm cavity, or into the anti-symmetric port, directly contributes to an apparent differential signal. Light scattered into the power recycling cavity, on the other hand, is less impactful due to the common mode rejection of the arm cavities.

The basic design approach for stray light control is to (a) capture all first-order ghost beams in beam dumps, (b) baffle all views of the vacuum envelope (which is not isolated from ground motion), (c) provide baffles and apertures with low light scattering surface properties (low

bidirectional reflectance distribution function (BRDF) surfaces), (d) provide baffle geometries which trap specular reflections into multiple reflections, (e) provide surfaces with some amount of absorption, and (f) vibration isolate the baffles. Surface treatments are restricted due to the need for ultra-high vacuum compatibility. The larger baffles and apertures are oxidized, polished stainless steel surfaces. The depth of the oxidized layer must be carefully controlled to maintain a well-bonded oxide layer and prevent a frangible layer. Smaller baffles and beam dumps are made of black glass. High power, in-vacuum, beam dumps are comprised of polished, chemical vapour deposited silicon carbide.

The locations of the primary baffles are shown in Error! Reference source not found.. An example of one of the baffle configurations is the Arm Cavity Baffle (ACB). This baffle has a “W” cross-section with an aperture slightly larger than the test mass diameter. A version of this baffle is placed in the arm cavity in front of each test mass optic. The small angle scatter from the far test mass (4 km away) is caught on the beam tube side of the ACB, and forced into multiple reflections in the acute angle ‘cavities’ formed by the baffle surfaces. Large angle scatter from the adjacent test mass is caught on the other side of this suspended baffle. The ACB is mounted with a single pendulum suspension (1.6 Hz), with a cantilevered spring for vertical isolation (2 Hz).

Light scattered off the test masses at even smaller angles is caught by the approximately two hundred baffles mounted along the beam tube. These baffles were installed for initial LIGO, but were designed to be effective for later generations of interferometers.

#### 10.5.8) Global sensing and control

Using primarily interferometrically generated error signals, active feedback is used to keep the interferometer at the proper operating point. This entails keeping the four interferometer cavities on resonance (two arm cavities, power- and signal-recycling cavity), and the Michelson at the dark fringe (or at a controlled offset from there). In addition, global controls are required to keep the whole interferometer at the proper angular alignment.

The optical sensing for both the length and alignment degrees-of-freedom is derived from photodetectors located at five output ports of the interferometer:

- Reflection port (REFL): the light reflected from the power recycling mirror; typically ~10% of the beam is detected.
- Power recycling cavity pick-off (POP): the beam transmitted by PR2 coming from the beamsplitter; typically ~10% of the beam is detected .
- Anti-symmetric port (AS): the beam exiting the signal recycling mirror; typically 99% of this beam is directed to the DC readout detectors, and 1% is directed to alignment and auxiliary detectors .
- ETM transmissions (TRX & TRY): beams transmitted by the two end test masses; typically a few percent of each beam is detected .

### Length sensing and control :

The length sensing scheme is similar to that used in initial LIGO , extended to sense the length of the new signal recycling cavity. As per standard practice, the arm cavity lengths are treated in the basis of common and differential modes: the former is the average arm length, equivalent to the laser frequency, and the latter is the arm length difference, which is also the gravitational wave signal mode.

Two sets of RF modulation sidebands are applied to the input laser field: one at 9 MHz and one at 45 MHz. Both pairs of RF sidebands are resonant in the power-recycling cavity, but not in the arm cavities. The Michelson contains the usual Schnupp asymmetry so that RF sideband power is transmitted to the AS port even when the carrier is at the dark fringe. In this case, we choose the asymmetry to couple the majority of the 45 MHz sideband power into the signal recycling cavity. This can be achieved either with a relatively small (several cm) or relatively large (tens of cm) asymmetry, but the former is preferred because it suppresses the 9 MHz power in the SRC, leading to better separation of error signals for the two recycling cavities. With our Schnupp asymmetry of 8 cm, and a SRM transmission of 35%, nearly all of the 45 MHz sideband power is transmitted to the AS output, while only about 0.3% of the 9 MHz power arrives there.

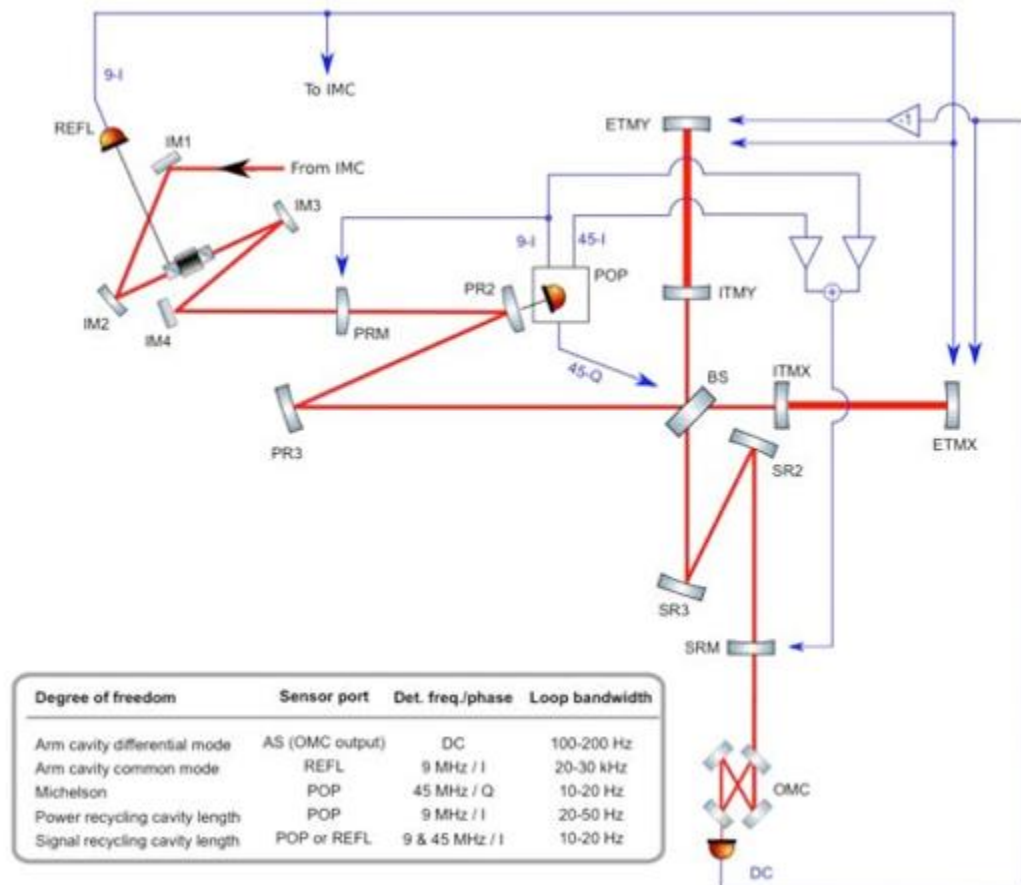


*Fig 55 : Length sensing and control scheme for Advanced LIGO. Though not shown, the Michelson signal is also fed back to the PRM and SRM, so that the BS actuation affects only the Michelson degree-of-freedom.*

Figure 55 summarizes the sensing and control scheme for the length degrees-of freedom. Except for the DC readout of the GW channel, the length signals are derived from photodetectors at the REFL and POP ports, by demodulating their outputs at one or more of the RF modulation frequencies. The feedback controls are implemented digitally, with a real-time sampling rate of 16,384 samples/sec. The arm common mode loop actuates on the laser frequency so that it follows the highly stable common arm length. The servo includes an analogue feedback path to achieve high bandwidth. The design of this complex common mode servo follows that of initial LIGO .

All of the photodetectors used for the length sensing during low-noise operation are located in vacuum chambers, mounted on seismically isolated platforms. This is done to reduce spurious noise effects in the signal detection, such as from vibrations of the detectors, acoustic modulation of paths in air, or from particulates falling through the beams.

For the auxiliary degrees-of-freedom (DoF) – all those other than the arm cavity differential mode – the control loop design involves a trade-off between having adequate loop gain to avoid non-linear effects, and limiting the coupling of noise into the GW channel. These auxiliary DoF couple weakly to the GW channel, at a level of order 10-2 or smaller (meters/meter). However, the shot-noise limited sensing of these channels is 35 orders of magnitude worse—in terms of equivalent displacement—than the GW channel. Thus if the sensing noise of the auxiliary channels is impressed onto these DoF through their feedback loops, it can easily spoil the GW sensitivity. This noise mechanism is mitigated partially through the design of the auxiliary DoF servo loops: the loop bandwidths are kept low, and low-pass filters with cut-offs just above the unity gain frequencies are employed. In addition, noise correction paths are implemented: the auxiliary loop control signals are appropriately scaled and filtered, then added to the GW channel control signal to remove their coupling (feed-forward noise suppression). These correction paths reduce the auxiliary DoF noise infiltration by 30-40 dB.

### **Alignment sensing and control :**

The residual angular motion of the arm cavity mirrors must be 1 nrad-rms or less to adequately suppress alignment noise effects . This is 2-3 orders of magnitude smaller than their locally-controlled angular motion. Somewhat less stringent angular stability requirements apply to the other interferometer optics. The alignment sensing and control scheme designed to provide this level of stability is an extension of the Initial LIGO design . The same phase modulation demodulation techniques used for the length sensing are used with quadrant photodiodes to produce an alignment wavefront sensor (WFS). A WFS produces an alignment signal via the interference between the fundamental TEM00 Hermite-Gaussian field component and the TEM01/TEM10 field components generated by misalignments. Several new aspects of the alignment control design must be considered for Advanced LIGO:

- High circulating power in the arms produces significant radiation pressure torques on the cavity mirrors
- Additional degrees-of-freedom: signal recycling introduces a new mirror that must be aligned; the folded recycling cavities introduce another four mirrors .
- Alignment control noise must be filtered out starting at a much lower frequency

The radiation pressure effects are typically described in terms of a soft and hard alignment mode, depending on whether the optical torque subtracts from or adds to the mechanical

stiffness of the suspension . This is illustrated in Figure 56 for a single cavity. In Advanced LIGO, the radiation pressure torque becomes greater than the suspension mechanical torque at arm cavity powers above 700 kW. Above this, the soft mode becomes dynamically unstable, and must be actively stabilized. As the unstable eigenfrequency stays low even at full power (less than 0.3 Hz), it is straightforward to stabilize even with low bandwidth.

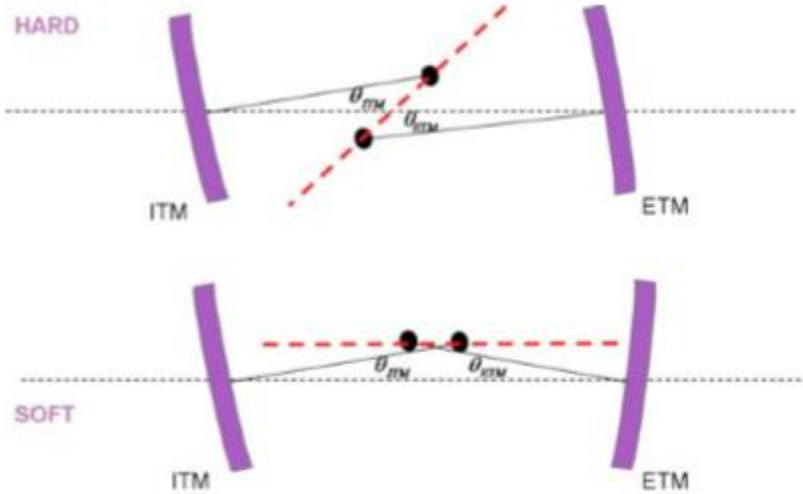


*Fig 56 : Representation of the hard and soft modes of cavity mirror alignment.*

The alignment WFS are located at the REFL and AS interferometer ports; two WFS are installed at different beam line positions at each port, such that they are separated in Gouy phase by 90 degrees. This allows combinations of WFS signals to be formed to reconstruct any Gouy phase. In addition to the WFS, several quadrant photodiodes (QPDs) provide relative beam position information. The TRX, TRY and POP ports each have two QPDs, with each pair separated by 90 degrees Gouy phase. Lastly, the AS port contains a single QPD (detecting a small fraction of the AS beam). As with the length sensors, all of the alignment sensors that are used in low-noise operation (both WFS and QPD) are located in vacuum chambers, mounted on seismically isolated platforms .

The control scheme for the arm cavity mirrors and the beamsplitter is summarized in Table 11. The other optics can be controlled using various combinations of the other WFS and QPD signals; these loops are implemented essentially for drift control, with bandwidths of 0.1 Hz or less.

Degree of freedom	Sensor type & port	Detection frequency/phase	Loop unity gain frequency
Arm cavity differential hard mode	WFS AS	45 MHz Q-phase	1-few Hz
Arm cavity common hard mode	WFS REFL	9 MHz I-phase	~1 Hz
Arm cavity differential soft mode	QPD TRX-TRY	DC	~1 Hz
Arm cavity common soft mode	QPD TRX+TRY	DC	~1 Hz
Beamsplitter	WFS AS	36 MHz Q-phase	~0.1 Hz

Table 11 : Alignment control scheme for the arm cavity mirror (test masses) and the beamsplitter.

### Output mode cleaner and DC readout :

The output mode cleaner (OMC) is designed to filter out all RF sideband and higher-order spatial mode light at the AS port, so that the main photodetectors receive only light that carries the gravitational wave signal. The OMC is a bowtie cavity with a moderate finesse (400); this is a trade-off between having a narrow bandwidth to filter out RF components, and maintaining a high transmission efficiency (> 95%). The OMC higher-order mode spacing is fine-tuned (via the cavity length) to avoid overlap with higher-order modes likely to exit the interferometer AS port. The nominal OMC round trip length is 1.13 m.

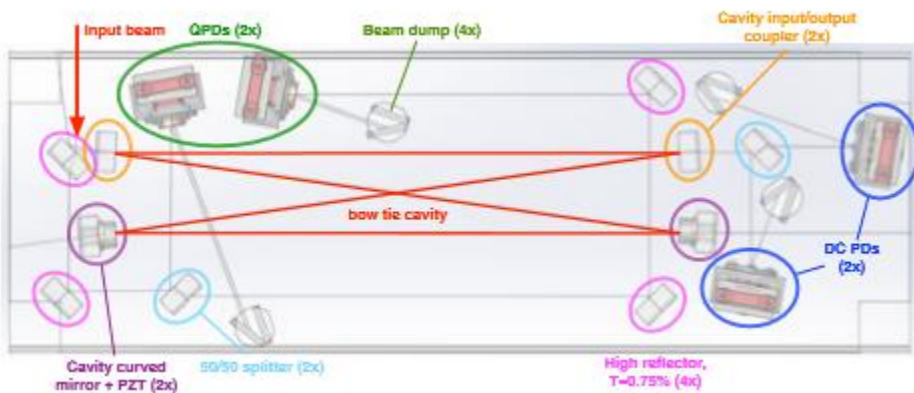


Fig 57 : Layout of the OMC on the fused silica breadboard (dimensions 45cm x 15cm x 4.1cm).

As shown in Figure 57 , the OMC cavity optics and the output photodiodes are all bonded to a single breadboard of fused silica. This minimizes relative motion between the OMC output beam and the diodes, which can otherwise be a source of noise. The breadboard also includes two QPDs for aid in alignment, and multiple beam dumps for scattered light. Two of the OMC mirrors are mounted on PZT actuators for length control of the cavity. The OMC cavity is locked to the AS port beam with a dither scheme: one of the PZTs applies a small modulation to the cavity length at a frequency of several kHz; the output detectors are demodulated at the

dither frequency, and the resulting error signal is fed back to the other PZT to maintain resonance. For vibration isolation, the whole breadboard is mounted in a two-stage suspension that has active damping and pointing capability. The OMC suspension is mounted in a HAM vacuum chamber on a HAM seismic isolation platform.

The AS port beam is directed into the OMC by three steering optics. These optics provide mode-matching to the OMC, and they are mounted in active single-stage suspensions for vibration isolation and pointing control. There are several possible schemes for alignment optimization and control of the beam into the OMC. A simple method is to dither the pointing direction of the AS port beam using the suspended steering optics, and demodulate the OMC transmitted signal at the dither frequencies.

### **Arm length stabilization and lock acquisition :**

Lock acquisition is the process of bringing the interferometer to its operating point, with all the cavities resonant so that power build up is at a maximum. Advanced LIGO implements a new lock acquisition scheme that incorporates two significant features:

- An arm length stabilization system is used to control the microscopic length of each arm cavity, independently of the other degrees-of-freedom .
- The vertex dual-recycled Michelson interferometer is initially locked with the third harmonic technique (3f-technique), providing more robust control during the acquisition process .

The idea of the arm length stabilization system (ALS) is to lock each arm cavity individually using a laser mounted behind each end test mass. The arm cavities are then held away from resonance for the main laser light by offsetting the frequency of the end station ALS lasers, relative to the main laser frequency. The ALS lasers are doubled Nd:YAG lasers, operating at 532 nm to distinguish them from the main laser light; they also have a 1064 nm output which is used to phase (frequency offset) lock them to the main laser light. The test masses have dichroic coatings designed to create a relatively low finesse cavity for 532 nm, with reasonable transmission of 532 nm light to the vertex beamsplitter.

In the vertex, one of the ALS beams is interfered with a doubled sample of the main laser light, and the two ALS beams are interfered with each other (see figure 58). The former produces a common mode signal that is used to control the frequency of the main laser. The latter produces a differential mode signal that is used to stabilize the differential arm length.

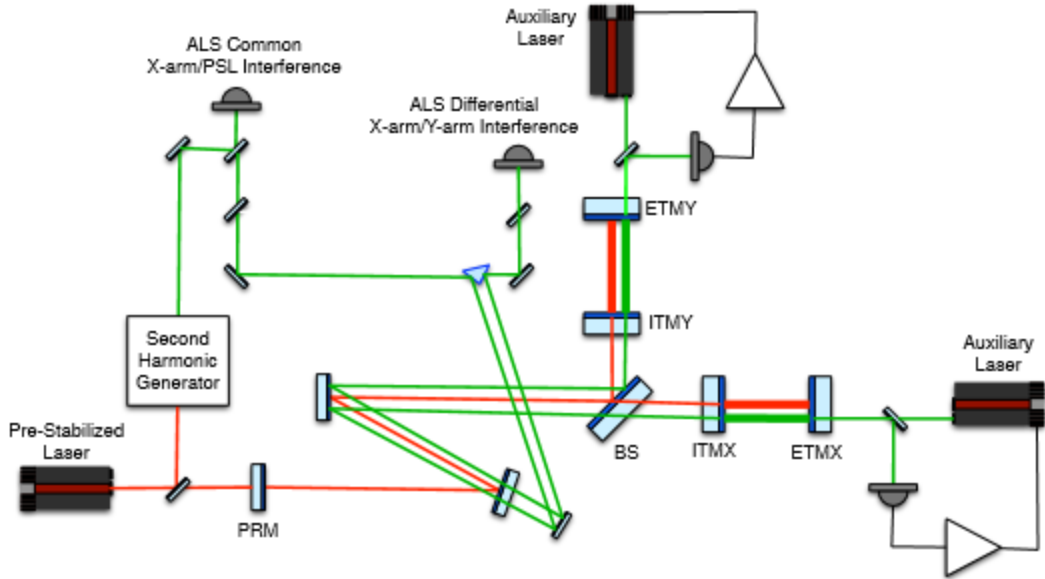


Fig 58 : Simplified schematic of the arm length stabilization system.

The acquisition process is as follows : Each ALS laser is locked to its arm cavity at 532 nm. The ALS common and differential mode loops are then engaged, using the vertex 532 nm heterodyne signals. The common mode frequency difference is set so that the main 1064 nm laser light is about 500 Hz away from resonance in the arm cavities. The vertex dual-recycled Michelson is then locked using the 3f-technique. Next, the common mode frequency offset is gradually reduced to zero to bring the interferometer to the operating point; this step is the most critical and in fact involves several transitions that are fully described in reference . At the operating point, all sensor signals are switched over to the low-noise .

#### 10.5.9) Calibration

The output signal of the LIGO detector is a calibrated time series of “external” differential length variation between two arm cavities, reconstructed from control and error point signals of the differential arm length servo by applying an appropriate response function.

Errors in the interferometer response function degrade the ability to detect gravitational waves and the ability to measure source properties of detected signals . Calibration accuracy is naturally more important for source parameter extraction than for detection. We have set the calibration accuracy requirements at 5% in amplitude and 16 $\mu$ sec in timing, over  $2\sigma$  confidence levels. This is consistent with requirements for detection of strong binary black-hole signals .

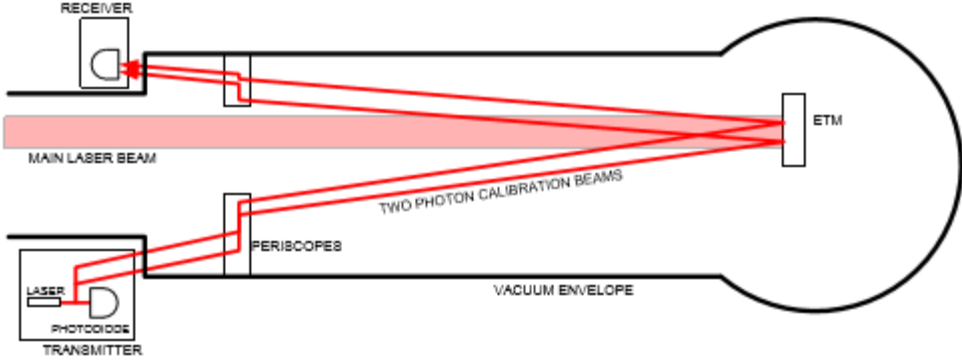


*Fig 59 : Schematic of the photon calibration system .*

Three different calibration methods are employed to allow cross-checks on accuracy: (a) free-swinging Michelson ; (b) frequency modulation ; (c) photon calibrator . In the free-swinging Michelson method the interferometer laser light is used as the length reference to calibrate Michelson interference fringes as the test masses either move freely or are forced through several microns of motion. This method calibrates ETM actuation with drive amplitude on the order of  $10^{-12}$  m. The frequency modulation method is used with a single resonant arm cavity. In this configuration, a known modulation of the laser frequency calibrates the cavity sensing signal in terms of equivalent length modulation. A simultaneous drive of the ETM actuator ( $10^{-14}$  m) at a slightly different frequency is then used to derive its actuation calibration.

The photon calibration method uses an auxiliary, power-modulated laser to create displacements via photon recoil off the surface of the ETM Figure 59. Two beams are used, offset symmetrically from the mirror centre. The offset moves elastic deformation caused by the photon pressure away from the location of the main interferometer beam, and the two-beam geometry avoids imposing torque. The laser power is measured with a temperature stabilized InGaAs photodetector mounted on an integrating sphere, which is calibrated against a NIST-calibrated standard. The lasers are 2 W continuous-wave, 1047nm Nd:YLF lasers. An AOM enables power modulation, up to a peak-to-peak sinusoidal modulation of 1 W, producing an ETM displacement of  $10^{-16}$  m-rms at 100 Hz.

#### 10.5.10) Physical environmental monitoring

To complete each LIGO detector, the interferometers described so far are supplemented with a set of sensors to monitor the local environment Figure 60 . Seismometers and accelerometers measure vibrations of the ground and various interferometer components; microphones monitor acoustic noise at critical locations; magnetometers monitor fields that could couple to the test masses or electronics; and radio receivers monitor RF power around the modulation frequencies. This is an expanded version of the environmental monitoring system employed in initial LIGO . These sensors are used to detect environmental disturbances that can couple to the gravitational wave channel .

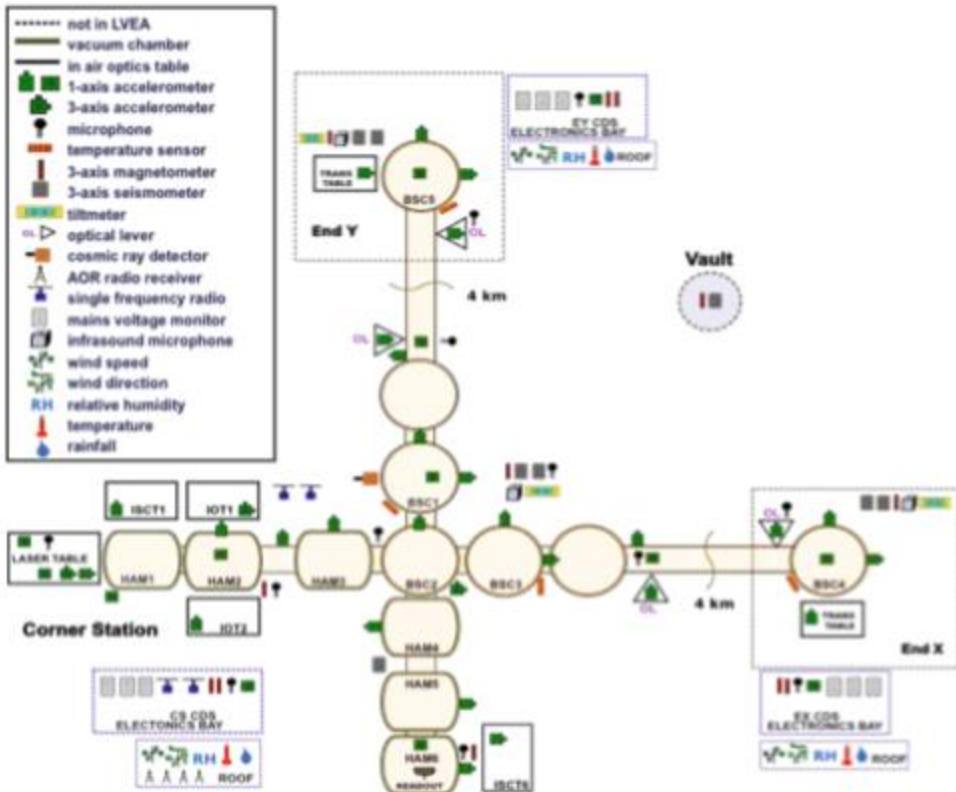
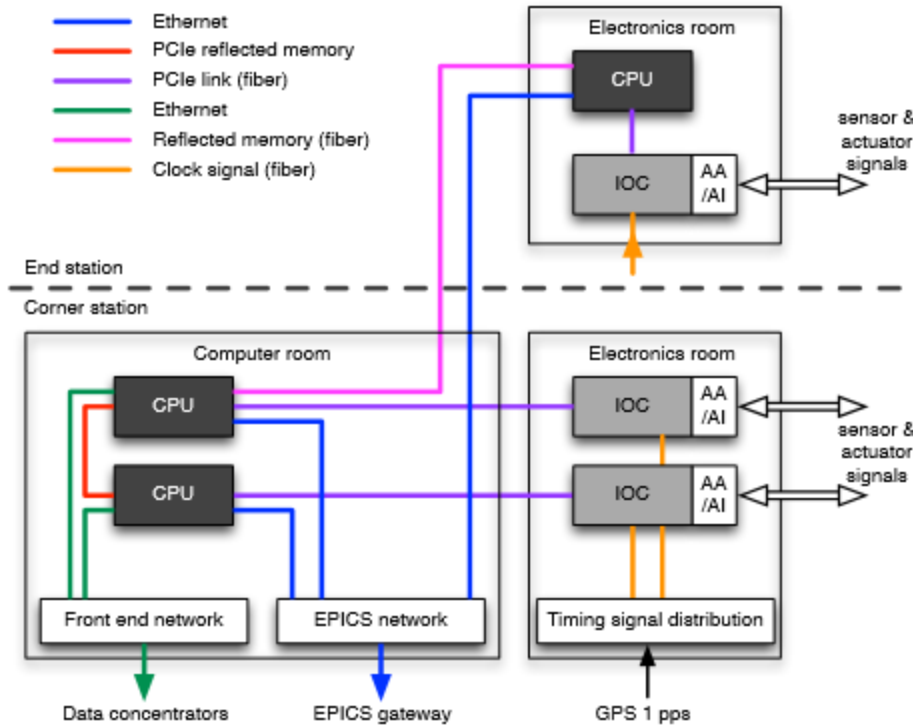


Fig 60 : Physical environmental monitoring sensors at LLO. The test masses are in the vacuum chambers BSC1/3 (ITMs) and BSC4/5 (ETMs), and the 50/50 beamsplitter is in BSC1.

### 10.5.11) Controls and data acquisition

Many of the subsystems employ real-time digital controls in their functioning; data from other subsystems and channels must be acquired in real-time for archiving and analysis. A custom data acquisition architecture, diagrammed in Figure 61, is implemented to serve these needs.



*Fig 61 : Schematic of the data acquisition architecture.*

Interferometer sensor and actuator signals flow through custom input-output chassis (IOC). Each IOC houses: a 17 slot PCI Express (PCIe) backplane; a timing module that provides accurate triggering at 65536 Hz and is synchronized with the interferometer timing distribution system; a commercial fibre optic PCIe uplink to a real-time control computer. The PCIe slots are populated specifically for each IOC, but primarily contain commercial multi-channel, simultaneous sampling 16-bit analogue-to-digital and 16 and 18-bit digital-to-analogue converters (ADCs and DACs). Custom anti-alias and anti image filters interface between the ADCs and DACs and the analogue signals. The IOCs and filters are located in rooms separate from the vacuum chamber areas to mitigate electronic and acoustic interference with sensitive interferometer components.

The real-time control computers are located yet further from the interferometer, in a separate computer room, and are linked via fibre. The computers are commercial, multicore rack mount units, specially selected for compatibility with real-time operation: there must be no uncontrollable system interrupts, and they must be capable of supporting the required number of PCIe modules.

The system is designed to support servo loop rates of up to 65536 Hz, which requires real-time execution to be precise and repeatable to within a few microseconds, and synchronized across the site. To attain this performance, the GPL Linux operating system is used on the control computers, but with a LIGO custom kernel patch. This patch allows the isolation of a given CPU core from the Linux system for exclusive use by a real-time control program.

Specific subsystem data acquisition and control programs are created with the aid of a real-time code generator (RCG). The RCG provides a set of custom software modules, as well as

support of many MATLAB Simulink parts. Using Simulink as the GUI, code is developed as a graphical model that describes the desired execution sequence. Standard scripts then produce executable software from the model.

A key RCG component is the IIR (infinite-impulse response) filter module, which is used to define control transfer functions and channel calibrations. A given control model may contain a few hundred of these modules, each module containing up to 10 second order section filters. The system supports reloading of filter coefficients during runtime, so that new filters can be implemented on the fly.

Real-time communications between RCG models is provided on several levels: via shared memory for applications running on the same computer; via a PCIe network for computers located within 300m of each other; via a reflected memory network for computers 4km apart. One core on each CPU is reserved for a special model known as the I/O processor (IOP). The IOP handles the interfacing to the I/O hardware modules, and synchronizes the user code execution with the interferometer timing system. The interferometer timing system distributes a 65536 Hz clock signal to all of the IOCs; this clock is synchronized to Global Positioning System time. Timing is also distributed to the front-end computers, to provide time-stamps for real-time communications between RCG models.

The control system also uses the Experimental Physics and Industrial Control System (EPICS) software to provide communications between real-time systems and user interfaces. Though not shown in Figure 61 , much of the slow controls hardware (switch settings, slow readbacks, etc.) is managed using an EtherCAT (Ethernet for Control Automation Technology) system.

A custom hierarchical state machine, known as Guardian, manages the global state of the interferometers. Written in Python, Guardian consists of a distributed set of automaton nodes, each handling automation for a distinct sub-domain of the instrument. Each node is loaded with a directed state graph that describes the dynamics of its subdomain. A master manager node at the top of the hierarchy communicates with multiple sub-manager nodes; these in turn communicate with device level nodes at the bottom of the hierarchy, which directly control the instrument through EPICS. Guardian provides automation of interferometer lock acquisition, as well as the subsequent transitioning to low-noise operation.

#### 10.5.12) Outlook

Both Advanced LIGO interferometers are currently in the commissioning phase, in which the lock acquisition scheme is implemented and the strain sensitivity is progressively improved. When the sensitivity reaches an astrophysically significant level, the instruments will be operated in observing runs: months- to years-long periods of continuous and coincident data collection. The first Advanced LIGO observing run started in 2015, with a duration of 3 months and a BNS detection range of 40— 80 Mpc. Subsequent observing runs will have increasing sensitivity and duration. A 6 month run in 2016-2017 with a BNS detection range of 80—120 Mpc, and a 9 month run in 2017-2018 at 120—170 Mpc. The full sensitivity corresponding to a 200 Mpc BNS range should be achieved by 2019.

## 11) CASE STUDY : GW150194

### 11.1 ) OBSERVATION

On September 14, 2015 at 09:50:45 UTC, the LIGO Hanford, WA, and Livingston, LA, observatories detected the coincident signal GW150914 shown in Figure 62. The initial detection was made by low-latency searches for generic gravitational-wave transients and was reported within three minutes of data acquisition. Subsequently, matched-filter analyses that use relativistic models of compact binary waveforms recovered GW150914 as the most significant event from each detector for the observations reported here. Occurring within the 10-ms intersite propagation time, the events have a combined signal-to-noise ratio (SNR) of 24.

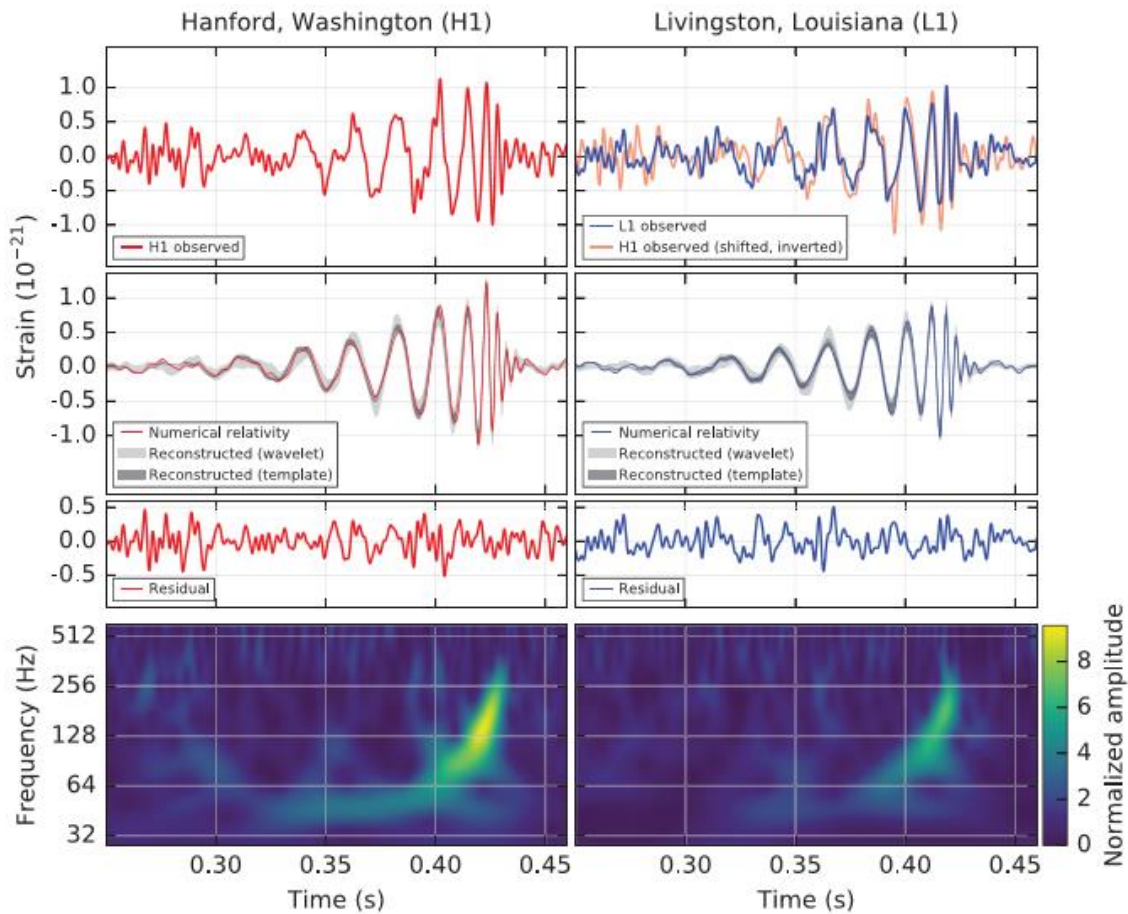


*Fig. 62 : The gravitational-wave event GW150914 observed by the LIGO Hanford (H1, left column panels) and Livingston (L1, right column panels) detectors. Times are shown relative to September 14, 2015 at 09:50:45 UTC. For visualization, all time series are filtered with a 35–350 Hz bandpass filter to suppress large fluctuations outside the detectors' most sensitive frequency band, and band-reject filters to remove the strong instrumental spectral lines. Top row, left: H1 strain. Top row, right: L1 strain. GW150914 arrived first at L1 and  $6.9^{+0.5}_{-0.4}$  ms later at H1; for a visual comparison, the H1 data are also shown, shifted in time by this amount*

*and inverted (to account for the detectors' relative orientations). Second row: Gravitational-wave strain projected onto each detector in the 35–350 Hz band. Solid lines show a numerical relativity waveform for a system with parameters consistent with those recovered from GW150914 confirmed to 99.9% by an independent calculation based on . Shaded areas show 90% credible regions for two independent waveform reconstructions. One (dark gray) models the signal using binary black hole template waveforms . The other (light gray) does not use an astrophysical model, but instead calculates the strain signal as a linear combination of sine-Gaussian wavelets . These reconstructions have a 94% overlap, as shown in . Third row: Residuals after subtracting the filtered numerical relativity waveform from the filtered detector time series. Bottom row :A time-frequency representation of the strain data, showing the signal frequency increasing over time.*

Only the LIGO detectors were observing at the time of GW150914. The Virgo detector was being upgraded, and GEO 600, though not sufficiently sensitive to detect this event, was operating but not in observational mode. With only two detectors the source position is primarily determined by the relative arrival time and localized to an area of approximately 600 deg<sup>2</sup> (90% credible region) .

The basic features of GW150914 point to it being produced by the coalescence of two black holes—i.e., their orbital inspiral and merger, and subsequent final black hole ring down Over 0.2s ,the signal increases in frequency and amplitude in about 8 cycles from 35 to 150 Hz, where the amplitude reaches a maximum. The most plausible explanation for this evolution is the inspiral of two orbiting masses, m<sub>1</sub> and m<sub>2</sub>, due to gravitational-wave emission. At the lower frequencies, such evolution is characterized by the chirp mass

$$\mathcal{M} = \frac{(m_1 m_2)^{3/5}}{(m_1 + m_2)^{1/5}} = \frac{c^3}{G} \left[ \frac{5}{96} \pi^{-8/3} f^{-11/3} \dot{f} \right]^{3/5},$$

where f and f ‘ are the observed frequency and its time derivative and G and c are the gravitational constant and speed of light. Estimating f and f from the data in Figure 62 , we obtain a chirp mass of M≈30M<sub>⊙</sub>, implying that the total mass M =m<sub>1</sub> + m<sub>2</sub> is≥70M<sub>⊙</sub> in the detector frame. This bounds the sum of the Schwarzschild radii of the binary components to 2GM/ c<sup>2</sup> ≥210 km. To reach an orbital frequency of 75 Hz (half the gravitational-wave frequency) the objects must have been very close and very compact; equal Newtonian point masses orbiting at this frequency would be only ≈350 km apart. A pair of neutron stars, while compact, would not have the required mass, while a black hole neutron star binary with the deduced chirp mass would have a very large total mass, and would thus merge at much lower frequency. This leaves black holes as the only known objects compact enough to reach an orbital frequency of 75 Hz without contact. Furthermore, the decay of the waveform after it peak is consistent with the damped oscillations of a black hole relaxing to a final stationary Kerr configuration. Below, we present a general-relativistic analysis of GW150914; Figure 63 shows the calculated waveform using the resulting source parameters.

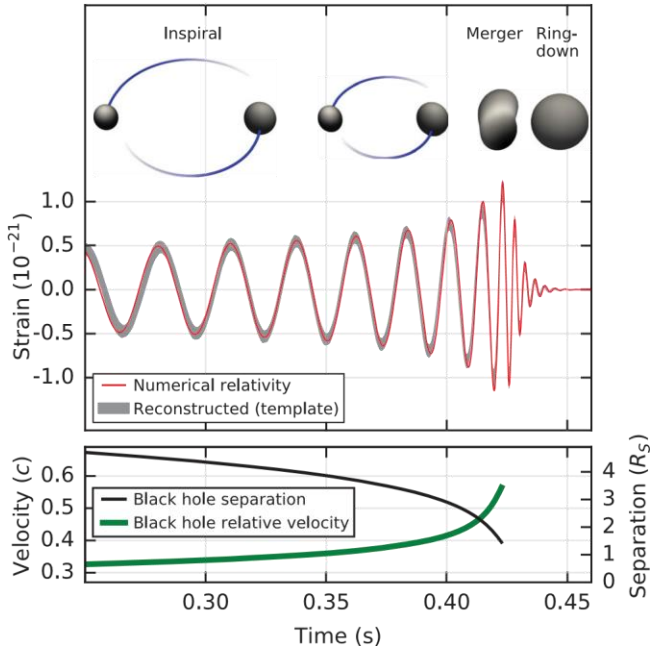


*Fig 63 :. Top: Estimated gravitational-wave strain amplitude from GW150914 projected onto H1. This shows the full bandwidth of the wave forms , without the filtering used for Figure 62 . The inset images show numerical relativity models of the black hole horizons as the black holes coalesce. Bottom: The Keplerian effective black hole separation in units of Schwarzschild radii ( $R_S=2GM/c^2$ ) and the effective relative velocity given by the post-Newtonian parameter  $v/c=(GM\pi f/c^3)^{1/3}$  , where  $f$  is the gravitational-wave frequency calculated with numerical relativity and  $M$  is the total mass*

## 11.2 ) VALIDATION OF DETECTORS

Both detectors were in steady state operation for several hours around GW150914. All performance measures, in particular their average sensitivity and transient noise behaviour, were typical of the full analysis period .

Exhaustive investigations of instrumental and environmental disturbances were performed, giving no evidence to suggest that GW150914 could be an instrumental artifact . The detectors' susceptibility to environmental disturbances was quantified by measuring their response to specially generated magnetic, radio-frequency, acoustic, and vibration excitations. These tests indicated that any external disturbance large enough to have caused the observed signal would have been clearly recorded by the array of environmental sensors. None of the environmental sensors recorded any disturbances that evolved in time and frequency like GW150914, and all environmental fluctuations during the second that contained GW150914 were too small to account for more than 6% of its strain amplitude. Special care was taken to search for long-range correlated disturbances that might produce nearly simultaneous signals at the two sites. No significant disturbances were found.

The detector strain data exhibit non-Gaussian noise transients that arise from a variety of instrumental mechanisms. Many have distinct signatures, visible in auxiliary data channels that

are not sensitive to gravitational waves; such instrumental transients are removed from our analyses . Any instrumental transients that remain in the data are accounted for in the estimated detector backgrounds described below. There is no evidence for instrumental transients that are temporally correlated between the two detectors.

### 11.3) SERCHES

The analysis of 16 days of coincident observations between the two LIGO detectors from September 12 to October 20, 2015 is as presented . This is a subset of the data from Advanced LIGO’s first observational period that ended on January 12, 2016.

GW150914 is confidently detected by two different types of searches. One aims to recover signals from the coalescence of compact objects, using optimal matched filtering with waveforms predicted by general relativity. The other search targets a broad range of generic transient signals ,with minimal assumptions about wave forms .These searches use independent methods, and their response to detector noise consists of different, uncorrelated, events. However , strong signals from binary black hole mergers are expected to be detected by both searches.

Each search identifies candidate events that are detected at both observatories consistent with the intersite propagation time. Events are assigned a detection-statistic value that ranks their likelihood of being a gravitational-wave signal. The significance of a candidate event is determined by the search background—the rate at which detector noise produces events with a detection-statistic value equal to or higher than the candidate event. Estimating this background is challenging for two reasons: the detector noise is nonstationary and non-Gaussian, so its properties must be empirically determined; and it is not possible to shield the detector from gravitational waves to directly measure a signal-free background. The specific procedure used to estimate the background is slightly different for the two searches, but both use a time-shift technique: the time stamps of one detector’s data are artificially shifted by an offset that is large compared to the intersite propagation time, and a new set of events is produced based on this time-shifted data set. For instrumental noise that is uncorrelated between detectors this is an effective way to estimate the background. In this process a gravitational wave signal in one detector may coincide with time-shifted noise transients in the other detector, thereby contributing to the background estimate . This leads to an over estimate of the noise background and therefore to a more conservative assessment of the significance of candidate events.

The characteristics of non-Gaussian noise vary between different time-frequency regions. This means that the search backgrounds are not uniform across the space of signals being searched .To maximize sensitivity and provide a better estimate of event significance, the searches sort both their background estimates and their event candidates into different classes according to their time-frequency morphology. The significance of a candidate event is measured against the background of its class. To account for having searched multiple classes, this significance is decreased by a trials factor equal to the number of classes .

### 11.3.1) A generic transient search

Designed to operate without a specific waveform model, this search identifies coincident excess power in time frequency representations of the detector strain data , for signal frequencies up to 1 kHz and durations up to a few seconds.

The search reconstructs signal waveforms consistent with a common gravitational-wave signal in both detectors using a multi detector maximum likelihood method. Each event is ranked according to the detection statistic

$$\eta_c = \sqrt{2E_c/(1 + E_n/E_c)},$$

where  $E_c$  is the dimensionless coherent signal energy obtained by cross-correlating the two reconstructed waveforms, and  $E_n$  is the dimensionless residual noise energy after the reconstructed signal is subtracted from the data. The statistic  $\eta_c$  thus quantifies the SNR of the event and the consistency of the data between the two detectors.

Based on their time-frequency morphology, the events are divided into three mutually exclusive search classes : events with time-frequency morphology of known populations of noise transients (class C1), events with frequency that increases with time (class C3), and all remaining events (class C2).

Detected with  $\eta_c = 20.0$  , GW150914 is the strongest event of the entire search. Consistent with its coalescence signal signature, it is found in the search class C3 of events with increasing time-frequency evolution. Measured on a background equivalent to over 67400 years of data and including a trials factor of 3 to account for the search classes, its false alarm rate is lower than 1 in 22500 years. This corresponds to a probability  $< 2 \times 10^{-6}$  of observing one or more noise events as strong as GW150914 during the analysis time, equivalent to  $4.6\sigma$ . The left panel of Figure 64 shows the C3 class results and background.

The selection criteria that define the search class C3 reduce the background by introducing a constraint on the signal morphology. In order to illustrate the significance of GW150914 against a background of events with arbitrary shapes, we also show the results of a search that uses the same set of events as the one described above but without this constraint .Specifically ,we use only two search classes: the C1 class and the union of C2 and C3 classes (C2+C3) . In this two-class search the GW150914 event is found in the C2+C3 class. The left panel of Figure 64 shows the C2+C3 class results and background. In the background of this class there are four events with  $\eta_c \geq 32.1$ , yielding a false alarm rate for GW150914 of 1 in 8400 years. This corresponds to a false alarm probability of  $5 \times 10^{-6}$  equivalent to  $4.4\sigma$ .

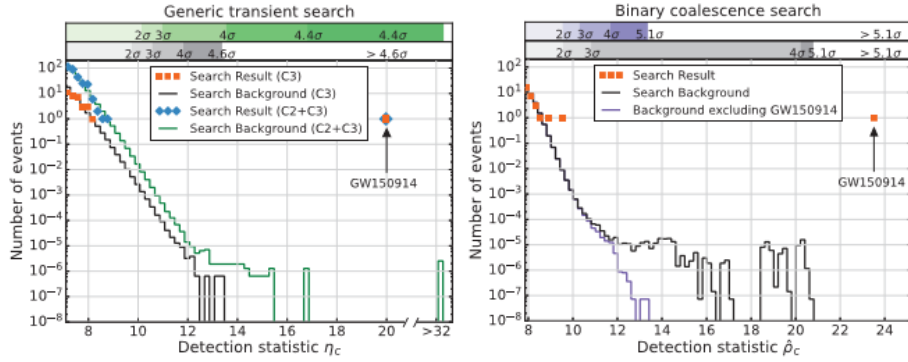


*Fig 64 : Search results from the generic transient search (left) and the binary coalescence search (right). These histograms show the number of candidate events (orange markers) and the mean number of background events (black lines) in the search class where GW150914 was found as a function of the search detection statistic and with a bin width of 0.2. The scales on the top give the significance of an event in Gaussian standard deviations based on the corresponding noise background. The significance of GW150914 is greater than  $5.1\sigma$  and  $4.6\sigma$  for the binary coalescence and the generic transient searches, respectively. Left: Along with the primary search (C3) we also show the results (blue markers) and background (green curve) for an alternative search that treats events independently of their frequency evolution (C2+C3). The classes C2 and C3 are defined in the text. Right: The tail in the black-line background of the binary coalescence search is due to random coincidences of GW150914 in one detector with noise in the other detector.(This type of event is practically absent in the generic transient search background because they do not pass the time-frequency consistency requirements used in that search.)The purple curve is the background excluding those coincidences, which is used to assess the significance of the second strongest event.*

For robustness and validation, we also use other generic transient search algorithms .A different search and a parameter estimation follow-up detected GW150914 with consistent significance and signal parameters.

### 11.3.2) Binary coalescence search:

This search targets gravitational-wave emission from binary systems with individual masses from  $1$  to  $99M_{\odot}$ , total mass less than  $100M_{\odot}$ , and dimensionless spins up to  $0.99$  . To model systems with total mass larger than  $4M_{\odot}$ ,we use the effective-one-body formalism ,which combines results from the post-Newtonian approach with results from black hole perturbation theory and numerical relativity. The waveform model assumes that the spins of the merging objects are aligned with the orbital angular momentum, but the resulting templates can, nonetheless, effectively recover systems with misaligned spins in the parameter region of GW150914. Approximately 250000 template waveforms are used to cover this parameter space .

The search calculates the matched-filter signal-to-noise ratio  $\rho(t)$  for each template in each detector and identifies maxima of  $\rho(t)$  with respect to the time of arrival of the signal , For each maximum we calculate a chi-squared statistic  $\chi^2_r$ to test whether the data in several

different frequency bands are consistent with the matching template . Values  $\chi^2_r$  of near unity indicate that the signal is consistent with a coalescence . The final step enforces coincidence between detectors by selecting event pairs that occur within a 15-ms window and come from the same template. The 15-ms window is determined by the 10-ms intersite propagation time plus 5 ms for uncertainty in arrival time of weak signals. We rank coincident events based on the quadrature sum  $p_c$  of the  $p$  from both detectors . To produce background data for this search the SNR maxima of one detector are time shifted and a new set of coincident events is computed. Repeating this procedure  $\sim 10^7$  times produces a noise background analysis time equivalent to 608,000 years.

To account for the search background noise varying across the target signal space, candidate and background events are divided into three search classes based on template length. The GW150914 detection statistic value of  $p_c = 23.6$  is larger than any background event, so only an upper bound can be placed on its false alarm rate. Across the three search classes this bound is 1 in 203,000 years. This translates to a false alarm probability  $< 2 \times 10^{-7}$ , corresponding to  $5.1\sigma$ .

A second, independent matched-filter analysis that uses a different method for estimating the significance of its events , also detected GW150914 with identical signal parameters and consistent significance.

Primary black hole mass	$36^{+5}_{-4} M_\odot$
Secondary black hole mass	$29^{+4}_{-4} M_\odot$
Final black hole mass	$62^{+4}_{-4} M_\odot$
Final black hole spin	$0.67_{-0.00..0705}$
Luminosity distance	$410_{-180..160}$ Mpc
Source redshift z	$0.09_{-0.00..0403}$

*Table 12 : Source parameters for GW150914. We report median values with 90% credible intervals that include statistical errors, and systematic errors from averaging the results of different waveform models. Masses are given in the source frame; to convert to the detector frame multiply by  $(1+z)$  . The source redshift assumes standard cosmology .*

When an event is confidently identified as a real gravitational-wave signal, as for GW150914, the background used to determine the significance of other events is reestimated without the contribution of this event. Based on this, the second most significant event has a false alarm rate of 1 per 2.3 years and corresponding Poissonian false alarm probability of 0.02. Waveform analysis of this event indicates that if it is astrophysical in origin it is also a binary black hole merger

## 11.4) Source discussion

The matched-filter search is optimized for detecting signals, but it provides only approximate estimates of the source parameters. To refine them we use general relativity-based models , some of which include spin precession, and for each model perform a coherent Bayesian analysis to derive posterior distributions of the source parameters . The initial and final masses, final spin, distance, and redshift of the source are shown in Table 12. The spin of the primary black hole is constrained to be  $< 0.7$  (90% credible interval) indicating it is not maximally spinning, while the spin of the secondary is only weakly constrained. These source parameters are discussed in detail in . The parameter uncertainties include statistical errors and systematic errors from averaging the results of different waveform models.

Using the fits to numerical simulations of binary black hole mergers in , we provide estimates of the mass and spin of the final black hole, the total energy radiated in gravitational waves, and the peak gravitational-wave luminosity . The estimated total energy radiated in gravitational waves is  $3.0^{+0.5}_{-0.5} M_{\odot}$  The system reached a peak gravitational-wave luminosity of  $3.6^{+0.5}_{-0.5} \times 10^{56} ergs/s$ , equivalent to  $200^{+30}_{-20} M_{\odot} c^2/s$  .

Several analyses have been performed to determine whether or not GW150914 is consistent with a binary black hole system in general relativity . A first consistency check involves the mass and spin of the final black hole. In general relativity, the end product of a black hole binary coalescence is a Kerr black hole, which is fully described by its mass and spin. For quasi circular inspirals, these are predicted uniquely by Einstein's equations as a function of the masses and spins of the two progenitor black holes. Using fitting formulas calibrated to numerical relativity simulations , it was verified that the remnant mass and spin deduced from the early stage of the coalescence and those inferred independently from the late stage are consistent with each other, with no evidence for disagreement from general relativity .

Within the post-Newtonian formalism, the phase of the gravitational waveform during the inspiral can be expressed as a power series in  $f^{1/3}$ . The coefficients of this expansion can be computed in general relativity. Thus, we can test for consistency with general relativity by allowing the coefficients to deviate from the nominal values, and seeing if the resulting waveform is consistent with the data. In this second check we place constraints on these deviations, finding no evidence for violations of general relativity.

Finally, assuming a modified dispersion relation for gravitational waves , our observations constrain the Compton wavelength of the graviton to be  $\lambda_g > 10^{13}$  km, which could be interpreted as a bound on the graviton mass  $m_g < 1.2 \times 10^{-22} eV/c^2$ . This improves on Solar System and binary pulsar bounds by factors of a few and a thousand, respectively, but does not improve on the model dependent bounds derived from the dynamics of Galaxy clusters and weak lensing observations . In summary, all three tests are consistent with the predictions of general relativity in the strong-field regime of gravity.

GW150914 demonstrates the existence of stellar-mass black holes more massive than  $\simeq 25 M_{\odot}$ , and establishes that binary black holes can form in nature and merge within a Hubble time. Binary black holes have been predicted to form both in isolated binaries and in dense

environments by dynamical interactions . The formation of such massive black holes from stellar evolution requires weak massive-star winds, which are possible in stellar environments with metallicity lower than  $\simeq 1/2$  the solar value.

Binary black hole systems at larger distances contribute to a stochastic background of gravitational waves from the superposition of unresolved systems. Predictions for such a background are presented in . If the signal from such a population were detected, it would provide information about the evolution of such binary systems over the history of the universe.

### 11.5) Conclusion

The LIGO detectors have observed gravitational waves from the merger of two stellar-mass black holes. The detected waveform matches the predictions of general relativity for the inspiral and merger of a pair of black holes and the ringdown of the resulting single black hole. These observations demonstrate the existence of binary stellar-mass black hole systems. This is the first direct detection of gravitational waves and the first observation of a binary black hole merger.

## **BIBLIOGRAPHY :**

- 1) STEVEN WEINBERG , GRAVITATION AND COSMOLOGY , WILEY , 1972 .
- 2) ROBERT RESNICK , INTRODUCTION TO SPECIAL RELATIVITY , WILEY , 1998 .
- 3) SATYA PRAKASH , MATHEMATICAL PHYSICS , SULTAN CHAND & SONS , 2012.
- 4) PETER R. SAULSON , DEPARTMENT OF PHYSICS SYRACUSE UNIVERSITY, SYRACUSE, NY 13244-1130 .
- 5) B.P. ABBOTT , ET AL , LIGO SCIENTIFIC COLLABORATION AND VIRGO COLLABORATION .
- 6) RONG-GEN CAI , ZHOUJIAN CAO , ZONG-KUAN GUO , SHAO-JIANG WANG , TAO YANG , arXiv : 1703.00187v2[gr-qc] 27 May 2017 .
- 7) K. RILES . PUBLISHED IN PROGRESS IN PARTICLE & NUCLEAR PHYSICS 68 (2013).
- 8) B.S. SATHYAPRAKASH, arXiv: 0903.0338v1 [gr-qc] Mar 2009 .
- 9) THE SENSITIVITY OF THE ADVANCED LIGO DETECTORS AT THE BEGINNING OF GRAVITATIONAL WAVE ASTRONOMY . arXiv:1604.00439v2 [astro-ph.2M] 22 Sep 2016.
- 10) A. I. LVOVSKY . arXiv :1401.4118v2 [ quant-ph] 28 jul 2016 .
- 11) C. MISNER, K. THORNE, J. WHEELER, GRAVITATION, FREEMAN, 1973 .